

FROM NANOCONTAINER TO NANOCATALYST: MECHANISTIC STUDIES OF [2+2]
PHOTODIMERIZATION OF COUMARIN DERIVATIVES WITHIN CUCURBIT[8]URIL

A Dissertation

Submitted to the Graduate Faculty

of the

North Dakota State University

of Agriculture and Applied Science

By

Barry Charles Pemberton

In Partial Fulfillment of the Requirements

for the Degree of

DOCTORATE OF PHILOSOPHY

Major Department:

Chemistry and Biochemistry

August 2012

Fargo, North Dakota

North Dakota State University
Graduate School

Title

FROM NANOCONTAINER TO NANOCATALYST: MECHANISTIC STUDIES OF
[2+2] PHOTODIMERIZATION OF COUMARIN DERIVATIVES WITHIN
CUCURBIT[8]URIL

By

Barry Charles Pemberton

The Supervisory Committee certifies that this *disquisition* complies with North Dakota State University's regulations and meets the accepted standards for the degree of

DOCTOR OF PHILOSOPHY

SUPERVISORY COMMITTEE:

Prof. Sivaguru Jayaraman

Chair

Prof. Seth C. Rasmussen

Prof. Wenfang Sun

Prof. Achintya N. Bezbaruah

Approved:

April 10th 2013

Date

Prof. Greg Cook

Department Chair

ABSTRACT

Controlling photoreactions remains a formidable challenge to chemists who have developed several approaches with varying degrees of success to achieve high reactivity/selectivity. Following nature's footprints, chemists have explored the use of confined media for controlling photoreactions. This thesis explores catalytic aspects of a water-soluble supramolecule known as a cucurbituril. Cucurbituril is a macrocyclic oligomer with a large enough cavity to sequester two guest molecules of appropriate size. The guest molecules explored in this thesis are coumarins. The model investigation involves host-guest complexes between cucurbit[8]uril (CB[8]) and coumarins to study the [2+2] photodimerization reaction in water through various spectroscopic techniques.

Our initial investigations explored the formation of host-guest complexes with coumarin guests that interacted with CB[8] host. This host guest complexation was used to explore and control photochemical reaction and photophysical properties of encapsulated coumarin guest molecules. The host-guest complexation was found to be dependent on the polarity of the coumarin and the volume constraints imparted by the CB[8] cavity. Observational insights from various coumarins provided an understanding into formation of host-guest complexes with CB[8]. Some coumarins do not form complexes but if they do they formed 1:1 and 1:2 host guest complexes as well as dynamic host-guest complexes (mixture of 1:1 and 1:2 host-guest complexes). Using dynamic host-guest complexes, we explored the use of CB[8] as a photocatalysts. Photodimerization of 6-methylcoumarin was explored as a model system to understand the supramolecular aspects of photocatalysis mediated by CB[8]. The mechanism of supramolecular photocatalysis mediated by CB[8] was elucidated using various spectroscopic techniques. Both steady state and time-resolved experiments were carried out to ascertain the thermodynamic and kinetic aspects of the supramolecular catalytic process. Spectroscopic investigations provided insights into vital role of dynamic host-guest complexes in the catalytic cycle as well as the extrusion of photoproduct from the cavity to enable turnover in the system. Thus this investigation provided an opportunity to build an overall picture of a novel supramolecular photocatalytic process in water. This will undoubtedly foster further development in the area of supramolecular photocatalysis.

ACKNOWLEDGEMENTS

“Nothing of me is original. I am the combined effort of everyone I've ever known.”

— Chuck Palahniuk, *Invisible Monsters*

I'd like to acknowledge and thank my advisor Prof. Sivaguru Jayaraman for his support and encouragement and guidance throughout my time at North Dakota State University. Without his vision and patience this process would have been much harder than it was. It has been a great honor to work with a man of such poise and character. Special thanks to my committee members, Prof. Seth C. Rasmussen, Prof. Wenfang Sun, and Achintya N. Bezbaruah for their suggestions and direction throughout this journey. Their dedication in guiding me through this process has been extremely helpful.

I thank my collaborators. Without their valuable contributions to the science I never would have been able to achieve this much progress. At NDSU, I thank Prof. DK Srivastava for his assistance with many of the experiments in the realm of biological studies and access to his group instrumentations. I thank Dr. Steffen Jockusch and the late Prof. Nicholas J. Turro at Columbia University for access to their ultrafast spectroscopy instrumentations, and for their valuable ideas discussions and collaborations. I gratefully acknowledge the valuable contributions of Prof. José Paulo Da Silva for his expertise and help in ion-trap mass spectrometry studies detailed in this thesis. Finally, I need to thank Prof. Cornelia Bohne and Dr. Hao Tang for their knowledge, expertise and patience in assisting me with stopped flow spectroscopic measurements detailed in this thesis.

I thank my lab mates, the staff and everyone else at NDSU who were there to make everyday one worth enjoying. I am indebted to my wonderful friends and family who have shown their own versions of patience, and motivation during my time at North Dakota State University. The friends from my past, those in the present and into my future will always be the best part of me.

I must thank the funding agencies for this project. I need to thank the National Science Foundation for generous support through the research award (CAREER CHE- 0748525 and CHE-1213880), I also thank the NSF ND-EPSCoR for the Seed grant program and a doctoral research

fellowship (2010-2012 doctoral fellowship) that enabled me to complete this journey (Grant EPS-0447679 and Grant EPS-0814442). I would also like to thank the national science foundation for generous support for the purchase of the single crystal XRD instrument through the NSF-CRIF program (CHE-0946990), I would like to thank the College of Science and Mathematics for acknowledging my research efforts through the graduate research award.

TABLE OF CONTENTS

ABSTRACT.....	iii
ACKNOWLEDGEMENTS.....	iv
LIST OF TABLES.....	ix
LIST OF FIGURES.....	xi
LIST OF SCHEMES.....	xviii
LIST OF EQUATIONS.....	xx
LIST OF APPENDIX TABLES	xxi
ACRONYMS.....	xxiii
CHAPTER 1. AN INTRODUCTION TO SUPRAMOLECULAR HOST-GUEST CHEMISTRY, SUPRAMOLECULAR CATALYSIS AND PHOTO-REACTIVITY OF COUMARINS.....	1
1.1. Motivation.....	1
1.2. Introduction.....	1
1.3. Organic Photochemistry.....	3
1.4. Supramolecular Catalysis.....	7
1.5. Supramolecular Scaffolds to Control Photochemical Reactions.....	8
1.6. Cucurbiturils.....	11
1.7. General Scheme for Cucurbituril Catalysis.....	19
1.8. Coumarins.....	21
1.9. Investigating Host-guest Complexes by Analytical Techniques.....	25
1.10. Conclusions.....	28
1.11. References.....	29
CHAPTER 2. CUCURBIT[8]URIL AS A SUPRAMOLECULAR TEMPLATE FOR [2+2] PHOTODIMERIZATION.....	35
2.1. Introduction.....	35
2.2. Determining the Stoichiometric Ratio of Host-guest Complexes Involving Cucurbit[8]urils.....	36
2.3. Volume Calculations of Coumarin Derivatives Photoproducts.....	52
2.4. Photoreactions of Coumarin Derivatives in Isotropic Media and In Presence of CB[8]....	54
2.5. Discussion.....	87

2.6.	General Methods.....	93
2.7.	References.....	108
CHAPTER 3. EVALUATING CUCURBIT[8]URIL AS A SUPRAMOLECULAR PHOTOCATALYST.....		
		112
3.1.	Introduction.....	112
3.2.	Evaluating CB[8] as a Supramolecular Catalyst for Photoreactions.....	112
3.3.	Rates of Reactions.....	117
3.4.	X-ray Crystal Structure of 1g@CB[8] Complex.....	124
3.5.	Conclusions.....	126
3.6.	General Methods.....	128
3.7.	References.....	131
CHAPTER 4. PHOTOPHYSICS OF 6-METHYLCOUMARIN IN THE PRESENCE OF CUCURBIT[8]URIL.....		
		133
4.1.	Introduction.....	133
4.2.	Photophysical Studies of 6-methylcoumarin 1g in Presence and Absence of CB[8].....	135
4.3.	Conclusions.....	155
4.4.	General Methods.....	156
4.5.	References.....	157
CHAPTER 5. KINETICS AND MECHANISTIC INVESTIGATIONS OF HOST-GUEST COMPLEXES INVOLVING 6-METHYLCOUMARIN AND CUCURBIT[8]URIL.....		
		159
5.1.	Introduction to Analytical Techniques to Understand Host-guest Complexes.....	159
5.2.	Eyring Plot Curves.....	160
5.3.	Stopped Flow Reaction Kinetics Measurements.....	163
5.4.	Inhibition Studies of Photoproducts.....	174
5.5.	Temperature Dependence on Photoreactions	177
5.6.	NMR Studies of CB[8]:1g Complex.....	180
5.7.	Ion-trap and Liquid Chromatography Mass Spectroscopy Studies	182
5.8.	Conclusion.....	198
5.9.	References	200

CHAPTER 6. MISCELLANEOUS INVESTIGATION: TIPS AND TRICKS LEARNED DURING INVESTIGATIONS.....	202
6.1. Introduction	202
6.2. Solid State Dimerization	202
6.3. Synthesis of <i>syn</i> -HT 4g Photoproduct	214
6.4. Miscellaneous Tips and Tricks	217
6.5. References	220
APPENDIX. COMPUTATIONAL OUTPUTS OF COUMARIN DERIVATIVES TO DETERMINE VOLUME AND GEOMETRIES OF PHOTOPRODUCTS.....	223
A1. Optimized Geometric Outputs for Photodimers of 1c.....	223
A2. Optimized Geometric Outputs for Photodimers of 1d	226
A3. Optimized Geometric Outputs for Photodimers of 1e.....	231
A4. Optimized Geometric Outputs for Photodimers of 1f.....	235
A5. Optimized Geometric Outputs for Photodimers of 1g.....	239
A6. Optimized Geometric Outputs for Photodimers of 1h.....	243
A7. Optimized Geometric Outputs for Photodimers of 1k.....	247

LIST OF TABLES

<u>Table</u>	<u>Page</u>
1.1 Non-covalent energies involved in supramolecular interactions	2
1.2 Physical properties of cyclodextrins and cucurbit[n]urils	13
2.1 Concentrations of 1a and CB[8] Host-guest chemistry for ¹ H NMR and UV-vis Jobs' plot studies.....	41
2.2 Concentrations and relative host-guest ratios between CB[8] and neutral coumarins (1b – 1k).....	43
2.3 Host-guest ratio of coumarin derivatives with CB[8] from UV-vis measurements and Job's plot analysis.....	52
2.4 Calculated total volume for coumarin photodimers.....	53
2.5 Photodimerization of coumarin derivatives in various media.....	56
2.6 The masses of various CsCl ion complexes	101
2.7 The masses of CB[n]-Cs ₂ complexes.....	101
3.1 Photodimerization conversion and product distribution of 6-Methylcoumarin 1g dimers.....	117
3.2 Comparison between the rates of dimerization using various mol% of CB[8] different concentrations of 1g.....	121
3.3 Concentrations of 6-Methylcoumarin 1g and CB[8] for saturation kinetics.....	123
3.4 Single crystal collection and refinement parameters for (1g) ₂ @CB[8] HG complex.....	126
4.1 The quantum yield of fluorescence and emission maximum in various mol% CB[8] in water.....	139
4.2 The binding constant analysis and fluorescence signals of CB[8]-6-Methylcoumarin host-guest complexes.....	142
4.3 Fluorescence lifetimes of 1g@CB[8] complexes.....	144
4.4 Triplet lifetimes (τ) and pre-exponential factors (A) of transient absorption decays of ³ (1g)* at 420 nm with various mol% CB[8].....	147
4.5 The quantum yield of photodimerization of 1g with various mol% of CB[8] in water.....	154
5.1 The experimental concentrations and pertinent equation for stopped flow kinetics to determine the k ⁺ ₁₁ and k ⁻ ₁₁ for on and off rate constants for 1:1 HG complex.....	166
5.2 Concentrations and k _{obs} values employed for dilution studies.....	170
5.3 Concentrations employed and observed k _{obs} rates for 1:2 host-guest complex.....	170

5.4	Results of global fitting analysis	173
5.5	Relative starting concentrations of CB[8] and 1g for inhibition studies.....	175
5.6	Pseudo 1 st order rates of reaction with various concentrations of 1g and photoproduct inhibitor.....	175
5.7	Mixing of various volumes of CB[8] and 1g for NMR studies	181
6.1	Single crystal X-ray parameters of 1g and 2g.....	215
6.2	Single crystal X-ray parameters of BF ₃ -1g complex.....	218

LIST OF FIGURES

<u>Figure</u>	<u>Page</u>
1.1	Jablonski diagram depicting several energetic pathways for absorbance and emission of light..... 4
1.2	Energy levels for absorbance and fluorescence 5
1.3	The energetic pathways between thermal (red) and photochemical (blue) reaction coordinates.....6
1.4	Pyrene fluorescence emissions from the monomeric and excimer species in methanol 11
2.1	The UV-vis traces (Left) and the Jobs' plot (Right) demonstrating a 1:2 HG complex between CB[8] and 1a in 35% HCl/H ₂ O at 25 °C.....38
2.2	¹ H NMR (DCI/D ₂ O) titration of 1a with CB[8] showing the shift in proton resonances from various equivalence of CB[8] indicated in the spectra at 25°C..... 40
2.3	NMR titration of CB[8] with 1a showing fast exchange of the coumarin species between solution and host at 25 °C.....42
2.4	(Left) Normalized UV-vis spectra of various concentrations of CB[8] and 1b. (Right) Jobs' plot depicting a HG ratio of 1:1.7 between CB[8] and 1b in water at 25 °C..... 43
2.5	(Left) Normalized UV-vis spectra of CB[8] and 1c in different ratios. (Right) Corresponding Jobs' plot indicating no HG complexation in water at 25 °C..... 44
2.6	(Left) Normalized spectra of CB[8] and 1d in different ratios. (Right) Jobs' plot indicating no HG complexation of 1d-CB[8] system in water at 25 °C 45
2.7	(Left) Normalized spectra of CB[8] and 1e in different ratios. (Right) Jobs' plot indicating 1:2 HG complexation of 1e-CB[8] system in water at 25 °C 46
2.8	(Left) Normalized spectra of CB[8] and 1f in different ratios. (Right) Jobs' plot indicating 1:1 HG complexation of 1f-CB[8] system in water at 25 °C..... 47
2.9	(Left) Normalized spectra of CB[8] and 1g in different ratios. (Right) Jobs' plot indicating 1:1.6 HG complexation of 1g-CB[8] system in water at 25 °C..... 48
2.10	(Left) Normalized spectra of CB[8] and 1h and (Right) corresponding Jobs' plot indicating 1:1 HG complexation in water at 25 °C 49
2.11	(Left) Normalized spectra of CB[8] and 1i and (Right) corresponding Jobs' plot indicating 1:1 HG complexation in water at 25 °C 50
2.12	(Left) Normalized spectra of CB[8] 1j and (Right) corresponding Jobs' plot indicating no HG complexation in water at 25 °C 50
2.13	The equilibrium between CB[8] host and coumarin guest in solution..... 51

2.14	¹ H NMR (DCI/D ₂ O) of 1a photoproduct selectivity differences between CB[8] – DCI/D ₂ O (Top) and DCI/D ₂ O (Bottom). Product ratio is based on relative integrations of the 4-methyl handle of the photoproducts.....	55
2.15	¹ H NMR (CD ₃ OD) spectra of 1k and photoproducts before and after irradiation in various solvents and in the presence of CB[8].....	58
2.16	Expanded ¹ H NMR (CD ₃ OD) spectra of 1k and photoproducts before and after irradiation in various solvents and in the presence of CB[8]	59
2.17	¹ H NMR (CDCl ₃) spectra of photoproducts of 1b in water in the presence and absence of CB[8]	64
2.18	¹ H NMR (CDCl ₃) spectra of 1c in presence and absence of CB[8].....	65
2.19	¹ H NMR (CDCl ₃) product selectivity of 1d after irradiation in various solvents.....	68
2.20	Expanded ¹ H NMR (CDCl ₃) of 1d showing the proton shifts from the photoproducts (methyl handle) after irradiation in various solvents.....	69
2.21	¹ H NMR (CDCl ₃) spectra of the [2+2] photodimerization products of 1e in isotropic media and CB[8]	73
2.22	Expanded ¹ H NMR (CDCl ₃) spectra of the [2+2] photodimerization products of 1e in isotropic media and CB[8].....	74
2.23	¹ H NMR (CDCl ₃) spectra of the [2+2] photodimerization products of 1f in isotropic media and CB[8]	75
2.24	Expanded ¹ H NMR (CDCl ₃) spectra of the [2+2] photodimerization products of 1f in isotropic media and CB[8].....	76
2.25	¹ H NMR (CDCl ₃) photo product selectivity of 1g in various solvents and H ₂ O/CB[8].....	78
2.26	Expanded ¹ H NMR (CDCl ₃) photo product selectivity of 1g irradiated in various solvents and H ₂ O/CB[8]	79
2.27	¹ H NMR (CDCl ₃) of 1i irradiated in various solvents and H ₂ O/CB[8].....	83
2.28	Expanded ¹ H NMR (CDCl ₃) of 1i irradiated in various solvents and H ₂ O/CB[8].....	84
2.29	¹ H NMR (CDCl ₃) of 1j irradiated in various solvents and H ₂ O/CB[8].....	85
2.30	Expanded ¹ H NMR (CDCl ₃) of 1j irradiated in various solvents and H ₂ O/CB[8].....	86
2.31	¹ H NMR of 1f in CDCl ₃	95
2.32	¹ H NMR of 1h in CDCl ₃	96
2.33	¹ H NMR of 1e in CDCl ₃	97
2.34	¹ H NMR of 1i in CDCl ₃	98
2.35	¹ H NMR of 1j in CDCl ₃	99

2.36	HRMS analysis of CB[6] in the presence of CsCl ions. (Top spectra) The M/Z = 631.055 is Cs ₂ @CB[6] and the M/Z = 1297.065 is Cs ₁ @CB[6]. (Bottom spectra) The predicted value of Cs ₂ @CB[6]. The $\Delta M/M$ value is 4.75×10^{-6}	102
2.37	Expanded HRMS analysis of CB[6] in the presence of CsCl ions. (Top spectra) The M/Z= 631.055 is Cs ₂ @CB[6]. (Bottom spectra) The predicted value of Cs ₂ @CB[6]. The $\Delta M/M$ value is 4.75×10^{-6}	103
2.38	Expanded HRMS analysis of CB[8] in the presence of CsCl ions. (Top spectra) The M/Z = 797.098 is Cs ₂ @CB[8]. (Bottom spectra) The predicted value of Cs ₂ @CB[8]. The $\Delta M/M$ value is 3.14×10^{-6}	104
3.1	¹ H NMR spectra of 6-Methylcoumarin 1g photoirradiation with 50 mol% CB[8] at 24 hours (Top) and 60 minutes (Bottom). The 24 hour spectra on top shows syn-HT 4g is the major product whereas the 60 minutes spectra on bottom shows syn-HH 2g as the major product	114
3.2	¹ H NMR (CDCl ₃) spectra of photoirradiated 6-Methylcoumarin 1g reaction mixture with 50 mol% CB[8] under various atmospheres	115
3.3	¹ H NMR (CDCl ₃) spectra of 6-Methylcoumarin 1g irradiation with various amounts of CB[8]	116
3.4	A) Monitoring the photodimerization process by measuring the decrease in absorbance of 1g in the presence of 50mol% CB[8] under N ₂ atmosphere by UV-vis spectroscopy. B) Monitoring the photodimerization process by measuring the decrease in absorbance of 1g under N ₂ atmosphere by UV-vis spectroscopy. C) Kinetics plot depicting the rates of reaction for 1g with and without 50 mol% CB[8]. D and E) Photoreaction under O ₂ and Air atmospheres monitored by UV-vis spectroscopy	118
3.5	A) Kinetics photodimerization of 1g at various mol% of CB[8]; B) Rate increase with various mol% of CB[8]	119
3.6	(Top) Saturation kinetics plot with an increasing concentration of 6-methylcoumarin 1g showing sigmoidal behavior. (Bottom) Hill plot with a slope of 1.8 demonstrating positive cooperativity	122
3.7	Single crystal X-ray of 1:2 H:G complex of CB[8] and 2 units of 1g. (Left) Top and side views show the inclusion complex. (Right) Packing of CB[8] along an axis. Thermal ellipsoids are shown at 50%, water and hydrogens were removed for clarity	125
4.1	The postulated reactive pathway for the dimerization of 1g	133
4.2	(Left) The molar extinction coefficient profile of 6-methylcoumarin in water. (Right) Absorbance changes of 6-Methylcoumarin 1g when in water and in water/CB[8]	136
4.3	Emission of 6-Methylcoumarin in the presence of varying concentrations of CB[8]	137
4.4	Quantum yield of fluorescence of 6-methylcoumarin 1g ([50 μ M]) with increasing concentration of CB[8]	139

4.5	(Top) the fluorescence curve of 1 μ M CB[8] and increasing concentration of 1g. (Bottom) Non-linear fit ($R^2 = 0.9900$) of $F-F_0$ of fluorescence data at 440 nm versus total concentration of 1g.....	141
4.6	Fluorescence lifetime decays at 298 K for the lamp profile in black ($\lambda_{ex} = 340$ nm, $\lambda_{em} = 340$ nm) 1g in blue ($\lambda_{ex} = 340$ nm, $\lambda_{em} = 411$ nm) and 1g@CB[8] in red ($\lambda_{ex} = 340$ nm, $\lambda_{em} = 443$ nm).....	143
4.7	The phosphorescence emission profile at 77K of 1g in water and various CB[8] complexes. $\lambda_{ex} = 345$ nm, $\lambda_{em} = 365-670$ nm, increments = 3 nm, 100 ms window, integration from 30 – 60 ms.....	145
4.8	Triplet-triplet absorbance spectra of 6-methylcoumarin 1g in deoxygenated water.....	146
4.9	The transient lifetime decays for 1g = 50 μ M with various mol% CB[8]. The blue line represents decay kinetics of 1g in water, red and black lines represent decay kinetics of 1g with 40 mol% and 190 mol% CB[8] respectively.....	146
4.10	The first order decay rate constants of triplet-triplet absorption by laser flash photolysis excitation (308 nm) in deoxygenated aqueous solution of various 1g monitored at 420 nm. The slope provides the bimolecular self-quenching rate constant of $^3(1g)^*$ by 1g.....	148
4.11	The first order decay rate constants of the triplet-triplet absorption generated by pulsed laser excitation (308 nm) and monitoring at 420 nm of aqueous solution of 1g in the absence (red) and presence (blue) of CB[8] under various O_2 concentrations....	149
4.12	The UV-vis absorbance spectra of iron-phenanthroline complex (green) and phenanthroline (black).....	150
4.13	UV-vis spectra recorded following the irradiation of the actinometer solution. Each run is an average of at least 3 runs.....	152
4.14	The plot of moles of Fe^{2+} formed over time determined from the absorbance plot in figure 4.13.....	152
4.15	The number of moles of photoproduct formed compared to the number of photons absorbed. The number of photons absorbed is related to the flux in figure 4.14.....	153
4.16	The quantum yield of dimerization plot vs. various mol% of CB[8] in water.....	154
5.1	Cartoon representing fluorescence stopped flow technique to ascertain kinetic pathways.....	159
5.2	Arrhenius temperature relationship for unimolecular reactions.....	160
5.3	Representation of Eyring plots.....	161
5.4	Line shape and relative chemical shift for a two-site exchange. The line shapes for “a” and “g” demonstrate a Lorentzian peak where the exchange rate is slower (a) than the measurement and the exchange rate is faster (g) than the measurement respectively. The line shapes for “b” through “f” demonstrate an exchange rate that is within the time scale of the measurement taken resulting peak broadening from inhomogeneity.....	163

5.5	Initial stopped flow studies of CB[8]-1g host-guest complex. The short component (Left) has a $k_{obs} = 1.09 \pm 0.07 \text{ s}^{-1}$ and the long component (Right) has a $k_{obs} = 0.18 \pm 0.02 \text{ min}^{-1}$. The excitation wavelength $\lambda_{ex} = 325 \text{ nm}$, the signal was monitored with a $< 395 \text{ nm}$ cutoff filter	165
5.6	Stopped flow spectra for k_{obs} for the 1:1 complex. Signals increase with increasing concentration of CB[8] (see Table 5.1). a) emission slit widths = 1 mm and b) emission slit widths = 0.1 mm	167
5.7	The plotted k_{obs} data versus concentration of CB[8] to determine k_{11}^+ and k_{11}^- terms at 1 mm (red) and 0.1 mm (blue) monochromatic light	168
5.8	(Left) Fluorescence spectra of 1g (1 μM) and various concentrations of CB[8]. (Right) Normalized signal intensity from fluorescence and stopped flow data for k_1 experiment.....	169
5.9	The stopped flow decay traces of mixing 1.05 μM CB[8] with various concentrations of 1g generating the 1:2 host-guest complexation. Each trace corresponds to an average of 25 injections	171
5.10	(Left) Fluorescence spectra of CB[8] (1.05 μM) and various concentrations of 1g. (Right) Normalized signal intensity from fluorescence and stopped flow data for k_1 experiment	172
5.11	The calculated relative concentrations of each species in the host-guest system over time with starting concentrations for CB[8] and 1g at 1.05 and 2.5 μM respectively	174
5.12	Inhibition studies of 1 μM CB[8] with various concentrations of photoproduct inhibitor and 1g	176
5.13	The long-term irradiation of pre-mixed (A) and mixed (B) of 1g (100 μM) and CB[8] (1 μM) with an average of four runs	177
5.14	Reaction velocity at various temperatures for [2+2] photodimerization of 1g at (50 μM) in water.....	178
5.15	Reaction velocity at various temperatures for [2+2] photodimerization of 1g at 50 μM with 10 mol% CB[8] in water	179
5.16	The Eyring plots for the dimerization of 1g in water (Top) and in water-CB[8] (Bottom). (Right) Cartoon depicting the rate of reaction versus temperature.....	180
5.17	(Left) The UV absorbance spectra of 1g and <i>syn</i> -photodimer from LC. (Right) LC-MS trace of the irradiated aqueous solution of 1g :CB[8] complex with 0.01% of HBr (>90% conversion). The mass assignments: $M/Z \ 321 = [\text{syn-photodimer} + \text{H}]^+$; $161 = [1\text{g} + \text{H}]^+$; $665 = [\text{CB}[8]+2\text{H}]^{2+}$	183
5.18	^1H NMR spectra of methyl resonances of 1g in the presence of various amounts of CB[8] in $\text{D}_2\text{O}/\text{DCI}$	184
5.19	Expanded ^1H NMR spectra showing methyl resonances of 1g in the presence of various amounts of CB[8] in $\text{D}_2\text{O}/\text{DCI}$	185

5.20	¹ H NMR (D ₂ O/DCI) line-shape analysis of (Top) free 1g showing a Lorentzian line shape and (Bottom) Free 1g methyl resonance fitted to Gaussian line shape in the presence of 1g-CB[8]	186
5.21	ESI-MS spectrum (full scan) Fragmentation of M/Z 825 (1:2 complex). Assignments: M/Z 825: [CB8 +2• 1g +2•H] ²⁺ ; 745: [CB8 + 1g +2•H] ²⁺ (1:1 complex); 665: [CB8 +2•H] ²⁺ (empty host); 161: [1g + H] ¹⁺	187
5.22	Fragmentation of M/Z 825 (1:2 complex). Assignments: M/Z 825: [CB8 +2• 1g +2•H] ²⁺ ; 745: [CB8 + 1g +2•H] ²⁺ (1:1 complex); 665: [CB8 +2•H] ²⁺ (empty host). The fragmentation of the 1:2 (M/Z 825) complex leads mainly to the loss of one guest and subsequent formation of the 1:1 complex (M/Z 745).	188
5.23	Fragmentation of m/z 745 (1:1 complex) by He bombardment using ion-trap mass spectrometry. Assignments: m/z 745: [CB8 + 1g + 2•H] ²⁺ ; 665: [CB8 + 2•H] ²⁺ . The fragmentation of the 1:1 complex (m/z 745) leads to the loss of the guest and consequent formation of the empty host (m/z 665)	189
5.24	ESI-MS spectrum (full scan) of an irradiated aqueous solution of 1g@CB[8]with HBr 0.01% (> 90% conversion). Assignments: M/Z 161 [1 + H] ⁺ ; 665 [CB8 +2•H] ²⁺ ; 834 [CB[8]-(H ₂ O) + syn-photodimer + 2•H] ²⁺	190
5.25	Fragmentation of CB[8]-photoproduct Assignments: M/Z 665 [CB[8] +2•H] ²⁺ ; 674 [CB[8] (H ₂ O) +2•H] ²⁺ . The loss of the syn-photodimer and the loss of a water molecule by M/Z 674 confirms the assignment.....	190
5.26	The CB[8] aggregation clusters formed at near saturation conditions as analyzed by ion-trap mass spectrometry. All assignments were determined based on fragmentation patterns	191
5.27	The 1g@CB[8] complexes in the presence of CB[8] aggregates at concentrations of 35 μM for 1g and near saturation conditions for CB[8]	192
5.28	The 1g@CB[8] complexes in the presence of CB[8] aggregates at concentrations of 78 μM for 1g and near saturation conditions for CB[8]	193
5.29	A comparison of host-guest complex (Top) with 0.3% HCl and (Bottom) in pure water of 1g@CB[8] at concentrations of 78 μM for 1g and near saturation conditions for CB[8]	193
5.30	Time dependent traces of various HG complexes observed in mass spectroscopic studies. The delay time from mixing to injection is approximately 30 seconds.....	194
6.1	The solid state emission spectra of 1g (red) and a 1:2 mixture of CB[8] : 1g at 298 K. (black). λ _{ex} = 340 nm, λ _{em} = 360 – 660 nm. Slit width = 4 nm. Front face detection.....	203
6.2	The solid state emission spectra of 1g (red) and a 1:2 mixture of CB[8] : 1g at 77 K. (black). λ _{ex} = 340 nm, λ _{em} = 360 – 660 nm. Slit width = 4 nm. Front face detection.....	204
6.3	Thermal ellipsoid plot showing the packing of 1g in the <i>syn</i> -HH 2g orientation in the vertical direction and <i>syn</i> -HT 4g in the horizontal direction. Thermal ellipsoids shown at 50%.	206

6.4	¹ H NMR spectra of solid state dimerization (1 h irradiation) of 1g with and without CB[8] after mechanical grinding	207
6.5	Powder x-ray diffraction of 1g with and without CB[8] at various time intervals. The poor baseline is likely due to x-ray reflections from the amorphous glass slide	208
6.6	¹ H NMR spectra of solid-state dimerization (1 h irradiation) of 1g with and without mechanical grinding: (Blue) 1g, (Red) with CB[8] and (Black) with thiourea.....	209
6.7	¹³ C NMR of syn-HH2g photoproduct.....	212
6.8	¹ H- ¹ H COSY-NMR spectra of syn-HH 2g photoproduct in CDCl ₃	213
6.9	¹ H NMR spectra of solid-state photodimerization (1 hour irradiation) of 1g upon mechanical grinding: (Blue) 1g, (Red) in the presence of CB[8], (black) in the presence of thiourea, (green) in the presence of adamantane	216
6.10	Top view of the thermal ellipsoid plot of 1g templated by BF ₃ with the thermal ellipsoids shown at 50%	217
6.11	Screen shots from DataStation v2.5 computer program showing the light scatter icon..	220

LIST OF SCHEMES

<u>Scheme</u>		<u>Page</u>
1.1	(Left) Structural representation of α -cyclodextrin and (Right) the conical geometrical shape of the molecules.	9
1.2	Synthetic scheme for cucurbiturils.	12
1.3	Catalytic cycle of CB[6] mediated [3+2] cycloaddition of azides and alkynes.....	15
1.4	Product selectivity of aminopyridine photoproduct derivatives in solution and in CB[7]....	16
1.5	Photo-induced metal mediated diazotization of bicyclic guests in confined environments of CB[7].....	17
1.6	Inhibition of photooxidation of sanguarine via encapsulation inside CB[7].....	18
1.7	Proposed catalytic mechanism for desilylation of trimethylsilylalkynyl derivatives in the presence of silver(I) salts and CB[7] or CB[8]	19
1.8	The proposed mechanism for catalysis within the cavity. The catalytic action relies on hydrophobic interactions between the guest and cavity.....	20
1.9	The proposed mechanism for the catalysis at the rim. The catalytic action relies on the interactions between the cavity portal, the portal interacting unit and reactant of interest	21
1.10	Mechanism for the Pechmann cyclization of coumarin molecules	22
1.11	Angle between parallel dyes producing either J or H aggregates	23
1.12	Coumarin [2+2] photodimerization products	24
1.13	Pictorial representation of a Jobs' plot.	26
2.1	Templating effects of CB[8] on cationic guests.....	36
2.2	Coumarins and the corresponding photoproducts investigated for templating effects of CB[8].....	37
2.3	The possible mechanisms to explain the photoproduct selectivity in the case of polar coumarin (1k with an OH-group is given as a representative example.....	61
2.4	Photodimerization of coumarin derivatives at the CB[8] portal/rim.....	66
2.5	Templating effects of polar groups (NH_3^+ , OH) on the carbonyl portals of CB[8].....	88
2.6	The HG interactions and stoichiometry to determine product selectivity.....	90
2.7	Synthetic scheme for various methylcoumarin derivatives. The NMR for the coumarins match the previous literature reports.....	94
2.8	Synthetic scheme for synthesizing 7-acetoxy coumarin derivatives.....	94

3.1	Proposed catalytic cycle for the [2+2] photodimerization of 1g mediated by CB[8].....	128
3.2	Photos of photo-box in both closed and open form. The glass window is for interchangeable photofilters and the two black sample holders will hold standard 10 mm x 10 mm cuvettes. The photobox was placed into the photochamber allowing the light from the lamp to irradiate the samples perpendicular to the window	131
4.1	The postulated photophysical/photochemical pathways for of 1g in solution and in the presence of CB[8]	134
4.2	Catalytic cycle for the [2+2] photodimerization of 1g in the presence of CB[8] in water.	155
5.1	Mechanism for rim bound precursory guests forming the 1:1 and 1:2 HG complexes...	196
5.2	Guest molecules interacting with CB[8] at the rim.....	197
5.3	The proposed bifurcated supramolecular catalytic cycle for the 1g-CB[8] system.....	198

LIST OF EQUATIONS

<u>Equation</u>		<u>Page</u>
1.1	Transmission of light in absorbance process.....	4
1.2	Beer-Lambert Law	4
1.3	Free energy relationship to binding affinities.....	26
3.1	Relative conversion equation for NMR studies.....	129
3.2	Mass balance equation for NMR studies.....	129
3.3	Percent conversion equation for NMR studies.....	130
4.1	Quantum yield of fluorescence.....	138
4.2	Sequential binding model equation.....	141
4.3	Quantum yield of photoreaction.....	149
5.1	Host-guest complex formation.....	164
5.2	Exponential decay model curve fitting.....	167
5.3	Exponential decay model curve fitting.....	167
5.4	Global k_{obs} fitting model.....	170
5.5	k_{obs} fitting.....	170
5.6	Global fitting analysis model.....	172
5.7	Eyring equation.....	179

LIST OF APPENDIX TABLES

<u>Tables</u>		<u>Page</u>
A1	Optimized geometric parameters for anti-HT dimer of 1c	223
A2	Optimized geometric parameters for anti-HH dimer of 1c.....	224
A3	Optimized geometric parameters for syn-HH dimer of 1c.....	225
A4	Optimized geometric parameters for syn-HT dimer of 1c	226
A5	Optimized geometric parameters for anti-HT dimer of 1d.....	227
A6	Optimized geometric parameters for <i>anti</i> -HH dimer of 1d	228
A7	Optimized geometric parameters for syn-HH dimer of 1d.....	229
A8	Optimized geometric parameters for syn-HT dimer of 1d	231
A9	Optimized geometric parameters for anti-HT dimer of 1e.....	232
A10	Optimized geometric parameters for anti-HH dimer of 1e.....	233
A11	Optimized geometric parameters for <i>syn</i> -HT dimer of 1e	234
A12	Optimized geometric parameters for syn-HH dimer of 1e.....	235
A13	Optimized geometric parameters for anti-HT dimer of 1f.....	236
A14	Optimized geometric parameters for anti-HH dimer of 1f.....	237
A15	Optimized geometric parameters for syn-HT dimer of 1f.....	238
A16	Optimized geometric parameters for syn-HH dimer of 1f.....	239
A17	Optimized geometric parameters for anti-HT dimer of 1g.....	240
A18	Optimized geometric parameters for anti-HH dimer of 1g.....	241
A19	Optimized geometric parameters for syn-HT dimer of 1g	242
A20	Optimized geometric parameters for syn-HH dimer of 1g.....	243
A21	Optimized geometric parameters for anti-HT dimer of 1h.....	244
A22	Optimized geometric parameters for anti-HH dimer of 1h.....	245
A23	Optimized geometric parameters for syn-HT dimer of 1h	246
A24	Optimized geometric parameters for syn-HH dimer of 1h.....	247
A25	Optimized geometric parameters for anti-HT dimer of 1k.....	248
A26	Optimized geometric parameters for anti-HH dimer of 1k.....	249

A27	Optimized geometric parameters for <i>syn</i> -HT dimer of 1k	250
A28	Optimized geometric parameters for <i>syn</i> -HH dimer of 1k.....	251

ACRONYMS

46DMC.....	4,6-dimethylcoumarin
47DMC.....	4,7-dimethylcoumarin
6MC.....	6-methylcoumarin
7A4MC	7-Amino-4-Methylcoumarin
7AcO4MC	7-acetoxy-4-methylcoumarin
7AcOC.....	7-acetoxycoumarin
7OH4MC.....	7-Hydroxy-4-Methylcoumarin
7MeO4MC.....	7-methoxy-4-methylcoumarin
7MeOC.....	7-methoxycoumarin
ATP	adenosine-5'-triphosphate
CD.....	cyclodextrin
α -CD.....	alpha cyclodextrin
β -CD.....	beta cyclodextrin
γ -CD.....	gamma cyclodextrin
CB.....	cucurbituril
CB[5]	cucurbit[5]uril
CB[6]	cucurbit[6]uril
CB[7]	cucurbit[7]uril
CB[8]	cucurbit[8]uril
HOMO	highest occupied molecular orbital
HH.....	head-to-head
HG.....	host-guest
HRMS.....	high resolution mass spectrometry
HT.....	head-to-tail
IC.....	internal conversion
IS.....	internal standard
ISC.....	intersystem crossing

K_a	binding association constant
K_d	binding dissociation constant
LUMO	lowest unoccupied molecular orbital
μs	microsecond
ms	millisecond
NADPH	nicotinamide adenine dinucleotide phosphate
NMR	nuclear magnetic resonance
ns	nanosecond
ps	picosecond
s	second
S_0	ground state
S_1	1 st excited Singlet State
T_1	1 st excited triplet state
TTA	triplet-triplet absorbance
UV-vis	ultra-violet/visible light

CHAPTER 1. AN INTRODUCTION TO SUPRAMOLECULAR HOST-GUEST CHEMISTRY, SUPRAMOLECULAR CATALYSIS AND PHOTO-REACTIVITY OF COUMARINS

1.1. Motivation

Controlling photochemical reactions in isotropic media can be a difficult process that is ultimately dependent on several factors including but not limited to: solvent, temperature, pH, concentration and the nature of the excited state. To limit the number of variables within a photoreaction scientists have taken a cue from nature by using confined media such as zeolites, cyclodextrins (CDs) and micelles.¹⁻⁴ These organized environments can control orientation, excited state configurations, and polarity via intermolecular interactions. The intermolecular interactions are often classified under the broad term of supramolecular chemistry. Expanding on these well established supramolecular hosts we have explored the use of Cucurbit[8]uril (CB[8]) as model for a feasible and predictable nanoreactor for photo-transformations. Additionally we have shown that CB[8] compounds can be employed in substoichiometric amounts to control photoreactions, thus establishing a working supramolecular photocatalysis.⁵

1.2. Introduction

Supramolecular chemistry is the non-covalent interactions of two or more molecules in a system and has been famously described as “chemistry beyond the molecule.”⁶ These non-covalent interactions include: Hydrogen bonding, halogen bonding, π - π stacking, and other coulombic forces are listed in Table 1.1.⁷ The studies performed to understand supramolecular chemistry in the laboratory have only been around for last the 30 years or so, yet nature has perfected the use of these interactions “ab aeterno” (from the beginning). Understanding how these interactions can be used will enable us to develop supramolecular catalysts that are as efficient and as broad in scope as catalysts in nature.

1.2.1. History of supramolecular chemistry

The field of supramolecular chemistry started well before Feynman’s seminal talk “there’s plenty of room at the bottom” in 1959.⁸ In 1937, Wolf and coworkers coined the word Übermoleküle (German for supermolecule) to describe coordination and interaction of a molecular system.⁶ Actually the infancy

started with a discovery of cyclodextrin in 1891 by Villiers and the “Lock and Key” mechanism postulated by Emil Fischer in 1894. Unbeknownst to either Villers or Fischer at the time, these two concepts would merge into the field of host-guest (HG) chemistry. The first known HG complex was an inclusion of chlorine gas in a frozen water matrix studied by Sir Humphrey Davy, eighty years before Fischer or Villers would define the principle requirements of supramolecular chemistry.⁹ Ultimately these milestones paved the way for what would be a revolution in chemistry that would lend itself wonderfully to both the world of physics and biology. In 1987 Cram, Pedersen, and Lehn received the Nobel Prize in chemistry for their seminal work in supramolecular systems, most notably in the work of carcerands, crown ethers and cryptands. Their ground breaking work in the 1960’s helped to define the interactions and rules required to obtain HG complexes.¹⁰

Table 1.1 Non-covalent energies involved in supramolecular interactions⁷

Interaction	Strength (kJ mol ⁻¹)	Example
Ion-ion	200-300	Tetrabutylammonium Bromide
Ion-dipole	50-200	Na ⁺ - Carbonyl interaction
Dipole-dipole	5-50	Formaldehyde
Hydrogen bonding	4-120	DNA base pairs
Cation- π	5-80	Na ⁺ - Benzene
$\pi - \pi$	0-50	Graphite layers
van der Waals	<5 – largely related to surface area interactions	Interactions between non-polar solvents
Hydrophobic / Hydrophilic	Solvent-solvent interactions (enthalpic/entropic) contributions	Inclusion compounds in cyclodextrins

One of the most prevalent supramolecular hosts in nature is the enzyme ribulose-1,5-biphosphate carboxylase oxygenase (RuBisCO). This enzyme is responsible for the first step in carbon fixation that provides plants with glucose energy from carbon dioxide. It is considered to be the most abundant protein on earth, comprising up to 50% of the biomass that drives photosynthesis in plants.¹¹ The enzyme

functions through the performing a carboxylation reaction on ribulose-1,5-biphosphate with a molecule of carbon dioxide. It is the first reaction in the process known as the Calvin cycle, which is the fundamental process of converting solar energy into chemical energy needed to sustain life on this planet.^{11,12}

Supramolecular chemistry does not begin and end there, everything in nature works through storage and conversion of energy from one form to another. Supramolecular chemistry creates the stable structural motifs that build complicated formations and provide complicated functions such as enzymes. Science can take cues from supramolecular chemistry by developing a ground up approach to designing useful molecular motifs to develop more advanced and broader impacting applications. The observation and understanding of how these processes and molecules function reveal the complexity of nature and life.

1.3. Organic Photochemistry

1.3.1. Introduction into organic photochemistry

Photochemistry is an ever-maturing field of science that involves the use of photons as a source of energy. Light is electromagnetic radiation with a specific wavelength; one packet of light is called a photon, and each wavelength of light corresponds to a specific energy value. A Jablonski diagram shows energetic pathways that occur when light and matter interact (Figure 1.1). To understand photochemical changes we need to establish a photochemical paradigm that can describe how molecules and photons interact with each other.

Typically when a small organic molecule interacts a photon of light with the correct quantized energy level an electron from the highest occupied molecular orbital (HOMO) of the ground state gets promoted to the lowest unoccupied molecular orbital (LUMO), a higher energy state (excited state). Once a molecule is in the excited state there are several pathways it can take to relax back to the ground state. While this process can relax the excited molecule back to its own ground state, under the right conditions the molecule can proceed via a reaction pathway to a photoproduct. Photochemical reactions will be discussed with further detail in section 1.3.2 where the differences between thermal and photoreactions are contrasted.

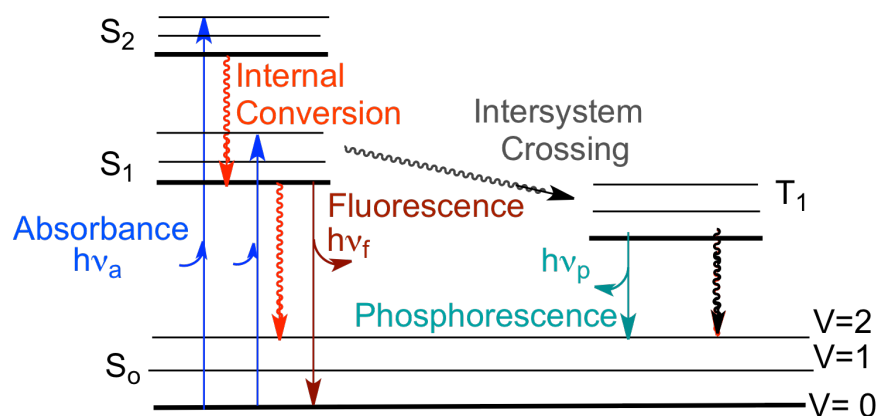


Figure 1.1 Jablonski diagram depicting several energetic pathways for absorbance and emission of light

Absorbance is the process by which a photon of light is absorbed into a molecule, exciting it to a higher energy level. This process is monitored by measuring the intensity of incoming light versus the light that passes through the sample and occurs on a femtosecond (10^{-15} s) timescale. The Beer-Lambert law describes the interaction and absorption of light while it passes through matter.¹³ The material ability of a molecule to absorb light is called the molar extinction coefficient (ϵ) which is related to the absorbance cross section (σ) and Avogadro's number ($6.022 \times 10^{23} \text{ mol}^{-1}$). The amount of radiation absorbed is directly proportional to the concentration (c) and thickness of the media (path length, b) This relationship can be described as transmittance (equation 1.1), indicating what percentage of light is transmitted through the material. It is more commonly described as absorbance "Abs" (equation 1.2), which describes how much radiation is absorbed by the sample.¹⁴

$$T = \frac{I}{I_0} \quad (1.1)$$

$$\text{Abs} = -\log\left(\frac{I}{I_0}\right) = \epsilon bc \quad (1.2)$$

Once in the first excited state (S_1), the molecule can undergo a number of relaxation processes. The most common process in molecules when they become excited is to thermally relax back down to the ground state (S_0) through a radiationless decay called internal conversion. This happens when molecules have a "loose bolt" or a part of the molecule that isn't sufficiently rigid, and removes the excess energy through vibrational motions that are essentially heat.³

The second way an excited state can relax to the ground state is by fluorescence. This is a radiative process that results in emission of a photon as the excited state of a molecule returns back to the ground state (Figure 1.2).¹⁵ In organic molecules, this typically happens within the nanosecond timescale and results in a photon of light that is lower in energy than the photon of light that was absorbed. The lower energy is primarily due to the loss through internal conversion (thermal relaxation) between discrete energy (vibronic) levels within the excited and ground states. Fluorescence spectroscopy is orders of magnitude more sensitive than absorbance spectroscopy as the wavelength of incoming light is at a different energy than the light being monitored; this allows the maximum signal changes at both the input and output.

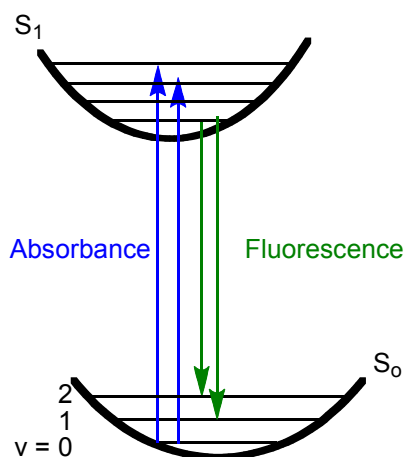


Figure 1.2 Energy levels for absorbance and fluorescence

To reach the first excited triplet state (T_1) by absorbing light, intersystem crossing (ISC) must occur from the excited state. This happens when an electron undergoes a spin flip (a forbidden process) resulting in two electrons in different orbitals with the same spin. The decay from the triplet state back to the singlet ground state is again another spin flip process, which is forbidden. Thermal (non-radiative) decay of a triplet to the ground state can also occur (when coupled to the molecule in the excited state) but typically molecules that can reach a triplet state live much longer and can phosphoresce (μs) compared to the fluorescence (ps - ns) in the singlet state decay. Since this is long lived, a molecule in such as state can encounter other molecules (such as dissolved oxygen) that may quench the

phosphorescence emission. To avoid this, phosphorescence spectra are often taken at 77 K in a frozen glass matrix or transient absorbance of the triplet state is monitored.

1.3.2. Contrasting thermal vs. photochemical reactions

Thermal reactions require enough energy to overcome a transition barrier. The activation energy associated with the transition barrier allows for greater chemical control because it allows for an optimum temperature for a reaction to proceed with specific molecular collisions driving the reaction trajectory (Figure 1.3). The photoreaction paradigm on the other hand, requires a reactant R to be excited to (R^*). This excited state R^* transitions into an intermediate I which is now in the ground state (Figure 1.3). From here the intermediate species can return to the original species R or proceed to the product P. This creates problems for molecules because the higher energy species can proceed to product, or potentially side products. This is a clear definition of why attempts at photochemically induced chiral induction using conventional methods employed for thermal reactions have ultimately failed. The energy difference in a thermal chiral reaction only need to be ~ 3 Kcal in differentiating diastereomeric transition states, whereas in a photochemical reaction the energy to create the intermediate species is almost barrier-less (downhill process), which is reflected in the product stereoselectivity. Efforts to develop chiral molecules through photosynthetic strategies has resulted in converting axially chiral molecules to point chiral molecules resulting in highly controllable stereoselectivity.¹⁶⁻²³

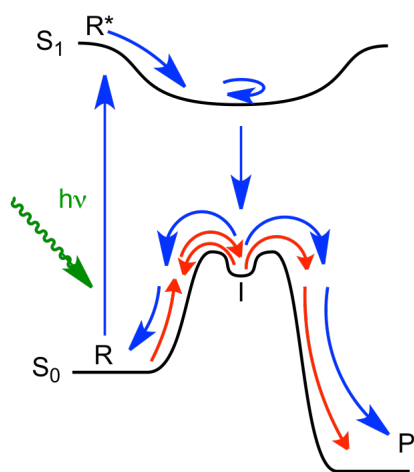


Figure 1.3 The energetic pathways between thermal (red) and diabatic photochemical (blue) reaction coordinates

1.4. Supramolecular Catalysis

1.4.1. Introduction to catalysis

A catalyst is a substance that increases the rate of a reaction without changing the overall free energy change while remaining unaffected at the end of the process. A catalyst works by decreasing the activation barrier, thus changing the required activation energy for the reaction. In thermal reactions, this allows the reaction to proceed under lower temperatures. This can prevent possible side reactions that can occur at higher temperatures. A common misconception is that a catalyst can only change the activation barrier at a transition state while preserving the mechanism and energy states of starting materials and products. Thermal catalysts obey the law of microscopic reversibility if the equilibrium of the overall reaction is preserved (with and without the presence of a catalyst) only if (1) the forward and reverse reactions occur through the same mechanism (and transition states). (2) The ground states of either the products or reactants are unaffected by presence of the catalyst.²⁴

Conversely, photochemical catalysts are seemingly barrier-less in the sense that the activation energy to perform a chemical change has been injected into the system by a photon of light. These photochemically activated species are higher energy species than a typical intermediate encountered in a thermal reaction. This is integral for organic photochemical reaction paradigm that requires a molecule to be excited into a higher energy state before it can proceed to product. Photochemical catalysis is problematic because the reaction rate (either uni or bimolecular) needs to compete with quenching of excited molecules with deactivation singlet excited state quenching rate constants around $\sim 10^9 \text{ s}^{-1}$. The triplet excited state quenching rate constants can be as fast as 10^6 s^{-1} with the orientation of the interacting molecular orbitals facilitating those transitions.

Supramolecular catalysts are often referred to as enzyme mimics since they are guided by similar molecular interactions. The first step in a reaction involves a molecular recognition step where the supramolecular host recognizes and reorders a reacting guest molecule through non-covalent interactions. This prepares the molecule for a “reaction ready” transition state. This process takes cues from nature’s enzymes that bind a molecule into a site-specific pocket, orienting the reactant in such a way that the energy that would be required to perform the reaction is significantly lowered (zinc fingers, hydrogen-bonded histidines). Complexation of reactants is very beneficial for both thermal and

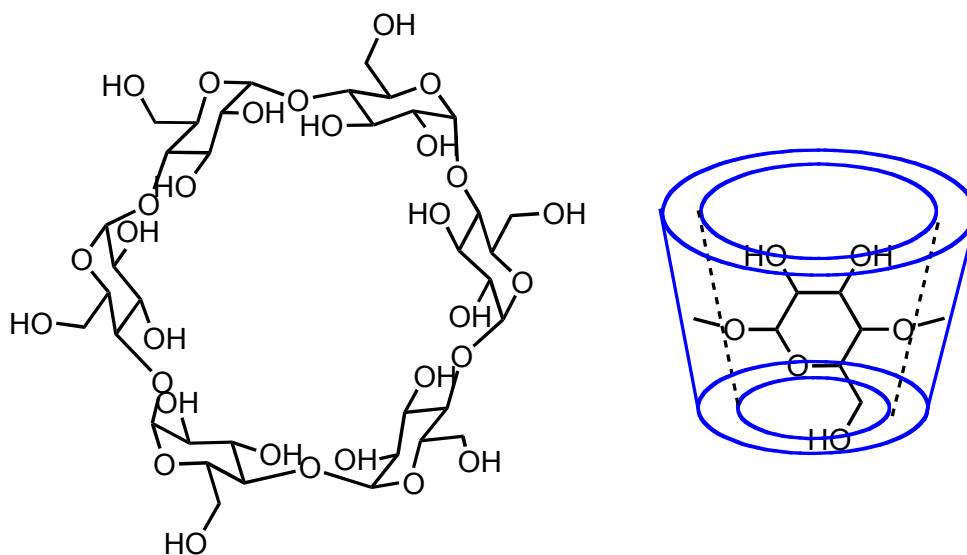
photoreactions since the competing side-reactions can be slowed or prevented outright. The problem with performing these reactions in a laboratory scale is limited by substrate scope for the reactions are very specific and finding such system is often a result of serendipity.

1.5. Supramolecular Scaffolds to Control Photochemical Reactions

Nature's most important role in sustaining life on earth is accomplished by converting carbon dioxide to oxygen through the process of photocatalysis. Chemists can use similar processes to develop ways of using light to catalyze photoreactions through HG interactions, light harvesting chromophores and initiating desirable photoreactions. However, major improvements are needed to control and perform photocatalysis for organic synthesis on the scale and with the efficiency that nature has developed over millions of years. Ultimate goal of organic photocatalysis is to provide a greener methodology for chemical synthesis. Solid phase photocatalysts like TiO_2 and ZnS offer unique features including high specificity, wide reaction scope and reduced cost, but solid phase catalysts efficiency is dependent on surface area and scaling up reactions beyond a laboratory setting can be difficult. Non-semiconducting heterogeneous photocatalysis has been limited in scope and application. However they offer advantages like controlling specific photochemical transformations, reduction of side-product formation and high photochemical efficiency.

1.5.1. Cyclodextrins

As previously mentioned, cyclodextrins (CDs) have played an integral part in the advancement of supramolecular chemistry. The structure of CDs consist of 1-4 linkages of α -D-glucopyranose sugars from six to eight units that resemble a cone with a truncated top section (Scheme 1.1). The narrow region of the CD is the location of the primary alcohol and the wider region is where the secondary alcohol units are interacting with each other. Unlike cucurbiturils (CB's) there are internal C-H hydrogen's within the CD cavity, this makes the cavity more hydrophobic, "alkane" like.²⁵ Due to their ability to sequester hydrophobic molecules CD's have been employed as hosts for various HG systems in commercial applications including deodorizers, solubilizing agents and drugs.²⁶



α -Cyclodextrin

Scheme 1.1 (Left) Structural representation of α -cyclodextrin and (Right) the conical geometrical shape of the molecules

Many investigations on host-guest (HG) interactions with CDs have been performed to determine binding constants, these experiments are performed through changes in fluorescence, absorbance, and NMR signals.²⁷ Since the discovery of inclusion complexes in the 1950's the goal has been to sequester and control various physical properties like solubility for drugs, as well as perform regiospecific chemical transformations and/or to increase the stability of the sequestered guest. There are several reviews on how CD's influence physical properties and alters the reactivity in both thermal and photochemical conditions.^{26,28} The poor photocatalytic nature of CD's can be attributed to weak binding affinities between the host and guest molecules.

1.5.2. Other supramolecular hosts (zeolites)

CD's are not the only host that alters the physical and chemical properties of the guest inside. There are numerous other hosts and one such class of host compounds are called zeolites. Zeolites are microporous aluminosilicate compounds that can be mined or synthetically grown. They have large

internal surface areas and highly controllable pore-size.¹ The major difference between the various types of zeolites is the alumina/silica ratio and the pore/ cavity size. The uniform pore size makes it possible to control host-guest complexation by restricting guests that are too large for the pore channels within the zeolite. Zeolites have many uses in industry because of their low cost and high surface area (reactivity). Some of the most common HG application for zeolites is used for cracking of crude oil into smaller straight chained hydrocarbons²⁹ at “acidic” active sites and water filtration³⁰ via cation exchange.

The cations inside zeolites are exchangeable it is possible to study heavy atom effects by replacing ions of Li^+ and Na^+ with larger cations such as Rb^+ , Cs^+ and Ag^+ . This provides a unique opportunity to study how heavy atoms can influence the intersystem crossing between the singlet and triplet states.⁴ Molecules that are classically considered as $\pi - \pi^*$ fluorophores (that typically show slow ISC rate constants) now undergo facile intersystem crossing via spin-orbit coupling with the heavy atom through a π -cation interaction. By studying how various molecules fit and interact within zeolites, scientists have developed a number of tests to figure out the orientation and volume availability within various host-cavities. These tests are invaluable for those looking to probe other HG systems for molecular recognition. Manipulating photochemical and photophysical processes by supramolecular effects have set the precedent for studying such interactions in water-soluble cucurbituril cavities(vide infra). Volumes effects of zeolite cavities can influence product selectivity of photoreactions.³¹

Luminescence probes have also been extensively used to study zeolites. Cationic species from the lanthanide and actinide series and transition metal cationic probes like $\text{Ru}(\text{bpy})_3^{2+}$ and organic probes such as pyrene have been all used with great degrees of success to understand the properties of zeolites.¹ Pyrene is a classic luminescence probe that can fluoresce as both a monomeric and dimeric (excimer) species (Figure 1.4). The monomer fluoresces between 370 and 450 nm, this happens when either the solution is dilute or if the cavity volume is sufficiently small and will not allow two pyrene units to be stacked near each other.³ While concentration controls the monomer to excimer formation in solution, the size of the cavity controls the emissive species in zeolites. If the zeolite cavity is large and two pyrenes are allowed to stack the excited state produces an excimer, which produces luminescence between 400 and 600 nm.

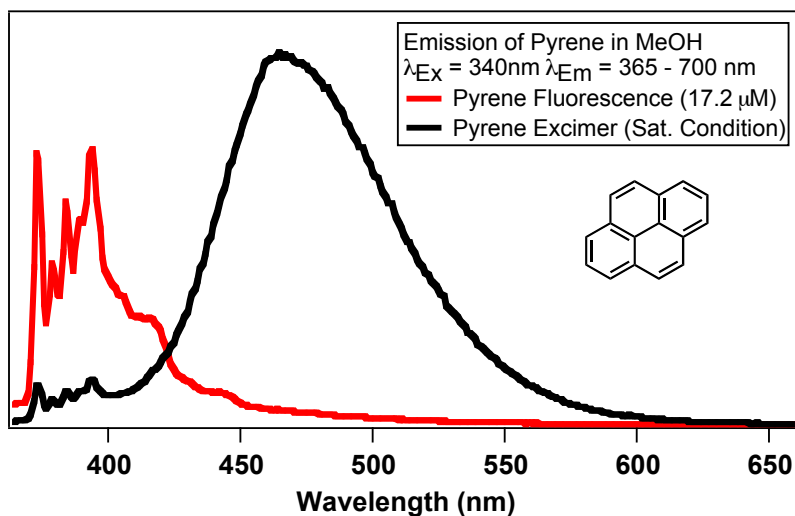
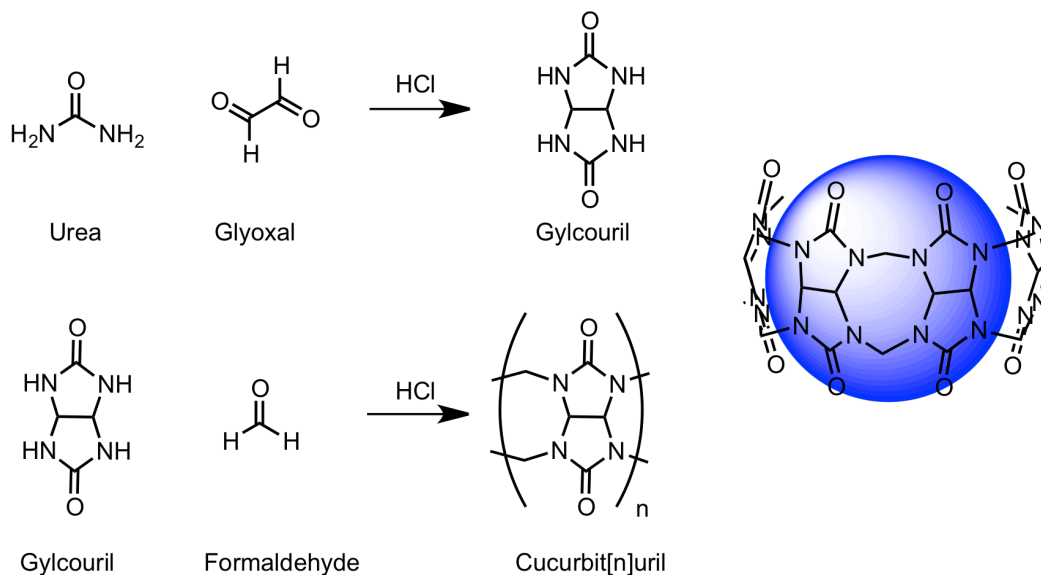


Figure 1.4 Pyrene fluorescence emissions from the monomeric and excimer species in methanol

1.6. Cucurbiturils

The story of how CBs became of scientific interest has taken some time to develop. Fourteen years after Villiers discovered cyclodextrins, in 1905 Berhend and co-workers performed a condensation reaction with glycouril and formaldehyde in acidic conditions to obtain a white amorphous solid that was only soluble in strong acids.³² The structure of the molecule was undeterminable but the researchers noted that it had the ability to bind to metal ions and dyes. It wasn't until 1981 when Mock and his co-workers repeated the experiment and obtained a crystal structure that revealed a toroidal macrocycle of six glycouril units bridged by N-methylene bridges (Scheme 1.2). Mock gave the name Cucurbituril after the plant family *cucurbitaceae* to shorten the IUPAC name. The systematic IUPAC name for CB[6] is dodecahydro-1*H*,4*H*,14*H*,17*H*-2,16:3,15-dimethano-5*H*,6*H*,7*H*,8*H*,9*H*,10*H*,11*H*,12*H*,13*H*,18*H*,19*H*,20*H*,21*H*,22*H*,23*H*,24*H*,25*H*, 26*H*,2,3,4*a*,5*a*,6*a*,7*a*,8*a*,9*a*,10*a*,11*a*,12*a*,13*a*,15,16,17*a*,18*a*,19*a*,20*a*,21*a*,22*a*,23*a*,24*a*,25*a*,26*a*-tetracosazabispentaleno[1''',6''':5'',6''']cycloocty[1'',2'',3'':3',4']pentaleno(1',6':5,6,7)-cycloocta(1,2,3-*gh*:1',2',3'-*g'h'*)cycloocta(1,2,3-*cd*:5,6,7-*c'd'*)dipentalene-1,4,6,8,10,12,14,17,19, 21,23, 25-dodecone.³³



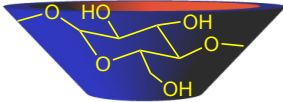
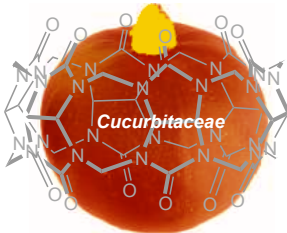
Scheme 1.2 Synthetic scheme for cucurbiturils

The number of research reports concerning CB[6] throughout the 1980's and 1990's were fairly limited but they identified a need for a larger molecule based on superior molecular recognition abilities to cyclodextrins. Larger cucurbiturils (CB[7,] CB[8], CB[10]) were isolated in 2001 by Kim's and Day's groups by subjecting the condensation reactions to a milder 9M HCl (compared to 18M H₂SO₄).^{34,35} The discovery of these larger CBs allowed for a wider scope of HG inclusions and soon many applications for HG chemistry were investigated and compared to previous host-guest systems observed with CDs.

The dimensions and volumes of CBs and CDs are very similar in a comparison between the numbers of units for each molecule Table 1.2. The similarities and differences between CBs and CDs were well established early in these investigations. CDs are both chiral and much more water-soluble compared with CBs of a similar size. This is likely a result of the connections between the oligomeric units, CDs are connected through a single sigma bond that allows the molecule to be more flexible compared to the two-methylene bridges that connect CB oligomers together. The enhanced flexibility of the CD molecules may provide the increased entropy allowing them to be more soluble, whereas the enhanced rigidity of the CB molecules decrease the solubility but can also account for the enhanced molecular recognition demonstrated by CB molecules. Rigidity is correlated to the strength of binding through molecular recognition by enhancing the enthalpic factors while reducing the entropic factors. As

a result CBs typically have a much larger binding constant and as a result the need for higher host concentrations in solution is nullified.

Table 1.2 Physical properties of cyclodextrins and cucurbit[n]urils³⁶

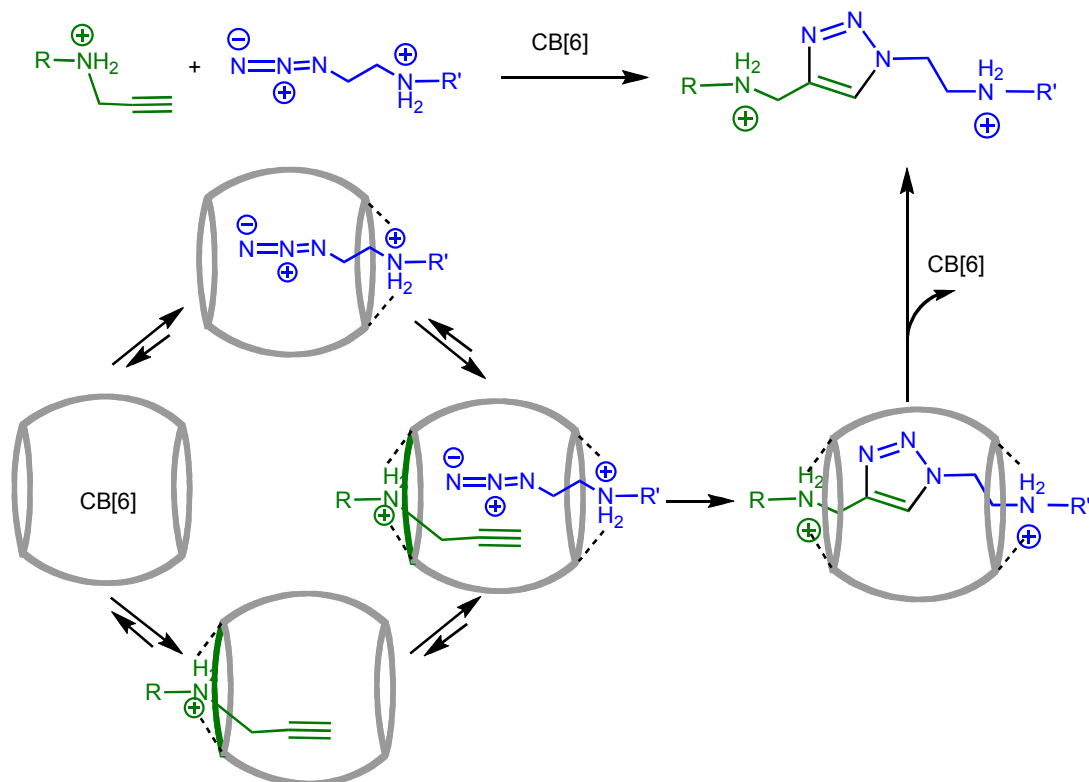
	Cyclodextrins			Cucurbit[n]urils		
						
	α -CD ²⁸	β -CD ²⁸	γ -CD ²⁸	CB [6] ³⁵	CB [7] ³⁵	CB [8] ³⁵
No of units	6	7	8	6	7	8
Mol. wt (anhydrous)	972	1135	1297	997	1163	1329
Water solubility (g/L)	145	18.5	232	<0.18	<35.0	<0.13
Cavity height (Å)	7.9	7.9	7.9	9.1	9.1	9.1
Outside diameter (Å)	13.7	15.3	16.9	14.4	16.0	17.5
Portal diameter (Å)	4.7	6.0	7.5	3.9	5.4	6.9
Inner cavity diameter (Å)	5.3	6.5	8.3	5.8	7.3	8.8
Cavity volume (Å³)	174	262	427	164	279	479

Taking advantage of CB[n]s ability to bind to guest molecules with high specificity has received the interest of pharmacologists for employment in drug delivery. CB's not only increase the solubility of a drug, but also can actually increase the binding of the drug to the target enzyme.³⁷ To make this commercially feasible researchers have tested CBs for toxicity and found that CB[n]s do not present danger to rat or humans, although further studies are needed.³⁸ Drug delivery has been an important field of chemistry since HG systems were first studied. It allows scientists better understand how to deliver drugs to targeted areas resulting in lower dosages, thus, reducing side effects.

1.6.1. Catalysis mediated by cucurbit[6]uril

The ability of cucurbiturils to promote chemical reactions has been known since Mock's follow-up to the synthesis of cucurbituril paper. He identified the ability of CB[6] to form complexes with cationic alkynes and cationic azides to promote [3+2] cycloadditions (Scheme 1.3).^{39,40} This report is a classic example where copper(I) ions are not required to perform the click reaction. This was accomplished by templating the cationic alkynes and azides to the carbonyl portal of the CB[6] cavity and the inclusion of hydrophilic functional groups within the cavity. Two interesting observations were made during this process. The first observation was that the reaction is kinetically very fast within the cavity with a 10^5 fold increase in reaction rate with CB[6] vs. free solution (absence of CB[6]). The initial "burst" of product formation was observed with a tailing rate of subsequent product formation steps. This occurs because the rate-determining step of the reaction is the release of the product. The slow release of the product is due to the size of the guest product that fits tightly inside the cavity interacting with the relatively small portal opening, thus preventing the cavity from releasing the guest. A follow-up experiment of replacing the methyl groups with a bulkier *tert*-butyl groups and observing the cessation of the catalytic cycle verified this phenomenon.

The alkyne moiety has a significantly higher dissociation constant ($K_d = 6.5 \times 10^{-4}$ M) than the azide moiety ($K_d = 2.5 \times 10^{-3}$ M) and as a result, a competitive inhibition preventing efficient reaction between the two reactants was observed. This meant that stoichiometric amounts of alkyne and azide resulted in a slower than expected reaction rate due to the favored complex of $\text{Alkyne}_2@CB6$. A work-around for the problem of competitive binding can be achieved by increasing the overall concentrations of the azide molecule. This highlighted why CB[n]'s ability to promote reactions, as well as inhibit the same reaction, is the very reason why it has taken 30 years to mature into the field of CB mediated supramolecular catalysis.



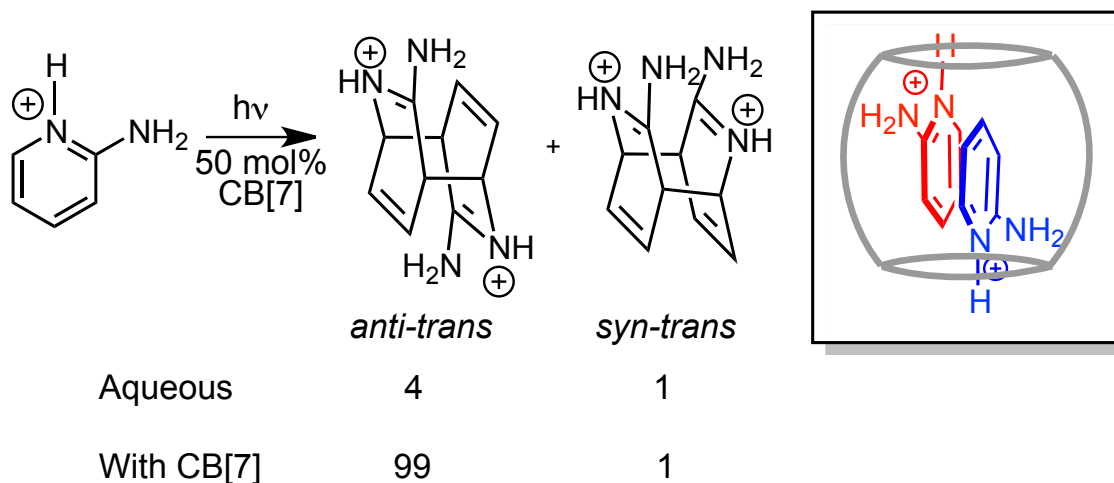
Scheme 1.3 Catalytic cycle of CB[6] mediated [3+2] cycloaddition of azides and alkynes[†]

1.6.2. Catalysis mediated by cucurbit[7]uril

When larger homologues of CB's were synthesized many research groups used CB[7] as their host of choice because of its increased solubility compared to the other homologues. CB[7] is best demonstrated as a HG diagnostics tool. The volume of CB[7] is 279 Å³ (Table 1.2) which allows for an adamantyl or aromatic compounds to bind with associative constants as high as 10¹³ M⁻¹.³⁸ These binding constants are close to the strongest of non-covalent interactions found in nature, specifically the binding of streptavidin-biotin which is around 10¹⁵ M⁻¹.⁷ Another remarkable and useful feature of CBs, not just CB[7] is the ability to bind fluorescent dyes and modulate their properties. This allows new and more sensitive biomedical applications including fluorescent labeling and photodynamic therapy.²⁵

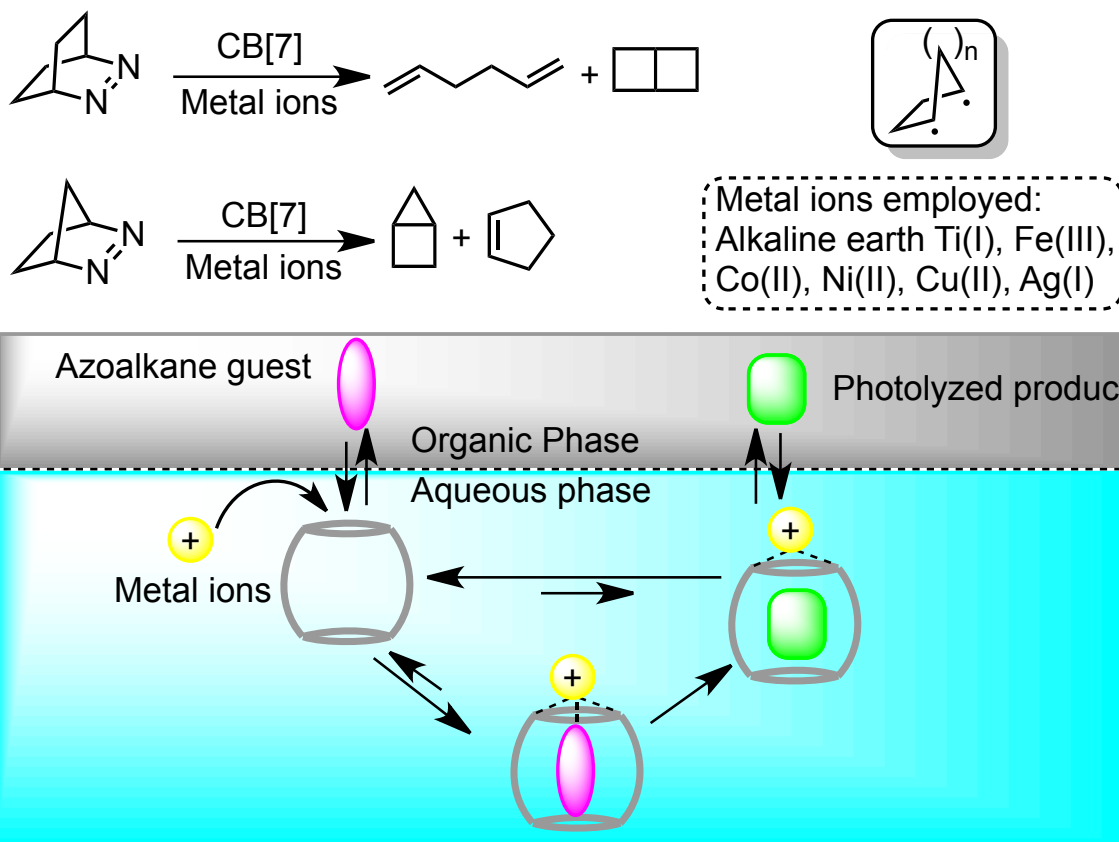
Photochemical transformations within CB[7] have been explored through bimolecular sequestration. The [4+4] photodimerization of aminopyridine derivatives within CB[7] was explored by Macartney and co-workers (Scheme 1.4).³⁷ They reported a selective photoreaction to yield exclusively *anti-trans* dimer in the presence of 50 mol% CB[7] while both *anti-trans* and *syn-trans* photoproducts were

formed in the absence of CB[7]. This reaction proceeds by binding two aminopyridine molecules within one CB[7] host, templating them in an *anti-trans* fashion. After the reaction, the stability of the photoproduct was enhanced when it was encapsulated within the cavity thereby preventing the re-aromatization, whereas in solution it reverses back to the starting materials.



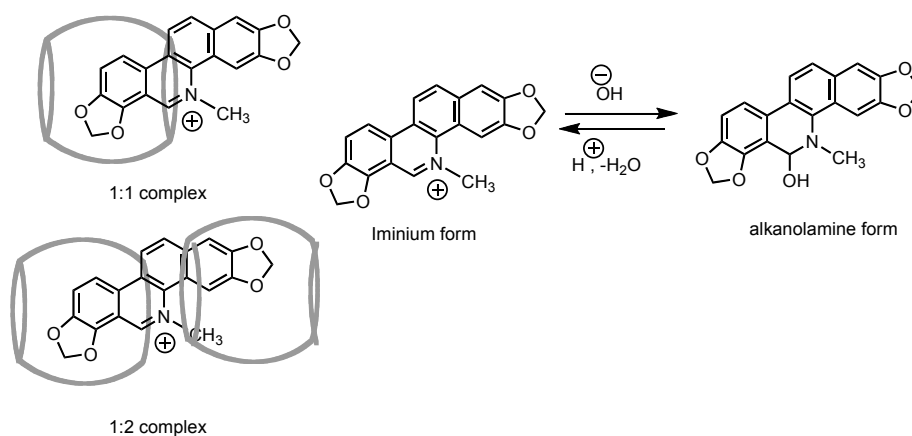
Scheme 1.4 Product selectivity of aminopyridine photoproduct derivatives in solution and in CB[7][†]

Achieving highly chemical and regioselective organic photoproducts from encapsulation has been known for some time.^{4,2} Nau and co-workers have investigated the photo-diazotization of bicyclic guests within CB[7] using metal mediated cations (Scheme 1.5).⁴¹ This study was achieved using a biphasic solution with a bicyclic azoalkane in the organic layer along with CB[7] and metal cation in the aqueous layer. The CB[7] extracted the bicyclic compound from the organic layer and sequestered a metal cation at the carbonyl portal where it interacted with the diazo functionality and promoted the diazotization, that led to photoproducts that are not favorable within isotropic media. The guest within the cavity is essentially trapped in the cavity when the reaction begins. The proximity of the radicals generated from the photoreaction allows the formation of what would be an unfavorable photoproduct if it were to take place in isotropic media.



Scheme 1.5 Photo-induced metal mediated diazotization of bicyclic guests within confined environments of CB[7]^{41,†}

With HG affinities well over 10^{10} M^{-1} it is possible to use CB[7] as a negative catalyst to inhibit reactions. Biczok and co-workers explored the ability of CB[7] to protect sanguinarine from both nucleophilic attack and photooxidation when it was present in the iminium form (Scheme 1.6).⁴² The binding affinity of the 1:1 and 1:2 complexes of CB[7] : sanguinarine are $1.0 \times 10^6 \text{ M}^{-1}$ and $\sim 10^3 \text{ M}^{-1}$ respectively. The binding of the guest resulted in a shift in the pKa by 3.69 units, enhancing the iminium form inside the CB[7] host. When encapsulated, the CB[7] prevented the nucleophilic attack of the imine carbon. This is a wonderful example on how encapsulation can protect compounds from unwanted reactivity.



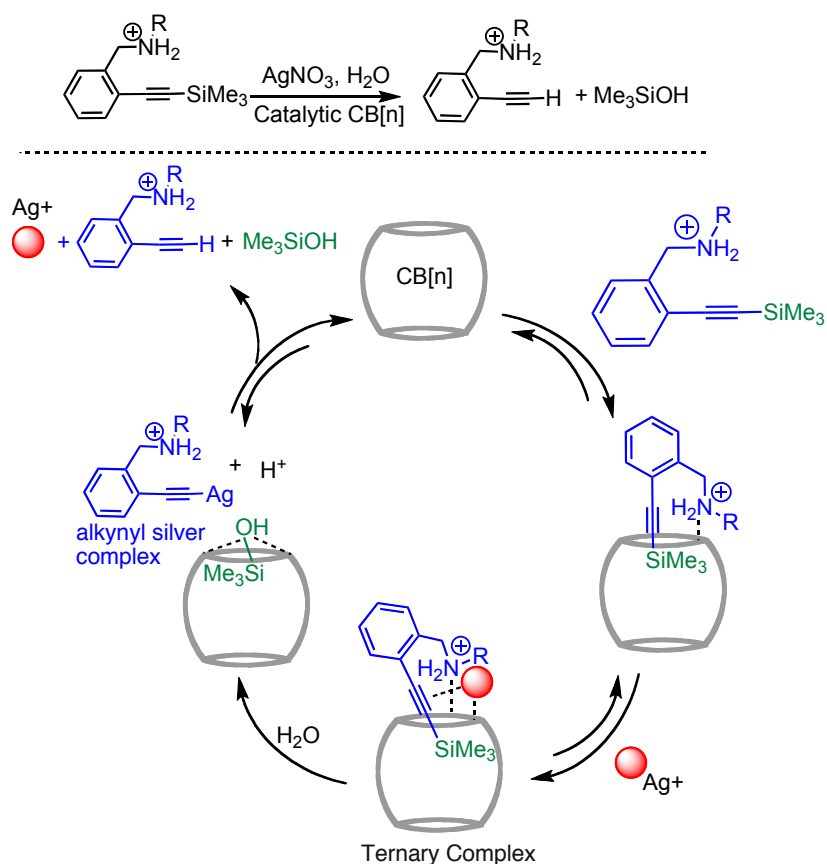
Scheme 1.6 inhibition of photooxidation of sanguarine via encapsulation inside CB[7][†]

1.6.3. Catalysis mediated by cucurbit[8]uril

As noted previously the volume of CB[8] is nearly twice that of CB[7] at 479 Å³ (Table 1.2) and allows for much larger guests to be sequestered within its cavity. Our work was the first example to demonstrate the use of CB[8] as a catalytic nano reaction vessel with as little as 10 mol% CB[8] to enhance the rate of [2+2]-photodimerization of coumarins (*vide infra*, subsequent chapters). Soon after our work was published a number of investigations using CB[8] as a catalyst appeared in literature.

The larger cavity size of CBs have also been exploited by Masson and co-workers when they used both CB[7] and CB[8] to catalyze the desilylation of trimethylsilylalkynyl derivatives using silver(I) salts (Scheme 1.7).⁴³ The HG complex revealed through NMR studies show a ternary complex where the silyl-groups are templated inside the cavity and the ammonium templates at the carbonyl rim. This orientation allows the silver ion to generate an alkynyl silver complex that is quickly hydrolyzed resulting in an alkynyl silver complex and a trimethylsilanol product.

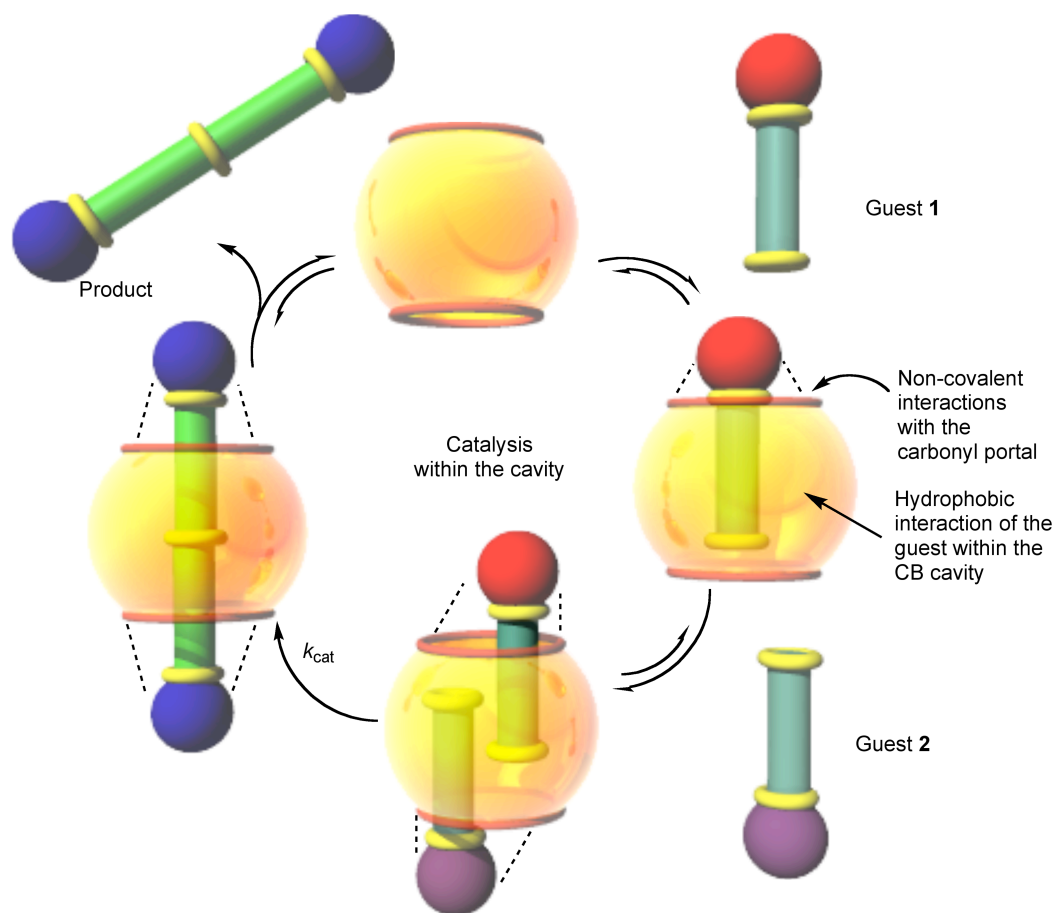
These highlighted reactions show that the catalysis can occur at both the rim and within the cavity. A need to rationalize how these reactions proceed in each case needs to be established so that further development to supramolecular catalysis can be achieved. Predicting how the HG interactions occur will also provide insights into the required spectroscopic techniques to study how the reaction proceeds.



Scheme 1.7 Proposed catalytic mechanism for desilylation of trimethylsilylalkynyl derivatives in the presence of silver(I) salts and $\text{CB}[7]$ or $\text{CB}[8]^{\dagger}$

1.7. General Scheme for Cucurbit[n]uril Catalysis

The catalytic cycle for all $\text{CB}[n]$ s function through a similar pathway (Scheme 1.8). The empty cavity binds the first guest and the second guest. The uptake of these guests can be either sequential or in a random association like fashion. The interaction of the two guests within the cavity allows for increased molecular collisions due to the proximity of the reactants. When bound in this orientation we can consider the reactants to be in a “reaction ready” form. The energy barrier for thermal reactions should be reduced due to the close proximity of reactants. In the case of photochemical reactions, one of the molecules absorbs a photon of light that brings the reactant to an excited state. From there, the excited reactant becomes an intermediate that is energetically favorable to form the product(s).

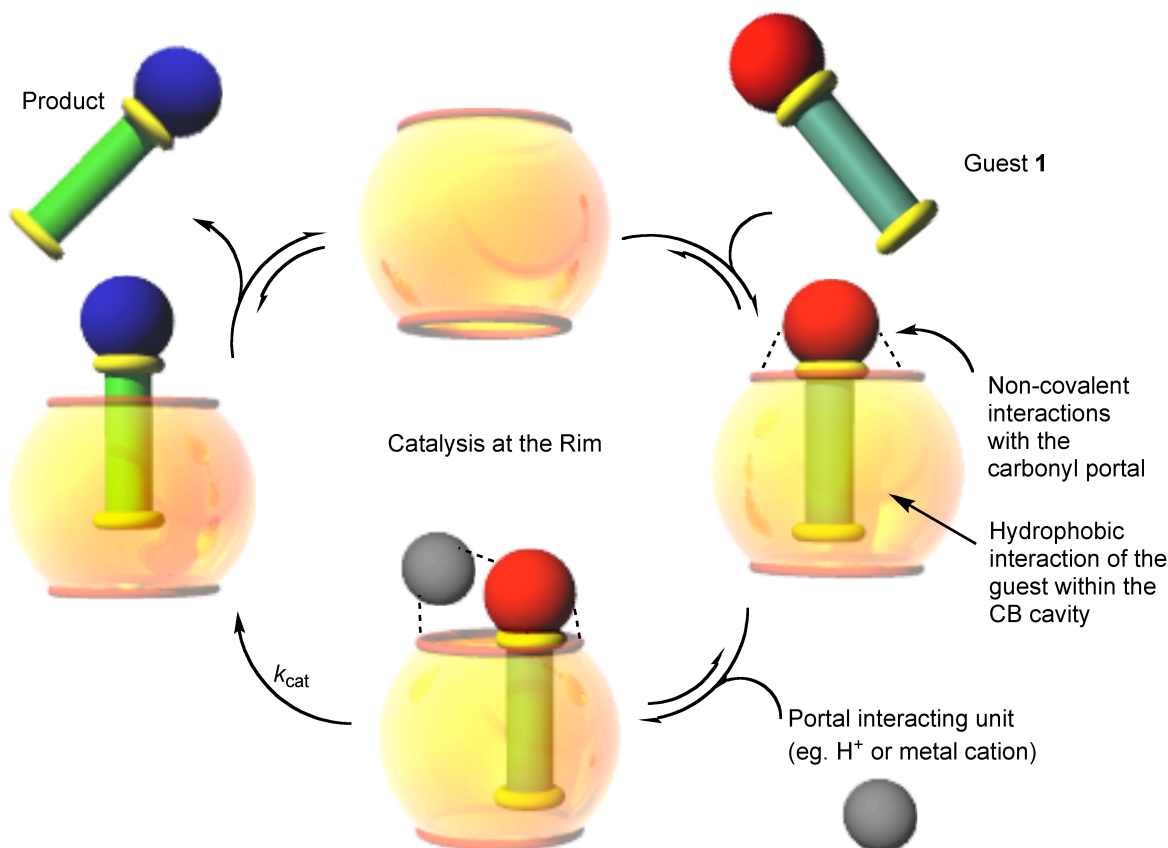


Scheme 1.8 The proposed mechanism for catalysis within the cavity. The catalytic action relies on hydrophobic interactions between the guest and cavity[†]

Reactions that take place at the rim typically involve the role of cations in the form of protons or metal ions. These species weakly interact with the guest in neat solution but are effective at initiating reactions when proximally located near the host and guest (Scheme 1.9). Prior to forming the reactive complex, the guest enters the cavity in a fashion where the reactive site is exposed at the carbonyl portal of the cavity. Then cation can interact with the carbonyls at the portal rim and in proximity of the reactive site of the guest molecule making the complex favorable for a reaction to occur.

Supramolecular catalysis either in the cavity or at the rim use noncovalent forces such as hydrophobic, hydrophilic and columbic interactions to produce metastable HG complexes. These complexes can easily proceed to the next step in a reaction mechanism since the reactant(s) are in a favorable orientation. These two descriptions are the general mechanism postulated to drive catalysis in

CBs. The biggest challenge for these systems to be catalytic is the off rate of the product, thus preventing inhibition. Prior to the demonstration of catalytic turnover, the product HG complex formed from the reaction(s) were more energetically favored than the HG complexes between the reactants and the CB host.



Scheme 1.9 The proposed mechanism for the catalysis at the rim. The catalytic action relies on the interactions between the cavity portal, the portal interacting unit and reactant of interest[†]

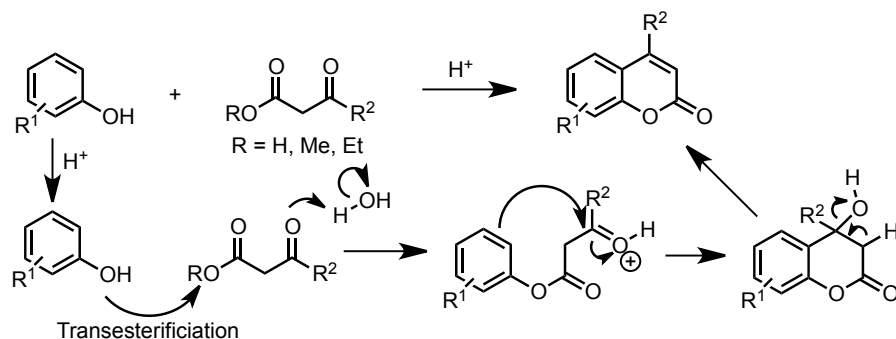
1.8. Coumarins

1.8.1. Introduction into coumarins

Coumarins are class of benzolactone compounds with interesting photophysical and photochemical proprieties. The lowest excited state of coumarins can either be from the $\pi-\pi^*$ or $n-\pi^*$ excited state depending on the location and type of substituent on the coumarin chromophore. Coumarins have a high molar absorptivity typically at 280 nm, 320 nm and higher wavelengths if further conjugated.

These molecules have been used as fluorescence tags, biomarkers, blood thinners, antioxidants, and sunscreens. They can also undergo photoreactions, specifically [2+2]-photodimerization.

Several synthetic strategies have been employed to make coumarin molecules. The Pechmann condensation reaction is extensively used for synthesizing substituted coumarins from appropriately substituted phenols and reacting it with a β -carbonyl acid or ester in acidic conditions (Scheme 1.10). The mechanism starts with a nucleophilic attack of the phenol to the ester, which is enhanced by a better leaving group (EtO > MeO > HO). The aromaticity is broken due to an attack on the β -carbonyl carbon, the aromaticity is regained upon elimination of H^+ leading to the coumarin product. Using meta-substituted phenols, 7-substituted coumarins can be synthesized as the major product and 5-substituted coumarins as the minor product. 3-substituted coumarins require a Knoevenagel reaction with appropriate substituted salicylaldehydes with electron deficient malonates.^{44,45} The synthesis of 3-substituted coumarins has been extensively studied, however these coumarins were not investigated in our study and will not be discussed.

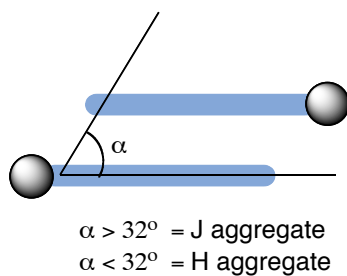


Scheme 1.10 Mechanism for the Pechmann cyclization of coumarin molecules

1.8.2. Photophysical properties of coumarins

Due to the ease of synthesis, the photophysical, photochemical and pharmacological properties of coumarins are often employed as fluorescent tags for biological markers. Many coumarins have been used as laser dyes which absorb at lower wavelengths (higher energy) and fluoresce at higher wavelengths (lower energy) with quantum efficiencies near 1.0. These laser dyes are used to increase signal from light sources and emit at a well established visible wavelength range. Depending on the substitution of the coumarin, the excitation of the chromophore to the S_1 singlet state can either be $n-\pi^*$ or

π - π^* transition.⁴⁶ The fluorescence emission of coumarins can change if two molecules are within close proximity to each other *viz.* aggregation. If coumarins form an aggregate the emission that follows will likely be shifted either to the red (lower energy) or blue (higher energy). When aggregates form they typically form in head-to-head (HH) or head-to-tail (HT) orientations. When head-to-head aggregates are formed the transition moments (dipole-dipole interactions) of the complex is greater than the individual species.⁴⁷ If H-aggregates emit, blue shift in the emission maxima will be observed. However these typically relax to the ground state through excitonic bands, and they are difficult to detect.⁴⁸ When head-to-tail aggregates are formed the transition moment is near zero, these aggregates are called J-aggregates and their emission results in a red shift in the emission maxima and is very easy to detect. This occurs when one molecule “slips” over another molecule (Scheme 1.11). The slip angle for a J-aggregate is typically greater than 32° . If the slip angle is less than 32° , a blue emission shift could be observed. The term J-aggregate is named after Jelly, one of the first people to investigate this phenomenon, whereas the term H-aggregate is named for the hypsochromic shift observed in the emission.



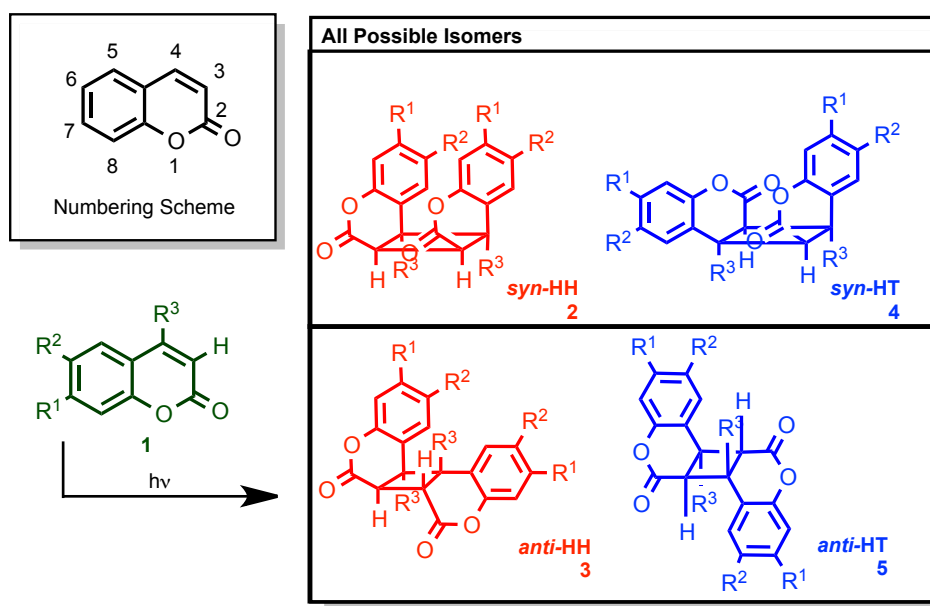
Scheme 1.11 Angle between parallel dyes producing either J or H aggregates

1.8.3. Dimerization of coumarin

Irradiation of coumarins result in [2+2]-photodimerization leading to four possible orientations, this depends on a number of factors including; solvent polarity, concentration, temperature, and time of irradiation (Scheme 1.12). Depending on the stereochemical orientation photoproducts formed can be described as *syn* or *anti* and HH or HT. *Syn* photoproducts describe a product where the substituents on the cyclobutyl-ring orient in the same direction whereas in *anti*-photoproducts the substituents on the cyclobutyl-ring are oriented in the opposite direction. The HH-configuration describes the carbonyl dipoles

orient in the same direction, whereas in the HT-configuration the carbonyl-dipoles are oriented in the opposite direction.

The NMR of photoproducts are easily determined by the resonances of the cyclobutyl protons and has been used to identify product selectivity since Hammond, Buchardt and many other groups started studying the dimerization of coumarins and carbostyrils in the 1960s and 1970s.⁴⁹⁻⁵⁹ The resonances of the protons are easily identified depending on the *syn* or *anti* configurations. The 3,4-H substituted *syn*-protons are found to resonate between 4.2 and 4.0 ppm whereas *anti*-protons are found to resonate between 3.9 - 3.6 ppm. The amount of shielding caused by aromatic group and carbonyl groups of the *anti*-products causes a greater upfield shift of the proton resonances.⁶⁰ For the 4-methyl substituted coumarins the resonance of methyl groups are used as NMR handles, these methyl groups resonate near ~1.6 ppm for *syn*-dimers and ~1.25 ppm for *anti*-dimers.



Scheme 1.12 Coumarin [2+2]-photodimerization products

1.8.4. Properties of coumarins in solution

Coumarin properties are highly influenced by their surroundings.¹⁵ The polarity of the solvent can influence the emission of the coumarin, provided that the singlet excited state proceeds through an $n-\pi^*$ transition. Increasing the solvent polarity will cause a red shift in the fluorescence emission because the

polarity of the solvent will stabilize the excited state of the molecule. If the coumarin reacts from a $\pi-\pi^*$ excited state, solvent polarity will have little to no effect on the emission in various solvents. However if the solvent or other factors promote aggregation in a head-to-tail fashion then a shift in emission will be observed.

1.8.5. Solid state dimerization

Coumarins not only dimerize in solutions, they also dimerize in the solid state. In order to dimerize in the solid state, the reacting double bonds must be within the Schmidt distance ($<4.2 \text{ \AA}$), the minimum distance required to make new bonds in solid-state photoreaction(s).⁶⁰ Crystalline packing is the major factor that describes product selectivity as well as reactivity. Typically the distance is less than 4.2 \AA , but there have been examples of distances as large as 4.7 \AA due to crystalline disorder.⁶⁰ The crystalline packing of coumarins can be very different with even minor substitutions. The majority of the studies have been employed to study the requirements of photodimerization since the rigidity of the solid allows easier rationalization of reactivities and product selectivities.

1.8.6. Coumarin complexes with large host molecules

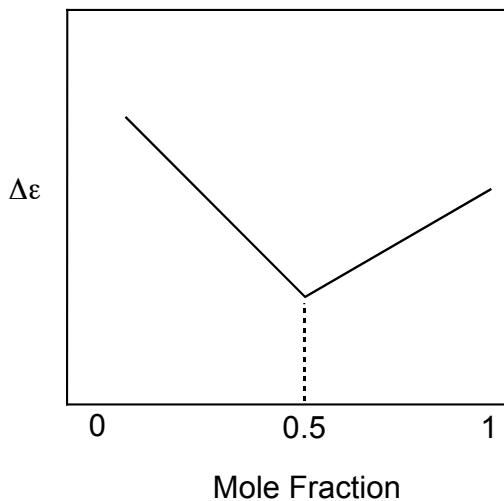
Coumarin dimerization within HG complexes has been investigated as a probe to determine product selectivity. It is possible to probe the host-molecule with small guests and determine the volume constraints within the host. This provides information about various supramolecular interactions between the host and guest, and how they will influence product selectivity. An elegant example has been reported by the groups of Wiess and Ramamurthy⁵⁵ where they have demonstrated the HG complex between β -cyclodextrin and various coumarins in solid state.

1.9. Investigating Host-guest Complexes by Analytical Techniques

1.9.1. Photophysical methods

A HG complex can be studied using numerous spectroscopic techniques. One of the most common and most versatile techniques is UV-vis absorbance. If there is an observed change in the molar absorptivity as the complex is formed it is possible to determine several different properties of the

complex. The most common observation using UV-vis is the stoichiometric ratio between the host and guest through an experiment called “method of continuous variation” (Jobs’ plot).¹³ This only works if the host and guest molecules obey the Beer-Lambert Law and the various ratios of the host and guest are mixed in such a way that the total concentration of the solution is kept constant.¹³ A graph of the change in epsilon versus the mole fraction results in a curve with an inflection point relating the relative mole fraction (Scheme 1.13).



Scheme 1.13 Pictorial representation of a Jobs’ plot

A titration of a HG complex using UV-vis can also reveal how tightly the complex is formed.²⁷ This is called a binding isotherm and it associates the equilibrium constant to the binding and unbinding of a complex. Scientists have two ways to denote binding constants, how tightly they associate (K_a) and how they dissociate (K_d). The value $K_d = (1/ K_a)$ is often the preferred method for denoting a binding affinity because it is described in units of concentration (M). The relationship between binding affinity and Gibbs free energy requires the association constant to be multiplied by a constant with dimensions of M^{-1} (Equation 1.3). The natural log of a number needs to be unitless. The values for the equation are the gas constant (R) the temperature (T) in Kelvin and the reference concentration (K_c), which, is one at standard temperature and pressure.²⁷

$$\Delta G = -RT \ln \frac{K_a}{K_c} \quad (1.3)$$

While ultraviolet-visible (UV-vis) absorption spectroscopy is sufficient for determining binding constants, fluorescence excels at it. Fluorescence emission is several orders of magnitude more sensitive because the emitted light intensity does not have to compete with the exciting light intensity due to the Stokes shift of the chromophore. The chromophore absorbs a photon of light at a higher energy (lower wavelength) and emits a photon through fluorescence at a lower energy (higher wavelength).

Fluorescence signals not only allow for studies of emission profiles, they can be used as the signal for stopped flow measurements. If a solution of host and guest are quickly added together in such a way that rapid mixing can occur before a HG complex can occur one can monitor the complex formation through a spectrophotometric technique known as stopped flow. If the reaction lifetime going from free host and guest to HG complex is longer than a few microseconds it is possible to monitor the progress of the formation. This method gives us the kinetic aspect of how long it takes to associate and dissociate a HG complex by determining the k_{on} and k_{off} rates. A key advantage of stopped flow is that, with the kinetic information, it can also verify the thermodynamic binding constants ($K = k_{on}/k_{off}$) of the HG complex. The limitation of monitoring of stopped flow kinetics using fluorescence is that the emission profile changes need to change as the ratio of HG complex changes. To work around this limitation other measurement techniques such as absorbance, electrical conductivity and optical rotation can be performed in unison with stopped flow measurements.

Fluorescence lifetimes can be used to deconvolute the environments the chromophore is located in, provided that the fluorescence lifetimes are sufficiently different and populated. This will result in a relative distribution of free and bound guests in solution at various concentrations since the quantum yield in these two environments are different. Deconvoluting absolute distributions of each may prove to be difficult. Since fluorescence lifetimes last only a few nanoseconds, it requires a very fast (<0.1 ns) flash lamp or laser pulse to irradiate the solution. A sensitive fluorescence lifetime measurement can deconvolute the bound and unbound form of the host or guest in solution provided there is sufficient population of each. This gives us an idea of the approximate value for the free and bound complexes at various concentrations.

1.9.2. NMR host-guest studies

When HG complexes are sufficiently soluble it is possible to monitor them using NMR.^{27,61} Organic HG complexes can be monitored by the shift in the resonance of a given nuclei. Often times the signal is broadened due to complexation. However, this is not always the case and is typically determined by rate of exchange between the bound and unbound forms of the complex. NMR provides an advantage over other forms of HG complex studies. The reason for this is ability to perform stoichiometric studies and visualize how the complex is formed based on the relative chemical shifts. While one of the most sensitive NMR techniques, proton NMR is not the only way to observe HG complexes. Carbon, fluorine and nitrogen NMR have all been employed to study various HG systems. The limiting factor for NMR studies of HG complexes is the solubility in the case of CB's as hosts.²⁷

1.9.3. Mass spectrometry host-guest studies

In the case of solubility issues, mass spectrometry (MS) can be used because of its ability to detect compounds in femto-molar concentrations. Here, the mass/charge ratio is measured (M/Z). This provides the ability to observe the host and guest along with HG complexes in a solution. However, there are limitations to consider in applying mass spectrometry to HG complexes. If the ionized HG complex is not stable, then detection will be nearly impossible. The ionization source needs to be relatively soft, meaning that the gas phase ions have been formed without a considerable amount of fragmentation. Fragmentation occurs when the ionized compound starts to break down into smaller pieces.

1.10. Conclusions

When applied to cucurbiturils, supramolecular chemistry can enhance selectivity and rates of reactions by pre-orienting guest molecules within host-environments in a similar manner to nature's enzymes. This application of chemistry can reach beyond the scope of traditional reactions to produce unique compounds that otherwise would be almost impossible to prepare. The ability for nature to produce complicated compounds is unparalleled in science today. By using supramolecular approaches to solving problems in chemistry scientists open up a new realm of possible solutions. This thesis pulls insights from several key genres of chemistry including photo, organic and biochemistry and

demonstrates the use of CBs as nano-reactors allowing control over photoreactions and the processes that make it catalytic.

1.11. References

- † Pemberton, B.C.; Raghunathan, R.; Volla, S.; Sivaguru, J.; From Containers to Catalysts: Supramolecular Catalysis within Cucurbiturils *Chem. Eur. J.*, 2012, 18, 12178-12190. Copyright Wiley-VCH Verlag GmbH & Co. KGaA. Reproduced with permission.
- (1) *Photochemistry and Photophysics*; CRC Press: Boston, 1991; Vol. III.
 - (2) *Photochemistry in Organized and Constrained Media*; Ramamurthy, V., Ed.; Wiley-VCH: New York, 1991.
 - (3) Turro, N. J.; Ramamurthy, V.; Scaiano, J. C. *Modern Molecular Photochemistry of Organic Molecules*; University Science Books: Sausalito, Ca, 2010.
 - (4) *Supramolecular Photochemistry*; John Wiley and Sons: New York, 2011.
 - (5) Pemberton, B. C.; Singh, R. K.; Johnson, A. C.; Jockusch, S.; Da, S. J. P.; Ugrinov, A.; Turro, N. J.; Srivastava, D. K.; Sivaguru, J. Supramolecular photocatalysis: insights into cucurbit[8]uril catalyzed photodimerization of 6-methylcoumarin *Chem. Commun.*, 47, 6323-6325.
 - (6) Steed, J. W.; Atwood, J. L. *Supramolecular Chemistry*; John Wiley & Sons: New York, 2009.
 - (7) Anslyn, E. V.; Dougherty, D. A. *Modern Physical Organic Chemistry*; University Science Books: Sausalito, Ca, 2006.
 - (8) Feynman, R. There's Plenty of Room at the Bottom *Caltech Engineering and Science* **1960**, 25, 22-36.
 - (9) Pauling, L.; Marsh, R. E. The Structure of Chlorine Hydrate *Proc. Natl. Acad. Sci. U. S. A.* **1952**, 38, 112-118.
 - (10) Lehn, J. M. Supramolecular chemistry *Science* **1993**, 260, 1762-1763.
 - (11) Feller, U.; Anders, I.; Mae, T. Rubiscolytics: fate of Rubisco after its enzymatic function in a cell is terminated *J. Exp. Bot.* **2008**, 59, 1615-1624.

- (12) Farazdaghi, H. The single-process biochemical reaction of Rubisco: A unified theory and model with the effects of irradiance, CO₂ and rate-limiting step on the kinetics of C₃ and C₄ photosynthesis from gas exchange *Biosystems*, **103**, 265-284.
- (13) Harris, D. C. *Quantitative Chemical Analysis*; 6th ed.; W.H. Freeman and Company: New York, 2003.
- (14) Rubinson, K. A.; Rubinson, J. F. *Contemporary Instrumental Analysis*; Prentice-Hall, inc: Upper Saddle, 2000.
- (15) Lakowicz, J. R. *Principles of Fluorescence Spectroscopy*; 3rd ed.; Springer: New York, 2006.
- (16) Ayitou, A. J.-L.; Sivaguru, J. Reactive spin state dependent enantiospecific photocyclization of axially chiral α -substituted acrylanilides *Chem. Commun.* **2011**, *47*, 2568-2570.
- (17) Jesuraj, J. L.; Sivaguru, J. Photochemical type II reaction of atropchiral benzoylformamides to point chiral oxazolidin-4-ones. Axial chiral memory leading to enantiomeric resolution of photoproducts *Chem. Commun.* **2010**, *46*, 4791-4793.
- (18) Ayitou, A. J.-L.; Jesuraj, J. L.; Barooah, N.; Ugrinov, A.; Sivaguru, J. Enantiospecific Photochemical Norrish/Yang Type II Reaction of Nonbiaryl Atropchiral α -Oxoamides in Solution - Axial to Point Chirality Transfer *J. Am. Chem. Soc.* **2009**, *131*, 11314-11315.
- (19) Ayitou, A. J.-L.; Sivaguru, J. Light-Induced Transfer of Molecular Chirality in Solution: Enantiospecific Photocyclization of Molecularly Chiral Acrylanilides *J. Am. Chem. Soc.* **2009**, *131*, 5036-5037.
- (20) Kumarasamy, E.; Jesuraj, J. L.; Omlid, J. N.; Ugrinov, A.; Sivaguru, J. Light-Induced Enantiospecific 4π Ring Closure of Axially Chiral 2-Pyridones: Enthalpic and Entropic Effects Promoted by H-Bonding *J. Am. Chem. Soc.* **2011**, *133*, 17106-17109.
- (21) Ayitou, A. J.-L.; Ugrinov, A.; Sivaguru, J. 6π -Photocyclization of O-tert-butylacrylanilides. N-substitution dictates the regiochemistry of cyclization *Photochem. Photobiol. Sci.* **2009**, *8*, 751-754.
- (22) Ayitou, A. J.-L.; Vallavoju, N.; Ugrinov, A.; Sivaguru, J. Enantiospecific 6π -photocyclization of atropisomeric α -substituted acrylanilides in the solid-state: role of crystalline confinement on enantiospecificity *Photochem. Photobiol. Sci.* **2011**, *10*, 1380-1383.

- (23) Bach, T.; Schröder, J. r.; Harms, K. Diastereoselective photocycloaddition of an axial chiral enamide *Tetrahedron Lett.* **1999**, *40*, 9003-9004.
- (24) Laidler, K. J.; Meiser, J. H.; Sanctuary, B. C. *Physical Chemistry*; 4th ed.; Houghton Mifflin Company: New York, 2003.
- (25) Nau, W. M.; Florea, M.; Assaf, K. I. Deep Inside Cucurbiturils: Physical Properties and Volumes of their Inner Cavity Determine the Hydrophobic Driving Force for Host–Guest Complexation *Isr. J. Chem.*, *51*, 559-577.
- (26) Breslow, R.; Dong, S. D. Biomimetic Reactions Catalyzed by Cyclodextrins and Their Derivatives *Chem. Rev.* **1998**, *98*, 1997-2012.
- (27) Connors, K. A. *Binding Constants*; John Wiley: New York, 1987.
- (28) Szejtli, J. Introduction and General Overview of Cyclodextrin Chemistry *Chem. Rev.* **1998**, *98*, 1743-1754.
- (29) Jung, J. S.; Park, J. W.; Seo, G. Catalytic cracking of n-octane over alkali-treated MFI zeolites *Appl. Catal., A* **2005**, *288*, 149-157.
- (30) Al-Haj Ali, A.; El-Bishtawi, R. ChemInform Abstract: Removal of Lead and Nickel Ions Using Zeolite Tuff *ChemInform* **1997**, *28*.
- (31) Sivaguru, J.; Natarajan, A.; Kaanumalle, L. S.; Shailaja, J.; Uppili, S.; Joy, A.; Ramamurthy, V. Asymmetric Photoreactions within Zeolites: Role of Confinement and Alkali Metal Ions *Acc. Chem. Res.* **2003**, *36*, 509-521.
- (32) Behrend, R.; Meyer, E.; Rusche, F. I. Ueber Condensationsproducte aus Glycoluril und Formaldehyd *Liebigs. Ann. Chem.* **1905**, *339*, 1-37.
- (33) Freeman, W. A.; Mock, W. L.; Shih, N. Y. Cucurbituril *J. Am. Chem. Soc.* **1981**, *103*, 7367-8.
- (34) Day, A.; Arnold, A. P.; Blanch, R. J.; Snushall, B. Controlling Factors in the Synthesis of Cucurbituril and Its Homologues *J. Org. Chem.* **2001**, *66*, 8094-8100.
- (35) Lee, J. W.; Samal, S.; Selvapalam, N.; Kim, H.-J.; Kim, K. Cucurbituril Homologues and Derivatives: New Opportunities in Supramolecular Chemistry *Acc. Chem. Res.* **2003**, *36*, 621-630.

- (36) Connors, K. A. The Stability of Cyclodextrin Complexes in Solution *Chem. Rev.* **1997**, *97*, 1325-1358.
- (37) Macartney, D. H. Encapsulation of Drug Molecules by Cucurbiturils: Effects on their Chemical Properties in Aqueous Solution *Isr. J. Chem.*, *51*, 600-615.
- (38) Walker, S.; Oun, R.; McInnes, F. J.; Wheate, N. J. The Potential of Cucurbit[n]urils in Drug Delivery *Isr. J. Chem.*, *51*, 616-624.
- (39) Mock, W. L.; Irra, T. A.; Wepsiec, J. P.; Manimaran, T. L. Cycloaddition induced by cucurbituril. A case of Pauling principle catalysis *J. Org. Chem.* **1983**, *48*, 3619-20.
- (40) Mock, W. L.; Irra, T. A.; Wepsiec, J. P.; Adhya, M. Catalysis by cucurbituril. The significance of bound-substrate destabilization for induced triazole formation *J. Org. Chem.* **1989**, *54*, 5302-8.
- (41) Kloeck, C.; Dsouza, R. N.; Nau, W. M. Cucurbituril-Mediated Supramolecular Acid Catalysis *Org. Lett.* **2009**, *11*, 2595-2598.
- (42) Biczók, L.; Wintgens, V.; Miskolczy, Z.; Megyesi, M. Fluorescence Response of Alkaloids and DAPI on Inclusion in Cucurbit[7]uril: Utilization for the Study of the Encapsulation of Ionic Liquid Cations *Isr. J. Chem.*, *51*, 625-633.
- (43) Lu, X.; Masson, E. Silver-Promoted Desilylation Catalyzed by Ortho- and Allosteric Cucurbiturils *Org. Lett.* **2010**, *12*, 2310-2313.
- (44) Ranu, B. C.; Jana, R. Ionic Liquid as Catalyst and Reaction Medium – A Simple, Efficient and Green Procedure for Knoevenagel Condensation of Aliphatic and Aromatic Carbonyl Compounds Using a Task-Specific Basic Ionic Liquid *Eur. J. Org. Chem.* **2006**, *2006*, 3767-3770.
- (45) Valizadeh, H.; Gholipur, H.; Shockravi, A. Microwave assisted synthesis of coumarins via potassium carbonate catalyzed knoevenagel condensation in 1-n-butyl-3-methylimidazolium bromide ionic liquid *J. Heterocycl. Chem.* **2007**, *44*, 867-870.
- (46) Seixas de Melo, J. S.; Becker, R. S.; Macanita, A. L. Photophysical Behavior of Coumarins as a Function of Substitution and Solvent: Experimental Evidence for the Existence of a Lowest Lying $1(n-\pi^*)$ State *J. Phys. Chem.* **1994**, *98*, 6054-6058.

- (47) Maiti, N. C.; Mazumdar, S.; Periasamy, N. J- and H-Aggregates of Porphyrin, Surfactant Complexes: Time-Resolved Fluorescence and Other Spectroscopic Studies, *J. Phys. Chem. B.* **1998**, *102*, 1528-1538.
- (48) Liu, S.; Wu, X.; Huang, Z.; Yao, J.; Liang, F.; Wu, C. Construction of pseudorotaxanes and rotaxanes based on cucurbit[n]uril *J. Inclusion Phenom. Macrocyclic Chem.* **2004**, *50*, 203-207.
- (49) Buchardt, O. The Photorearrangement of Quinoline-N-oxide *Acta Chem. Scand.* **1963**, *17*, 1461-1462.
- (50) Buchardt, O. The Structure of the Photodimers of Carbostryls and N-Methylcarbostryls *Acta Chem. Scand.* **1964**, *18*, 1389-1396.
- (51) Buchardt, O. *Photochemistry of Heterocyclic Compounds*; John Wiley & Sons: New York, 1976.
- (52) Buchardt, O.; Christensen, J. J.; Harrit, N. The photocycloaddition of cyclohexene to carbostryls *Acta Chem. Scand.* **1976**, *30*, 189-192.
- (53) Kumler, P. L.; Buchardt, O. Photochemical studies. XIV. The photolysis of 3,6-diphenylpyridazine N-oxide. Detection of a transient diazo compound *J. Am. Chem. Soc.* **1968**, *90*, 5640-5641.
- (54) Brett, T. J.; Alexander, J. M.; Stezowski, J. J. Chemical insight from crystallographic disorder-structural studies of supramolecular photochemical systems. Part 2. The β -cyclodextrin-4,7-dimethylcoumarin inclusion complex: a new β -cyclodextrin dimer packing type, unanticipated photoproduct formation, and an examination of guest influence on β -CD dimer packing *J. Chem. Soc., Perkin Trans. 2* **2000**, 1095-1103.
- (55) Moorthy, J. N.; Venkatesan, K.; Weiss, R. G. Photodimerization of coumarins in solid cyclodextrin inclusion complexes *J. Org. Chem.* **1992**, *57*, 3292-3297.
- (56) Yu, X.; Scheller, D.; Rademacher, O.; Wolff, T. Selectivity in the Photodimerization of 6-Alkylcoumarins *J. Org. Chem.* **2003**, *68*, 7386-7399.
- (57) Leenders, L. H.; Schouteden, E.; De Schryver, F. C. Photochemistry of nonconjugated bichromophoric systems. Cyclomerization of 7,7'-polymethylenedioxy coumarins and polymethylenedicarboxylic acid 7-coumarinyl diesters *J. Org. Chem.* **1973**, *38*, 957-66.
- (58) Morrison, H. A.; Curtis, H.; McDowell, T. Solvent effects on the photodimerization of coumarin *J. Am. Chem. Soc.* **1966**, *88*, 5415-19.

- (59) Hammond, G. S.; Stout, C. A.; Lamola, A. A. Mechanisms of photochemical reactions in solution. XXV. The photodimerization of coumarin *J. Am. Chem. Soc.* **1964**, *86*, 3103-6.
- (60) Gnanaguru, K.; Ramasubbu, N.; Venkatesan, K.; Ramamurthy, V. A study on the photochemical dimerization of coumarins in the solid state *J. Org. Chem.* **1985**, *50*, 2337-2346.
- (61) Sandstrom, J. *Dyanmic NMR Spectroscopy*; Academic Press: New York, 1982.

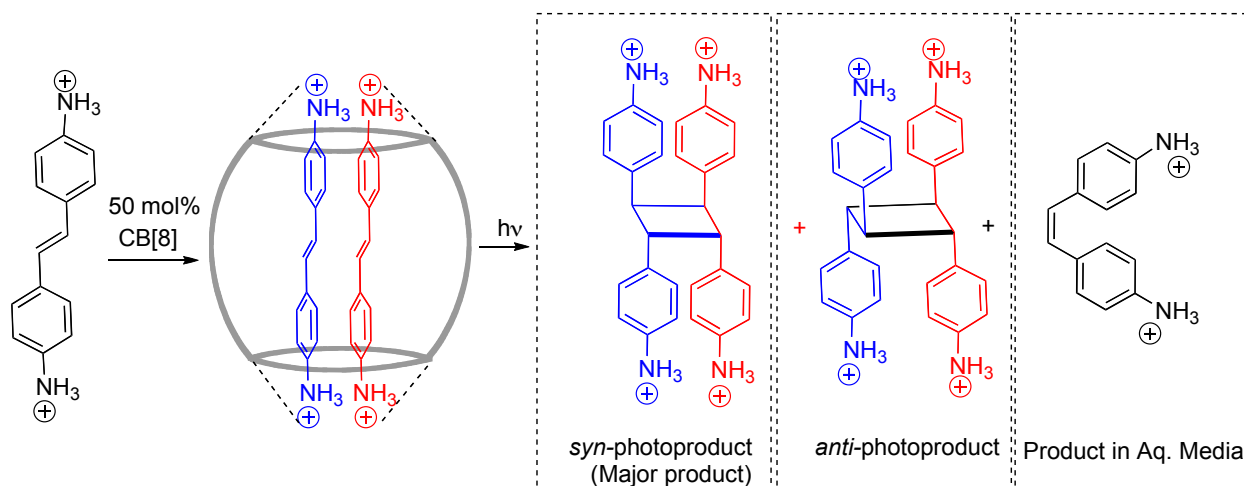
CHAPTER 2. CUCURBIT[8]URIL AS A SUPRAMOLECULAR TEMPLATE FOR [2+2] PHOTODIMERIZATION**

2.1. Introduction

Confined environments provide an opportunity to template guest molecules and allow reactions to proceed efficiently often with a degree of (chemo, regio and or stereo) selectivity. Understanding how these environments orient the guest molecules is a critical step in enhancing the further application and scope for reactions. Templating effects take into consideration a) the supramolecular interactions between the host and the guest b) the free volume of the host and volume of the guest(s) and c) the overall structural rigidity of the host system to impart a limited number of orientation(s) of the guest molecule.

The first reported guests complexed within cucurbit[8]urils (CB[8]) were cationic in nature typically in acidic media (acid/D₂O) that allowed high enough concentrations to be studied via ¹H NMR.¹ These molecules often bind with high affinities of guests ($K_a > 10^6 \text{ M}^{-1}$) and the templating effects involving cation – dipole interactions controlled the orientation and product formation in a chemical reaction (thermal and photochemical).²⁻⁷ Previous CB[n] templated photoreactions have included cationic stilbenes, azastilbenes and cinnamic acids resulting in photoproducts that are typically not formed in aqueous solution.⁸⁻¹⁰ Product selectivity for these compounds were based on the most stable configuration dictated by cation-dipole interactions at the portals of CB and by the hydrophobic interactions within the cavity. Without the templating nature of the CBs, the alkene starting materials (stilbenes, azastilbenes, and cinnamic acids) underwent *E-Z* isomerization, while in the presence of CBs they underwent [2+2] photodimerization with excellent product selectivity (Scheme 2.1).

Along with using cationic groups to template at the portals, investigations of how templating effects are influenced by increasing guest volumes have been performed. The increased volume of the guest imparts steric considerations within the cavity and plays a role in determining product selectivity. To increase the general application of cucurbiturils, it was essential to template neutral guest molecules inside the cavity.



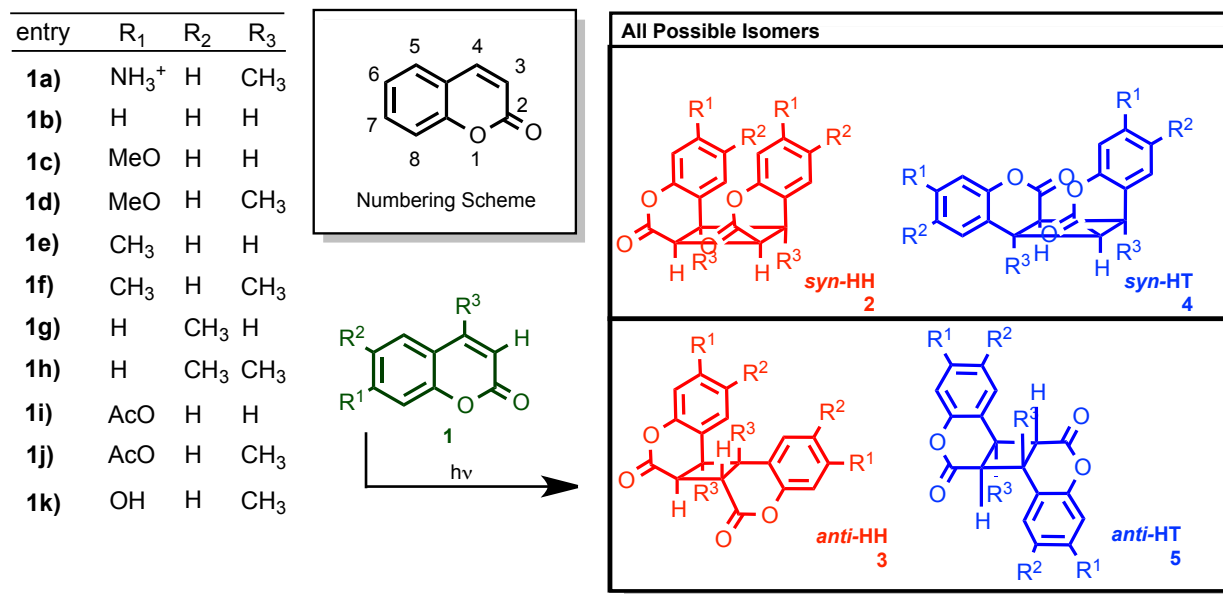
Scheme 2.1 Templating effects of CB[8] on cationic guests

To address this we carried out a systematic study by probing the templating effect of the CB[8] cavity with coumarin guests of various polarities and volumes to decipher the supramolecular interactions responsible for the host-guest (HG) formation and photoproduct selectivity upon irradiation. Additionally, we selected coumarin due to the ease of synthesis with various substitutions (as detailed in chapter 1) and its availability in both the cationic and neutral forms. The hypothesis was that product selectivity mediated by hydrogen bond / cation-dipole interactions between CB[8] and coumarin would have a different “reaction ready” orientation. The coumarins screened (Scheme 2.2) were previously reported to photodimerize with low efficiency leading to different product selectivities in various isotropic media and when sequestered by γ CD in the solid state.¹¹⁻²⁰ The photoreactions in isotropic media or in solid state typically required irradiation for greater than 72 hours. NMR studies of photoproducts had been previously established. The orientation of photoproducts allows for facile identification of the products observed after irradiation (chapter 1).

2.2. Determining the Stoichiometric Ratio of Host-guest Complexes Involving Cucurbit[8]urils

Predicting whether or not a photoreaction will take place inside a cavity without any evidence for complexation is inefficient at best. There are numerous techniques that can be employed to see if a complex between a host (CB[8]) and a guest (coumarin **1a-k**) will be formed. Since CB[8] is poorly soluble in water, the viability to perform NMR HG studies will be relegated to the specific case of 7-amino-

4-methylcoumarin **1a** that can be made cationic by dissolving in acidic solution. The cationic nature of the guest **1a** in acidic media increases the affinity for HG complexation with CB[8] and it enables us to follow the complexation by ^1H NMR in $\text{DCI}/\text{D}_2\text{O}$. UV-vis absorbance studies and Jobs' plots enabled us to investigate the remaining coumarin to determine if a HG complex is formed with CB[8] and in what ratio. While this test does not answer the question of whether a photoreaction will occur within a cavity, it will be a tool used to predict what is happening in the solution in terms of HG complex formation.



Scheme 2.2 Coumarins and the corresponding photoproducts investigated for templating effects of CB[8]

2.2.1. Host-guest complexation of 7-amino-4-methylcoumarin **1a** with CB[8]

As detailed in chapter 1, solubility is an issue when dealing with CB[8] HG. To get around this, many researchers have employed acidic media and metal cations to enhance the solubility of CBs, and specifically CB[8].²¹ The target guests for encapsulation into these cavities have been imbued with an amino functionality so that they can become protonated in acidic solution. The investigation of 7-amino-4-methyl coumarin (**1a**) is ideal to understand the nuances of HG complexation within CB[8] in the case of coumarin derivatives (Scheme 2.2).

The stoichiometric ratio of **1a** to CB[8] was determined by two independent methods, the first was the UV-vis Jobs' plot²² and the second method was via NMR.²³ These two experiments are performed at different concentrations of CB[8] and **1a**. The results of these two methods are in agreement on the

stoichiometry of the CB[8]-**1a** HG complex. The Jobs' plot (Figure 2.1) was performed by preparing several samples containing various concentrations of **1a** and CB[8] while keeping the total concentration constant in 35% HCl / H₂O. The UV-vis of each sample was taken at known concentrations of host and guest (Table 2.1) to determine the corrected absorbance values versus the mole-fraction resulting in the stoichiometric ratio of 1:2 HG complex. The corrected absorbance is essentially a change in the absorbance or epsilon value from a HG complex. This is a required correction since the UV-vis Jobs' plot method of continuous variation, must obey Beer's Law.²²

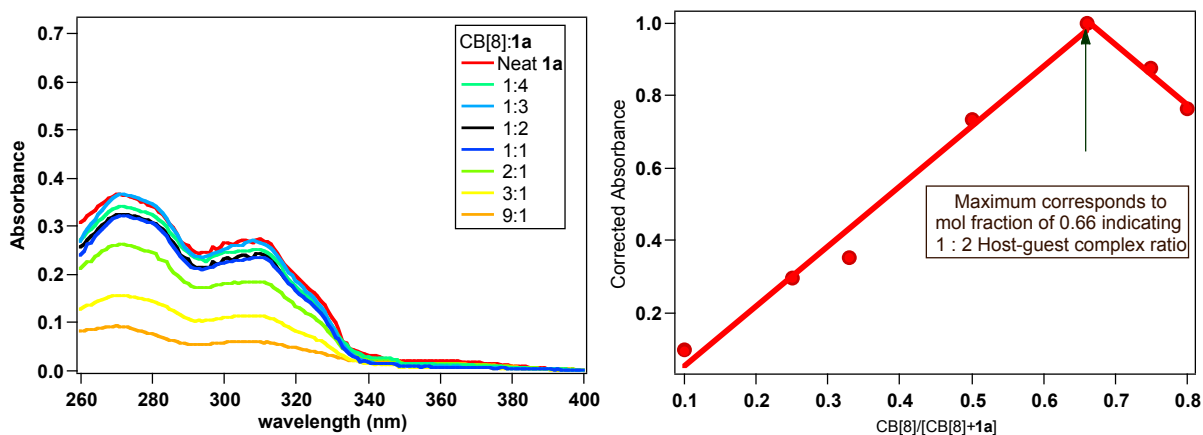


Figure 2.1 The UV-vis traces (Left) and the Jobs' plot (Right) demonstrating a 1:2 HG complex between CB[8] and **1a** in 35% HCl/H₂O at 25 °C

The NMR titration of CB[8] and **1a** (Figure 2.2) tells the same story of the 1:2 HG formation (as indicated by UV-vis Jobs' plot in Figure 2.1) and adds new information to what is actually happening in solution. The concentration employed for ¹H NMR is given in Table 2.1. As a known amount of CB[8] was added into the solution of **1a** in DCI-D₂O the methyl peak broadened and shifted (Figure 2.2) upfield. While the peak broadening was significant, the line remains relatively sharp from 0.5 to 1.0 equivalents of CB[8]. This indicated that the exchange of the **1a** was relatively fast and cannot reside in either the cavity or solution long enough to give distinct ¹H NMR resonances within the NMR time scale. In other words, under the conditions of acquisition of the ¹H NMR spectra, the signal is an average of the coumarin resonances in both free coumarin in solution and within the CB[8] cavity as either 1:1 or 1:2 HG complexes. As the amount of CB[8] in the system increases beyond a 1:1 ratio, the broadening increases,

which is indicative of a longer sequestering of the guest inside the host due to anisotropic conditions. These anisotropic conditions likely occur as the molecules lose their directional degrees of freedom. This results in the protons developing slightly different magnetic shielding based on their relative-position in each CB[8] cavity. This slight difference in magnetic shielding is reflected in enhanced broadening of the proton NMR resonances.

Tuning the tables and titrating CB[8] with **1a** (Figure 2.3) we observe a single peak through the entire titration, while the HG complex is formed. This experiment reiterates what has already been mentioned, but it's important to look at how the HG complex is formed in the presence of both excess host and excess guest. As the amount of **1a** increases, the peak becomes sharper but the proton shift for the methyl group remains almost constant at 2.51 ppm since the CB[8] exchange weighs heavily on where the complexation occurs. If the complex species were sufficiently long-lived in both solution and in the cavity we would expect to see two methyl peaks for the unbound and bound species respectively. From the inspection of Figures 2.2 and 2.3, it's clear that the exchange is fast for the CB[8]-**1a** HG system under the experimental conditions.

Inspection of Table 2.1 shows the concentrations employed for the HG complexation studies performed by ^1H NMR and UV-vis spectroscopy. Both analytical methods demonstrated the similar stoichiometric HG ratios under different concentrations. It appears the HG equilibrium under low concentrations and under high concentrations is approximately the same value. This simply means that high concentrations of CB[8] are not always required to form HG complexes. Since the molecular recognition of CB[8] is typically orders of magnitude higher than other similar hosts (CDs, etc) the resulting concentration of both host and guest can be considerably less.²⁴⁻²⁷ This raises the question; if the HG complex for cationic species can be monitored at low concentrations, does that allow for other compounds with lower solubilities to be studied using the same methodology? Since the solubility of CB[8] is considerably lower than that of γ -CD it is possible to use a smaller concentration to achieve HG complexes.

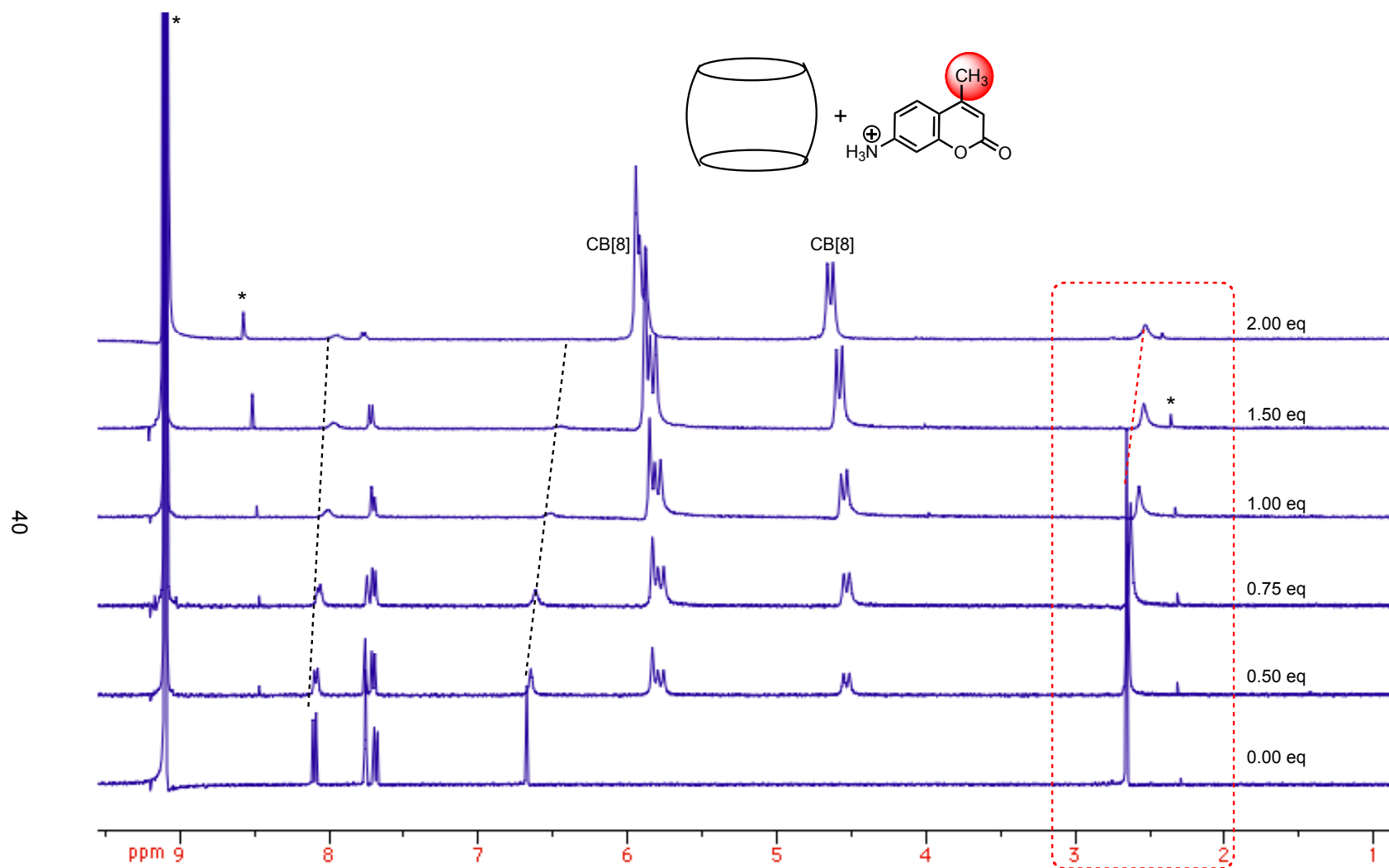


Figure 2.2 ^1H NMR ($\text{DCI}/\text{D}_2\text{O}$) titration of **1a** with CB[8] showing the shift in proton resonances from various equivalence of CB[8] indicated in the spectra at $25\text{ }^\circ\text{C}$

Table 2.1 Concentrations of **1a** and CB[8] Host-guest chemistry for ¹H NMR and UV-vis Jobs' plot studies

NMR Studies ^a			UV-vis Jobs' plot studies ^b		
[CB[8]]	[1a]	H:G Ratio	[CB[8]]	[1a]	H:G Ratio
0.000 M	0.056 M	0:1 eq	0.180 mM	0.020 mM	9:1
0.028 M	0.056 M	1:2 eq	0.150 mM	0.050 mM	3:1
0.042 M	0.056 M	2:3 eq	0.133 mM	0.067 mM	2:1
0.056 M	0.056 M	1:1 eq	0.100 mM	0.100 mM	1:1
0.084 M	0.056 M	3:2 eq	0.067 mM	0.133 mM	1:2
0.112 M	0.056 M	2:1 eq	0.050 mM	0.150 mM	1:3
-	-	-	0.040 mM	0.160 mM	1:4

^aValues for NMR studies for Figure 2.2: DCI/D₂O as ¹H NMR solvent. ^bValues for UV-vis studies with HCl-H₂O as solvent for Figure 2.1.

2.2.2. Host-guest complexation of coumarin **1b** with CB[8]

The Jobs' plot of coumarin (**1b**) via UV-vis spectroscopy was investigated to see if neutral coumarins would complex inside CB[8]. Unlike previous HG reports where cationic (typically ammonium) species at high concentrations were studied, these conditions would need to be at lower concentrations due to the decreased solubility of the guest as well as the CB[8] host. The maximum solubility for CB[8] is around 0.1 mM whereas the screened coumarins molecules have a solubility between 0.2 mM and 0.2M (depending on the type of coumarin). The total concentrations of host and guest mixtures are reported in Table 2.2. Hence, it is important when performing Jobs' plot studies to know the limits of solubility, concentration, and volumes that could be employed so that the number of data points on each side of the stoichiometric end point can be measured.

The HG ratio from the Jobs' plot of the UV-vis data for **1b** and CB[8] was determined to be 1:1.7 (Figure 2.4). This is not a clear 1:1 or 1:2 HG complex, instead it is somewhere in between the two. Since a HG complex was observed, the values indicate that both 1:1 and 1:2 complexes are present in solution. In other words, the system is likely dynamic with all three species (free, 1:1 and 1:2) co-existing in solution (chapter 3). This also raises the questions like, what role does substitutions on coumarin have in the HG formation? How will sterics affect the formation of a 1:2 or 1:1 complex? Will it be dynamic?

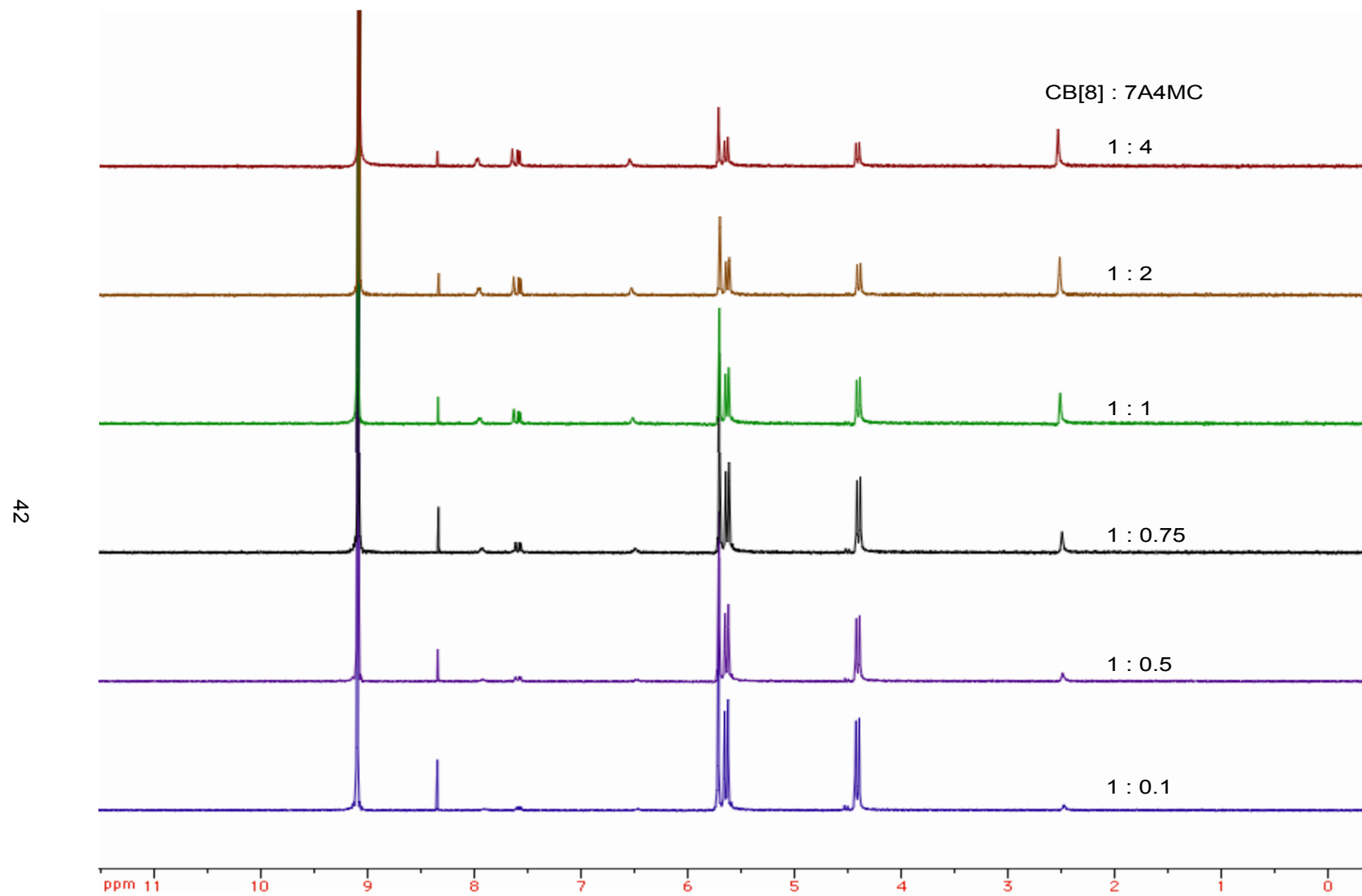


Figure 2.3 NMR titration of CB[8] with **1a** showing fast exchange of the coumarin species between solution and host at 25 °C

Table 2.2 Concentrations and relative host-guest ratios between CB[8] and neutral coumarins (**1b-1k**)

Concentration		Ratio of CB[8]:coumarin
CB[8] (M)	Coumarin (M) (1b-1k)	
1.33×10^{-4}	3.33×10^{-5}	4:1
1.17×10^{-4}	3.33×10^{-5}	3.5:1
1.00×10^{-4}	3.33×10^{-5}	3:1
6.67×10^{-5}	3.33×10^{-5}	2:1
5.00×10^{-5}	3.33×10^{-5}	1.5:1
3.33×10^{-5}	3.33×10^{-5}	1:1
2.53×10^{-5}	3.33×10^{-5}	1:1.5
1.67×10^{-5}	3.33×10^{-5}	1:2
1.40×10^{-5}	3.33×10^{-5}	1:2.4
1.20×10^{-5}	3.33×10^{-5}	1:2.7
1.00×10^{-5}	3.33×10^{-5}	1:3
8.67×10^{-6}	3.33×10^{-5}	1:3.8
6.67×10^{-6}	3.33×10^{-5}	1:5
3.33×10^{-6}	3.33×10^{-5}	1:10

Solutions were prepared by mixing stock solutions of CB[8] (0.14 mM) and coumarin (1.0 mM) **1b-1k** into 3 mL cuvettes and diluting with H₂O to obtain final concentrations.

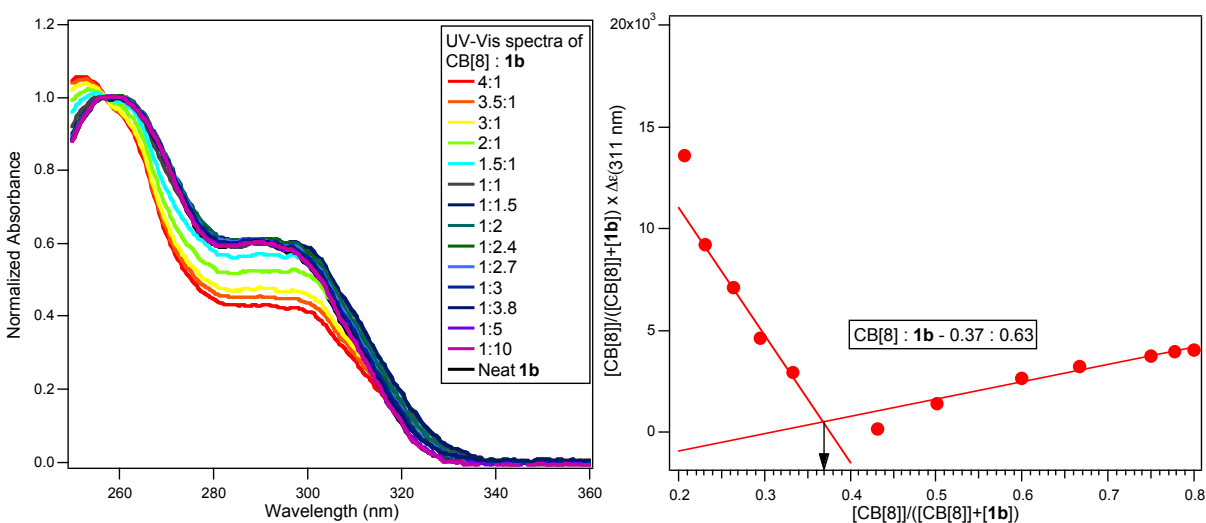


Figure 2.4 (Left) Normalized UV-vis spectra of various concentrations of CB[8] and **1b**. (Right) Jobs' plot depicting a HG ratio of 1:1.7 between CB[8] and **1b** in water at 25 °C

2.2.3. Host-guest complexation of 7-methoxycoumarin **1c** with CB[8]

The Jobs' plot of 7-methoxycoumarin (**1c**) was performed under identical conditions to unsubstituted coumarin **1b**. The UV-vis spectra showed a spectral shape change for each ratio of CB[8] to **1c**. The Jobs' plot indicated that there is not a discernable complex formation (Figure 2.5). The slope appears to be linear for the mole fraction / concentration employed for HG complexation. It is important to remember that, while the HG complex ratio was not observed, it does not mean a HG complex does not exist. In other words, the concentration of HG complex does not exist in appreciable amounts to be detected by UV-vis spectroscopy in the case of **1c**-CB[8] system.

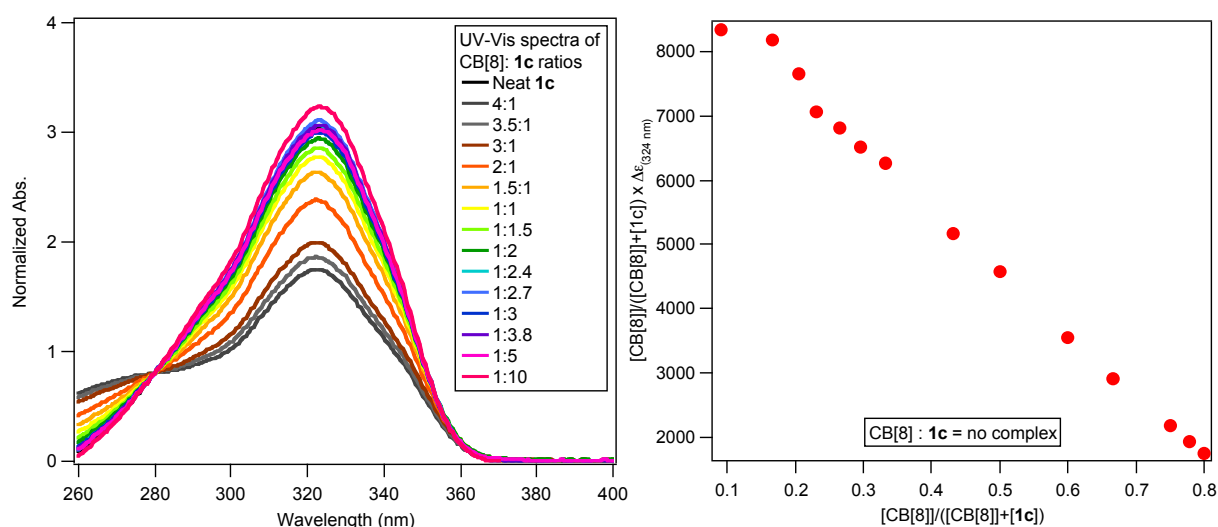


Figure 2.5 (Left) Normalized UV-vis spectra of CB[8] and **1c** in different ratios. (Right) Corresponding Jobs' plot indicating no HG complexation in water at 25 °C

2.2.4. Host-guest complexation of 7-methoxy-4-methylcoumarin **1d** with CB[8]

The addition of a methyl group to the 4-position of 7-methoxycoumarin (**1d**) offers an increase in the volume of the coumarin. The UV-vis Jobs' plot of 7-methoxy-4-methylcoumarin (**1c**) and CB[8] was performed and the result was almost the same as **1c** (Figure 2.6). The Jobs' plot was linear indicating no observed HG complexation between **1d** and CB[8].

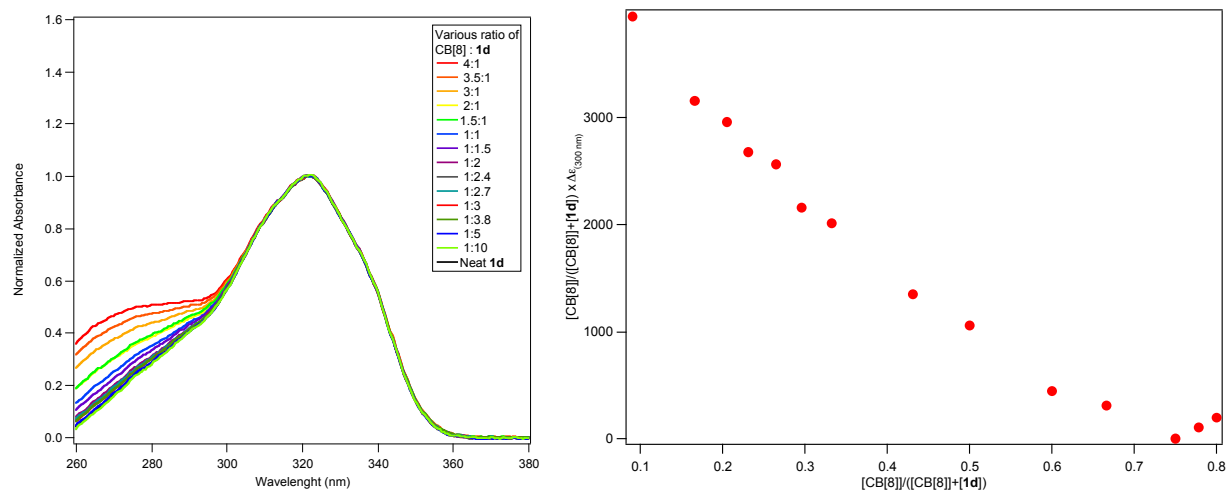


Figure 2.6 (Left) Normalized spectra of CB[8] and **1d** in different ratios. (Right) Jobs' plot indicating no HG complexation of **1d**-CB[8] system in water at 25 °C

2.2.5. Host-guest complexation of 7-methylcoumarin **1e** with CB[8]

Changing the functional group from a methoxy to a methyl should have an effect on the binding if the hydrophobicity plays a role in the HG complexation. The Jobs' plot for 7-methylcoumarin (**1e**) with CB[8] was performed for this very reason. Tailoring guests to bind to the host is not an exact science and often time, the guests that you would expect to form complexes do not and those you wouldn't expect to form inclusion complexes will. The solubility of **1e** is about 0.5 mM, much more insoluble than either of the methoxy derivatives. It stands to reason that **1e** should bind more tightly and give a better Jobs' plot due to the complexation with CB[8] as it will prefer to reside inside the hydrophobic cavity (Figure 2.7).

The resulting UV-vis spectra and Jobs' plot show a clear 1:2 HG complex. The replacement of the methoxy group with a methyl group presumably gave stronger binding due to the enhanced hydrophobicity and poor solubility of **1e**. This is a promising HG complex because of the possibility of two trapped molecules undergoing efficient [2+2]-photodimerization. As the CB[8] concentration increases, the molar absorptivity of the guest decreases. This has been observed for **1a**, coumarin **1b** and **1e** whereas the methoxy derivatives increased. This might be a trend that could possibly explain how the host-guest complexes are formed with CB[8] in aqueous media.

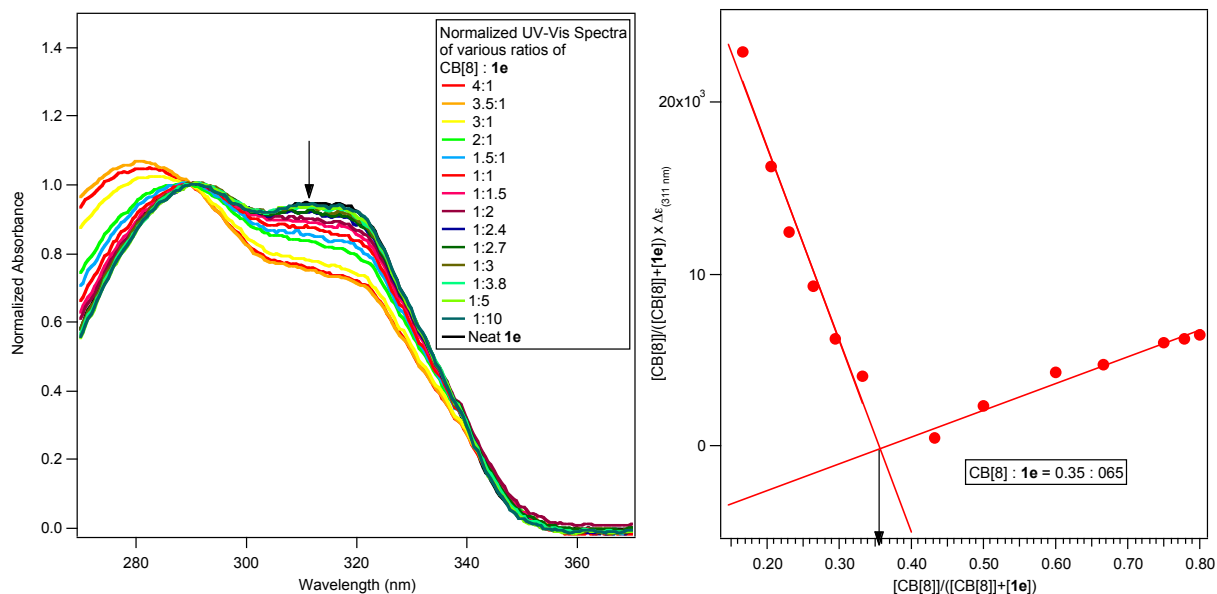


Figure 2.7 (Left) Normalized spectra of CB[8] and **1e** in different ratios. (Right) Jobs' plot indicating 1:2 HG complexation of **1e**-CB[8] system in water at 25 °C

Since **1e** formed a clear HG complex with a HG ratio of 1:2, it posed a question. Will other methylcoumarins behave in a similar manner? If our hypothesis is correct, a methyl substitution at the 4-position should again increase hydrophobicity and drive the guest into the host forming stable HG complexes (either 1:1 or 1:2). It is important to address the available volume within the CB[8] cavity as well, so that one does not attempt to create a HG complex where the guest cannot fit within the CB[8] cavity. Since the ratio is 1:2 for the case of **1e**, it is also plausible that the reaction from within the cavity is markedly different than the reaction in solution. If the reactive double bonds are within an acceptable distance of each other the reaction rate will likely increase in the presence of CB[8]. On the contrary, if they are not within an acceptable distance of each other, one could expect the reaction to be inhibited by complexation within the CB[8] host.

2.2.6. Host-guest complexation of 4,7-dimethylcoumarin **1f** with CB[8]

If increasing the hydrophobicity of a coumarin derivative leads to better HG complexes with clearer ratios of host to guest then 4,7-dimethylcoumarin (**1f**) should produce a result similar to the HG ratios observed with **1e**. The inspection of UV-vis spectra shows a decrease in the longer wavelength

absorption band as the amount of CB[8] increases. The Jobs' plot shows a very clear inflection point, but the HG ratio is actually closer to 1:1 than 1:2. This implies that one molecule of **1f** is present in each CB[8] cavity

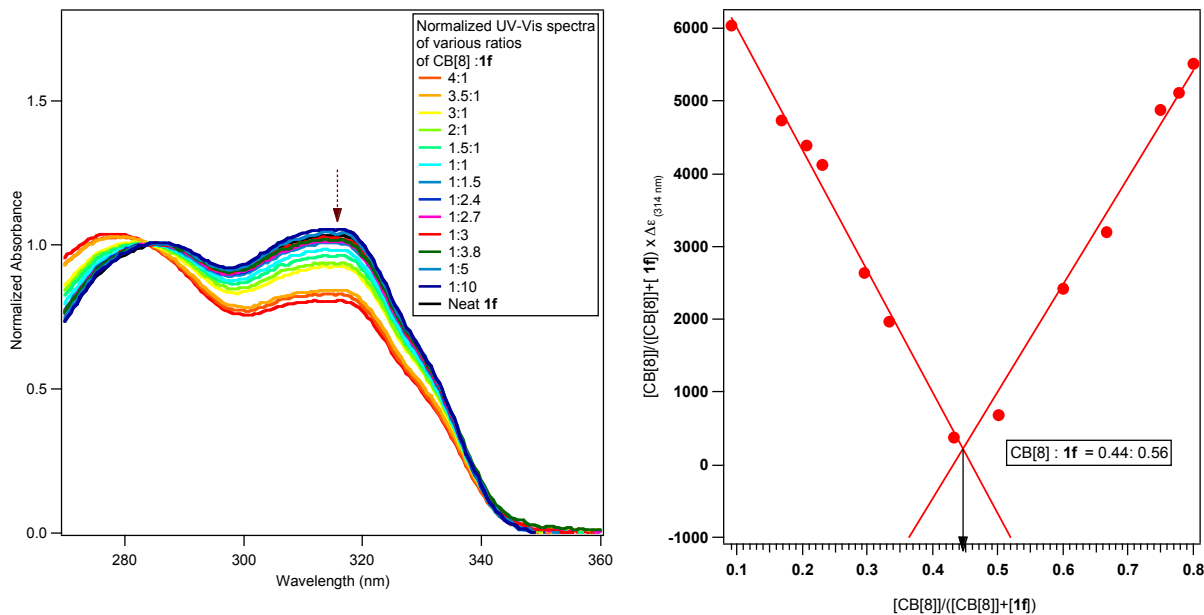


Figure 2.8 (Left) Normalized spectra of CB[8] and **1f** in different ratios. (Right) Jobs' plot indicating 1.1 HG complexation of **1f**-CB[8] system in water at 25 °C

The observed ratio from the Jobs' plot for **1f** is 1:1.3, which is a similar result to the regular coumarin complex (Figure 2.8). It's not quite 1:1 and it's not quite 1:2, it's somewhere in between. The decrease in a HG ratio from **1e** to **1f** could likely be attributed to the increased volume guests occupy the host cavity. This is not an unreasonable conclusion, as there are numerous examples in literature where volume plays a role in HG complexation and these issues will be addressed later in this chapter (vide infra).^{10,28}

2.2.7. Host-guest complexation 6-methylcoumarin **1g** with CB[8]

For HG complexation, subtle changes like switching a methyl group from the 7-position to the 6-position on a coumarin can have tremendous impact on systems. 6-methylcoumarin (**1g**) was investigated because the location of the methyl group makes the molecule more "linear" like and should

then be less sterically hindered when complexing with CB[8]. The Jobs' plot demonstrates this fact as it shows a stoichiometric ratio of 1:1.6 (Figure 2.9).

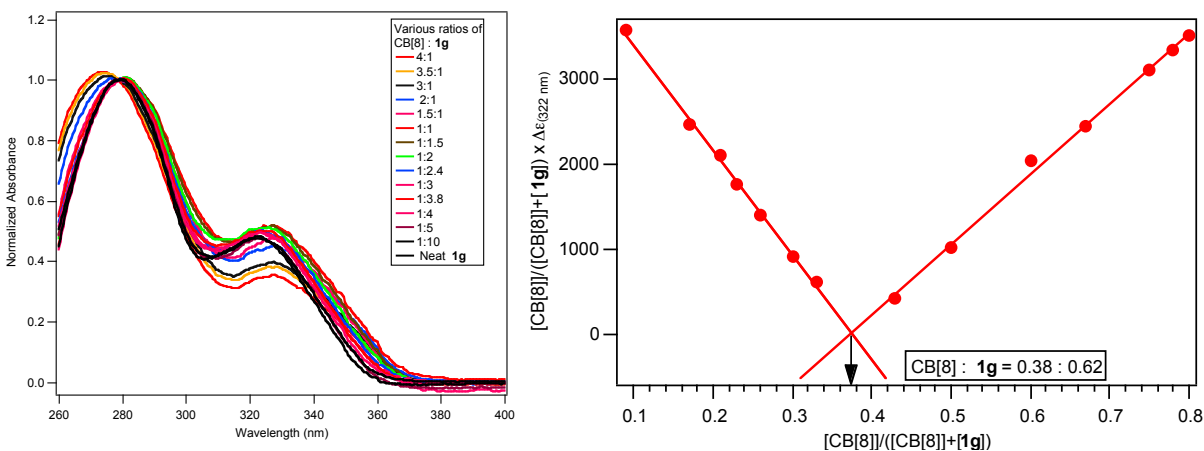


Figure 2.9 (Left) Normalized spectra of CB[8] and **1g** in different ratios. (Right) Jobs' plot indicating 1:1.6 HG complexation of **1g**-CB[8] system in water at 25 °C

If the steric bulk of **1g** is compared to coumarin **1b**, the results are almost identical; one can assume that the guest coumarin molecule can easily move in and out of the cavity. This might reflect the close relationship in the Jobs' plot and the HG ratios between the two (1:1.6 for **1g** and 1:1.7 for **1b**). The cross-sectional area of the coumarin allows it to only enter length-wise, therefore the length of the coumarin should greatly affect the HG ratio stoichiometry. Thus it is clear that the factors that affect the host guest ratio appear to be volume and hydrophobicity.

2.2.8. Host-guest complexation of 4,6-dimethylcoumarin **1h** with CB[8]

If we increase the cross-sectional area by substituting the hydrogen at the 4-position of **1g** with a methyl group we should see a change similar to the one observed with **1e** and **1f**. The investigation for the UV-vis Jobs' plot of 4,6-dimethylcoumarin (**1h**) mirrors that of the **1f** observation. While a HG complex exists, it appears to be a 1:1 HG complex. The addition of a methyl group at the 4-position of coumarin likely influenced the ease of entry for the first coumarin guest, but the ease of entry for the second coumarin guest molecule is likely hindered. The larger the substituent on the 4-position of coumarin (by

changing from 'H' to 'Me'), the less likely a complexation between coumarin and CB[8] leading to a 1:2 HG complex as observed.

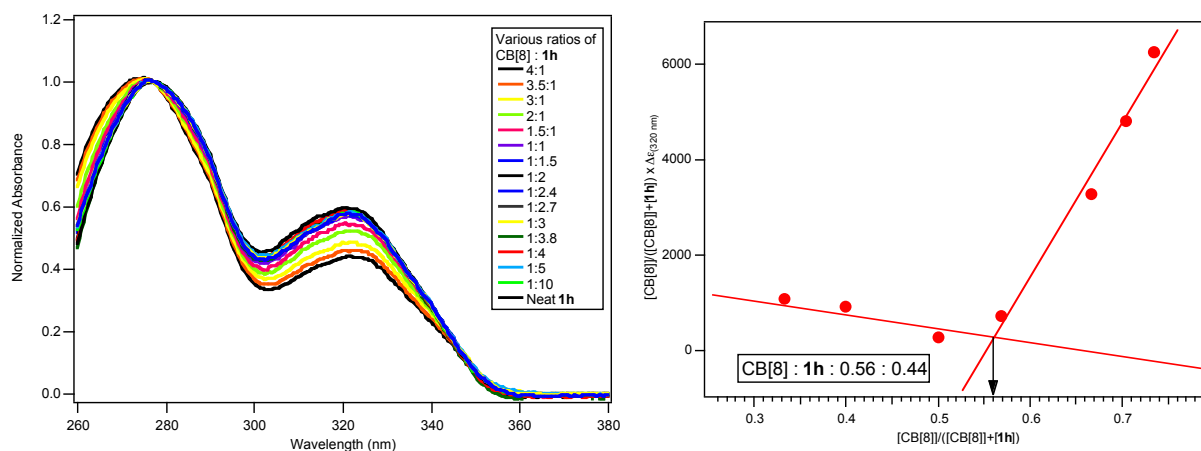


Figure 2.10 (Left) Normalized spectra of CB[8] and **1h** and (Right) corresponding Jobs' plot indicating 1:1 HG complexation in water at 25 °C

2.2.9. Host-guest complexation of 7-acetoxycoumarin **1i** and 7-acetoxy-4-methylcoumarin **1j** with CB[8]

Expanding the scope of coumarin derivatives leads us to studying HG complexation of 7-acetoxycoumarin (**1i**, Figure 2.11) and 7-acetoxy-4-methylcoumarin (**1j**, Figure 2.12) respectively. The rationale for studying this system was to see if the acetoxy-group would interact with the carbonyl functionality at the portals of CB[8], through electrostatics and/or hydrogen bonding mediated interactions. The increased sterics from the methyl group at the 4-position of coumarin like in the previous examples is likely going to cause a hindrance in the complexation, leading to a different HG complex ratio.

The UV-vis Jobs' plots revealed a 1:1 binding of **1i** CB[8] while complexation for the **1j** was not observed (Figures 2.11 and 2.12) with CB[8]. Considering the previously mentioned trend for complexation, these results are not very surprising. The increase in cross-sectional area by adding the methyl group at the 4-position of coumarin does not allow the coumarin to "fit" into the available space in the cavity. One can expect that the photo-reactivity for the acetoxy derivatives within the CB[8] cavity are nearly non-existent since there is no observation of a 1:2 complex. In other words, similar product selectivity in the presence and in the absence of the cavity could be observed for coumarin **1j**.

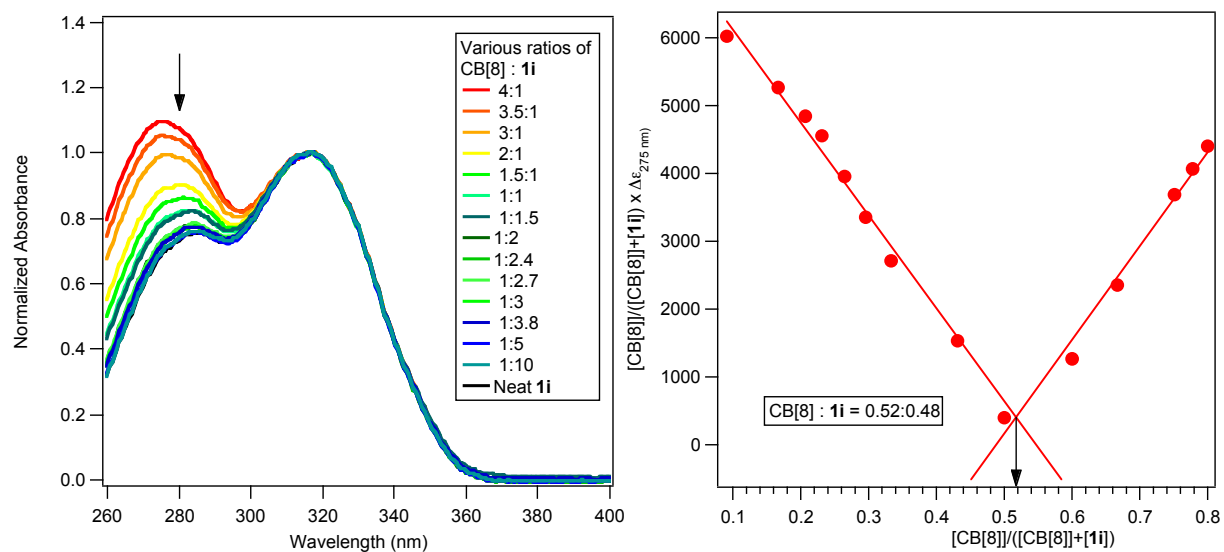


Figure 2.11 (Left) Normalized spectra of CB[8] and **1i** and (Right) corresponding Jobs' plot indicating 1:1 HG complexation in water at 25 °C

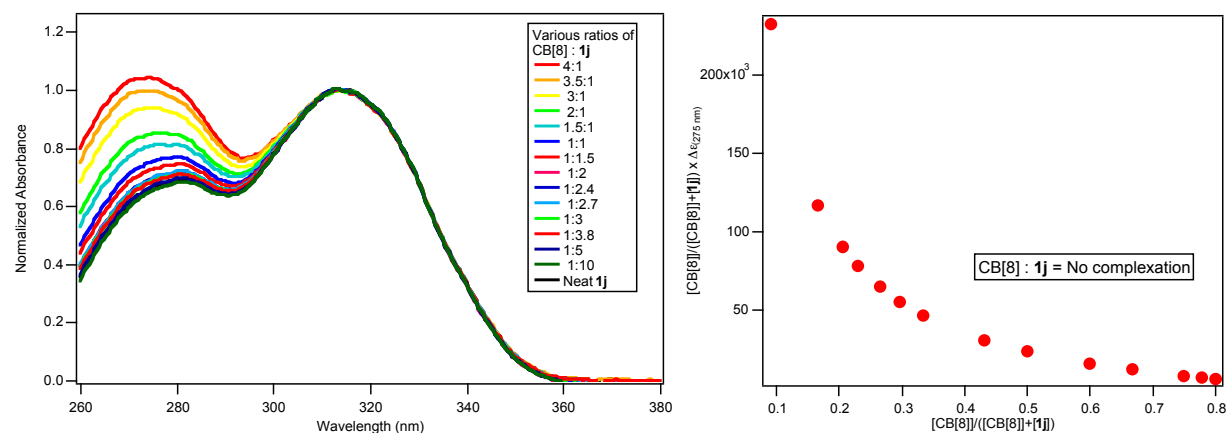


Figure 2.12 (Left) Normalized spectra of CB[8] **1j** and (Right) corresponding Jobs' plot indicating no HG complexation in water at 25 °C

2.2.10. Conclusions/ Inference from host-guest complexation studies involving CB[8] and coumarin derivatives

From the HG complexation studies we have shown that coumarin form HG complexes with CB[8] at varying stoichiometric ratios (Table 2.3). Lack of HG complexation appears to be the result of weak or

1c, 1d. The coumarin complexes that favor a 1:1 HG ratio, include **1h** and **1i** are likely as a result of steric or cross-sectional bulk that only allows one molecule to enter the CB[8] cavity at a time. A 1:2 HG complex was observed with the cationic **1a** and neutral **1e**. Interestingly, HG ratio complexes were not whole numbers as one would expect. These odd ratios cannot be due to a multicomponent system since the guest is too small to be shared between multiple host molecules. The ratios of 1:1.3, 1:1.6 and 1:1.7 for **1f**, **1g** and coumarin **1b** respectively likely represent HG complexation somewhere between 1:1 and 1:2. The “middle” ratios between the integer ratios are likely due to a dynamic balance that slightly favors the formation of both 1:1 and 1:2 HG complexes that coexist with uncomplexed coumarins in solution (Figure 2.13). Details of kinetic and thermodynamic studies will be discussed in chapter 5 to better understand this phenomenon.

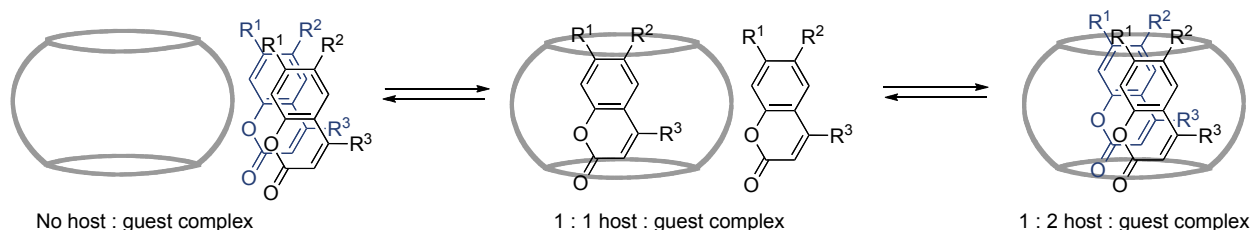


Figure 2.13 The equilibrium between CB[8] host and coumarin guest in solution

If it is a matter of thermodynamics, then it can be assumed that these systems are constantly shuttling in and out of the cavity due to their equilibrium (Figure 2.13) leading to the most stable HG complex. This means there is a form of dynamic exchange of the guests and the CB[8] host. This could be ascertained by ^1H NMR and by stopped flow measurements. For example, in the case of **1a** we see some form of fast dynamic exchange as evidenced by the NMR spectra taken at various concentrations of host and guest (Figure 2.2. and 2.3). This brings up a few questions that need to be addressed. Does this mean that all of the observed complexes are dynamic between coumarins and CB[8]? How do the volumes for the starting coumarins and their photoproducts influence the product selectivity? We have performed detailed investigations to answer these questions and the results of our investigation are presented in subsequent chapters.

Table 2.3 Host-guest ratio of coumarin derivatives with CB[8] from UV-vis measurements and Jobs' plot analysis

Entry	Coumarin substrate	Host:Guest ratio (from Abs.)	Inferred Host:Guest ratio
1 ^a	1a	1:2	1:2
2 ^b	1b	0.37:0.63	1:1.7
3 ^b	1c	No complexation	-
4 ^b	1d	No complexation	-
5 ^b	1e	0.35:0.65	1:2
6 ^b	1f	0.44:0.56	1:1.3
7 ^b	1g	0.38:0.62	1:1.6
8 ^b	1h	0.54:0.46	1:1
9 ^b	1i	0.52:0.48	1:1
10 ^b	1j	No complexation	-

^aUV-vis measurements were performed in HCl-H₂O with concentrations of 0.056 M for **1a**.

^bUV-vis measurements were performed in H₂O with concentrations of 3.33 x 10⁻⁵ M for **1b-1j**.

2.3. Volume Calculations of Coumarin Derivatives Photoproducts

2.3.1. Volume calculations

The ability to predict photoproducts, like predicting HG complexes using supramolecular interactions can be difficult. By calculating the volumes of various photoproducts and comparing them to the available space within a CB[8] cavity, we can make a logical guess to see if the photoproduct can be formed inside the CB[8] cavity. If the photoproduct formed is too large to reasonably fit within the CB[8] cavity. Then it is safe to assume that they were formed by some mechanism outside the cavity other than the templating inside the nanocavity due to templating effect.

The volume calculations (Table 2.4) were computed from optimized structures of the photoproducts. The photoproducts were optimized using the Gaussian 03 package²⁹ at a RB3LYP/6-31G(d,p) basis set with no imaginary frequencies. The output coordinates for minimized energy and frequency calculations can be found in appendix A. The volumes for the photoproducts were calculated by measuring the length by width by height (vol = l x w x h). The length was determined to be the longest edge of the molecule, whereas the width and the height were perpendicular to this line. While being a crude approximation, this will provide insights to whether the photoproduct will fit within CB[8] cavity.

Table 2.4 shows the calculated volumes for the coumarin derivatives along with the observed value for two isolated x-ray crystal structures. The marginal difference between the volumes calculated by

deviations between the simulated structure and XRD crystal structure may occur because the computer simulation is performed under “gas phase” conditions, unlike the crystalline solid. Further, the slight difference in volumes between gas phase computational values and XRD structures could be due to the “molecular breathing” that has been established in literature.³⁰ It is important to remember that the available volume for CB[8] in 479 Å³ from the calculated crystal structure. This suggests that the only coumarin photoproducts cannot fit into the cavity are *syn*-HH, *syn*-HT and *anti*-HH for the photoproducts of **1k**, and *syn*-HH, *syn*-HT and *anti*-HT photoproducts of **1d** (table 2.4). However, the remaining photoproducts could possibly fit within the confines of the CB[8] cavity.

Table 2.4 Calculated total volume for coumarin photodimers

		Computed Volume ^a			
		<i>syn</i> photoproducts		<i>anti</i> photoproducts	
Entry	Compound	<i>syn</i> -HH	<i>syn</i> -HT	<i>anti</i> -HH	<i>anti</i> -HT
1	1k	536	521	537	471 [430] ^b
2	1c	351	391	294	282
3	1d	500	590	410	545
4	1g	254 [220] ^b	274	265	307
5	1h	397	379	265	307
6	1e	383	450	322	271
7	1f	428	495	323	410
8	1i	-	-	-	-
9	1j	-	-	-	-
10	1b	-	-	-	-

^a All optimizations were performed using Gaussian 03 package at the RB3LYP/6-31G(d,p) level.²⁹ The volumes were calculated by measuring the length, width, and height at right angles to the longest line.^b The values in parentheses have been calculated from X-ray crystal structures.

Another critical aspect is revealed upon inspection of Table 2.4. The photoproducts with the methyl group at the 4-position of coumarin are all much larger than their unsubstituted counterparts. Photoproducts from **1g** and **1e** can fit within the confines of the CB[8] cavity. By switching the methyl group from the 6-position to the 7-position of coumarin there is a 10 - 30% increase in calculated volumes in the respective photoproducts. Only by performing the photoreactions could one rationalize the mechanism of photoproduct selectivity and the influence of the available volume from non-covalent interactions.

2.4. Photoreactions of Coumarin Derivatives in Isotropic Media and In Presence of CB[8]

2.4.1. Photoreactions of 7-amino-4-methylcoumarin **1a** (with CB[8] and isotropic media)

The photoreaction of **1a** was performed at a sufficiently high enough concentration to be monitored by ^1H NMR spectroscopy. The solution was prepared by dissolving 1.0 mg (0.012 M) of **1a** and 3.9 mg (0.006 M) of CB[8] in an NMR tube with 0.5 mL of 35% DCI-D₂O solvent. The control was prepared using the same 1.0 mg of **1a** in 0.5 mL of 35% DCI-D₂O amount without CB[8] added. The two solutions were irradiated for 36 hours and monitored by ^1H NMR. As expected the product distribution between the control and the reaction in the presence of CB[8] was different (Figure 2.13). The control resulted in a major photoproduct of *syn*-HH **2a** at 70% of product distribution with two minor products of *syn*-HT **4a** and *anti*-HT **5a** forming at 19% and 11% respectively. When templated inside CB[8], the major product selectivity changed. However, the overall product ratio of was observed to be 27:20:53 *syn*-HH:*syn*-HT:*anti*-HT respectively (Table 2.5).

The product selectivity is largely due to the templated effects of the cationic ammonium ions interacting with the carbonyl portals. The fact that the minor products *syn*-HH and *syn*-HT are still observed in the reaction is evidence of the fast exchange observed in the ^1H NMR. This allows the guest to react freely in solution or near the portals while exchanging. We have already established fast exchange based on ^1H NMR titration studies (Figures 2.2 and 2.3). Additionally the volumes computed for the 7-hydroxy-4-methylcoumarin (**1k** an analogous coumarin) photoproducts *syn*-HH, *anti*-HH, and that *syn*-HT are too large ($>500 \text{ \AA}^3$) to result in photoproducts within the cavity, whereas the *anti*-HT analog photoproduct is smaller (Table 2.3) and can fit inside the CB[8] cavity.

We believe that the selectivity observed in the concentration of **1a** in the presence of CB[8] is likely dictated by electrostatic interactions between the ammonium functionality of the coumarin and the carbonyls located at the CB[8] portal. Additionally, we believe the H-bonding interactions between the ammonium functionality and CB[8] dictates the formation of selective photoproducts during irradiation.

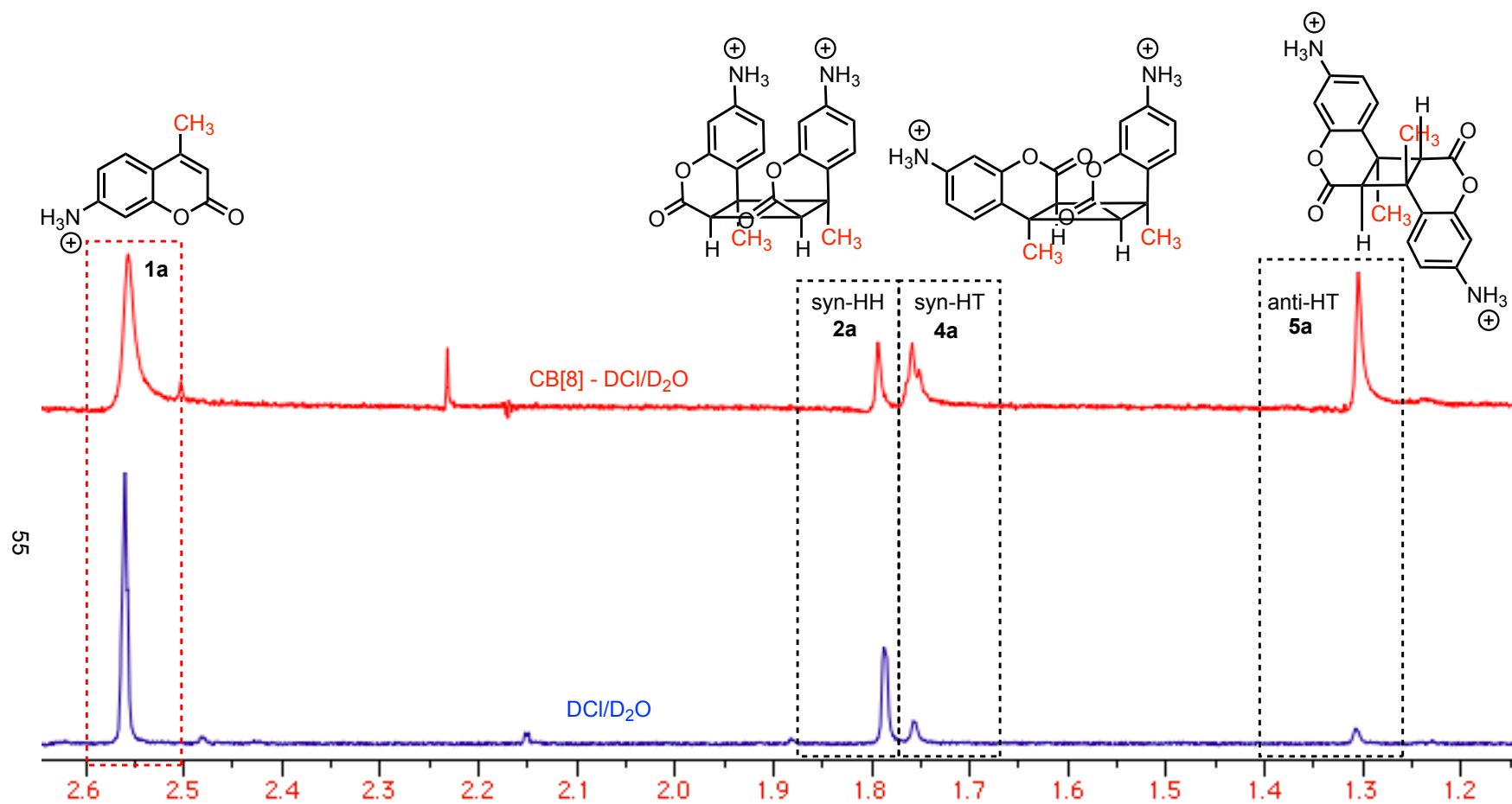


Figure 2.14 ¹H NMR (DCI/D₂O) of **1a** photoproduct selectivity differences between CB[8] – DCI/D₂O (Top) and DCI/D₂O (Bottom). Product ratio is based on relative integrations of the 4-methyl handle of the photoproducts

Table 2.5 Photodimerization of coumarin derivatives in various media

Entry	Solvent	Time	Product ^{a, b, c}
			<i>syn</i> -HH: <i>syn</i> -HT: <i>anti</i> -HH: <i>anti</i> -HT
1a	DCI-D ₂ O	36	70:19:11:0
	CB[8]/DCI-D ₂ O	36	27:20:53:0
1b	H ₂ O	15	51:49:0:0
	CB[8]/H ₂ O	15	43:57:0:0
1c	CHCl ₃	15	17:83:0:0
	CH ₃ OH	15	31:69:0:0
	H ₂ O	18	13:87:0:0
	CB[8]/H ₂ O	18	30:70:0:0
1d	CHCl ₃	24	76:0:24:0
	CH ₃ OH	15	76:0:24:0
	H ₂ O	15	76:0:24:0
	CB[8]/H ₂ O	24	48:0:12:40
1e	CHCl ₃	12	0:0:>99:0
	H ₂ O	12	48:32:20:0
	CB[8]/H ₂ O	12	99:0:0:0
1f	CHCl ₃	12	0:0:>99:0
	CH ₃ OH/sens ^{3*}	14	41:0:59:0
	H ₂ O	12	23:0:46:31
	CB[8]/H ₂ O	12	36:0:40:24
1g	CHCl ₃	36	0:0:>99:0
	CH ₃ OH	36	0:0:>99:0
	H ₂ O	24	52:15:33:0
	CB[8]/H ₂ O	24	31:69:0:0
1h	CHCl ₃	12	0:0:>99:0
	CH ₃ OH	12	0:39:44:17
	H ₂ O	12	25:0:75:0
	CB[8]/H ₂ O	12	73:0:27:0
1i	CDCl ₃	12	0:0:>99:0
	H ₂ O	18	34:66:0:0
	CB[8]/H ₂ O	24	22:78:0:0
1j	CHCl ₃	15	0:0:83:17
	CH ₃ OH	15	17:37:22:24
	H ₂ O	18	32:0:22:46
	CB[8]/H ₂ O	18	32:0:22:46
1k	CH ₃ OH	36	98:0:2:0
	CH ₃ OH/sens ^{3*}	36	75:0:25:0
	H ₂ O ^d	24	trace
	CB[8]/H ₂ O	36	32:0:0:68

^aAll irradiations were performed using a 450 W medium pressure Hg-lamp with <300 nm cut off filter.

Based on relative integration of ¹H NMR signals of the photoproducts. ^bReported values are based on an average of minimum 3 runs with ±5% error. Product yields within CB[8] were between 30–60% depending on the time of irradiation. ^cThe assignments of the dimer were based on previous literature reports. Ref. 11-15. ^dThe conversion in water was less than 5%.

2.4.2. Photoreactions of 7-hydroxy-4-methylcoumarin **1k** (with CB[8] and isotropic media)

Photoreaction of 7-hydroxy-4-methylcoumarin (**1k**) was investigated because we hypothesized that the polar OH-group would still interact with the portal of the coumarin and template the hydrophobic part of the molecule inside CB[8] in a similar fashion to **1a**, albeit at a lower concentration since the molecule is neutral. Direct photoirradiation of **1k** in neat methanol results in a *syn*-HH:*syn*-HT ratio of 98:2 and when triplet-sensitized with benzophenone, the product *syn*-HT increased to 25% (Table 2.5). In water after 24 hour irradiation, there was only a trace of *anti*-HH photoproduct and could not be quantified. In the presence of CB[8] two photoproducts are formed with the major product being *anti*-HT at 68% along with 32% of *syn*-HH appear after 36 hours of irradiation. The increase of irradiation time from 36 to 72 hours resulted in a slight increase in the *anti*-HT photoproduct compared to *syn*-HH with a ratio of 72:28 (2.14- 2.15).

The photodimerization in water was performed by preparing a 0.2 mM solution of **1k** in water (200 mL). The solution was irradiated in a 450 W medium pressure Hg lamp for 24 hours. The photoproducts were extracted with ethylacetate or diethylether and dried over Na₂SO₄. The solvent was removed in vacuo and without further purification, the product distribution was analyzed by ¹H NMR spectroscopy in CD₃OD. The photodimerization of **1k** in the presence of CB[8] was performed by preparing an aqueous solution (200 mL) consisting of 0.2 mM (2 eq.) of **1k** and 0.1 mM (1 eq) of CB[8]. The solution was sonicated for 3 hours at 60 °C and then cooled to room temperature, followed by irradiation for 36 hours. After irradiation, the photoproduct(s) were extracted with ethylacetate or diethylether and dried over Na₂SO₄. The solvent was removed in vacuo. Without further purification, the product distribution was analyzed by ¹H NMR spectroscopy in CD₃OD. The photoreaction performed in methanol was done using 0.003 M (1 eq) of **1k** and 0.003 M (0.125 eq) of benzophenone as a triplet sensitizer. The samples were then irradiated for 36 hours. After irradiation, the solvent was removed in vacuo. Without further purification, the product distribution was analyzed ¹H NMR spectroscopy in CD₃OD.

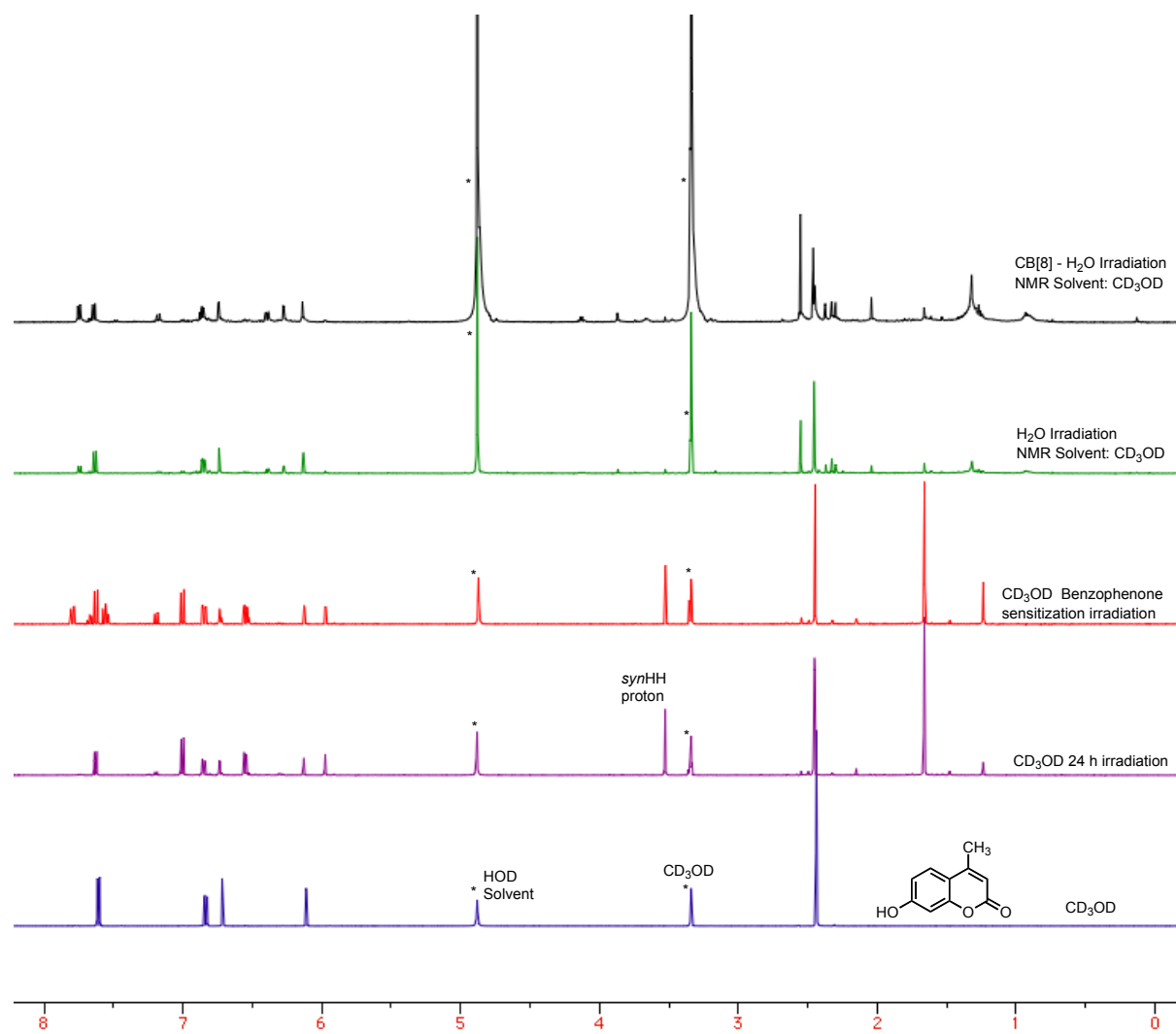


Figure 2.15 ^1H NMR (CD_3OD) spectra of **1k** and photoproducts before and after irradiation in various solvents and in the presence of CB[8]

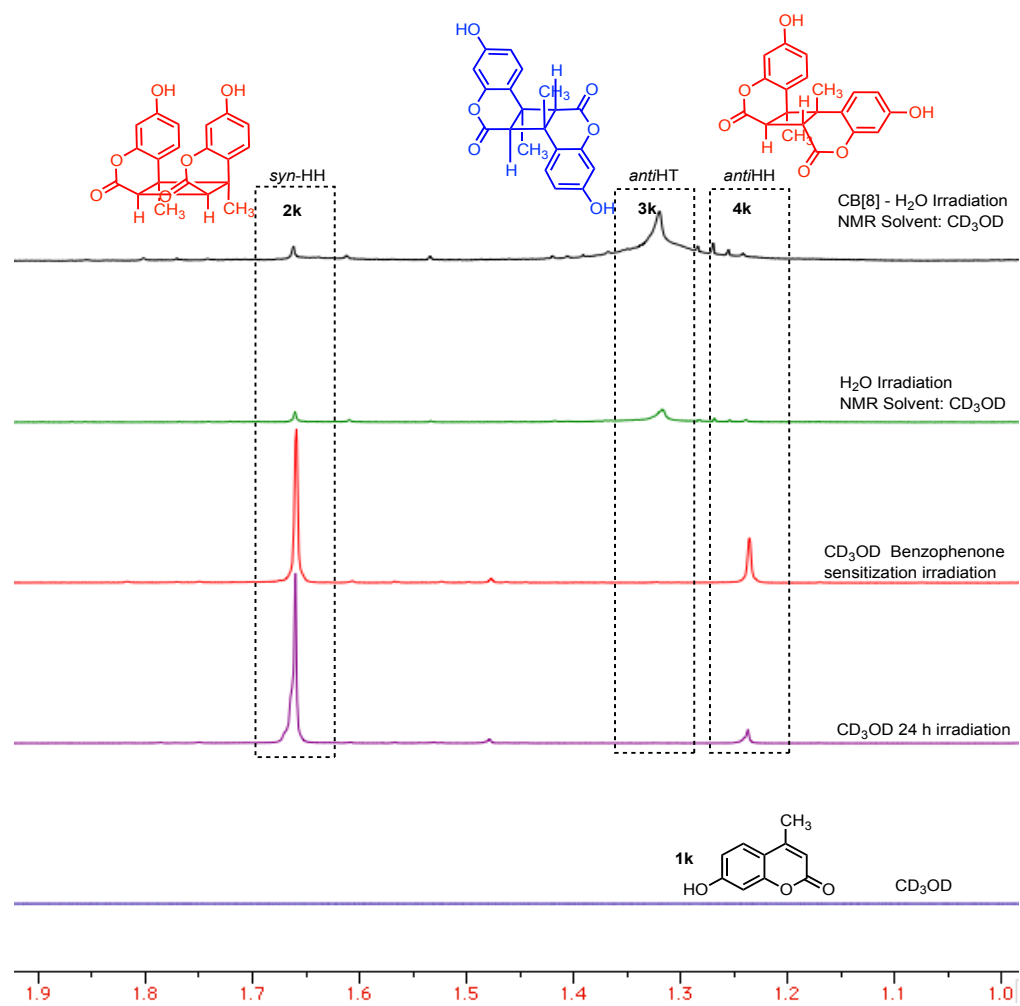
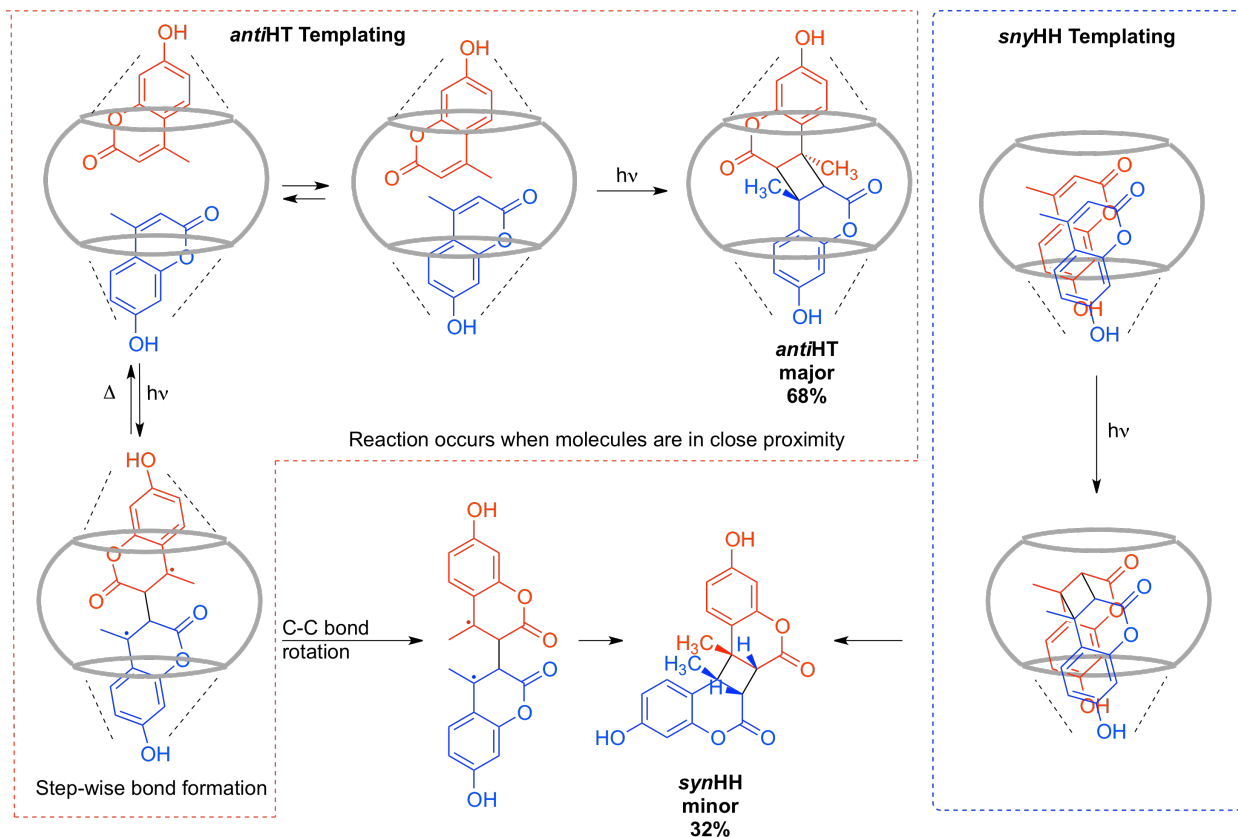


Figure 2.16 Expanded ¹H NMR (CD₃OD) spectra of **1k** and photoproducts before and after irradiation in various solvents and in the presence of CB[8]

Mechanistically, the formation of *syn*-HH and *anti*-HT was rather intriguing if we assume the polar groups on the molecules are interacting with the cavity. When the molecule is excited and reacts with another molecule, the mechanism to formulate the cyclobutane ring is typically considered concerted. However, if the distance between the bonds is large, one can presume that reaction is step-wise and slow especially when there is supramolecular constraints due to encapsulation. In a case where the guests are constantly entering and leaving the cavity through dynamic exchange, we can visualize two scenarios as shown in scheme 2.3. In the first scenario, the two reacting molecules within the CB[8] cavity are close to each other and the reaction proceeds in a concerted manner. Due to the volume restrictions within the CB[8] cavity, the molecules are oriented in an *anti*-HT fashion to minimize the likely interactions between the methyl groups while maximizing the interactions with the hydroxyl groups and the cavity portal. In the second scenario, the molecules are relatively far away and when excited, the two closest bonds form. Once this happens, we can presume a 1,4 diradical located on a 3°-benzyl carbon and this stabilizes long enough for the molecules to reorganize with a 180 degree rotation of the C-C bond between the two coumarin units. The reorganization can occur either in the CB[8] cavity and this would be fairly slow and difficult due to the volume. It could happen outside the cavity, which might be relatively fast. A point to emphasize is that the release of the guest-dimer might be prohibited by other interactions. If the reorientation reaction is slow, it is possible that the 1,4 diradical would thermally return back to the parent guest molecules. In either case it would plausibly explain why the *anti*-HT photoproduct is favored over the *syn*-HH. The volumes as previously mentioned only allow for the *anti*-HT to form within the cavity. Another plausible mechanism that allows the guests to form a *syn*-HH product is from a host-to-head orientation of the guest (Scheme 2.3). This interaction could be considered energetically less favorable than the *anti*-HT configuration, which is why the *syn*-HH product formed as the minor product.

When polar coumarins interact with the CB[8] cavity, the hydrogen bonding aided by the solvent (water) allows the polar substituent to slightly stick outside the cavity, increasing the distance between double bonds, leading to the formation of the *anti*-HT photoproduct. The polar coumarins that demonstrate this possible reaction are the **1a** (with NH₃⁺ group interacting with the carbonyl portal) and **1k** (with OH group interacting with the carbonyl portal). Since *anti*-HT is the major photoproduct, but not the exclusive photoproduct, it is possible that there is a dynamic equilibrium between the CB[8] host and

the coumarin guest **1a** and **1k** respectively leading to the HG complex (dynamic nature established by ^1H NMR for **1a**, refer to Figures 2.2 and 2.3). This dynamic aspect in HG complex allows for other minor products to form (likely outside the cavity).



Scheme 2.3 The possible mechanisms to explain the photoproduct selectivity in the case of polar coumarin (**1k** with an OH-group is given as a representative example)

2.4.3. Photoreactions of coumarin **1b** (with CB[8] and isotropic media)

Switching from polar to non-polar coumarins was expected to change the product selectivity during the dimerization reaction in CB[8] as the nature of the non-bonding interactions between the host and the guest are likely to be different. Non-polar coumarins are poorly soluble in aqueous solvents compared to cations/polar coumarin and when given the option to dissolve in water or sit inside a hydrophobic cavity, energetics drives them toward the latter option. This raises an important question; How would CB[8] template the non-polar coumarin guests and in what orientation?

Unsubstituted coumarin **1b** was used to determine what effects the volume of the photoproducts would impart on product selectivity. All the photoproducts for the unsubstituted coumarin are rather quite small compared to the photoproducts from the substituted coumarins (especially 4-substituted coumarins). The hypothesis was that all the photoproducts could form within the cavity if the coumarins form a HG complex. Through UV-vis and Jobs' plot, the HG ratio was determined to be 1:1.7 in the case of **1b**. Because of this relatively high ratio of guest to host, the photoreaction was expected to give selective products if the reaction occurred with the cavity. The reaction in neat water resulted in a 51:49 ratio of *syn*-HH to *syn*-HT photoproduct (Table 2.4, Figure 2.16). When complexed in H₂O/CB[8] the product selectivity changed slightly to a 43:57 ratio of *syn*-HH:*syn*-HT photoproducts. There are two possibilities, either the reaction is not selective enough to alter the product selectivity drastically or the majority of the reactions are occurring outside the cavity because the reaction inside the CB[8] cavity is inefficient. A single crystal complex with two coumarins within a CB[8] molecule was grown and the photoreaction from the crystalline state was investigated.³² The results showed that the reactive double bonds from the coumarins were beyond the Schmidt distance (<4.2 Å) for dimerization and no photoproduct was observed. This implies that the reaction occurred effectively outside the cavity compared to the reaction inside the CB[8] cavity (Scheme 2.5)

The photodimerization in water was performed by preparing a 0.2 mM solution of **1b** in water (200 mL). The solution was irradiated in a 450 W medium pressure Hg lamp for 15 hours. The photoproducts were extracted with ethylacetate or diethylether and dried over Na₂SO₄. The solvent was removed in vacuo and without further purification the product distribution was analyzed by ¹H NMR spectroscopy. The photodimerization of **1b** in the presence of CB[8] was performed by preparing an aqueous solution (200 mL) consisting of 0.2 mM (2 eq.) of **1b** and 0.1 mM (1 eq) of CB[8]. The solution was sonicated for 3 hours at 60 °C and the solution was then cooled to room temperature. The solution was then irradiated for 15 hours. The photoproducts were extracted with ethylacetate or diethylether and dried over Na₂SO₄. The solvent was removed in vacuo and without further purification, the product distribution was analyzed by ¹H NMR spectroscopy.

2.4.4. Photoreactions of 7-methoxycoumarin **1c** with CB[8] and in isotropic media

Since there was no clear HG ratio for **1c** with CB[8], it was expected that the photoproduct would mirror those observed in solution. In isotropic media (chloroform, water) the photoreaction proceeded at a slow rate, with trace amount of *syn*-photoproducts after 36 hours of irradiation (Table 2.5, Figure 2.17). Once complexed with CB[8] the reaction proceeded cleanly in 18 hours to give *syn*-HH and *syn*-HT photoproducts in a 31:69 HH:HT ratio. In isotropic media and in H₂O/CB[8] the product selectivity for **1c** is exclusively *syn*-photoproducts. However, the conversion in the presence of CB[8] is slightly higher.

This is interesting considering the Jobs' plot of **1c** does not describe a clear HG ratio between CB[8] and **1c**. Instead, what was observed from the Jobs' plot spectra was a steady decrease in $\Delta\epsilon$ as the mole fraction of CB[8] increases past 1:1 and 1:2 HG ratio. This could be indicative of two possibilities. First, the complexation of **1c** within CB[8] (Figure 2.3) was not clearly defined as the $\Delta\epsilon$ changes but there with no clear inflection point. This scenario was difficult to comprehend as there was a significant increase in photoconversion between reaction in H₂O and H₂O/CB[8]. The second scenario is the binding of **1c** at the concentration where the Jobs' plot was performed does not promote the formation of the inclusion complex. Hence, the majority of coumarin at this concentration is either found free in solution, outside the cavity. This presents a likely scenario where the photodimerization is occurring at the rim instead of inside the cavity leading to enhanced rate of the reaction (Scheme 2.6).

If the complexation of **1c** was not strong enough to bind tightly to CB[8] in solution, perhaps increasing the lipophilicity by methylating at the 4-position could favor the HG complexation. **1d** was studied to ascertain if we could enhance the binding by increasing the hydrophobicity of the coumarin when compared to **1c**. The product selectivity was 30:70 *syn*-HH:*syn*-HT for **1c** of CB[8] compared to 13:87 *syn*-HH:*syn*-HT for **1c** in water. In the presence of CB[8], the *anti*-HT dimer was formed as well as *syn*-HH and *anti*-HH in a 40:48:12 ratio respectively (Table 2.4, Figure 2.18).

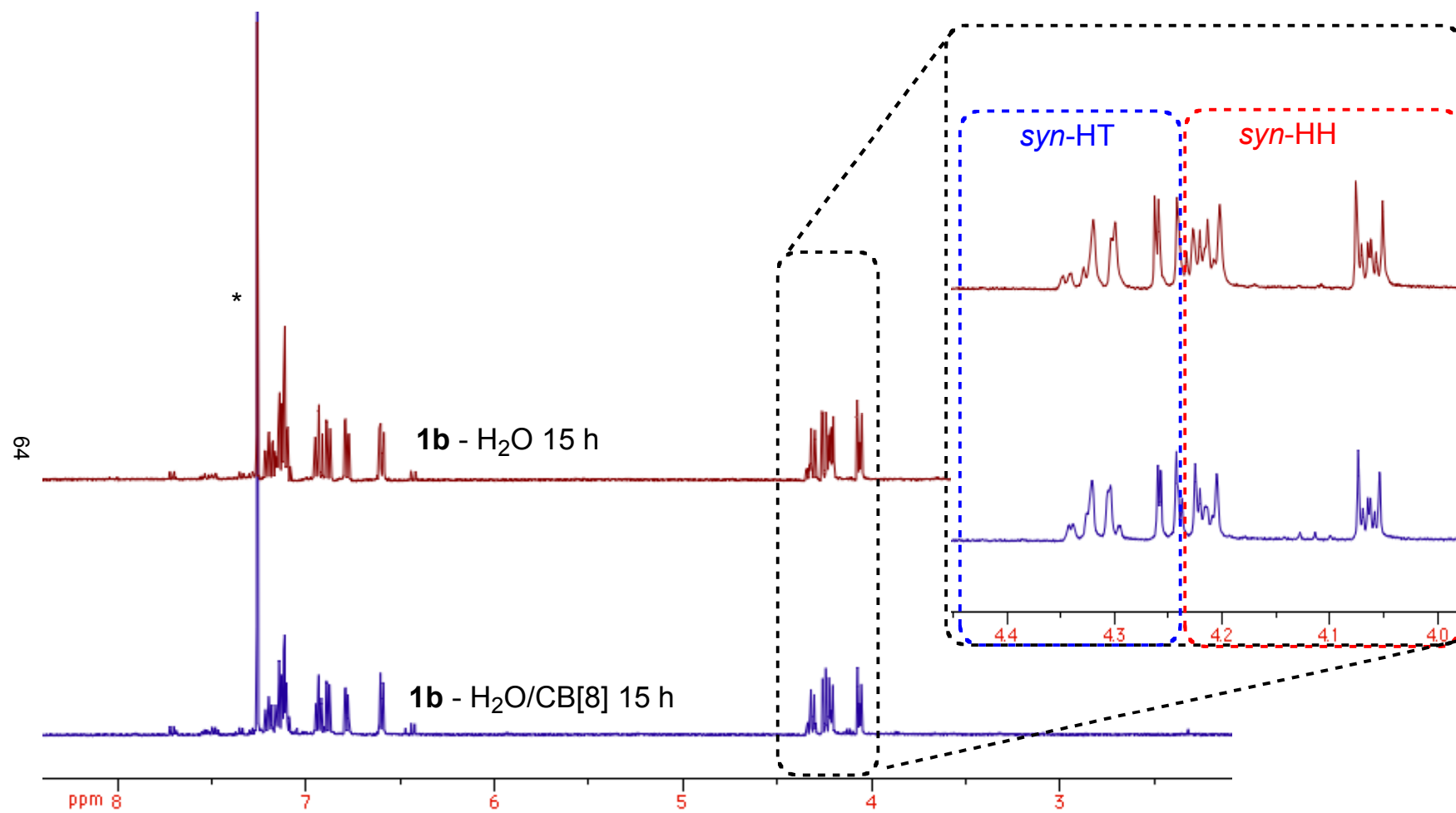


Figure 2.17 ^1H NMR (CDCl_3) spectra of photoproducts of **1b** in water in the presence and absence of CB[8]

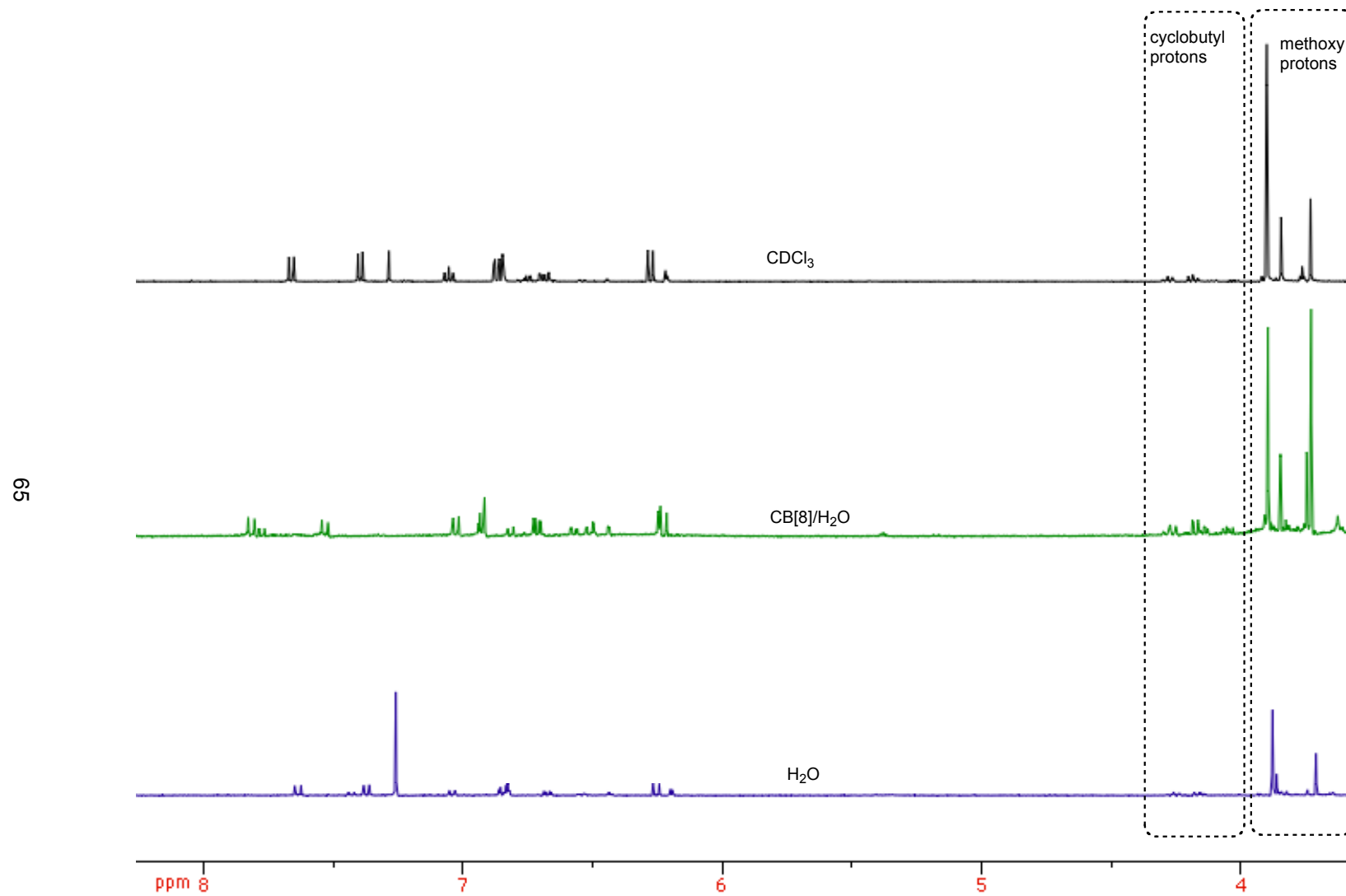
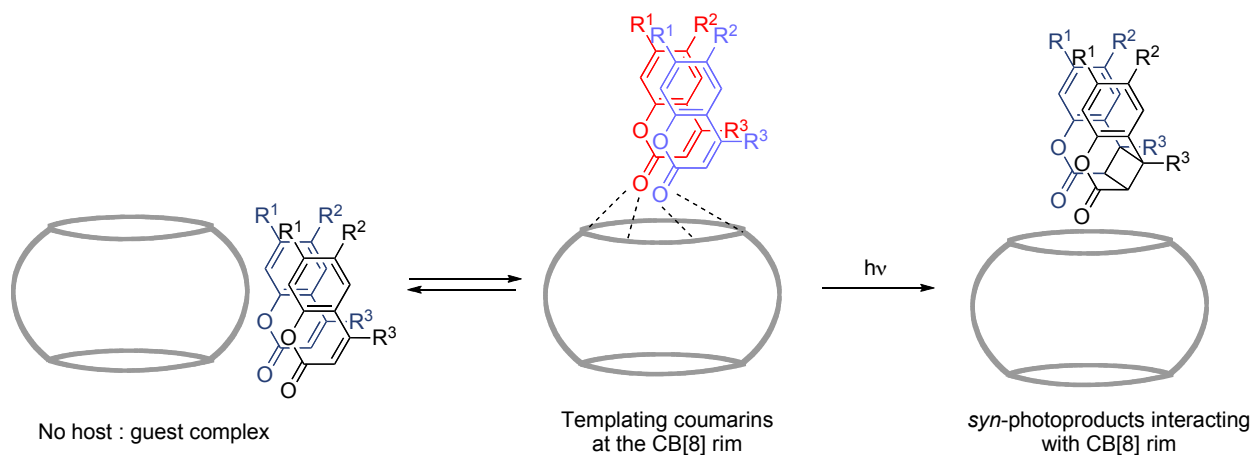


Figure 2.18 ¹H NMR (CDCl₃) spectra of **1c** in presence and absence of CB[8]



Scheme 2.4 Photodimerization of coumarin derivatives at the CB[8] portal/rim.

The photodimerization in water was performed by preparing a 0.2 mM solution of **1c** in water (200 mL). The solution was irradiated in a 450 W medium pressure Hg lamp for 18 hours. The photoproducts were extracted with ethylacetate or diethylether and dried over Na_2SO_4 . The solvent was removed in vacuo and without further purification the product distribution was analyzed by ^1H NMR spectroscopy. The photodimerization of **1c** in the presence of CB[8] was performed by preparing an aqueous solution (200 mL) consisting of 0.2 mM (2 eq.) of **1c** and 0.1 mM (1 eq) of CB[8]. The solution was sonicated for 3 hours at 60 °C and the solution was then cooled to room temperature. The solution was then irradiated for 18 hours. The photoproducts after irradiation was extracted with ethylacetate or diethylether and dried over Na_2SO_4 . The solvent was removed in vacuo and, without further purification, the product distribution was analyzed by ^1H NMR spectroscopy. The photoreaction performed in methanol was prepared by making a 0.003 M (1 eq) solution of **1c** in methanol. The samples were irradiated for 15 hours. After irradiation, the solvent was removed in vacuo and without further purification the product distribution was analyzed by ^1H NMR spectroscopy in CDCl_3 . The photoreaction in CDCl_3 was performed by preparing 0.08 M of **1c** in 500 μL in an NMR tube and irradiating for 15 hours. The NMR was recorded without further purification.

2.4.5. Photoreactions of 7-methoxy-4-methylcoumarin **1d** with CB[8] and in isotonic media

Will the addition of the methyl group at the 4-position as in **1d** alter the product selectivity? The calculated volumes for should limit the selectivity of the photoproducts that are synthesized within the CB[8] cavity. The coumarin **1d** was studied to see if we could enhance the binding by increasing the hydrophobicity of the coumarin when compared to **1c**. There was a moderate success by adding a methyl-group to the 4-position of coumarin. The photoproduct selectivity in isotropic media (both CDCl₃ and methanol) gave *syn*-HH and *anti*-HH photoproducts in a ratio of 76:24. In water in the presence of CB[8] the product selectivity changed to *anti*-HT, *syn*-HH and *anti*-HH in a 40:48:12 ratio respectively.

The photodimerization in water was performed by preparing a 0.2 mM solution of **1d** in water (200 mL). The solution was irradiated in a 450 W medium pressure Hg lamp for 15 hours. The photoproducts were extracted with ethylacetate or diethylether and dried over Na₂SO₄. The solvent was removed in vacuo and without further purification the product distribution was analyzed by ¹H NMR spectroscopy. The photodimerization of **1d** in the presence of CB[8] was performed by preparing an aqueous solution (200 mL) consisting of 0.2 mM (2 eq.) of **1d** and 0.1 mM (1 eq) of CB[8]. The solution was sonicated for 3 hours at 60 °C and the solution was then cooled to room temperature. The solution was then irradiated for 24 hours. The photoproducts were extracted with ethylacetate or diethylether and dried over Na₂SO₄. The solvent was removed in vacuo and without further purification the product distribution was analyzed by ¹H NMR spectroscopy. The photoreaction in methanol was performed in a 0.003 M (1 eq) solution of **1d**. The samples were irradiated for 15 hours. After irradiation the solvent was removed in vacuo and without further purification the product distribution was analyzed ¹H NMR spectroscopy in CDCl₃. The photoreaction in CDCl₃ was performed by preparing 0.08 M of **1d** in 500 μL and irradiating for 24 hours. The NMR was recorded without further purification.

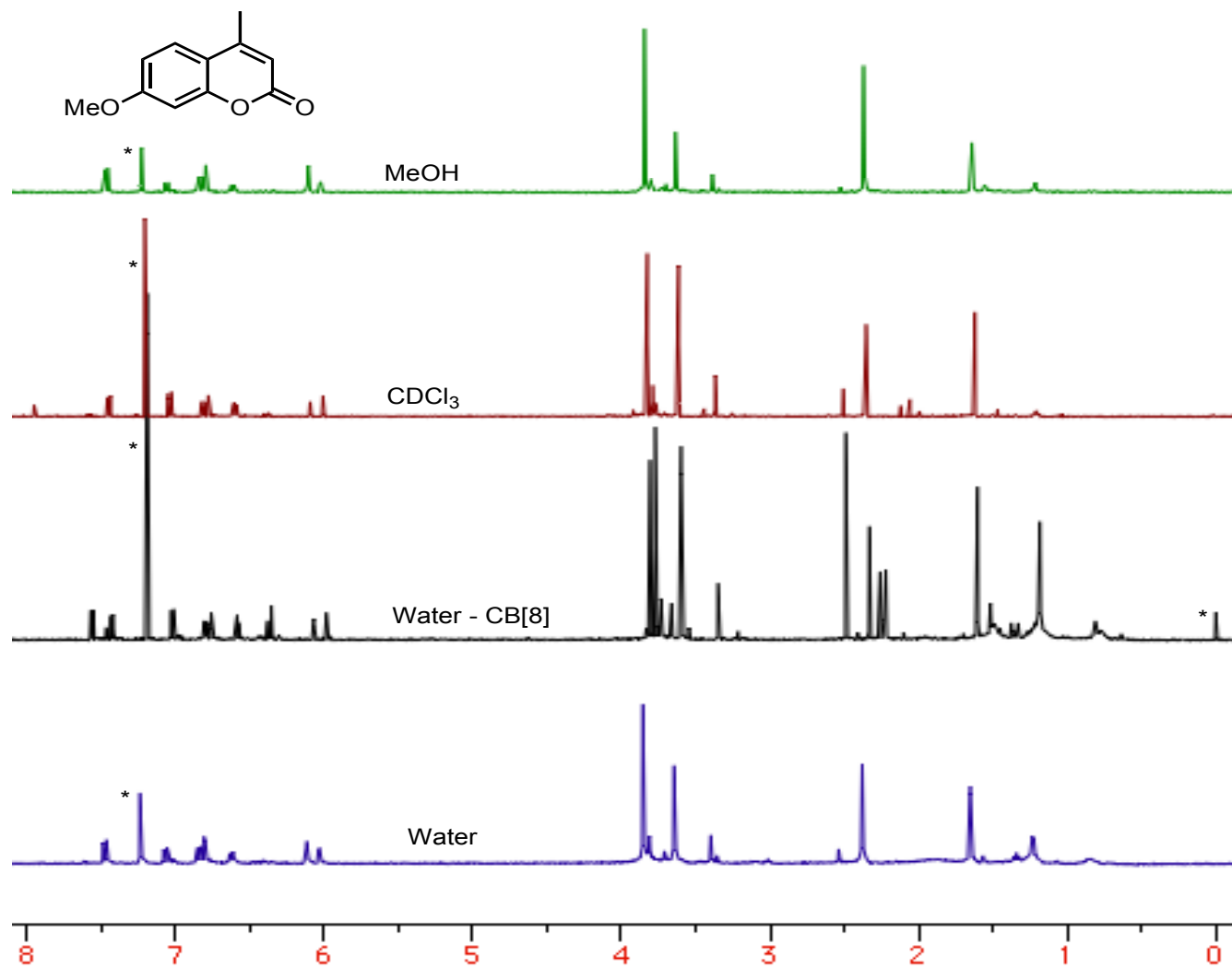


Figure 2.19 ^1H NMR (CDCl_3) product selectivity of **1d** after irradiation in various solvents

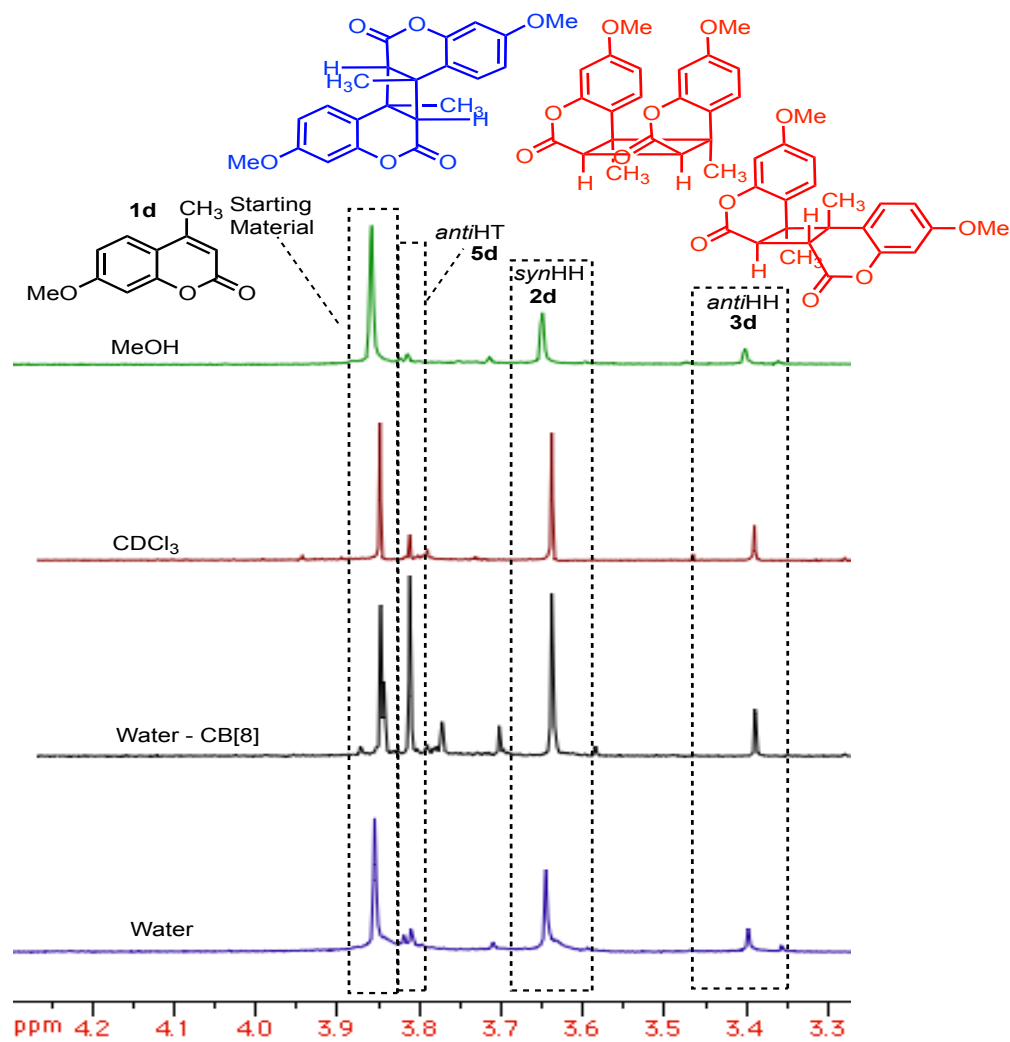


Figure 2.20 Expanded ¹H NMR (CDCl₃) of **1d** showing the proton shifts from the photoproducts (methyl handle) after irradiation in various solvents

Presumably, by increasing the hydrophobicity in the case of **1d** by adding a methyl group to at the 4-position there is a considerable enhancement of complexation within CB[8] to change product selectivity. The Jobs-plot revealed a lack of a clear HG complexation with CB[8]. This mirrored the result from **1c** where there were changes in $\Delta\epsilon$ from the Jobs' plots but a clear inflection point was not observed (Figure 2.4). There was a slight inflection point at 0.75 mole-fraction CB[8] which could be indicative of a weak complexation within CB[8] that is slightly stronger than **1c**. The issue of mole-fraction and binding is limited to the maximum solubility of CB[8] and if the binding constants are not within the range employed for our Jobs' plot experiment, the observation of a HG complex under more dilute conditions is difficult. But for the photoreaction to be influenced by the CB[8] cavity, the minor amount of the 1:2 HG complex if present in solution can accelerate the reaction due to templating effect leading to the photoproduct. This reactive 1:2 HG complex can be regenerated upon expulsion of the photoproduct from the cavity.

Comparing the volume change between **1c** and **1d** reveals that there is a significant volume increase when adding the methyl-position at the 4-position. This could account for the selectivity in the photoproduct when comparing **1c** and **1d** coumarins (Table 2.5). The volume of the photoproducts for the **1c** are all considerably smaller than the available volume inside the CB[8] cavity of 479 \AA^3 . The only photoproduct from **1d** that can be formed inside the CB[8] cavity is *anti*-HH dimer which is the minor product observed when in the presence of $\text{H}_2\text{O}/\text{CB}[8]$. This observation presents an alternate option for the formation of certain photoproducts that can occur at the rim of the cavity through weak interactions (Scheme 2.4).

2.4.6. Photoreactions of 7-methylcoumarin **1e** with CB[8] and in isotropic media

The Jobs' plot from **1e** shows a clear 1:2 HG ratio like **1a**. Being a neutral coumarin, the hydrophobicity of **1e** is higher than the cationic **1a** and hence the binding should be tighter. We've seen examples from the methoxy coumarins **1c** and **1d** that an apparent HG ratio isn't required to change product conversion or selectivity (Figures 2.18 and 2.19). The observation of the definitive HG ratio means the equilibrium was favored the formation of the HG complex and the experiment/concentration has been performed within the binding regime. The stoichiometric ratio of the HG complex is almost essential in the photoreaction for the dimerization of **1e** to prevent background reactions in solution

outside the cavity. The observation of the product from **1e** in CB[8] was exclusively *syn*-HH. This is a definitive discovery providing evidence that neutral molecules can be effectively templated within CB[8] and the photoreaction can be controlled effectively with excellent selectivity.

The photodimerization of coumarin in water was performed by preparing a 0.2 mM solution of **1e** in water (200 mL). The solution was irradiated in a 450 W medium pressure Hg lamp for 12 hours. The photoproducts were extracted with ethylacetate or diethylether and dried over Na₂SO₄. The solvent was removed in vacuo and without further purification the product distribution was analyzed by ¹H NMR spectroscopy. The photodimerization of **1e** in the presence of CB[8] was performed by preparing an aqueous solution (200 mL) consisting of 0.2 mM (2 eq.) of **1e** and 0.1 mM (1 eq) of CB[8] the solution was sonicated for 3 hours at 60 °C and the solution was then cooled to room temperature. The solution was irradiated for 12 hours. The photoproducts were extracted with ethylacetate or diethylether and dried over Na₂SO₄. The solvent was removed in vacuo and without further purification the product distribution was analyzed by ¹H NMR spectroscopy. The photoreaction in CDCl₃ was performed by preparing 0.08 M of **1e** in 500 μL and irradiating for 12 hours. The NMR was recorded without further purification.

2.4.7. Photoreactions of 4,7-dimethylcoumarin **1f** with CB[8]

Since the host to guest ratio of CB[8] and **1f** is 1:1.3, the product selectivity would be dictated by the relative reactivity of the 1:2 HG complex and the competing reaction outside the cavity. Photodimerization in the presence of CB[8] showed a slight change in product selectivity from the reaction in neat water, but not as drastic as one would expect from the previous results. This poor product selectivity is like due to the dynamic nature of the HG complex in aqueous media (reactions happening both inside and outside the CB[8] cavity).

All the photoproducts of **1f** from [2+2] dimerization with the exception of *syn*-HT can be synthesized by irradiation in various solvents (Figure 2.22-2.23). *Anti*-HH was observed as the exclusive photoproduct upon 12 hour irradiation in chloroform. Irradiation with a sensitizer (benzophenone) in methanol resulting in both *syn*-HH and *anti*-HH in a 41:59 ratio respectively (Table 2.5). When the dimerization was carried out in water, three products were observed, *viz.*, *anti*-HT:*anti*-HH:*syn*-HH appearing in a ratio of 31:46:23 respectively (Table 2.5). In the presence of CB[8] in water,

photodimerization led to a product ratio of 24:40:36 (Table 2.5). The increase in *syn*-HH photoproduct again was observed for non-polar coumarins in the presence of CB[8].

The photodimerization of coumarin in water was performed by preparing a 0.2 mM solution of **1f** in water (200 mL). The solution was irradiated in a 450 W medium pressure Hg lamp for 12 hours. The photoproducts were extracted with ethylacetate or diethylether and dried over Na₂SO₄. The solvent was removed in vacuo and without further purification the product distribution was analyzed by ¹H NMR spectroscopy. The photodimerization of **1f** in the presence of CB[8] was performed by preparing an aqueous solution (200 mL) consisting of 0.2 mM (2 eq.) of **1f** and 0.1 mM (1 eq) of CB[8]. The solution was sonicated for 3 hours at 60 °C and the solution was then cooled to room temperature. The solution was then irradiated for 12 hours. The photoproducts were extracted with ethylacetate or diethylether and dried over Na₂SO₄. The solvent was removed in vacuo and without further purification the product distribution was analyzed by ¹H NMR spectroscopy. Sensitized photoreaction in methanol was performed with a 0.003 M (1 eq) solution of **1f** And 0.003 M (0.125 eq) of benzophenone. The samples were irradiated for 14 hours. After irradiation the solvent was removed in vacuo and without further purification the product distribution was analyzed ¹H NMR spectroscopy in CDCl₃. The photoreaction in CDCl₃ was performed by preparing 0.08 M of **1e** in 500 μL and irradiating for 12 hours. The NMR was recorded without further purification.

2.4.8. Photoreactions of 6-methylcoumarin **1g** with CB[8] and isotropic media

Switching of the methyl group from the 7-position to the 6-position in coumarin likely reduced the overall volume of the photoproducts. It also likely changed the HG ratio from 1:2 for **1e** to 1:1.6 for **1g** which is pretty close in terms of stoichiometric ratio. The photoproduct selectivity for **1e** was exclusively *syn*-HH and relatively efficient compared to the background reactions. It should be noted that **1g** is considerably more soluble than **1e** concentrations up to 4 mM compared to 0.5 mM for **1e**. This might explain why the Jobs' plot showed a 1:1.6 HG complex for **1g**

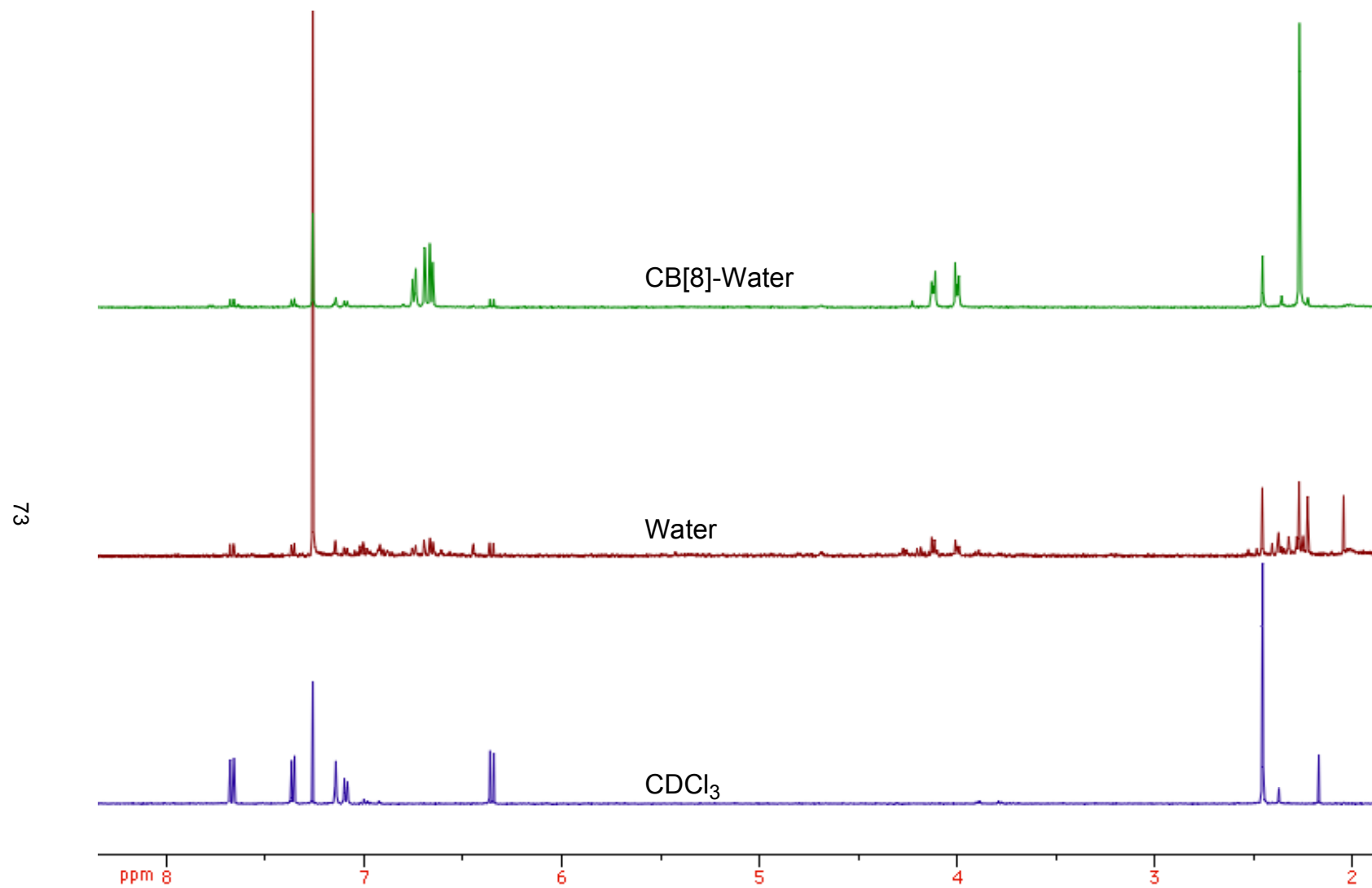


Figure 2.21 ^1H NMR (CDCl_3) spectra of the [2+2] photodimerization products of **1e** in isotropic media and CB[8]

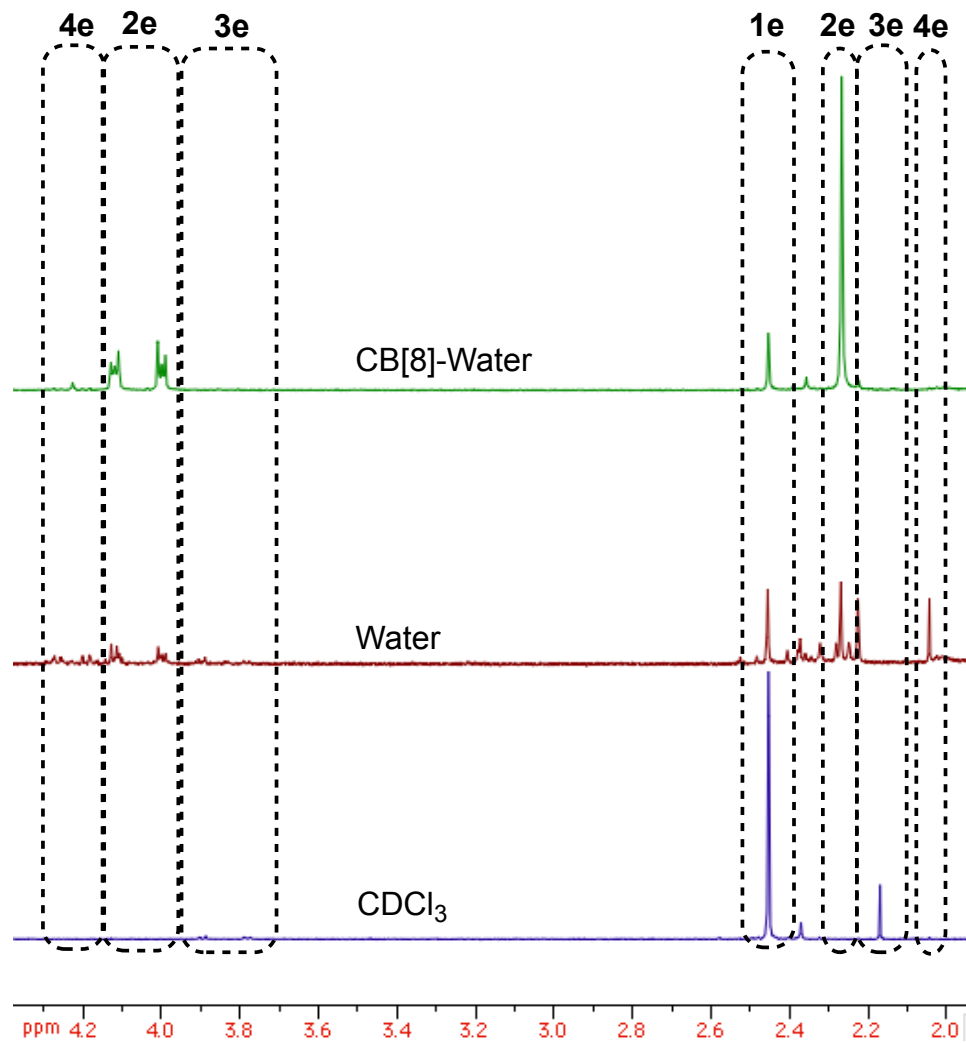


Figure 2.22 Expanded ¹H NMR (CDCl₃) spectra of the [2+2] photodimerization products of **1e** in isotropic media and CB[8]

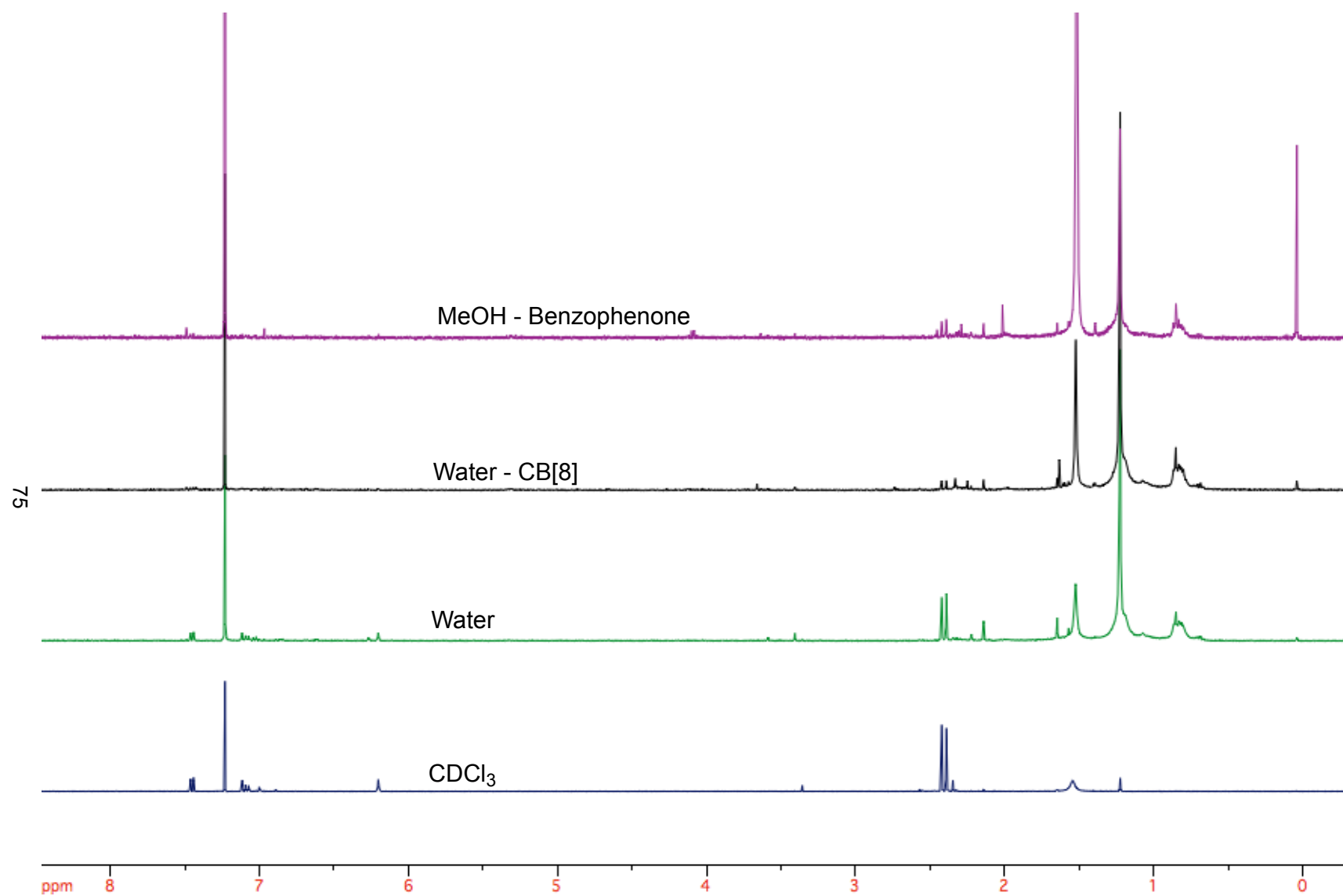


Figure 2.23 ¹H NMR (CDCl₃) spectra of the [2+2] photodimerization products of **1f** in isotropic media and CB[8]

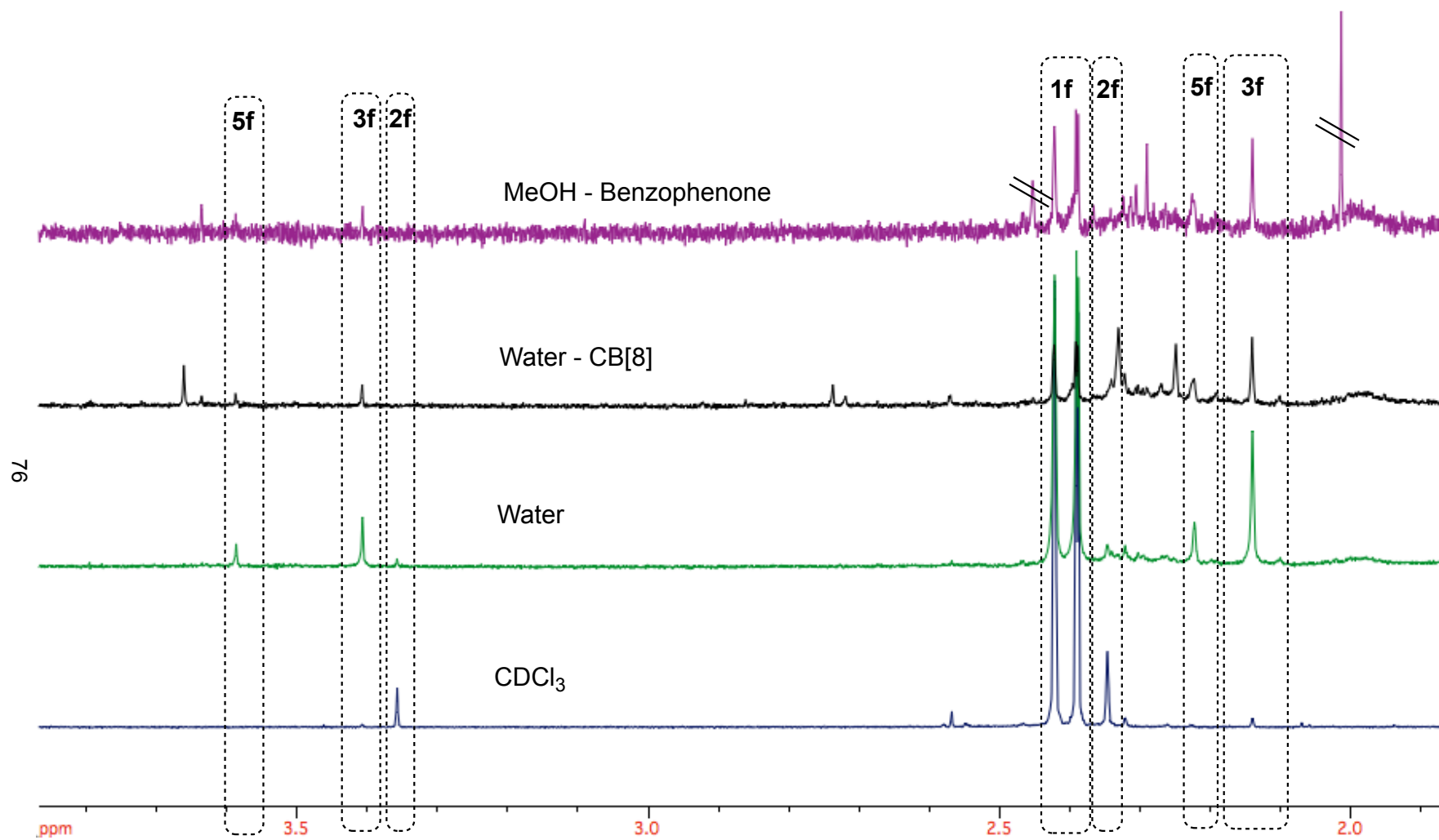


Figure 2.24 Expanded ¹H NMR (CDCl₃) spectra of the [2+2] photodimerization products of **1f** in isotropic media and CB[8]

The photoconversion of **1g** in chloroform and methanol led exclusively to *anti*-HH products (Table 2.5), however the reaction was very slow and inefficient. In water the reaction is also very slow, but three photoproducts *syn*-HH:*syn*-HT:*anti*-HH are formed in a ratio of 52:15:33 respectively (Table 2.5). The photoreaction in the presence of CB[8] revealed exclusively *syn*-HH and *syn*-HT photoproducts in a ratio of 31:69 (Table 2.5).

The photodimerization in water was performed by preparing a 0.2 mM solution of **1g** in water (200 mL). The solution was irradiated in a 450 W medium pressure Hg lamp for 24 hours. The photoproducts were extracted with ethylacetate or diethylether and dried over Na₂SO₄. The solvent was removed in vacuo and without further purification the product distribution was analyzed by ¹H NMR spectroscopy. The photodimerization of **1g** in the presence of CB[8] was performed by preparing an aqueous solution (200 mL) consisting of 0.2 mM (2 eq.) of **1g** and 0.1 mM (1 eq.) of CB[8]. The solution was sonicated for 3 hours at 60 °C and the solution was then cooled to room temperature. The solution was then irradiated for 24 hours. The photoproducts were extracted with ethylacetate or diethylether and dried over Na₂SO₄. The solvent was removed in vacuo and without further purification the product distribution was analyzed by ¹H NMR spectroscopy. The photoreaction performed in methanol was prepared by making a 0.003 M (1 eq) solution of **1g** in methanol. The samples were irradiated for 36 hours. After irradiation the solvent was removed in vacuo and without further purification the product distribution was analyzed ¹H NMR spectroscopy in CDCl₃. The photoreaction in CDCl₃ was performed by preparing 0.08 M of **1g** in 500 μL in an NMR tube and irradiating the sample for 36 hours. The NMR was recorded without further purification.

The volume of the photoproducts for **1g** are all within the available size limitations of the CB[8] cavity (Table 2.4). The *syn*-photoproducts along with the *anti*-HH photoproduct are all relatively small and within the same computed volume. These photoproducts are well within the ideal 55% volume theory proposed by Rebek.³³ The photoproducts *syn*-HH, *syn*-HT and *anti*-HH occupy 53%:57% and 55% of the available volume of CB[8] respectively (Table 2.4). This means that other factors like, but not limited to, thermodynamics and kinetics of the photoreactions inside and outside of the CB[8] are likely controlling the photoreaction process.

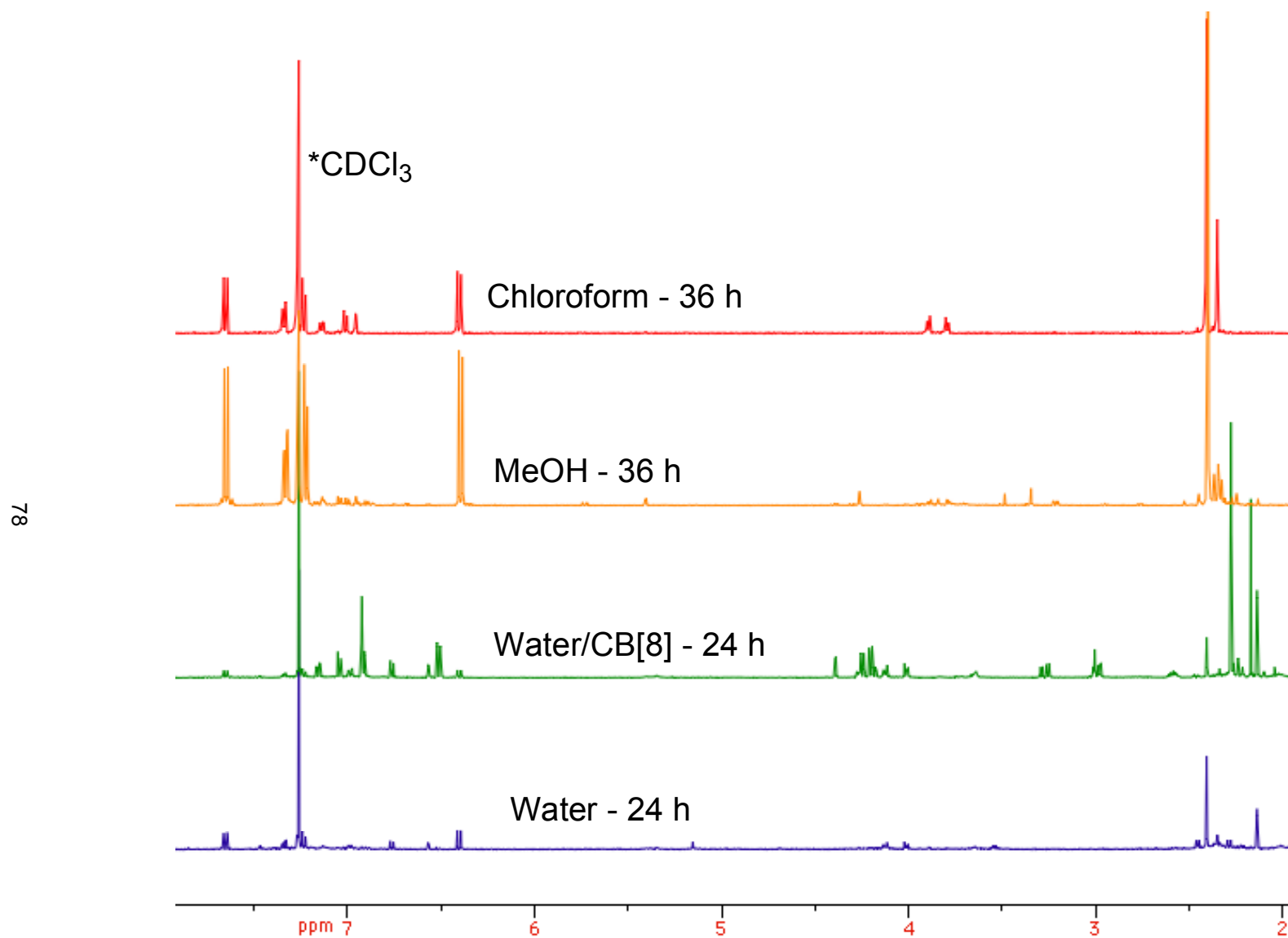


Figure 2.25 ¹H NMR (CDCl₃) photo product selectivity of **1g** irradiated in various solvents and H₂O/CB[8]

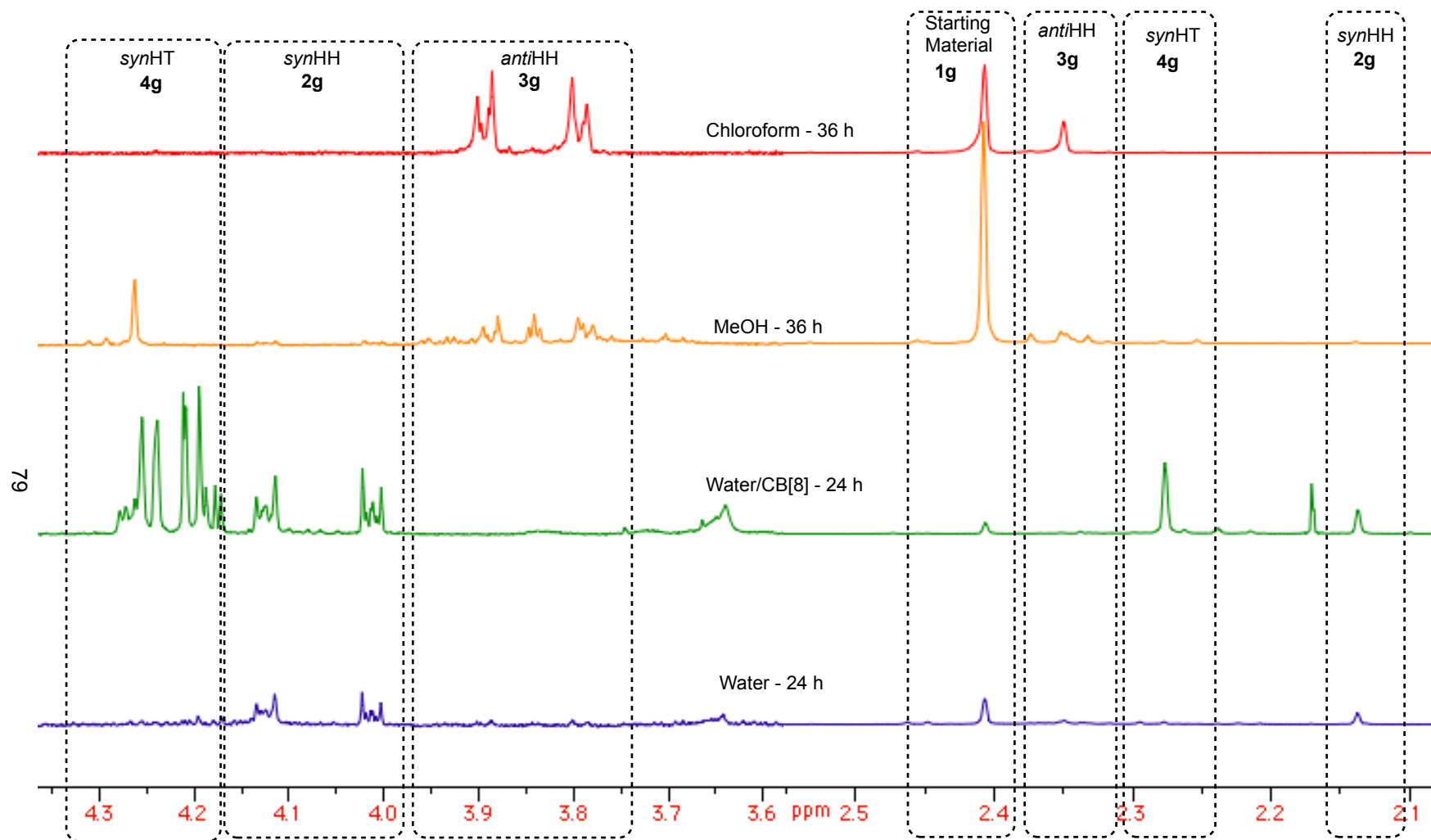


Figure 2.26 Expanded ^1H NMR (CDCl_3) photo product selectivity of **1g** irradiated in various solvents and $\text{H}_2\text{O}/\text{CB}[8]$

2.4.9. Photoreactions of 4,6-dimethylcoumarin **1h** with CB[8] and in isotropic media

Continuing the theme of methylation at the 4-position of **1g** considerably increased the volume of coumarin **1h** as well as its photoproducts. The Jobs' plot showed a 1:1 HG ratio (Table 2.3), and based on our results thus far this is not always indicative of photo-selective reactions within the CB[8] cavity. Similar to the other non-polar coumarins, photodimerization of **1h** in CHCl₃ resulted in an *anti*-HH photoproduct (Table 2.54). Photodimerization in methanol resulted in three photoproducts, *syn*-HT:*anti*-HH:*anti*-HT in a ratio of 39:44:17 respectively. Photodimerization in H₂O resulted in *syn*-HH and *anti*-HH as the two photoproducts formed in a ratio of 25:75. Interestingly, in the presence of CB[8] the product selectivity was almost completely reversed to 73:27, favoring the *syn*-HH over the *anti*-HH (Table 2.5).

The photodimerization of in water was performed by preparing a 0.2 mM solution of **1h** in water (200 mL). The solution was irradiated in a 450 W medium pressure Hg lamp for 12 hours. The photoproducts were extracted with ethylacetate or diethylether and dried over Na₂SO₄. The solvent was removed in vacuo and without further purification the product distribution was analyzed by ¹H NMR spectroscopy. The photodimerization of **1h** in the presence of CB[8] was performed by preparing an aqueous solution (200 mL) consisting of 0.2 mM (2 eq.) of **1h** and 0.1 mM (1 eq) of CB[8]. The solution was sonicated for 3 hours at 60 °C and then cooled to room temperature. The solution was then irradiated for 12 hours. The photoproducts were extracted with ethylacetate or diethylether and dried over Na₂SO₄. The solvent was removed in vacuo and without further purification the product distribution was analyzed by ¹H NMR spectroscopy. The photoreaction performed in methanol was prepared by making a 0.003 M (1 eq) solution of **1h**. The samples were irradiated for 12 hours. After irradiation the solvent was removed in vacuo and without further purification the product distribution was analyzed ¹H NMR spectroscopy in CDCl₃. The photoreaction in CDCl₃ was performed by preparing 0.08 M of **1h** in 500 μL in an NMR test tube and irradiating the samples for 12 hours. The NMR was recorded without further purification.

The reversal of photoproducts is interesting because when the Jobs' plot revealed a HG ratio of 1:1. One would expect that the reactivity should mirror that of neat water irradiations if the reaction occurred outside the cavity. Instead it is likely that an apparent 1:1 HG complex (observed in Jobs' plot) might have a microscopic amount of 1:2 HG complex (Not detected by UV-vis changes). If the photoreaction within the cavity is more efficient than the reaction in solution it is possible to achieve a

catalytic supramolecular photocycloaddition, provided the other requirements are met *viz.* product release and exchange of coumarin guests between the solution and the CB[8] host . It is likely that the photoreaction that occurred within the cavity is at a faster rate resulting in an increase in the *syn*-HH photoproduct, whereas the *anti*-HH photoproduct is likely formed in solution as the major product.

The volume constraints for the **1h** photoproducts are all smaller than the available volume that CB[8] provides. The methyl-group in the 6-position provides the starting material and photoproducts with a smaller cross-sectional area. This increases the distance in only one direction as opposed to two directions in the case of 7-substitued coumarins. It is possible that the product selectivity from within the cavity is exclusively *syn*-HH whereas the small amount of free guest in water produces majority *anti*-HH photoproduct. This could be similar to the observation from **1f** where the increase in *syn*-HH photoproduct was observed while there was a decrease in the *anti* adducts. Thus a small amount of 1:2 HG complexation in solution could significantly change the product distribution even though the 1:2 HG complex might not be observed by UV-vis spectroscopy. Coumarins that appear to be non-polar in nature prefer the *syn* adducts over the *anti*. Knowing that a small amount of complexation can influence selectivity in a photoreaction we returned to two coumarin derivatives that initially did not show a complex during the initial investigation.

2.4.10. Photoreactions of 7-acetoxycoumarin **1i and 7-acetoxy-4-methylcoumarin **1j** with CB[8]**

The final two coumarins to be discussed for the [2+2] photodimerization are **1i** and **1j**. The HG complex stoichiometry for 7-acetoxycoumarin (**1i**) was observed to be near 1:1 whereas 7-acetoxy-4-methylcoumarin (**1j**) did not show any HG complexation with CB[8] by UV-vis Jobs' plot experiments. Although the HG ratio for the Jobs' plots have been unreliable in predicting the reactivity within the water CB[8] complex, dynamics involved in the supramolecular system, they do offer insights into the interactions between the host and the coumarin guest.

The photodimerization of **1i** performed in chloroform resulted in exclusively *anti*-HH photoproducts. The product distribution in water and in the presence of CB[8] resulted in exclusively *syn* photoproducts, although the product distribution (ratio HH/HT) was slightly different. The product distribution in water was 34:66 for *syn*-HH:*syn*-HT, whereas in the presence of CB[8] the product

selectivity became 22:78 for *syn*-HH:*syn*-HT. This is not a drastic change, but it does signal that the interactions are strong enough to assist in the formation of the *syn*-HT dimer formation (Figures 2.26 and Figures 2.27).

The photodimerization of coumarin in water was performed by preparing a 0.2 mM solution of **1i** in water (200 mL). The solution was irradiated in a 450 W medium pressure Hg lamp for 18 hours. The photoproducts were extracted with ethylacetate or diethylether and dried over Na₂SO₄. The solvent was removed in vacuo and without further purification the product distribution was analyzed by ¹H NMR spectroscopy. The photodimerization of **1i** in the presence of CB[8] was performed by preparing an aqueous solution (200 mL) consisting of 0.2 mM (2 eq.) of **1i** and 0.1 mM (1 eq) of CB[8]. The solution was sonicated for 3 hours at 60 °C and the solution was then cooled to room temperature. The solution was irradiated for 24 hours. The photoproducts were extracted with ethylacetate or diethylether and dried over Na₂SO₄. The solvent was removed in vacuo and the product distribution was analyzed by ¹H NMR spectroscopy without further purification. The photoreaction in CDCl₃ was performed by preparing 0.08 M of **1i** in 500 μL and irradiating for 12 hours.

The product selectivity for the [2+2] photoreaction of **1j** was 83:17 *anti*-HH:*anti*-HT in chloroform when irradiated for 15 hours. In methanol all the photoproducts were formed, however the distribution switched from predominantly *anti*-photoproducts to *syn*. The product distribution was 17:37:22:24 for *syn*-HH:*syn*-HT:*anti*-HH:*anti*-HT. The product selectivity in water and in CB[8] was exactly the same at a ratio of 32:22:46 for *syn*-HH:*anti*-HH:*anti*-HT. This lack of selectivity demonstrates the lack of interaction between the coumarin and CB[8] to influence photoreactivity which is observed in the Jobs plot in Figure 2.12.

The lack of interaction is contrary to the hypothesis that adding aliphatic groups should drive the equilibrium of the coumarin to template easier into hydrophobic cavity. It's not clear why **1i** will form a complex whereas **1j** won't. Perhaps it has to do with the increased volume, or other factors that cannot be clearly deciphered with these experiments. Whatever the reason, nature has decided to make it work that way.

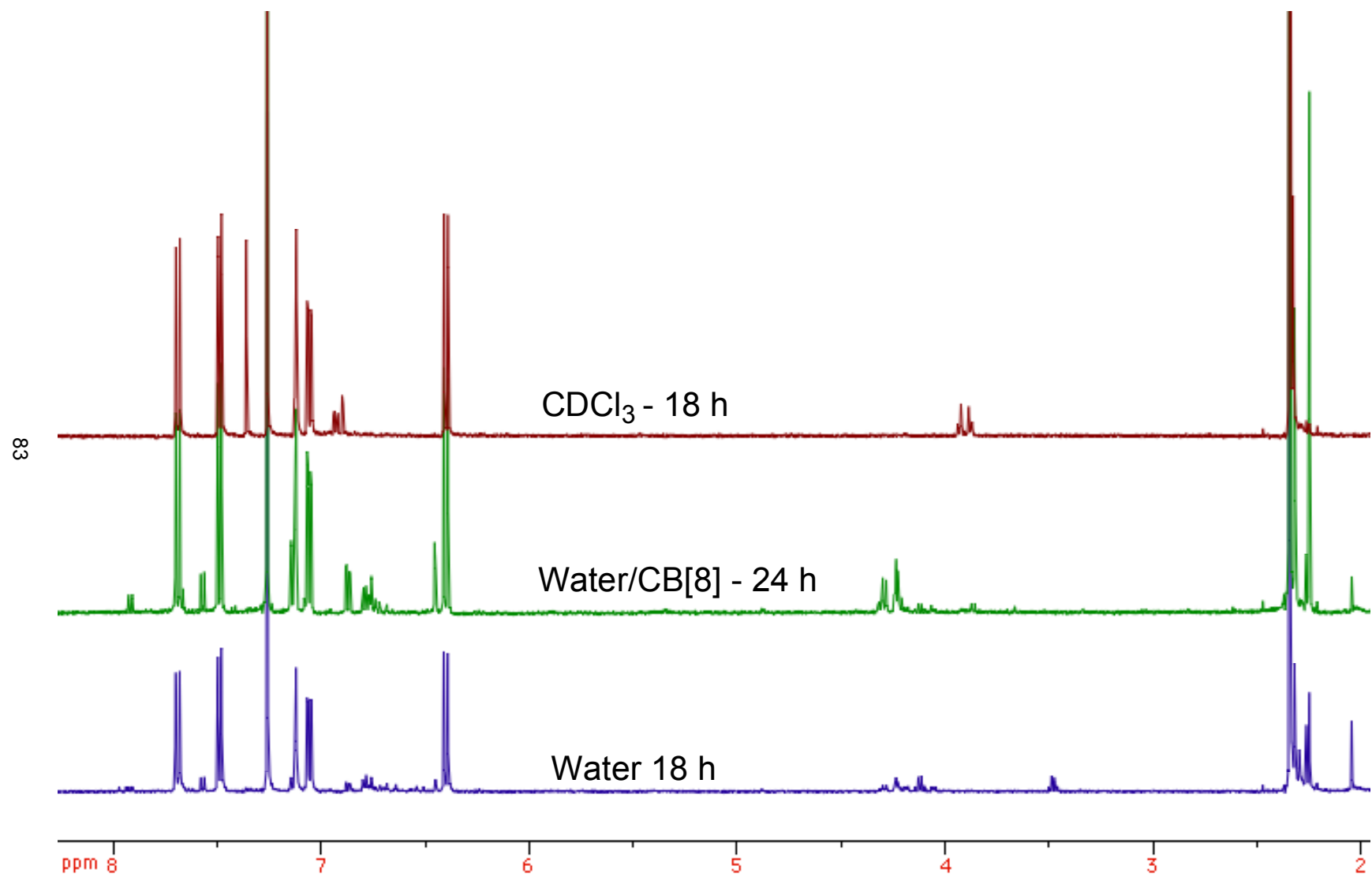


Figure 2.27 ¹H NMR (CDCl₃) of **1i** irradiated in various solvents and H₂O/CB[8]

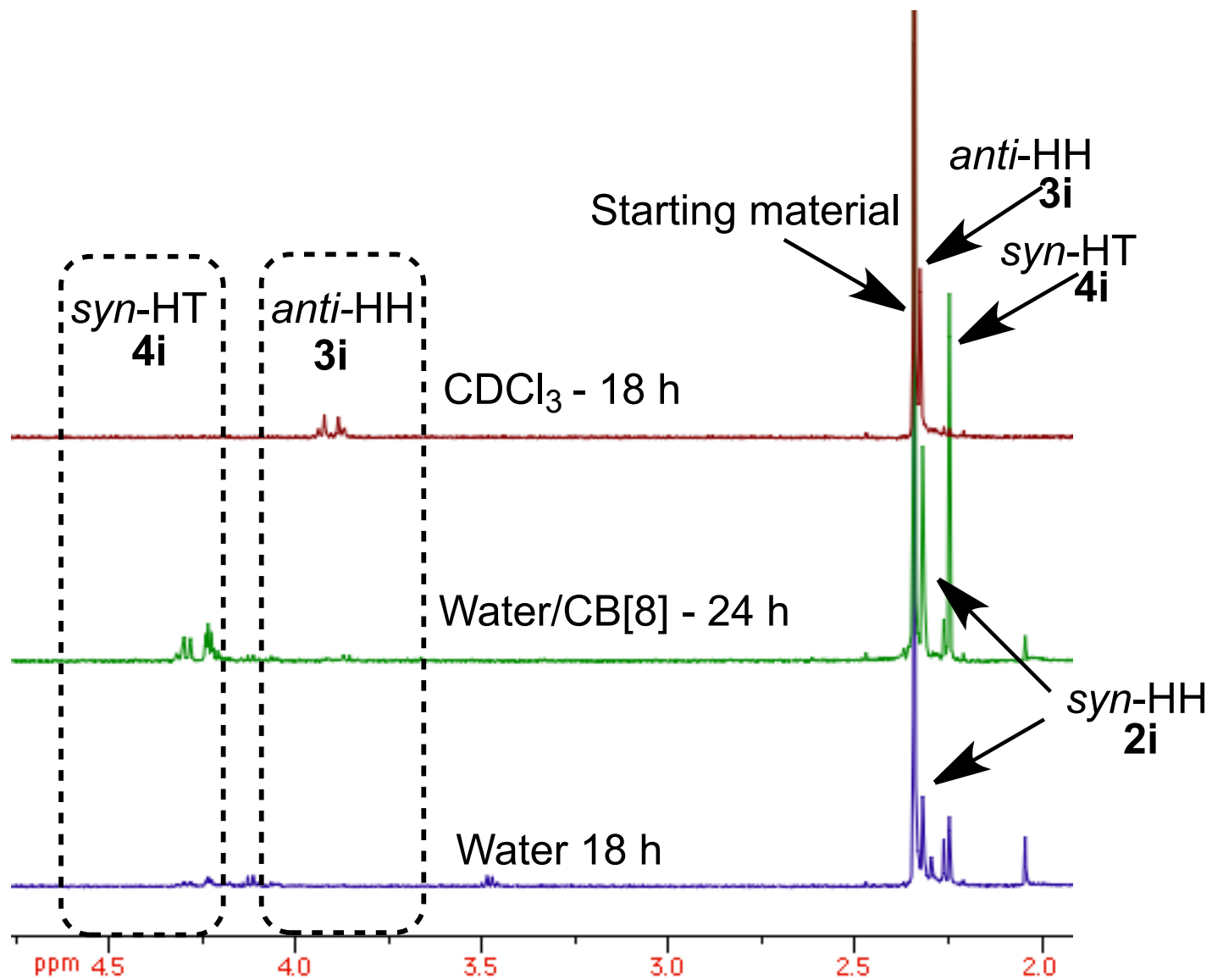


Figure 2.28 Expanded ^1H NMR (CDCl_3) of **1i** irradiated in various solvents and $\text{H}_2\text{O}/\text{CB}[8]$

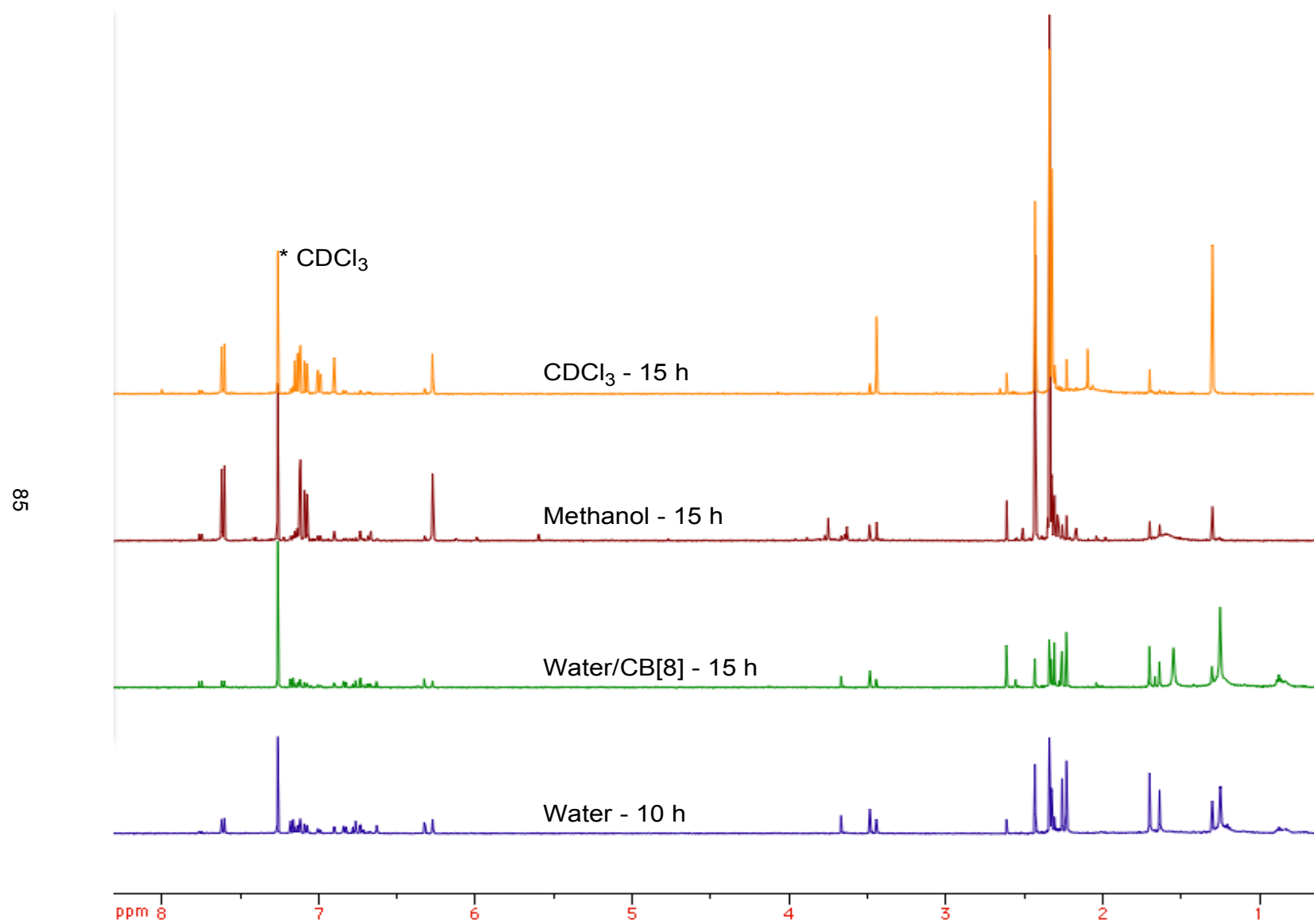


Figure 2.29 ^1H NMR (CDCl_3) of **1j** irradiated in various solvents and $\text{H}_2\text{O}/\text{CB}[8]$

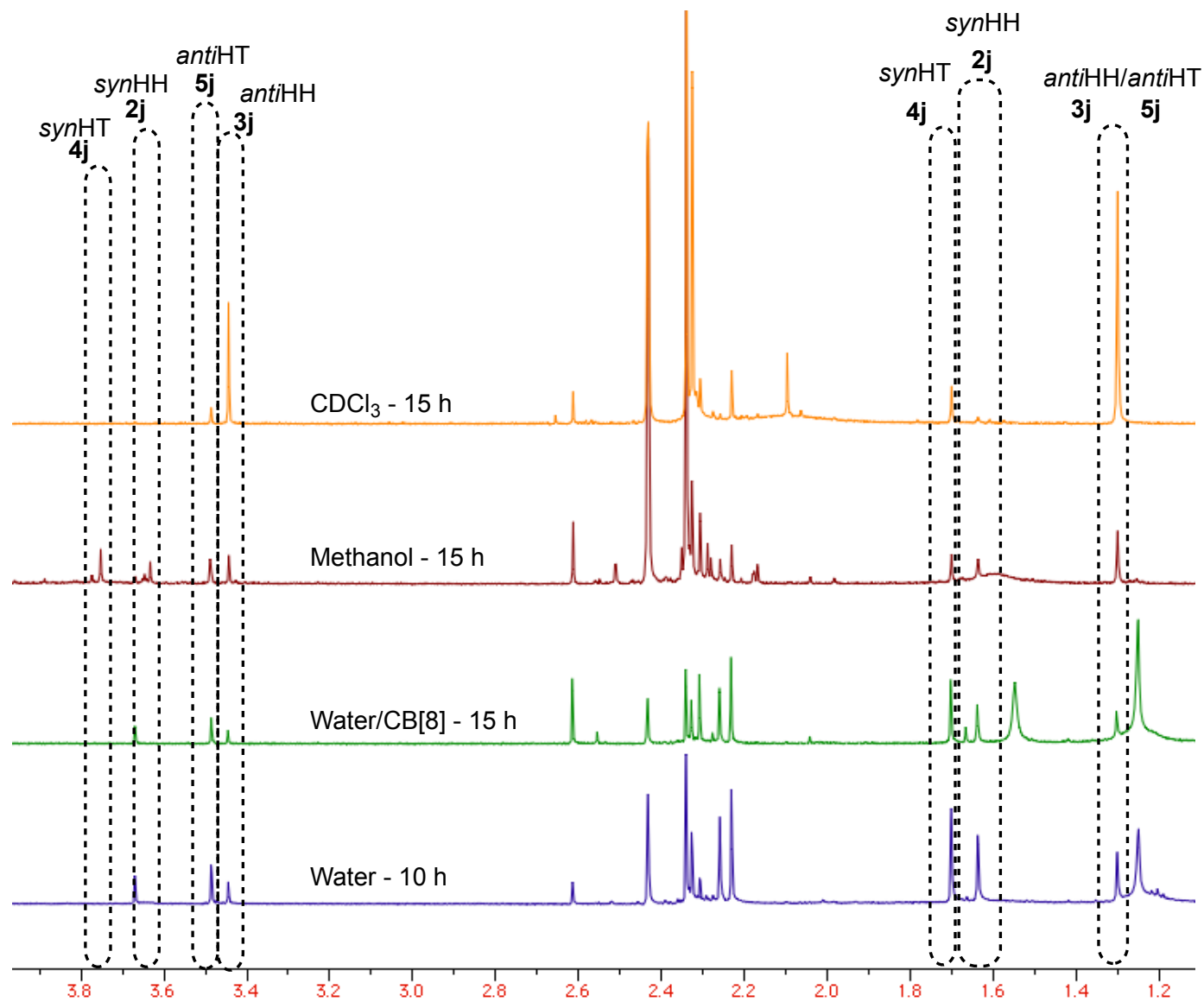


Figure 2.30 Expanded ^1H NMR (CDCl_3) of **1j** irradiated in various solvents and $\text{H}_2\text{O}/\text{CB}[8]$

The photodimerization in water was performed by preparing a 0.2 mM solution of **1j** in water (200 mL). The solution was irradiated in a 450 W medium pressure Hg lamp for 18 hours. The photoproducts were extracted with ethylacetate or diethylether and dried over Na₂SO₄. The solvent was removed in vacuo and without further purification the product distribution was analyzed by ¹H NMR spectroscopy. The photodimerization of **1j** in the presence of CB[8] was performed by preparing an aqueous solution (200 mL) consisting of 0.2 mM (2 eq.) of **1j** and 0.1 mM (1 eq) of CB[8]. The solution was sonicated for 3 hours at 60 °C and the solution was then cooled to room temperature. The solution was then irradiated for 18 hours. The photoproducts were extracted with ethylacetate or diethylether and dried over Na₂SO₄. The solvent was removed in vacuo and without further purification the product distribution was analyzed by ¹H NMR spectroscopy. The photoreaction performed in methanol was prepared by making a 0.003 M (1 eq) solution of **1j** in methanol. The samples were irradiated for 15 hours. After irradiation the solvent was removed in vacuo and without further purification the product distribution was analyzed ¹H NMR spectroscopy in CDCl₃. The photoreaction in CDCl₃ was performed by preparing 0.08 M of **1j** in 500 μL and irradiating for 15 hours. The NMR was recorded without further purification.

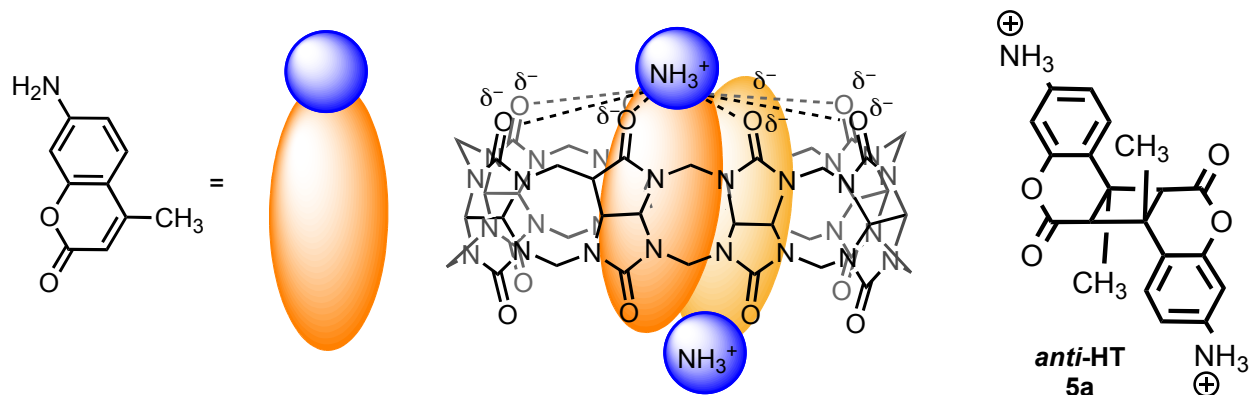
2.5. Discussion

2.5.1. Understanding photoreactivity of coumarins 1a-1k with CB[8]

In total 11 coumarin derivatives were screened via Jobs' plot for complexation with CB[8] (Table 2.3) the volume of their photoproducts were calculated (2.4) and photoproduct selectivity was monitored by ¹H NMR (Table 2.5). These represent a wide range of coumarins with polar and non-polar functionality. With respect to the 1:2 HG complexes, these include 7-amino-4-methylcoumarin and 7-methylcoumarin. We also observed non-complexation with CB[8] however even with non-complexation we observed the cavity could alter the product selectivity. The majority of the complexes appeared to be dynamic and favor the 1:2 complexation with product selectivity or would favor the empty cavity which can account for the product distribution to be similar to the reaction in water without CB[8]. The most interesting aspect of screening coumarins was the observation that if we could tailor a dynamic HG system along with a reaction that was far more efficient in the cavity. This observation could potentially have implication in developing a truly photocatalytic system mediated by supramolecular container.

2.5.2. Rationale for product selectivities in CB[8] in the presence of CB[8] – polar vs. Non-polar coumarins

Inspection of Table 2.5 shows a clear difference in reactivity for polar and non-polar coumarins when templated with CB[8]. The dimerization of polar coumarins resulted in *anti*-HT photoproducts whereas the non-polar coumarins formed *syn*-photoproducts. Rationalizing why the polar substituents prefer the *anti*-HT orientation for the photoproducts in the presence of CB[8] could be rationalized by hydrogen bonding interactions from the hydroxy group of **1k** and the ion-dipole interactions from the ammonium cation group of **1a** with the portals of the CB[8] (Scheme 2.4). This brings the reactive alkene bonds within a close proximity to each other. When molecules absorb a photon of light, they react forming the *anti*-HT photoproducts.



Scheme 2.5 Templating effects of polar groups (NH_3^+ , OH) on the carbonyl portals of CB[8]

Explaining why non-polar coumarins prefer the *syn*-photoproducts is a little bit more difficult to comprehend. The strong hydrogen bonding or cation-dipole interactions are lost as well as the *anti*-photoproduct selectivity. A reasonable explanation is since the non-polar compounds are more “hydrophobic” they are more likely to “hide” within the CB[8] cavity. This would allow the π - π interactions that might dictate aggregation to take over, thereby controlling the coumarin orientation within the CB[8] cavity. If this is the case, we should see a possible aggregation and subsequent redshift in fluorescence spectroscopy (or) an H-aggregated that will be hypsochromically shifted. Another often over looked but quiet relevant aspect is the removal of the H-bonded interactions between the non-polar coumarins

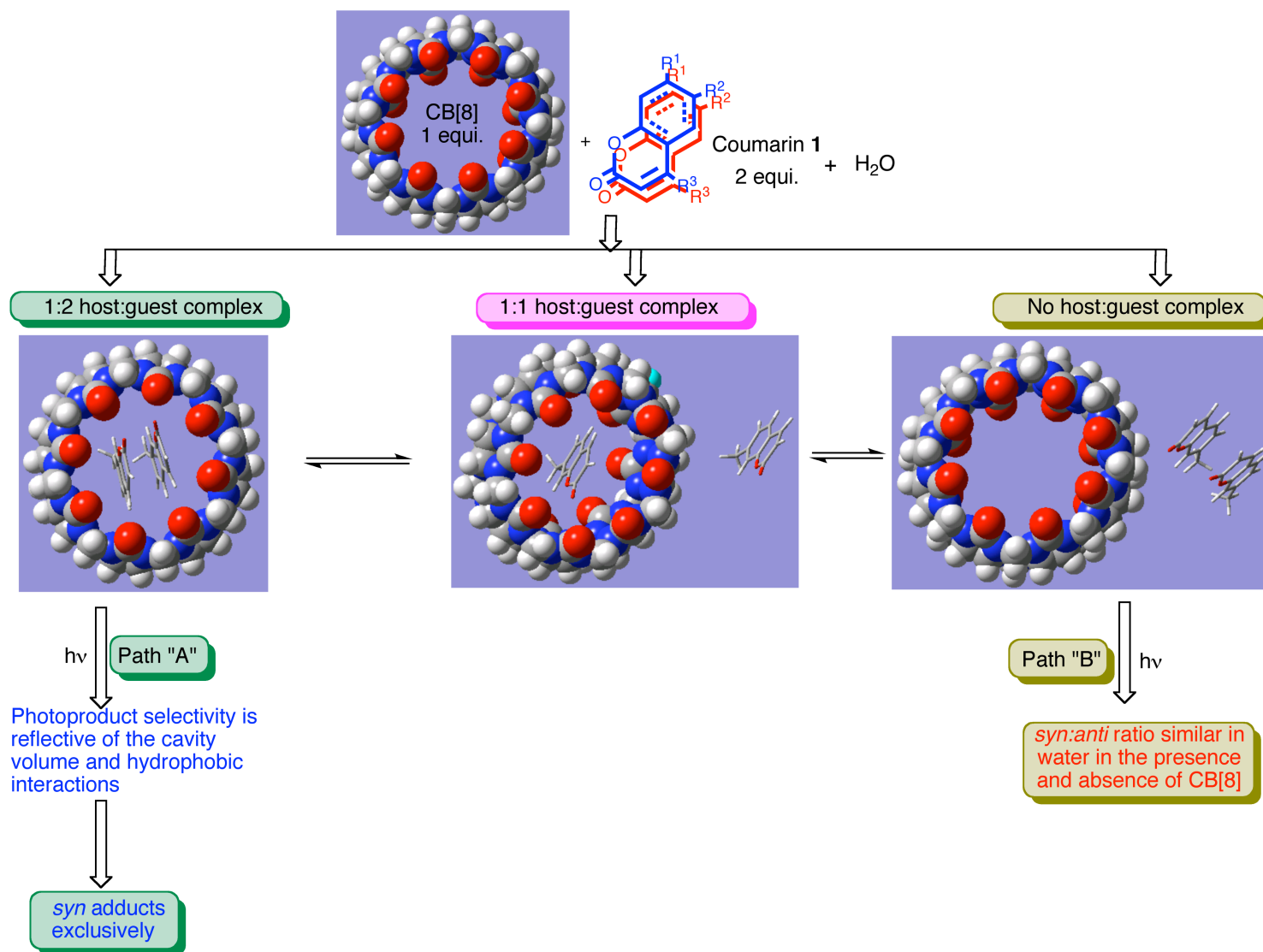
carbonyl functionality and CB[8] portals. The removal of H₂O associated with CB[8] as well as the coumarins likely influenced the HG complex formation due to entropic effects.

2.5.3. Case for reactivity and selectivity for photodimerization of non-polar coumarins within CB[8]

There are three possible mechanisms that explain the photodimerization results; Based on Jobs' plots as well as product selectivity (Scheme 2.5) we can rationalize these distinct scenarios. The cases break down into three categories; the first being an ideal 1:2 HG complex reacts differently within CB[8] leading to different photoproducts than in neat water. The second HG complexes are "dynamic" in nature and the relative reactivity inside and outside the cavity dictate the product selectivity. The third case results from non-complexation and reaction occurs exclusively in water irrespective of the presence or absence of CB[8] (Scheme 2.5).

The easiest of the three cases to explain product selectivity is the case for non-complexation. In this scenario, identical selectivity will be observed both in the presence and absence of CB[8] as the dimerization occurs outside the cavity (Scheme 2.5 path "B") Coumarin derivatives **1c**, **1d**, and **1j** did not form HG complexes with CB[8] in water (Table 2.3) Photodimerization of the methoxycoumarin derivatives **1c** -**1d** in water in the presence and absence of CB[8] was noticeably different even though we were unable to characterize a HG complex by absorbance measurements. In the case of **1j**, photodimerization leads to similar product distribution both in the presence and absence of CB[8] and it is quite likely that the dimerization occurs outside the CB[8] cavity as illustrated in Scheme 2.5, Path "B" .

The stoichiometric 1:2 HG complexes that react to form nearly exclusive products are also very easy to rationalize. In this scenario, the product selectivity during the dimerization is reflective of the available free volume and non-bonding interaction that develops within the CB[8] cavity (Scheme 2.5 path "A"). Photodimerization of **1e** most likely occurs *via* this pathway (Scheme 2.5; Path "A") as it forms a 1:2 HG complex (Table 2.3). As shown in Table 2.4, based on the volume, all four photoproducts from **1e** could be encapsulated within the CB[8] cavity. Clearly the product distribution changes in the presence of CB[8] in water (Table 2.5). Exclusive formation of *syn* adducts from non-polar coumarin starting materials is reflective of the templating effect of CB[8].



Scheme 2.6 The HG interactions and stoichiometry to determine product selectivity

The idea of a dynamic guest exchange is the third example. In this scenario, the photoreactivity/selectivity within CB[8] depends on the complexation equilibrium, stability (life time) of the 1:2 complex and the relative quantum yield of dimerization inside and outside the cavity. Inspection of Table 2.3 reveals that **1g** forms dynamic host –guest complex (1:1.6 host –guest ratio) indicative of an exchange between [uncomplexed **1g**], [1:1] **1g**@CB[8] HG complex and [1:2] **1g**@CB[8] HG complex. Photodimerization of **1g** in the presence of CB[8] in water leads to *syn*-HT **4g** (69%) as the major photoproduct and *syn*-HH **2g** (31%) as the minor photoproduct (Table 2.5;). In the absence of CB[8] in water, the photoproduct distribution (Table 2.5) was different viz., *syn*-HH **2g** (52%), *anti*-HH **3g** (33) *syn*-HT **4g** (15%). Similarly in the case of **1h**, the photoproduct distribution in water in the absence and in the presence of CB[8] was noticeably different, even though it forms a 1:1 host –guest complex (Table 2.3). Photodimerization of **1h** in the presence of CB[8] in water leads to *syn*-HH **2h** as the major photoproduct (73%) and *anti*-HH **3h** as the minor photoproduct (27%). In the absence of CB[8] in water, the *anti*-HH **3h** (75%) and *syn*-HH **2h** (25%) are the major and minor photoproducts respectively (Table 2.5;). We speculate that in the case of coumarins **1g** and **1h** the photoproduct distribution is reflective of a dynamic equilibrium between uncomplexed coumarins, 1:1 coumarin@CB[8] complex and 1:2 coumarin@CB[8] complex in water. This implies that the relative quantum yield of dimerization within CB[8] cavity and in water along with the complexation equilibrium determines the product distribution ratio. Hence, as in case (i) the selectivity will be reflective of the available free volume, the non-bonding interaction that develops within the cavity (Scheme 2.5; Path “A”). At present we are unable to provide the quantum yields of dimerization in water and within the cavity. Nevertheless, it is tempting to hypothesize that the change in selectivity is reflective of the templating effect of CB[8] as indicated in Scheme 2.5 (Path “A”).

Photodimerization could also occur outside CB[8] cavity for coumarins that form dynamic 1:1 complex in water. In this scenario, identical selectivity will be observed both in the presence and absence of CB[8] in water as two coumarin monomers are not encapsulated within the CB[8] cavity during the dimerization process (Scheme 2.5, Path “B”). Coumarin derivative **1f**, with a HG complex ratio of 1:1.3 (dynamic complex) most likely dimerize outside the cavity resulting in the observed photoproduct distribution that is similar in water both in the presence and absence of CB[8] (Table 2.5; entries 6 and 7). In the case of coumarin derivative **1b** and **1i** that form a 1:1 host –guest complex, similar product

distribution in water both in the presence and absence of CB[8] is observed indicating that photodimerization occurs more efficiently outside the cavity than within the cavity.

In the case of **1b** a HG complex such of 1:1.7 was observed but the majority of the reaction occurs outside the cavity leading to photoproducts ratios that are very similar to the reactions that occur in neat water. In these cases the product selectivity with and without the cavity are nearly identical. Under these conditions we can assume the majority of the reactions occur outside in solution, however there can be a small amount of reactions that occur within the cavity.

The vast majority of HG complexes experience some form of dynamic exchange. Under the realm of dynamic exchange there are two directions in which the reaction can go. Reactions that are dynamic occur when a Jobs' plot indicating with a 1:1.3 or 1:1.6 HG ratio, but the product selectivity is different than in water. The dimerizations of these compounds often result in both reactions with exclusive products, like in the case of **1g**, but can also result in a mixture of reactions within the cavity as well as reactions outside the cavity like in the case of **1a**, **1h** and **1d**. Depending on the selectivity with and without CB[8] we can estimate the product selectivity and rate of conversion in the cavity and in solution. It appears the relative photoreactivity inside and outside the cavity will determine the reaction efficiency as well as the product selectivity.

2.5.4. Conclusion

Our study has showed that not only cationic derivatives can be templated within CB[8], but also non-polar coumarins can be templated so that their photochemical reactivity could be influenced effectively. The host-guest complex appears to be controlled by the available volumes the guests within the host-cavity. Upon irradiation the photoproduct selectivity appears to be controlled by the polarity of the coumarin itself. Additionally dynamic HG complexes were observed with non-polar coumarins and the product selectivity with CB[8] was dictated by photochemical efficiency inside and outside the cavity. Unexpected observations of dynamic HG systems provided an opportunity for us to investigate the feasibility of using CB[8] as an organic supramolecular photocatalysts and will be discussed in the subsequent chapters.

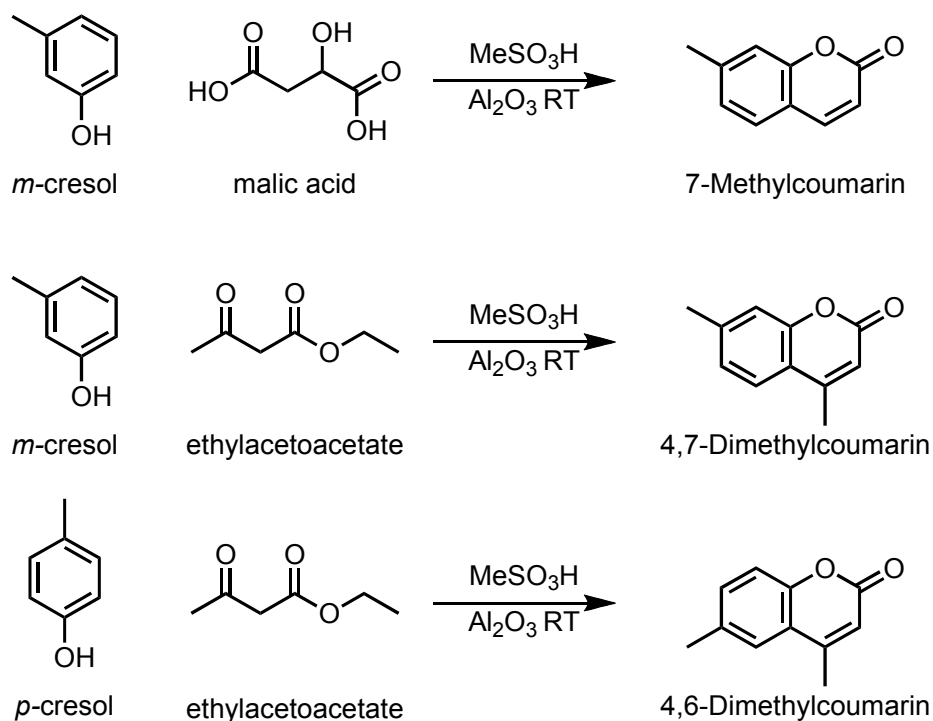
2.6. General Methods

2.6.1. General methods for experimental conditions

The following coumarin derivatives were purchased from Alfa Aesar® and were used without further purification, **1d**, **1a**, **1k**, **1g**. The synthesis for **1e**, **1f**, **1h**, **1i** and are detailed in section 2.6.2. Ethyl acetate and diethyl ether were used for the extraction processes were used as received without any further purification. Barnstead Nanopure deionized water with a resistivity greater than 17.8 MΩ was used unless indicated otherwise. The Jobs' plots were performed on either a Shimadzu UV-2501 PC UV-vis or a Cary500 recording spectrophotometer UV-vis. The concentrations of host and guest for the Jobs' plots are listed in Table 2.2. The photoreactions were irradiated with a 450 W medium pressure Hg-lamp at room temperature. ¹H NMR and ¹³C NMR spectra were obtained on Varian 400 MHz or 500 MHz spectrometer. Coupling constants (J) are reported in hertz (Hz). Standard abbreviations indicating multiplicity were used as follows: s (singlet), br (broad), d (doublet), t (triplet), q (quartet), m (multiplet). Electro spray ionization spectra were recorded on a Bruker BioTof mass spectrometer in positive (ESI+) ion mode. All computations were done using Gaussian 03²⁹ package at RB3LYP/6-31G(d,p) level.

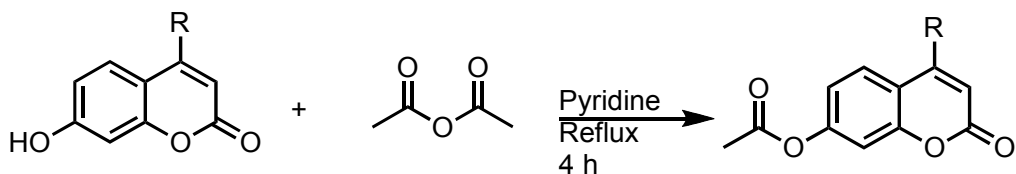
2.6.2. Synthesis and characterization of coumarin derivatives

The synthesis of **1e**, **1h** and **1f** was performed using the same procedure reported by Shargi and co-workers³⁴ (Scheme 2.6). The following procedure was employed for the synthesis of 7-methylcoumarin **1e**. To a round bottom flask 3.2 g (1.9 eq) of aluminum oxide powder and 1.6 g (1.0 eq.) of methylsulfonic acid were added together and stirred at room temperature. Malic acid (2.6 grams 1.2 eq) was added while the solution with constant stirring. An addition of *p*-cresol (1.0 eq) was made over the period of an hour and the mixture continued to stir at room temperature overnight. The reaction was quenched by the addition 10 mL of methanol and it was refluxed for 4 hours. The alumina was filtered off using a Büchner funnel followed by the addition of a saturated potassium carbonate solution to the liquor until bubbling ceased. The precipitate was filtered and recrystallized two times using methanol/water (50/50 v/v mixture). Final yield was approximately 50%.



Scheme 2.7 Synthetic scheme for various methylcoumarin derivatives. The NMR for the coumarins match the previous literature reports³⁴

Synthesis of **1i** and **1j** was performed starting either with 7-hydroxycoumarin or 7-hydroxy-4-methylcoumarin respectively. These coumarins were purchased from Alfa Aesar and used without further purification. The respective hydroxycoumarin (400 mg) and pyridine (10 mL) was added to a two neck round bottom. The reaction was stirred at room temperature for 30 min while 1.1 eq (0.26 mL) of acetic anhydride was added slowly. Once the acetic anhydride was added the reaction was heated to reflux (~120 °C) for 4 hours. The reaction was quenched by pouring it over a beaker full of ice. The iced solution was melted and the pH was tested for acidity. The organic layer was extracted three times using ethylacetate and dried under vacuo. The solid was then recrystallized three times from hot ethanol.



Scheme 2.8 Synthetic scheme for synthesizing 7-acetoxy coumarin derivatives

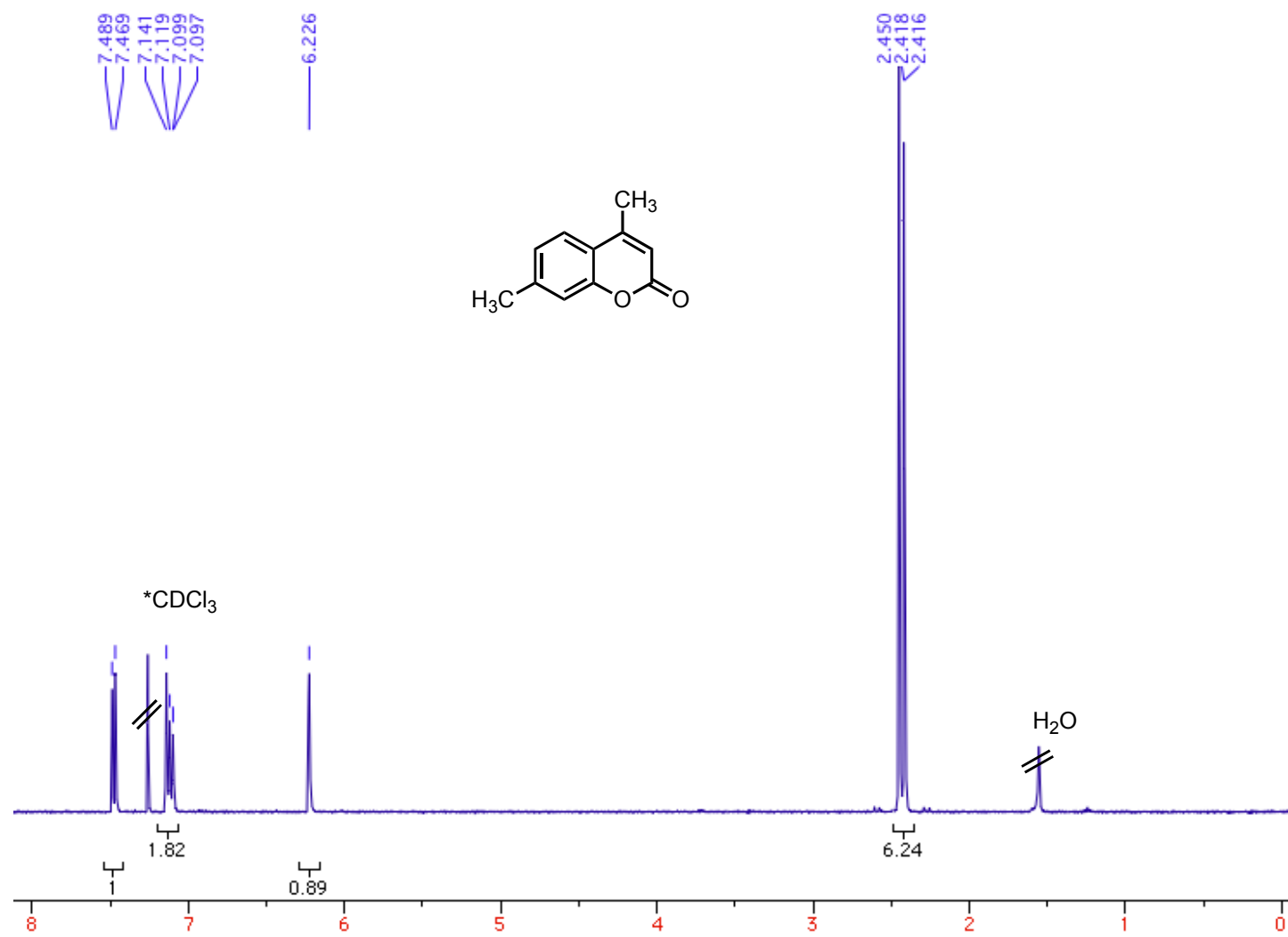


Figure 2.31 ^1H NMR of **1f** in CDCl_3

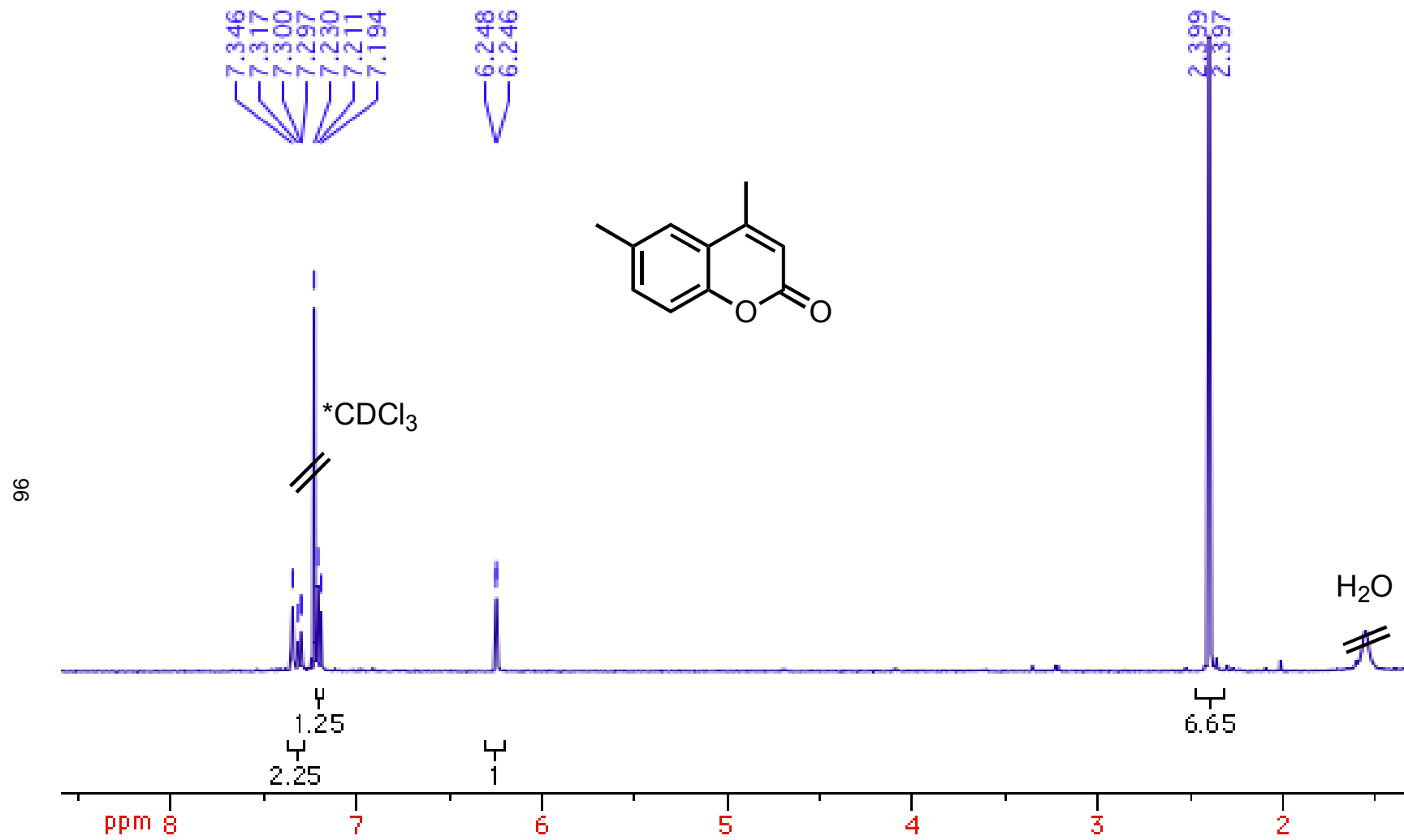


Figure 2.32 ¹H NMR of 1h in CDCl₃

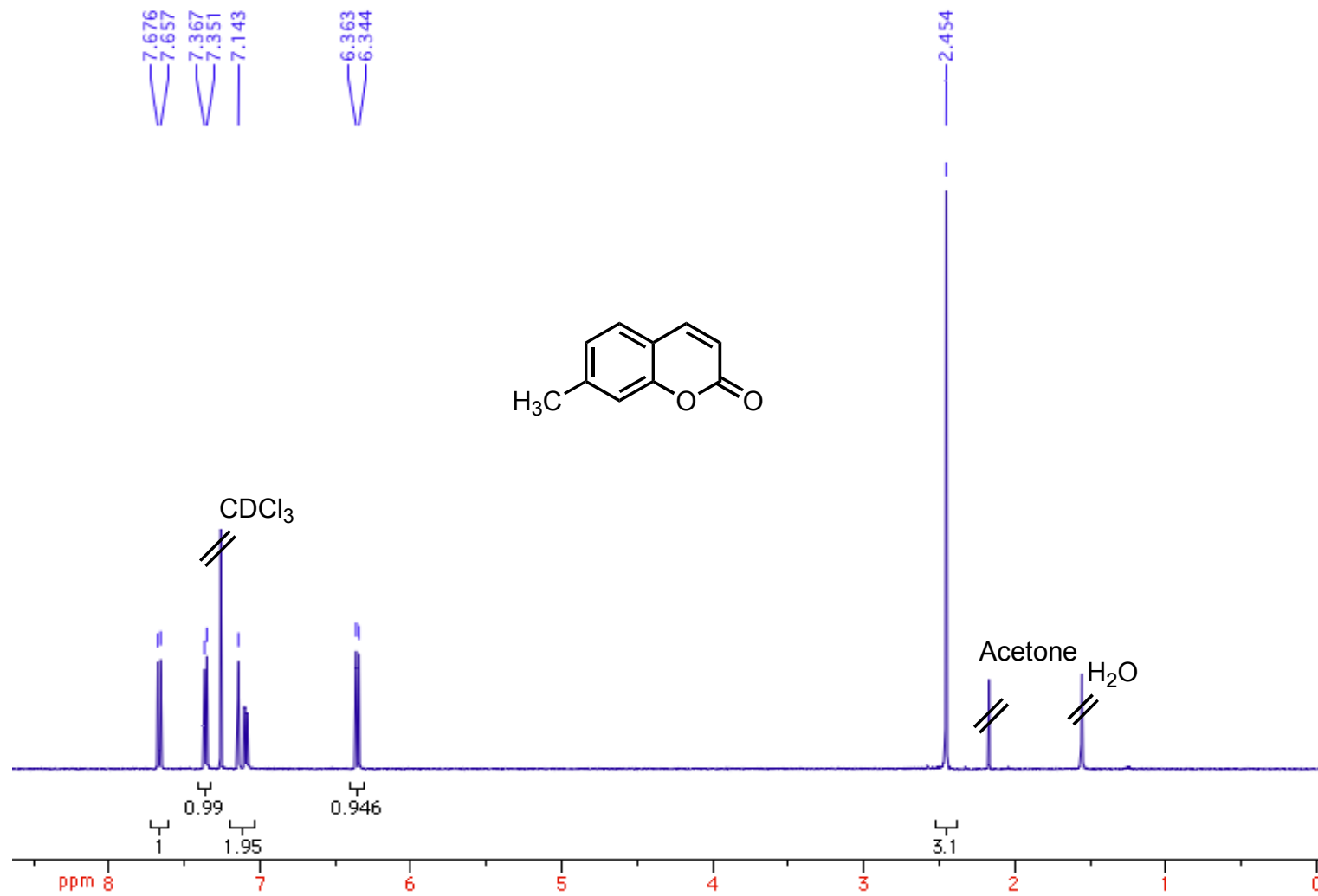


Figure 2.33 ^1H NMR of **1e** in CDCl_3

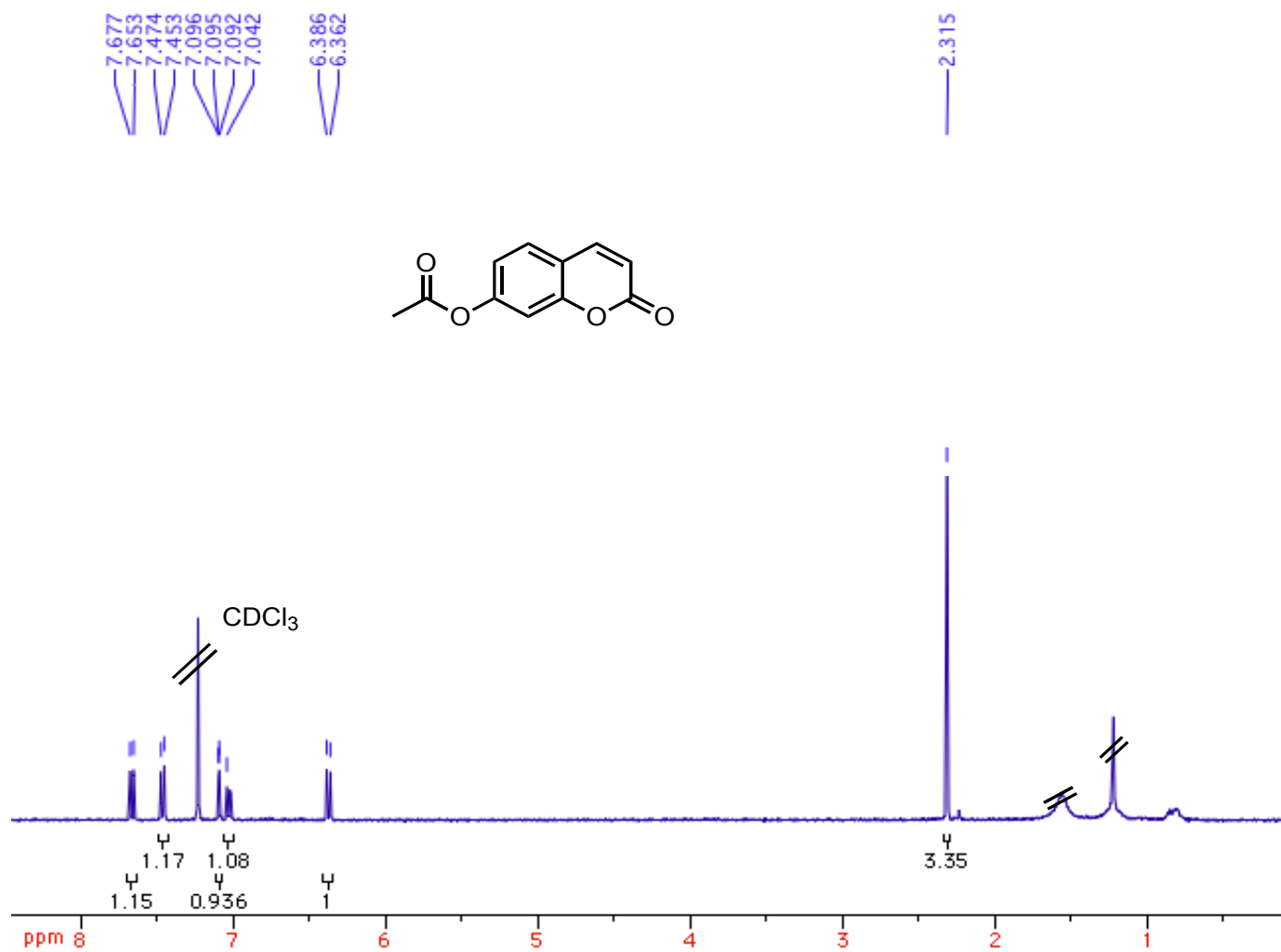


Figure 2.34 ^1H NMR of **1i** in CDCl_3

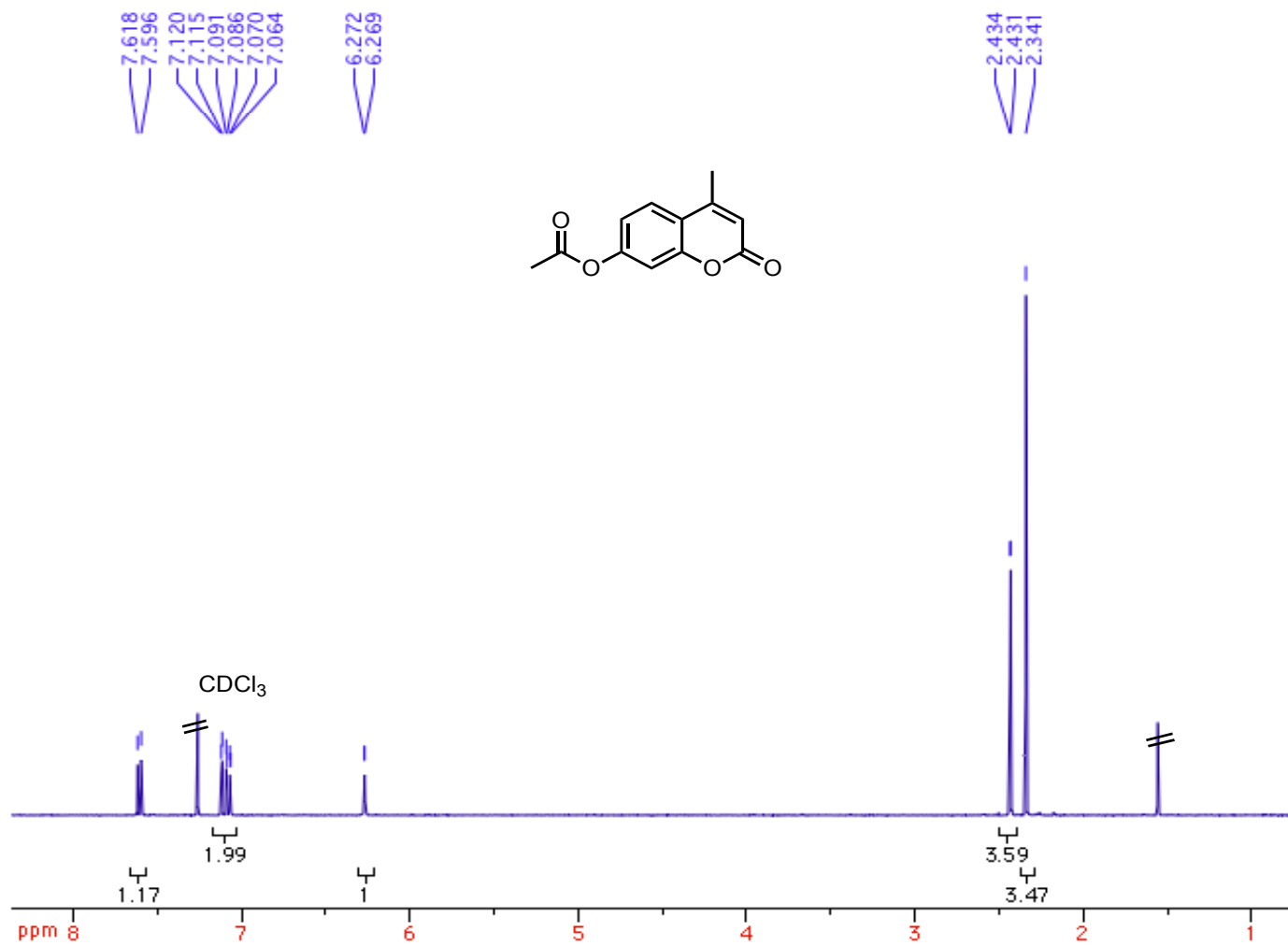


Figure 2.35 ^1H NMR of **1j** in CDCl_3

2.6.3. Synthesis and characterization of CB[8]

The synthesis of CB[8] was performed by following the procedures outlined by Day.³⁵ Paraformaldehyde (4.2 g) and glycouril (10 g) are mixed in a 250 mL round-bottom flask and stirred until the powder was homogenous. An ice cold concentrated solution of HCl (14.2 mL) is quickly poured into the flask with stirring until the solid mixture inside becomes rock hard. The solid is then heated to 100 °C for 18 hours. After 18 hours, more HCl was added if solid product was seen in the flask. If there was no solid mass then the flask was removed from heating and allowed to cool. Crystallization occurs in various crops (CB[6], CB[7], CB[8]) and these need to be tested by HRMS and purified.

Purifying CB[8] is accomplished by washing the precipitate with small amounts of 60 % formic acid/H₂O mixtures. These samples are carefully sonicated and centrifuged. The white undissolved solid is triturated 3 times with deionized water to remove excess acid. The solids are then dried in an oven at 150 °C for several hours. These samples are then tested to check for purity. If residual CB[5], CB[6] or CB[7] remains they are rewashed with a smaller amount of 60% formic acid/ water to prevent complete solvation of the solid.

To check purity a small amount (~ 0.5 mg) of white sample is added to a small vial along with CsCl (0.5 mg) and deionized water is added until solution is clear. The solution is then analyzed by mass-spectrometry. The cesium ion serves two purposes, the first purpose is to bind to the two CB[n] portals and give the complex a charge (Z=2). The second purpose is that cesium chloride in water provides an internal standard by creating ion complexes with the following formula Cs_nCl_{n-1}. The ion complexes then provide the following M/Z peaks as indicated in Table 2.6.

Due to the complexation of two cesium cations to the CB[n] molecules the mass of the analyte is the mass of the CB[n] molecule plus two cesium atoms divided by the overall charge of the complex which is 2 (Table 2.7). The mass spectrometer is then calibrated to the cesium chloride internal standard and the mass of CB[n] is observed. The predicted masses of CB[n] are generated to assess the purity of the sample by calculating the difference between the observed mass and calculated mass divided by the observed mass. If this value is within 5 ppm then the sample is considered pure.

Table 2.6 The masses of various CsCl ion complexes

Entry	N	Formula Cs_nCl_{n-1}	M/Z ^a
1	1	Cs^+	132.91
2	2	$Cs_2Cl_1^+$	300.78
3	3	$Cs_3Cl_2^+$	469.62
4	4	$Cs_3Cl_2^+$	636.53
5	5	$Cs_4Cl_3^+$	804.40
6	6	$Cs_5Cl_4^+$	972.28

^aSimulated Masses of various Cs_nCl_{n-1} complexes

Table 2.7 The masses of CB[n]-Cs₂ complexes

Entry	CB[n]	Complex formula	Complex mass ^a	CB[n] mass
1	5	$(C_6H_6N_4O_2)_5Cs_2$	548.03	830.25
2	6	$(C_6H_6N_4O_2)_6Cs_2$	631.05	996.29
3	7	$(C_6H_6N_4O_2)_7Cs_2$	714.08	1162.34
4	8	$(C_6H_6N_4O_2)_8Cs_2$	797.10	1328.39

^aSimulated masses of various CB[n]

2.6.4. Characterization of photodimers of various coumarin derivatives (1a-1k) by ¹H NMR spectroscopy.

The dimerization of the various coumarins (Scheme 2.2) have been previously studied so the ¹H NMR signals from the methyl groups and cyclobutyl protons were easily compared to values reported in literature.¹¹⁻²⁰

2.6.4.1. Reaction in DCI/D₂O

1a: ¹H NMR (500 MHz, DCI/D₂O, δ ppm): 1.28 (s, 3H, *anti*-HT), 1.73 (s, 3H, *syn*-HT), 1.77 (s, 3H, *syn*-HH), 3.80 (s, 1H, *anti*-HT), 3.91 (s, 1H, *syn*-HH), 4.12 (s, 1H, *syn*-HT), 6.65-7.45 (m, aromatic protons).

2.6.4.2. Reaction in DCI/D₂O-CB[8]

1a: ¹H NMR (500 MHz, DCI/D₂O, δ ppm): 1.28 (s, 3H, *anti*-HT), 1.73 (s, 3H, *syn*-HT), 1.77 (s, 3H, *syn*-HH), 3.80 (s, 1H, *anti*-HT), 3.91 (s, 1H, *syn*-HH), 4.12 (s, 1H, *syn*-HT), 6.65-7.45 (m, aromatic protons)

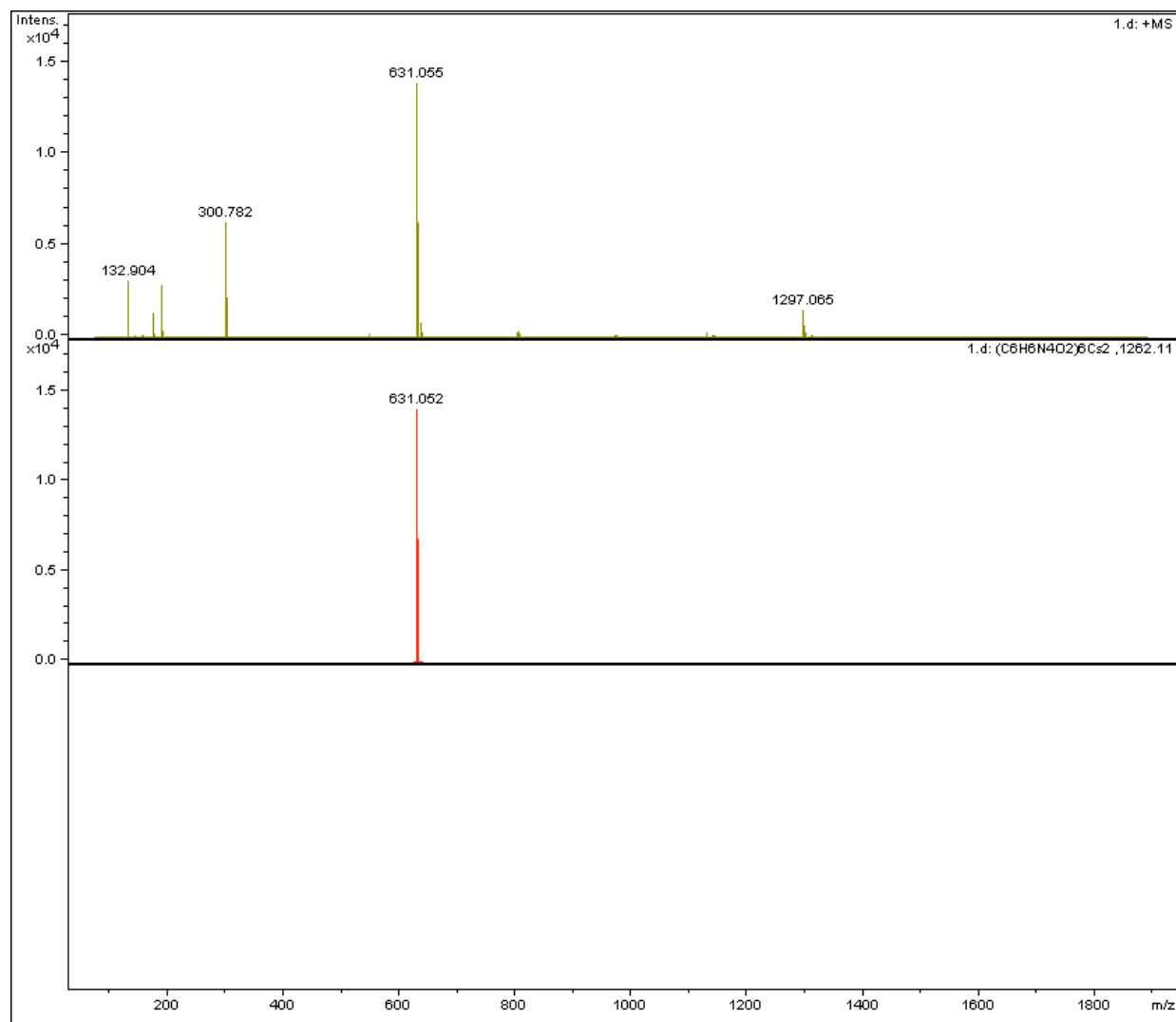


Figure 2.36 HRMS analysis of CB[6] in the presence of CsCl ions. (Top) The $M/Z = 631.055$ is $Cs_2@CB[6]$ and the $M/Z = 1297.065$ is $Cs_1@CB[6]$. (Bottom) The predicted value of $Cs_2@CB[6]$. The $\Delta M/M$ value is 4.75×10^{-6}

2.6.4.3. Reaction in H₂O

1b: ¹H NMR (500 MHz, CDCl₃, δ ppm): 4.07(dd, 1H, $J = 9.5$ Hz, *syn*-HH), 4.20 (dd, 1H, $J = 9.5$ Hz, *syn*-HH), 4.26 (dd, 1H, $J = 10.5$ Hz, *syn*-HT), 4.30 (dd, 1H, $J = 10.5$ Hz, *syn*-HT), 6.58-7.21(m, aromatic protons).

1c: ^1H NMR (400 MHz, CDCl_3 , δ ppm): 3.71 (s, 3H, *syn*-HT), 4.17 (dd, 1H, $J = 9$ Hz, *syn*-HT), 4.24 (dd, 1H, $J = 9$ Hz, *syn*-HT), 6.19 (d, 1H, $J = 2.5$ Hz, *syn*-HT), 6.68 (d, 1H, $J = 8.5$ Hz, *syn*-HT), 7.03 (d, 1H, $J = 8.5$ Hz, *syn*-HT)

1d: ^1H NMR (500 MHz, CDCl_3 , δ ppm): 1.24 (s, 3H, *anti*-HH/HT), 1.67 (s, 3H, *syn*-HH), 3.41 (s, 1H, *anti*-HH), 3.66 (s, 1H, *syn*-HH), 3.84 (s, 1H, *anti*-HT), 6.05 (d, 1H, $J = 2.5$ Hz, *syn*-HH), 6.62-7.05(m, aromatic protons, *anti*-HH/HT), 7.09 (d, 1H, $J = 8.5$ Hz, *syn*-HH), 7.35 (s, 1H, *syn*-HH).

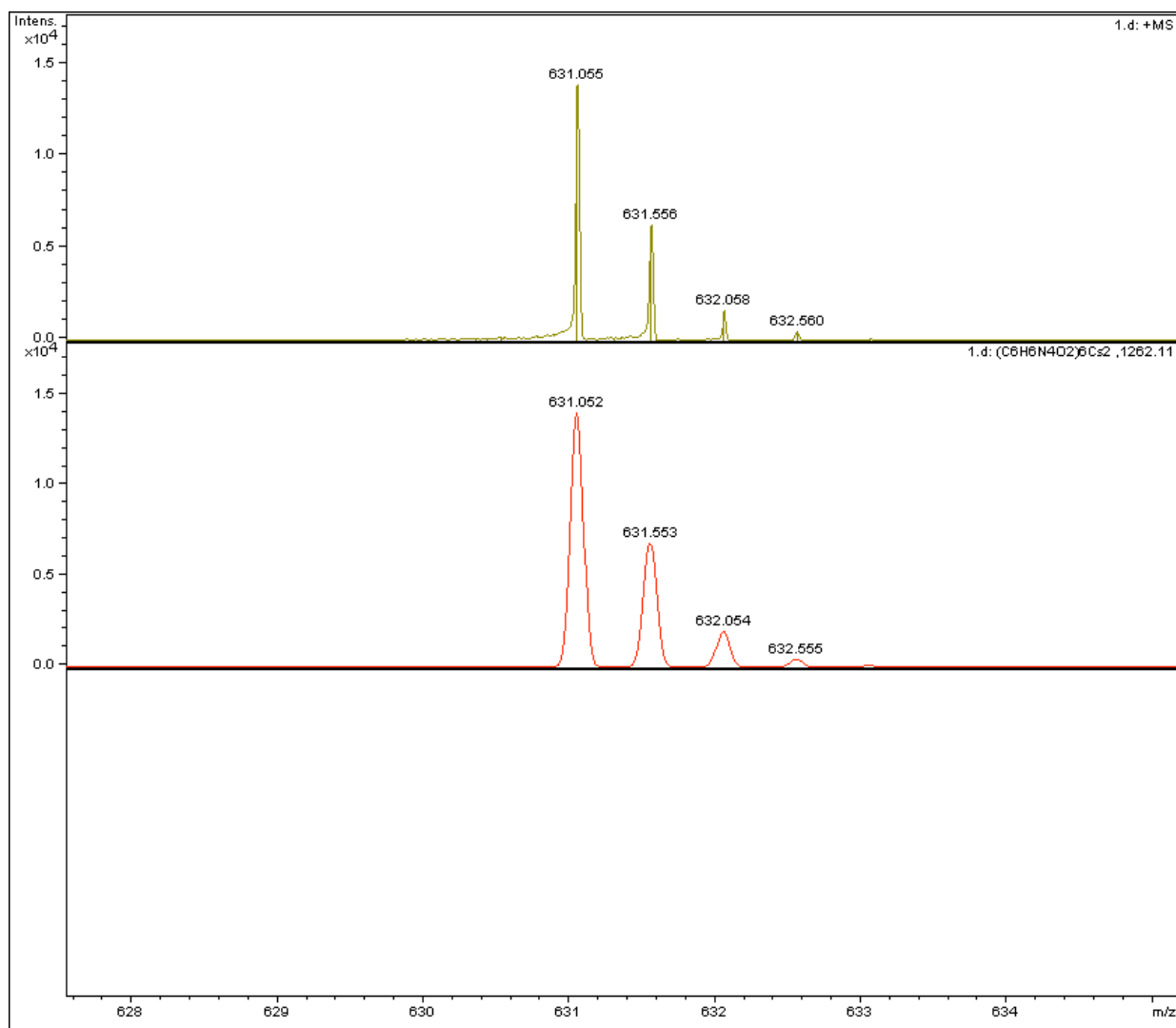


Figure 2.37 Expanded HRMS analysis of CB[6] in the presence of CsCl ions. (Top) The $M/Z = 631.055$ is $\text{Cs}_2@CB[6]$. (Bottom) The predicted value of $\text{Cs}_2@CB[6]$. The $\Delta M/M$ value is 4.75×10^{-6}

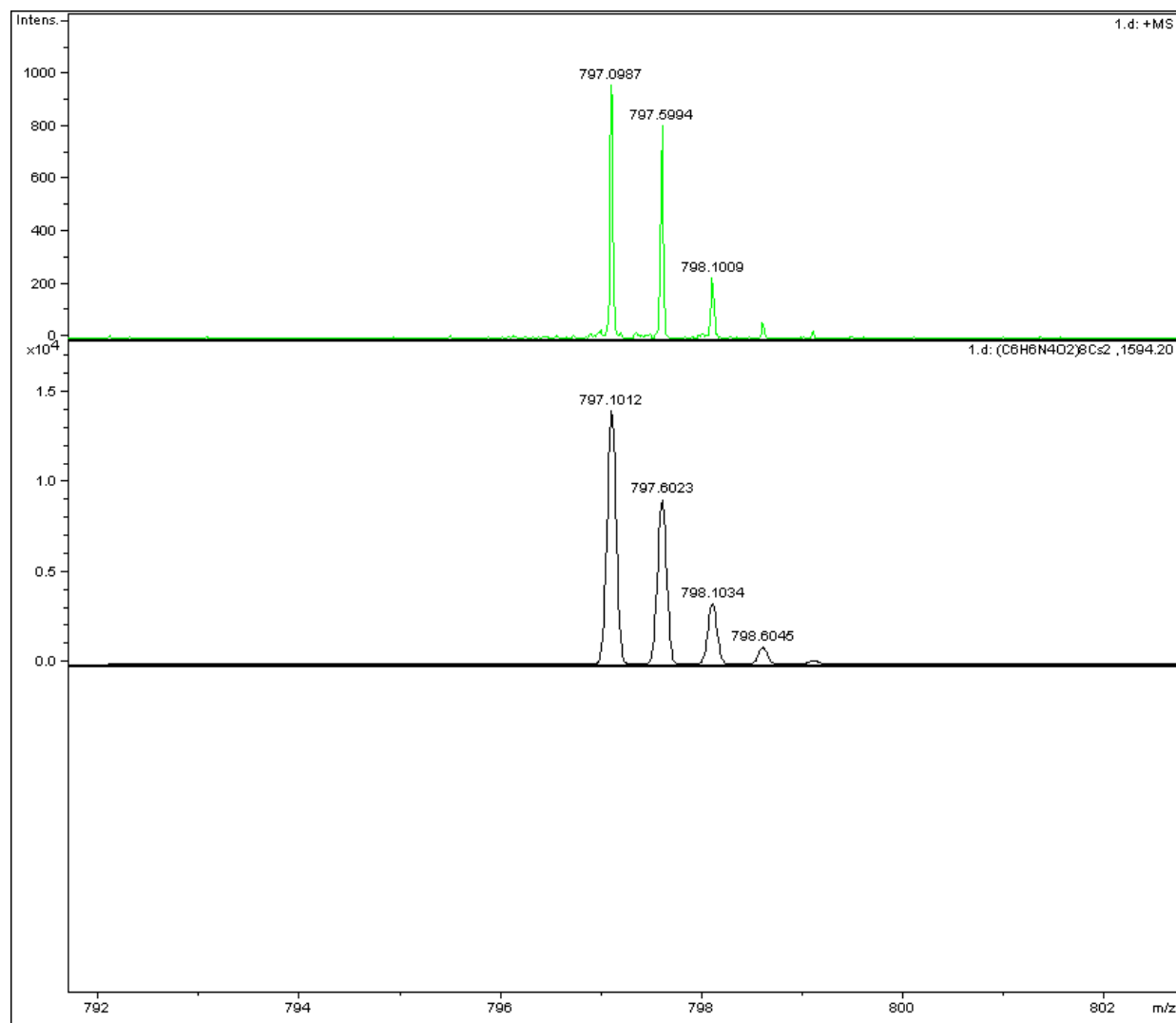


Figure 2.38 Expanded HRMS analysis of CB[8] in the presence of CsCl ions. (Top) The $M/Z = 797.098$ is $\text{Cs}_2@CB[8]$. (Bottom) The predicted value of $\text{Cs}_2@CB[8]$. The $\Delta M/M$ value is 3.14×10^{-6}

1e: ^1H NMR (500 MHz, CDCl_3 , δ ppm): 2.22 (s, 3H, *syn*-HT), 2.26 (s, 3H, *syn*-HH), 2.37 (s, 3H, *anti*-HH), 3.78 (d, 1H, $J = 8$ Hz, *anti*-HH), 3.88 (d, 1H, $J = 8$ Hz, *anti*-HH), 3.98 (dd, 1H, $J = 7$ Hz, *syn*-HH), 4.11 (dd, 1H, $J = 7$ Hz, *syn*-HH), 4.18 (dd, 1H, $J = 8$ Hz, *syn*-HT), 4.25 (dd, 1H, $J = 8$ Hz, *syn*-HT), 6.65-7.02 (m, aromatic protons).

1f: ^1H NMR (500 MHz, CDCl_3 , δ ppm): 1.25 (s, 3H, *anti*-HH), 2.37 (s, 3H, *anti*-HH), 2.42 (s, 3H, *syn*-HH), 3.38 (s, 1H, *anti*-HH), 3.60 (s, 1H, *syn*-HH), 6.61-7.06 (m, aromatic protons).

1g: ^1H NMR (500 MHz, CDCl_3 , δ ppm): 2.13 (s, 3H, *syn*-HH), 4.02 (dd, $J = 8$ Hz, 1H, *syn*-HH), 4.12 (dd, $J = 8$ Hz, 1H, *syn*-HH), 6.57 (s, 1H), 6.75 (d, 1H, $J = 8.5$ Hz), 6.98 (d, 1H, $J = 8$ Hz).

1h: ^1H NMR (500 MHz, CDCl_3 , δ ppm): 1.26 (s, 3H, *anti*-HH), 1.64 (s, 3H, *syn*-HH), 2.37 (s, 3H, *anti*-HH), 2.63 (s, 3H, *syn*-HH), 3.37 (s, 1H, *anti*-HH), 3.61 (s, 1H, *syn*-HH), 6.51-7.12 (m, aromatic protons)

1i: ^1H NMR (500 MHz, CDCl_3 , δ ppm): 2.24 (s, 3H, *syn*-HH), 2.26 (d, 1H, $J = 8$ Hz, *syn*-HT), 4.04 (dd, 1H, $J = 9.5$ Hz, *syn*-HH), 4.17 (dd, 1H, $J = 9.5$ Hz, *syn*-HH), 4.22 (dd, 1H, $J = 7.5$ Hz, *syn*-HH), 4.29 (dd, 1H, $J = 7.5$ Hz, *syn*-HH), 6.45-6.88 (m, aromatic protons, *syn*-isomer).

1j: ^1H NMR (500 MHz, CDCl_3 , δ ppm): 1.30 (s, 3H, *anti*-HH/HT), 1.63 (s, 3H, *syn*-HH), 2.23 (s, 3H, *anti*-HT), 2.26 (s, 3H, *syn*-HH), 2.32 (s, 3H, *anti*-HH), 3.44 (s, 1H, *anti*-HH), 3.48 (s, 1H, *anti*-HT), 3.47 (s, 1H, *syn*-HH), 6.32-7.00 (m, aromatic protons), 7.13-7.17 (m, aromatic protons).

1k: ^1H NMR (400 MHz, CD_3OD , δ ppm): 3.71 (s, 3H, *syn*-HT), 4.17 (dd, $J = 9$ Hz, *syn*-HT), 4.24 (dd, $J = 9$ Hz, *syn*-HT), 6.19 (d, 1H, $J = 2.5$ Hz, *syn*-HT), 6.68 (d, 1H, $J = 8.5$ Hz, *syn*-HT), 7.03 (d, 1H, $J = 8.5$ Hz, *syn*-HT)

2.6.4.4. Reaction in CB[8]- H_2O

1b: ^1H NMR (500 MHz, CDCl_3 , δ ppm): 4.07 (dd, 1H, $J = 9.5$ Hz, *syn*-HH), 4.20 (dd, 1H, $J = 9.5$ Hz, *syn*-HH), 4.26 (dd, 1H, $J = 10.5$ Hz, *syn*-HT), 4.30 (dd, 1H, $J = 10.5$ Hz, *syn*-HT), 6.58-7.21 (m, aromatic protons)

1c: ^1H NMR (400 MHz, CDCl_3 , δ ppm): 3.71 (s, 3H, *syn*-HT), 4.17 (dd, 1H, $J = 9$ Hz, *syn*-HT), 4.24 (dd, 1H, $J = 9$ Hz, *syn*-HT), 6.19 (d, 1H, $J = 2.5$ Hz, *syn*-HT), 6.68 (d, 1H, $J = 8.5$ Hz, *syn*-HT), 7.03 (d, 1H, $J = 8.5$ Hz, *syn*-HT)

1d: ^1H NMR (500 MHz, CDCl_3 , δ ppm): 1.24 (s, 3H, *anti*-HH/HT), 1.67 (s, 3H, *syn*-HH), 3.41 (s, 1H, *anti*-HH), 3.66 (s, 1H, *syn*-HH), 3.84 (s, 1H, *anti*-HT), 6.05 (d, 1H, $J = 2.5$ Hz, *syn*-HH), 6.62-7.05 (m, aromatic protons, *anti*-HH/HT), 7.09 (d, 1H, $J = 8.5$ Hz, *syn*-HH), 7.35 (s, 1H, *syn*-HH)

1e: ^1H NMR (500 MHz, CDCl_3 , δ ppm): 2.26 (s, 3H, *syn*-HH), 3.88 (d, 1H, $J = 8$ Hz, *anti*-HH), 3.98 (dd, 1H, $J = 7$ Hz, *syn*-HH), 4.11 (dd, 1H, $J = 7$ Hz, *syn*-HH), 6.65-7.02 (m, aromatic protons)

1f: ^1H NMR (500 MHz, CDCl_3 , δ ppm): 1.25 (s, 3H, *anti*-HH), 2.37 (s, 3H, *anti*-HH), 2.42 (s, 3H, *syn*-HH), 3.38 (s, 1H, *anti*-HH), 3.60 (s, 1H, *syn*-HH), 6.61 - 7.06 (m, aromatic protons).

1g: ^1H NMR (500 MHz, CDCl_3 , δ ppm): 2.13 (s, 3H, *syn*-HH), 2.27 (s, 3H, *syn*-HT), 4.02 (dd, $J = 8$ Hz, *syn*-HH), 4.12 (dd, $J = 8$ Hz, *syn*-HH), 4.19 (dd, $J = 8$ Hz, *syn*-HT), 4.24 (dd, $J = 8$ Hz, *syn*-HT), 6.50 (d, 1H, $J = 9.5$ Hz, *syn*-HT), 6.57 (s, 1H, *syn*-HH), 6.75 (d, 1H, $J = 8.5$ Hz, *syn*-HH), 6.90 (d, 1H, $J = 7$ Hz, *syn*-HT), 6.98 (d, 1H, $J = 10$ Hz, *syn*-HH), 7.03 (d, 1H, $J = 8.5$ Hz, *syn*-HT).

1h: ^1H NMR (500 MHz, CDCl_3 , δ ppm): 1.25 (s, 3H, *anti*-HH), 2.37 (s, 3H, *anti*-HH), 2.42 (s, 3H, *syn*-HH), 3.38 (s, 1H, *anti*-HH), 3.60 (s, 1H, *syn*-HH), 6.61-7.06 (m, aromatic protons)

1i: ^1H NMR (500 MHz, CDCl_3 , δ ppm): 2.24 (s, 3H, *syn*-HH), 2.26 (d, 1H, $J = 8$ Hz, *syn*-HT), 4.04 (dd, 1H, $J = 9.5$ Hz, *syn*-HH), 4.17 (dd, 1H, $J = 9.5$ Hz, *syn*-HH), 4.22 (dd, 1H, $J = 7.5$ Hz, *syn*-HH), 4.29 (dd, 1H, $J = 7.5$ Hz, *syn*-HH), 6.45-6.88 (m, aromatic protons, *syn*-isomer)

1j: ^1H NMR (500 MHz, CDCl_3 , δ ppm): 1.30 (s, 3H, *anti*-HH/HT), 1.63 (s, 3H, *syn*-HH), 2.23 (s, 3H, *anti*-HT), 2.26 (s, 3H, *syn*-HH), 2.32 (s, 3H, *anti*-HH), 3.44 (s, 1H, *anti*-HH), 3.48 (s, 1H, *anti*-HT), 3.47 (s, 1H, *syn*-HH), 6.32-7.00 (m, aromatic protons), 7.13-7.17 (m, aromatic protons)

1k: ^1H NMR (500 MHz, CD_3OD , δ ppm): 1.32 (s, 3H, *anti*-HT), 1.66 (s, 3H, *syn*-HH), 3.52 (s, 1H, *syn*-HH), 3.82 (s, 1H, *anti*-HT), 6.25-6.67 (m, aromatic protons), 7.00-7.45 (m, aromatic protons)

2.6.4.5. Reaction in CDCl_3

1c: ^1H NMR (500 MHz, CDCl_3 , δ ppm): 3.71 (s, 3H, *syn*-HT), 3.74 (s, 3H, *syn*-HH), 4.00 (dd, $J = 10$ Hz, *syn*-HH), 4.06 (dd, $J = 10$ Hz, *syn*-HH), 4.17 (dd, $J = 9$ Hz, *syn*-HT), 4.24 (dd, $J = 9$ Hz, *syn*-HT), 6.19 (d, 1H, $J = 2.5$ Hz, *syn*-HT), 6.43 (m, 1H, *syn*-HH), 6.68 (d, 1H, $J = 8.5$ Hz, *syn*-HT), 6.82 (d, 1H, $J = 8.5$ Hz, *syn*-HH), 7.03 (d, 1H, $J = 8.5$ Hz, *syn*-HT), 7.36 (d, 1H, $J = 8.5$ Hz, *syn*-HH)

1d: ^1H NMR (500 MHz, CDCl_3 , δ ppm): 1.24 (s, 3H, *anti*-HH), 1.67 (s, 3H, *syn*-HH), 3.41 (s, 1H, *anti*-HH), 3.66 (s, 1H, *syn*-HH), 6.05 (d, 1H, $J = 2.5$ Hz, *syn*-HH), 6.62- 6.65 (m, aromatic protons, *anti*-HH), 7.05 (d, 1H, $J = 9$ Hz, *anti*-HH), 7.09 (d, 1H, $J = 8.5$ Hz, *syn*-HH), 7.35 (s, 1H, *syn*-HH).

1e: ^1H NMR (500 MHz, CDCl_3 , δ ppm): 2.37 (s, 3H, *anti*-HH), 3.78 (d, 1H, $J = 8$ Hz, *anti*-HH), 3.88 (d, 1H, $J = 8$ Hz, *anti*-HH), 6.67-7.05 (m, aromatic protons).

1f: ^1H NMR (500 MHz, CDCl_3 , δ ppm): 1.25 (s, 3H, *anti*-HH), 2.37 (s, 3H, *anti*-HH), 3.38 (s, 1H, *anti*-HH), 6.91 (s, 1H, *anti*-HH), 7.02 (t, 2H, $J = 8$ Hz, *anti*-HH).

1g: ^1H NMR (500 MHz, CDCl_3 , δ ppm): 2.35 (s, 3H, *anti*-HH), 3.78 (d, $J = 7.5$ Hz, 1H, *anti*-HH), 3.89 (d, $J = 7.5$ Hz, 1H, *anti*-HH), 6.95 (s, 1H), 7.00 (d, 1H, $J = 8.5$ Hz), 7.12 (d, 1H, $J = 8$ Hz).

1h: ^1H NMR (500 MHz, CDCl_3 , δ ppm): 1.26 (s, 3H, *anti*-HH), 2.37 (s, 3H, *anti*-HH), 3.37 (s, 1H, *anti*-HH), 6.91 (s, 1H, *anti*-HH), 7.00 (d, 1H, $J = 10.5$ Hz, *anti*-HH), 7.11 (d, 1H, $J = 10.5$ Hz, *anti*-HH).

1i: ^1H NMR (500 MHz, CDCl_3 , δ ppm): 2.32 (s, 3H, *anti*-HH), 3.88 (d, 1H, $J = 8$ Hz, *anti*-HH), 3.92 (d, 1H, $J = 8$ Hz, *anti*-HH), 6.90 (d, 1H, $J = 2$ Hz, *anti*-HH), 6.92 (d, 1H, $J = 2$ Hz, *anti*-HH), 6.94 (d, 1H, $J = 2$ Hz, *anti*-HH).

1j: ^1H NMR (500 MHz, CDCl_3 , δ ppm): 1.30 (s, 3H, *anti*-HH), 2.32 (s, 3H, *anti*-HH), 3.44 (s, 1H, *anti*-HH), 3.48 (s, 1H, *anti*-HT), 6.63-6.83(m, aromatic protons, *anti*-HT), 6.90 (d, 1H, $J = 2$ Hz, *anti*-HH), 6.99 (d, 1H, $J = 2$ Hz, *anti*-HH), 7.00 (d, 1H, $J = 2$ Hz, *anti*-HH).

2.6.4.6. Reaction in MeOH

1d: ^1H NMR (500 MHz, CDCl_3 , δ ppm): 1.24 (s, 3H, *anti*-HH), 1.67 (s, 3H, *syn*-HH), 3.41 (s, 1H, *anti*-HH), 3.66 (s, 1H, *syn*-HH), 6.05 (d, 1H, $J = 2.5$ Hz, *syn*-HH), 6.62- 6.65(m, aromatic protons, *anti*-HH), 7.05 (d, 1H, $J = 9$ Hz, *anti*-HH), 7.09 (d, 1H, $J = 8.5$ Hz, *syn*-HH), 7.35 (s, 1H, *syn*-HH).

1f: (with and without triplet sensitization of benzophenone) ^1H NMR (500 MHz, CDCl_3 , δ ppm): 1.25 (s, 3H, *anti*-HH), 2.37 (s, 3H, *anti*-HH), 2.42 (s, 3H, *syn*-HH), 3.38 (s, 1H, *anti*-HH), 3.60 (s, 1H, *syn*-HH), 6.61-7.06 (m, aromatic protons).

1g: ^1H NMR (500 MHz, CDCl_3 , δ ppm): 2.35 (s, 3H, *anti*-HH), 3.78 (d, $J = 7.5$ Hz, 1H, *anti*-HH), 3.89 (d, $J = 7.5$ Hz, 1H, *anti*-HH), 6.95 (s, 1H), 7.00 (d, 1H, $J = 8.5$ Hz), 7.0 (d, 1H, $J = 8$ Hz).

1h: ^1H NMR (500 MHz, CDCl_3 , δ ppm): 1.26 (s, 6H, *anti*-HH/HT), 1.64 (s, 3H, *syn*-HT), 2.23 (s, 3H, *anti*-HT), 2.37 (s, 3H, *anti*-HH), 2.60 (s, 3H, *syn*-HT), 3.37 (s, 1H, *anti*-HH), 3.42 (s, 1H, *anti*-HT), 3.47 (s, 1H, *syn*-HT), 6.80-7.16 (m, aromatic protons)

1j: ¹H NMR (500 MHz, CDCl₃, δ ppm): 1.30 (s, 6H, *anti*-HH/ *anti*-HT), 1.66 (s, 3H, *syn*-HH), 1.72 (s, 3H, *syn*-HT), 2.25 (s, 3H, *anti*-HH), 2.31 (s, 3H, *anti*-HT), 2.33 (s, 3H, *syn*-HH), 2.35 (s, 3H, *syn*-HT), 3.44 (s, 1H, *anti*-HH), 3.49 (s, 1H, *anti*-HT), 3.65 (s, 1H, *syn*-HH), 3.77 (s, 1H, *syn*-HT), 6.63-7.03 (m, aromatic protons)

1k: ¹H NMR (500 MHz, CD₃OD, δ ppm): 1.66 (s, 3H, *syn*-HH), 3.52 (s, 1H, *syn*-HH), 6.25 (s, 1H), 6.54 (d, 1H, *J* = 7 Hz), 7.02 (d, 1H, *J* = 6 Hz)

2.7. References

** The material in this chapter was co-authored by Barry C Pemberton (BCP), Nilopital Barooah (NB), Alexander C. Johnson (ACJ) and J. Sivaguru (JS). BCP had primary responsibility for preparing samples and collecting data, whereas ACJ and NB assisted in collection of data. BCP processed the data and with help of JS was the primary developer of the conclusions that are advanced here. NB and ACJ synthesized BCP also drafted and revised all versions of this chapter. JS served as proofreader and checked the math in the statistical analysis conducted by BCP.

- (1) Mock, W. L.; Shih, N. Y. Structure and selectivity in host-guest complexes of cucurbituril *J. Org. Chem.* **1986**, *51*, 4440-6.
- (2) Burnett, C. A.; Witt, D.; Fettinger, J. C.; Isaacs, L. Acyclic Congener of Cucurbituril: Synthesis and Recognition Properties *J. Org. Chem.* **2003**, *68*, 6184-6191.
- (3) Lee, J. W.; Samal, S.; Selvapalam, N.; Kim, H.-J.; Kim, K. Cucurbituril Homologues and Derivatives: New Opportunities in Supramolecular Chemistry *Acc. Chem. Res.* **2003**, *36*, 621-630.
- (4) Kim, H.-J.; Heo, J.; Jeon, W. S.; Lee, E.; Kim, J.; Sakamoto, S.; Yamaguchi, K.; Kim, K. Selective inclusion of a hetero-guest pair in a molecular host: formation of stable charge-transfer complexes in cucurbit[8]uril *Angew. Chem., Int. Ed.* **2001**, *40*, 1526-1529.
- (5) Ko, Y. H.; Hwang, I.; Lee, D.-W.; Kim, K. Ultrastable Host-Guest Complexes and Their Applications *Isr. J. Chem.*, *51*, 506-514.

- (6) Moghaddam, S.; Yang, C.; Rekharsky, M.; Ko, Y. H.; Kim, K.; Inoue, Y.; Gilson, M. K. New Ultrahigh Affinity Host-Guest Complexes of Cucurbit[7]uril with Bicyclo[2.2.2]octane and Adamantane Guests: Thermodynamic Analysis and Evaluation of M2 Affinity Calculations *J. Am. Chem. Soc.*, **133**, 3570-3581.
- (7) Kim, H.-J.; Jeon, W. S.; Ko, Y. H.; Kim, K. Inclusion of methylviologen in cucurbit[7]uril *Proc. Natl. Acad. Sci. U. S. A.* **2002**, *99*, 5007-5011.
- (8) Choi, S.; Park, S. H.; Ziganshina, A. Y.; Ko, Y. H.; Lee, J. W.; Kim, K. A stable cis-stilbene derivative encapsulated in cucurbit[7]uril *Chem. Commun.* **2003**, 2176-2177.
- (9) Maddipatla, M. V. S. N.; Kaanumalle, L. S.; Natarajan, A.; Pattabiraman, M.; Ramamurthy, V. Preorientation of Olefins toward a Single Photodimer: Cucurbituril-Mediated Photodimerization of Protonated Azastilbenes in Water *Langmuir* **2007**, *23*, 7545-7554.
- (10) Pattabiraman, M.; Kaanumalle, L. S.; Natarajan, A.; Ramamurthy, V. Regioselective Photodimerization of Cinnamic Acids in Water: Templatation with Cucurbiturils *Langmuir* **2006**, *22*, 7605-7609.
- (11) Hammond, G. S.; Stout, C. A.; Lamola, A. A. Mechanisms of photochemical reactions in solution. XXV. The photodimerization of coumarin *J. Am. Chem. Soc.* **1964**, *86*, 3103-6.
- (12) Morrison, H. A.; Curtis, H.; McDowell, T. Solvent effects on the photodimerization of coumarin *J. Am. Chem. Soc.* **1966**, *88*, 5415-19.
- (13) Leenders, L. H.; Schouteden, E.; De Schryver, F. C. Photochemistry of nonconjugated bichromophoric systems. Cyclomerization of 7,7'-polymethylenedioxy coumarins and polymethylenedicarboxylic acid 7-coumarinyl diesters *J. Org. Chem.* **1973**, *38*, 957-66.
- (14) Yu, X.; Scheller, D.; Rademacher, O.; Wolff, T. Selectivity in the Photodimerization of 6-Alkylcoumarins *J. Org. Chem.* **2003**, *68*, 7386-7399.
- (15) Moorthy, J. N.; Venkatesan, K.; Weiss, R. G. Photodimerization of coumarins in solid cyclodextrin inclusion complexes *J. Org. Chem.* **1992**, *57*, 3292-3297.
- (16) Brett, T. J.; Alexander, J. M.; Stezowski, J. J. Chemical insight from crystallographic disorder-structural studies of supramolecular photochemical systems. Part 2. The β -cyclodextrin-4,7-dimethylcoumarin inclusion complex: a new β -cyclodextrin dimer packing type, unanticipated

- photoproduct formation, and an examination of guest influence on β -CD dimer packing *J. Chem. Soc., Perkin Trans. 2* **2000**, 1095-1103.
- (17) Lewis, F. D.; Howard, D. K.; Oxman, J. D. Lewis acid catalysis of coumarin photodimerization *J. Am. Chem. Soc.* **1983**, *105*, 3344-3345.
- (18) Gnanaguru, K.; Ramasubbu, N.; Venkatesan, K.; Ramamurthy, V. A study on the photochemical dimerization of coumarins in the solid state *J. Org. Chem.* **1985**, *50*, 2337-2346.
- (19) Muthuramu, K.; Ramamurthy, V. Photodimerization of coumarin in aqueous and micellar media *J. Org. Chem.* **1982**, *47*, 3976-9.
- (20) Vishnumurthy, K.; Row, T. N. G.; Venkatesan, K. Unusual Photodimerization of 7-fluoro-4-methylcoumarin and 6-fluoro-4-methylcoumarin in Solid State *Tetrahedron* **1998**, *54*, 11235-11246.
- (21) Walker, S.; Oun, R.; McInnes, F. J.; Wheate, N. J. The Potential of Cucurbit[n]urils in Drug Delivery *Isr. J. Chem.*, *51*, 616-624.
- (22) Harris, D. C. *Quantitative Chemical Analysis*; 6th ed.; W.H. Freeman and Company: New York, 2003.
- (23) Connors, K. A. *Binding Constants*; John Wiley: New York, 1987.
- (24) Huang, W.-H.; Zavalij, P. Y.; Isaacs, L. Chiral recognition inside a chiral cucurbituril *Angew. Chem., Int. Ed.* **2007**, *46*, 7425-7427.
- (25) Liu, S.; Shukla, A. D.; Gadde, S.; Wagner, B. D.; Kaifer, A. E.; Isaacs, L. Ternary complexes comprising cucurbit[10]uril, porphyrins, and guests *Angew. Chem., Int. Ed.* **2008**, *47*, 2657-2660.
- (26) Ma, D.; Zavalij, P. Y.; Isaacs, L. Acyclic Cucurbit[n]uril Congeners Are High Affinity Hosts *J. Org. Chem.*, *75*, 4786-4795.
- (27) Huang, W.-H.; Zavalij, P. Y.; Isaacs, L. Folding of Long-Chain Alkanediammonium Ions Promoted by a Cucurbituril Derivative *Org. Lett.* **2008**, *10*, 2577-2580.
- (28) *Photochemistry in Organized and Constrained Media*; Ramamurthy, V., Ed.; Wiley-VCH: New York, 1991.
- (29) Frisch, M. J.; Trucks, G. W.; Schlegel, H. B.; Scuseria, G. E.; Robb, M. A.; Cheeseman, J. R.; Montgomery, J. A., Jr.; Vreven, T.; Kudin, K. N.; Burant, J. C.; Millam, J. M.; Iyengar, S. S.;

- Tomasi, J.; Barone, V.; Mennucci, B.; Cossi, M.; Scalmani, G.; Rega, N.; Petersson, G. A.; Nakatsuji, H.; Hada, M.; Ehara, M.; Toyota, K.; Fukuda, R.; Hasegawa, J.; Ishida, M.; Nakajima, T.; Honda, Y.; Kitao, O.; Nakai, H.; Klene, M.; Li, X.; Knox, J. E.; Hratchian, H. P.; Cross, J. B.; Bakken, V.; Adamo, C.; Jaramillo, J.; Gomperts, R.; Stratmann, R. E.; Yazyev, O.; Austin, A. J.; Cammi, R.; Pomelli, C.; Ochterski, J. W.; Ayala, P. Y.; Morokuma, K.; Voth, G. A.; Salvador, P.; Dannenberg, J. J.; Zakrzewski, V. G.; Dapprich, S.; Daniels, A. D.; Strain, M. C.; Farkas, O.; Malick, D. K.; Rabuck, A. D.; Raghavachari, K.; Foresman, J. B.; Ortiz, J. V.; Cui, Q.; Baboul, A. G.; Clifford, S.; Cioslowski, J.; Stefanov, B. B.; Liu, G.; Liashenko, A.; Piskorz, P.; Komaromi, I.; Martin, R. L.; Fox, D. J.; Keith, T.; Al-Laham, M. A.; Peng, C. Y.; Nanayakkara, A.; Challacombe, M.; Gill, P. M. W.; Johnson, B.; Chen, W.; Wong, M. W.; Gonzalez, C.; Pople, J. A.; revision B.03 ed.; Gaussian, Inc.: Wallingford, CT, 2004.
- (30) Jiao, H.; Schleyer, P. V. R. Large Effects of Medium on Geometries. An ab Initio Study *J. Am. Chem. Soc.* **1994**, *116*, 16.
- (31) Brett, T. J.; Alexander, J. M.; Stezowski, J. J. Chemical insight from crystallographic disorder-structural studies of supramolecular photochemical systems. Part 3. The β -cyclodextrin-7-hydroxy-4-methylcoumarin inclusion complex: direct observation of photodimerization by X-ray crystallography *J. Chem. Soc., Perkin Trans. 2* **2000**, 1105-1111.
- (32) Wang, R.; Bardelang, D.; Waite, M.; Udachin, K. A.; Leek, D. M.; Yu, K.; Ratcliffe, C. I.; Ripmeester, J. A. Inclusion complexes of coumarin in cucurbiturils *Org. Biomol. Chem.* **2009**, *7*, 2435-2439.
- (33) Mecozzi, S.; Rebek, J. J. The 55% Solution: A Formula for Molecular Recognition in the Liquid State *Chem.--Eur. J.* **1998**, *4*, 1016-1022.
- (34) Sharghi, H.; Jokar, M. ChemInform Abstract: Al₂O₃/MeSO₃H (AMA) as a Novel Heterogeneous System for Synthesis of Coumarins under Mild Conditions *ChemInform* **2008**, 39
- (35) Day, A.; Arnold, A. P.; Blanch, R. J.; Snushall, B. Controlling Factors in the Synthesis of Cucurbituril and Its Homologues *J. Org. Chem.* **2001**, *66*, 8094-8100.

CHAPTER 3. EVALUATING CUCURBIT[8]URIL AS A SUPRAMOLECULAR PHOTOCATALYST**

3.1. Introduction

Chapter 2 had previously highlighted some fundamental aspects that are critical for CB[8] to act as a supramolecular catalyst to facilitate photochemical transformations. First, the supramolecular systems must exist in dynamic equilibrium so that the host and guest can exchange freely in solution. Second, the photoreaction within the supramolecular environment must be more efficient than in solution. The third requirement is that the photoproduct must not bind as tightly as the initial guest as it will result in the inhibition of the catalytic cycle. Of the coumarins screened, 6-methylcoumarin (**1g**) appeared to be the most viable candidate to test as a model system because it seemingly met the first two of the three requirements prior to an in-depth study.

With regards to the dynamic host-guest complex in the case of **1g**, we observed Jobs' plot with a ratio of 1:1.6 which is between 1:1 and a 1:2 host-guest complex. The second requirement was met since it is postulated that **1g** reacted from the triplet state.¹⁻³ This allowed reactions in solution to be minimized by quenching the outside reaction with oxygen or some other triplet quencher. Additionally in the case of **1g** the reaction formed within CB[8] resulted in *syn*-photodimers whereas the reaction outside the cavity resulted in *anti*-photodimers. This provided us the opportunity to pinpoint if the reactions occurred within the cavity (*syn*-isomers will be enhanced) or outside the cavity (*anti*-dimer will be enhanced) when we employ catalytic amounts of CB[8]. Whether or not the third requirement (product extrusion from CB[8]) would be met was unknown. However, if the photoproduct inhibits the reaction the process cannot be catalytic and this needs to be ascertained to evaluate supramolecular photocatalysis.

3.2. Evaluating CB[8] as a Supramolecular Catalyst for Photoreactions

3.2.1. Photoreactions of **1g** with shortened irradiation times

The photoreactions in chapter 2 involved long irradiation times. The photoreaction between **1g** and CB[8] was originally performed for 24-36 hours. The background reaction of **1g**

in water after 24 hours resulted in less than 5% conversion so if the reaction is sufficiently quicker in CB[8] we can shorten the irradiation time to enhance the overall rate of the reaction. When the reaction was irradiated under N₂ for 1 hour at a stoichiometric amount of CB[8] we observed a 76% conversion with a product distribution of 69:31 for the *syn*-HH **2g**:*syn*-HT **4g** product ratio. This is interesting in itself because the photoreaction after 24 hours was almost reversed with a product distribution of 31:69 for *syn*-HH **2g**:*syn*-HT **4g** product ratio (Figure 3.1). Product ratios have been shown to be time dependant in coumarin photodimerization reactions due to the photoreversibility because the dimerization depends on the wavelength of irradiation. More importantly the conversion of **1g** to photoproduct was 72% after 1 hour of irradiation in the presence of CB[8] compared to a meager 9% in water in the absence of CB[8].^{1,2}

3.2.2. Photoreactions of 1g under various atmospheres in the presence of CB[8]

Another promising observation was that the reaction within the cavity was not effected by the atmosphere as the change in conversion under N₂, air, and O₂ were 72%, 70%, and 67% respectively (Figure 3.2). This observation was important because the **1g** was postulated to react from a triplet state in solution.² The class of cucurbituril compounds has been reported to “protect” triplet states from external quenchers.^{4,5} This will be investigated in the photophysical studies in chapter 4. Thus our preliminary observation shows that the photoreaction either occurs from the singlet excited state (or) it still occurs from the a triplet excited state with the cavity protecting the triplet excited chromospheres from external quenchers by encapsulations.

3.2.3. Photoreactions of 1g with various amounts (mol %) of CB[8]

The photoreactions in chapter 2 contained a stoichiometric amount of CB[8] so that we form (1:2) HG complex. To determine whether or not the system is catalytic there needs to be a systematic investigation of the reactivity at substoichiometric amounts of CB[8] i.e. less than 0.5 eq. The first investigation involved 30 mol% of CB[8]. The overall conversion of product was 59% which is still indicative of a catalytic system with a turnover number (TON) greater than 1. If the reaction was not catalytic because the photoproduct sufficiently inhibited the reaction the total

product conversion would only be 30%. Since the conversion was nearly twice that amount, one would assume there is a turnover with CB[8] mediating the photochemical transformation. Continuing on the path of using a substoichiometric amount of catalyst, the reaction was performed using 5, 10, 20, 40, 70 and 100 mol% under various atmospheres (Figure 3.4 and Table 3.1). Besides 5 mol% the rest of the reactions gave nearly the same product distribution as the 50 mol% reactions (*syn*-HH:*syn*-HT = 70:30). The most exciting observation was the 10 mol% reaction produced exclusively *syn*-photoproducts with a 23% conversion under N₂ atmosphere and 18% conversion under an O₂ atmosphere. The difference between the conversion under N₂ and O₂ atmospheres was about 5% which is within the experimental error.

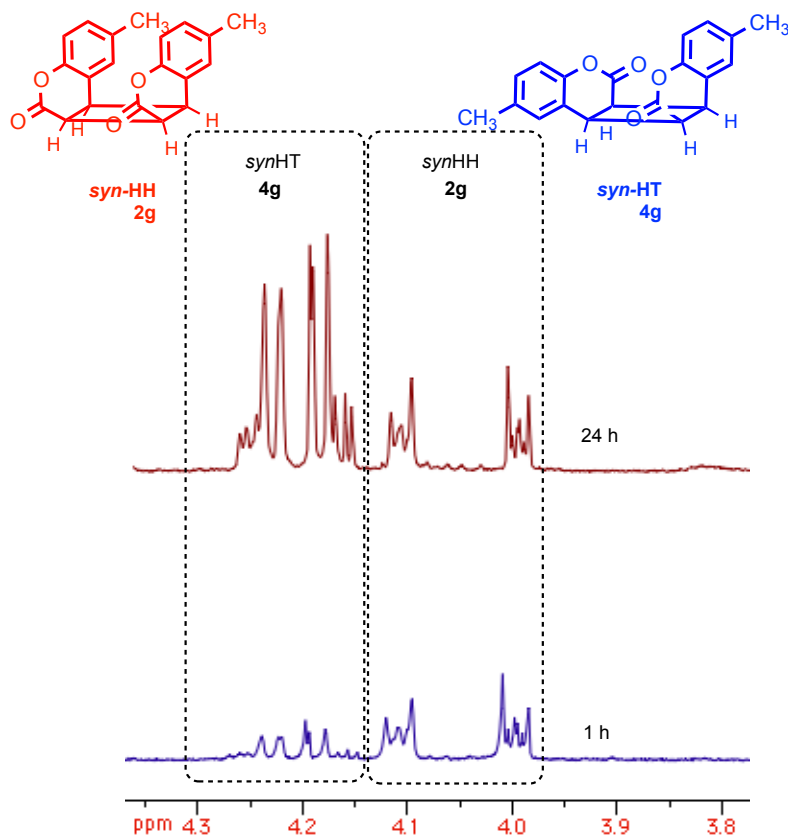


Figure 3.1 ¹H NMR spectra of 6-methylcoumarin **1g** photoirradiation with 50 mol% CB[8] for 24 hours (Top) and 60 minutes (Bottom) the cyclobutyl resonances are shown. The 24 hour spectra on top revealed *syn*-HT **4g** is the major product whereas the 60 minutes spectra on bottom revealed *syn*-HH **2g** as the major product

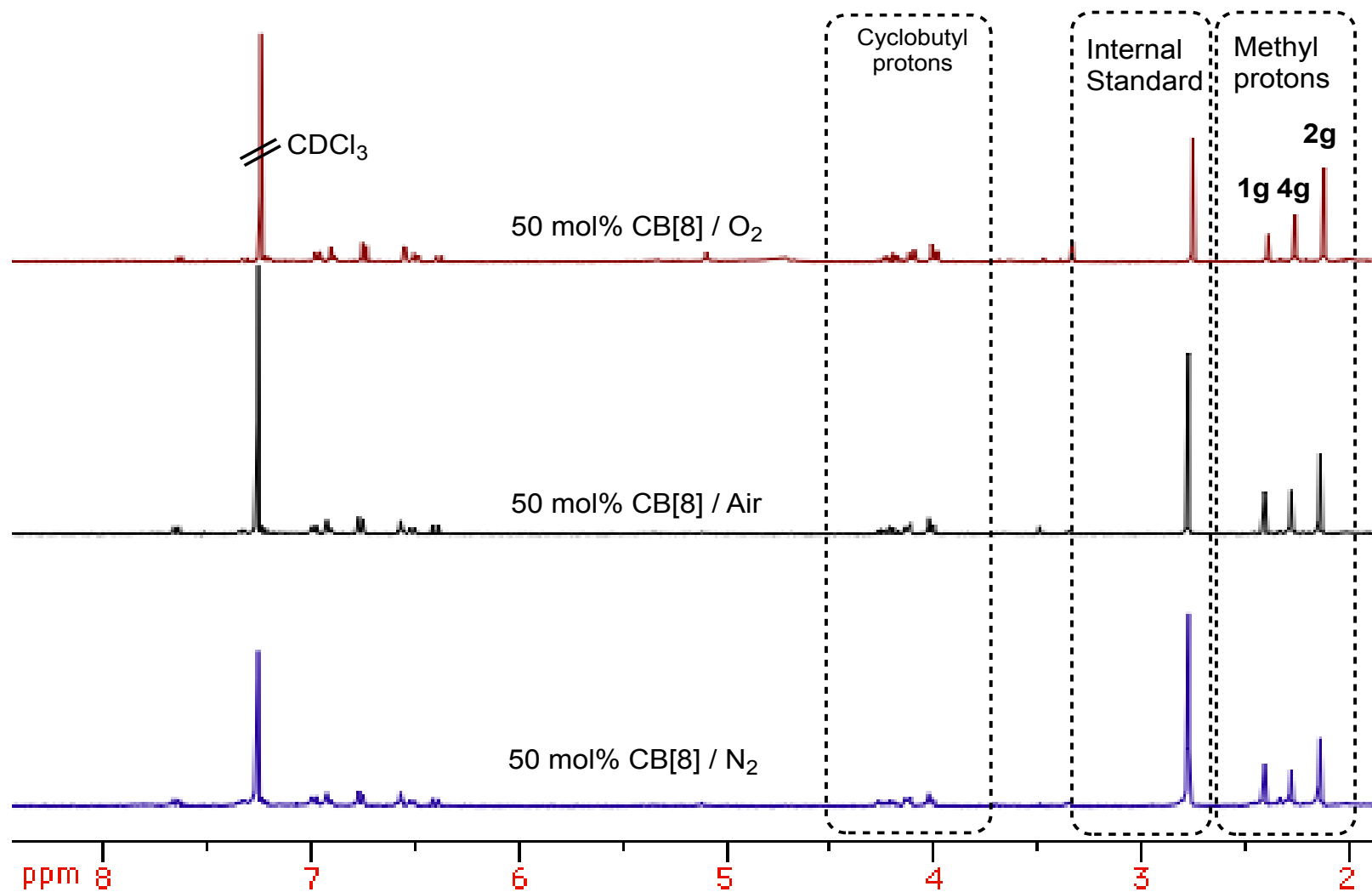


Figure 3.2 ^1H NMR (CDCl_3) spectra of photoirradiated 6-methylcoumarin **1g** reaction mixture with 50 mol% CB[8] under various atmospheres

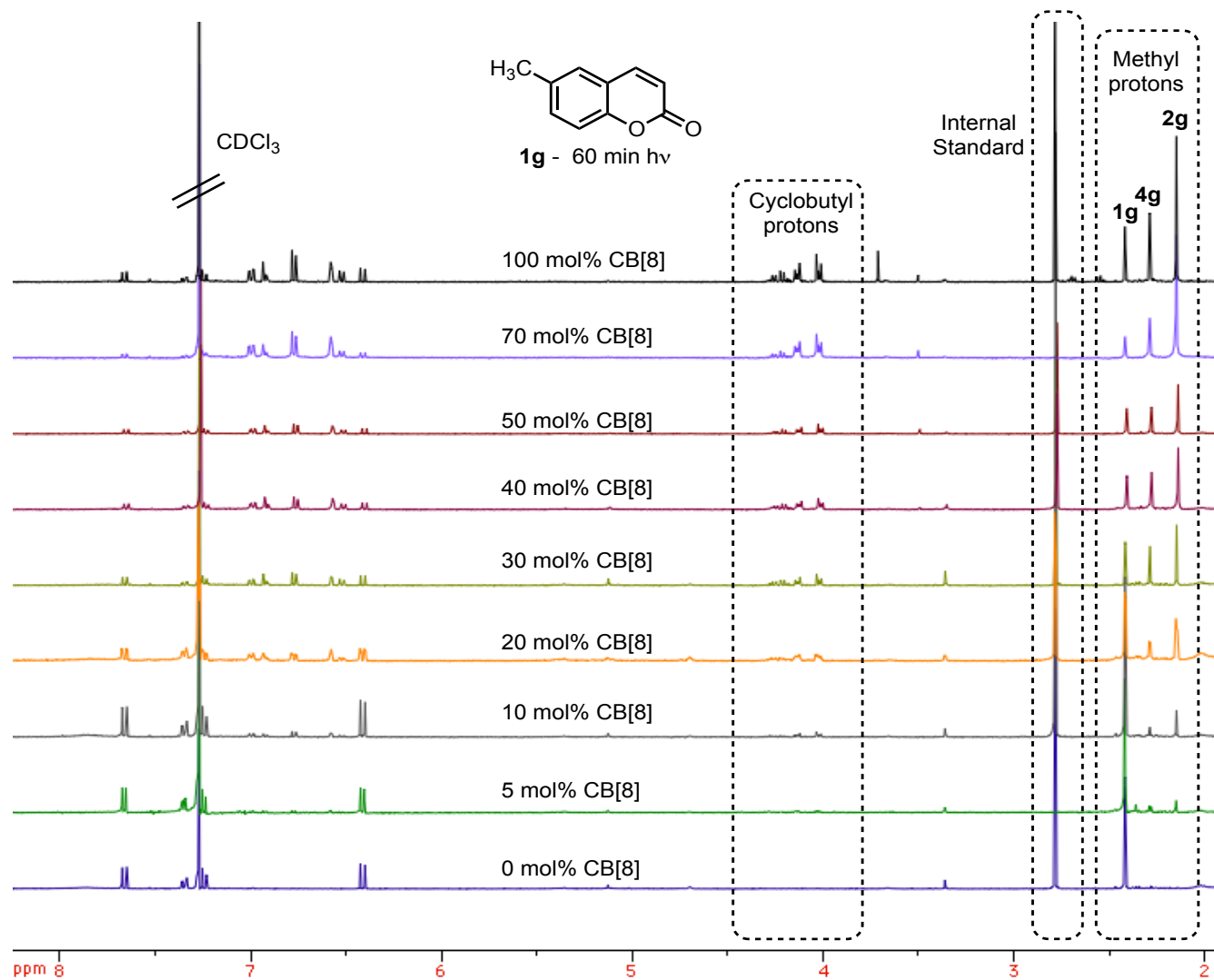


Figure 3.3 ¹H NMR (CDCl₃) spectra of 6-methylcoumarin **1g** irradiation with various amounts of CB[8]

Table 3.1 Photodimerization conversion and product distribution of 6-methylcoumarin **1g** dimers^a

Entry	CB[8] (mol%)	Time / min	<i>syn</i> -HH: <i>syn</i> -HT : <i>anti</i> -HH: <i>anti</i> -HT 2g:4g:3g:5g	Relative % Conversion ^b	Mass balance ^a
1	0 / air	60	Trace	Trace	-
2	0 / N ₂	60	29:29:13:29	9	-
3	0 / O ₂	60	No reaction	-	-
4	0 / Ar	120	22:76:2:0	23	-
5	5 / N ₂	60	41:41:18:0	20	-
6	10 / N ₂	60	69:31:0:0	23	97%
7	10 / O ₂	60	63:37:0:0	18	-
8	20 / N ₂	60	67:33:0:0	34	95%
9	30 / N ₂	60	68:32:0:0	59	95%
10	40 / N ₂	60	67:33:0:0	61	98%
11	50 / N ₂	60	68:32:0:0	72	99%
12	50 / air	60	66:34:0:0	70	98%
13	50 / O ₂	60	67:33:0:0	67	-
14	70 / N ₂	60	68:32:0:0	71	-
15	100 / N ₂	60	69:31:0:0	76	80%

^a Previously reported product distributions.² ¹H NMR measurements carry a 10% error.

^b Conversion % calculations based on relative integration of ¹H NMR methyl proton signals. ^c Mass Balance calculations based on relative integration of ¹H NMR methyl proton signals of photoproducts, remaining starting material with succinimide internal standard. Table reproduced with permission from RSC.

3.3. Rates of Reactions

3.3.1 Kinetic aspects of photodimerization mediated by CB[8]

As CB[8] mediated photocatalysis was effective the next question to answer is at what rate does the reaction proceed? The rates of dimerization were monitored by UV-vis at definite 1-minute intervals (0,1,2,3,4,5,6,7,8,9,10 min) during irradiation. Prior to irradiation the samples were purged with various atmospheres (N₂, air, and O₂). The reaction by UV-vis was setup to the same concentrations as the reactions that were monitored by ¹H NMR (50 μM **1g** plus various mol% of CB[8]). The decrease in absorbance of **1g** was calculated at 321 nm and was employed to calculate the rate constant (Figure 3.4). The catalyzed rates were significantly higher than the rate of dimerization without CB[8] in water.

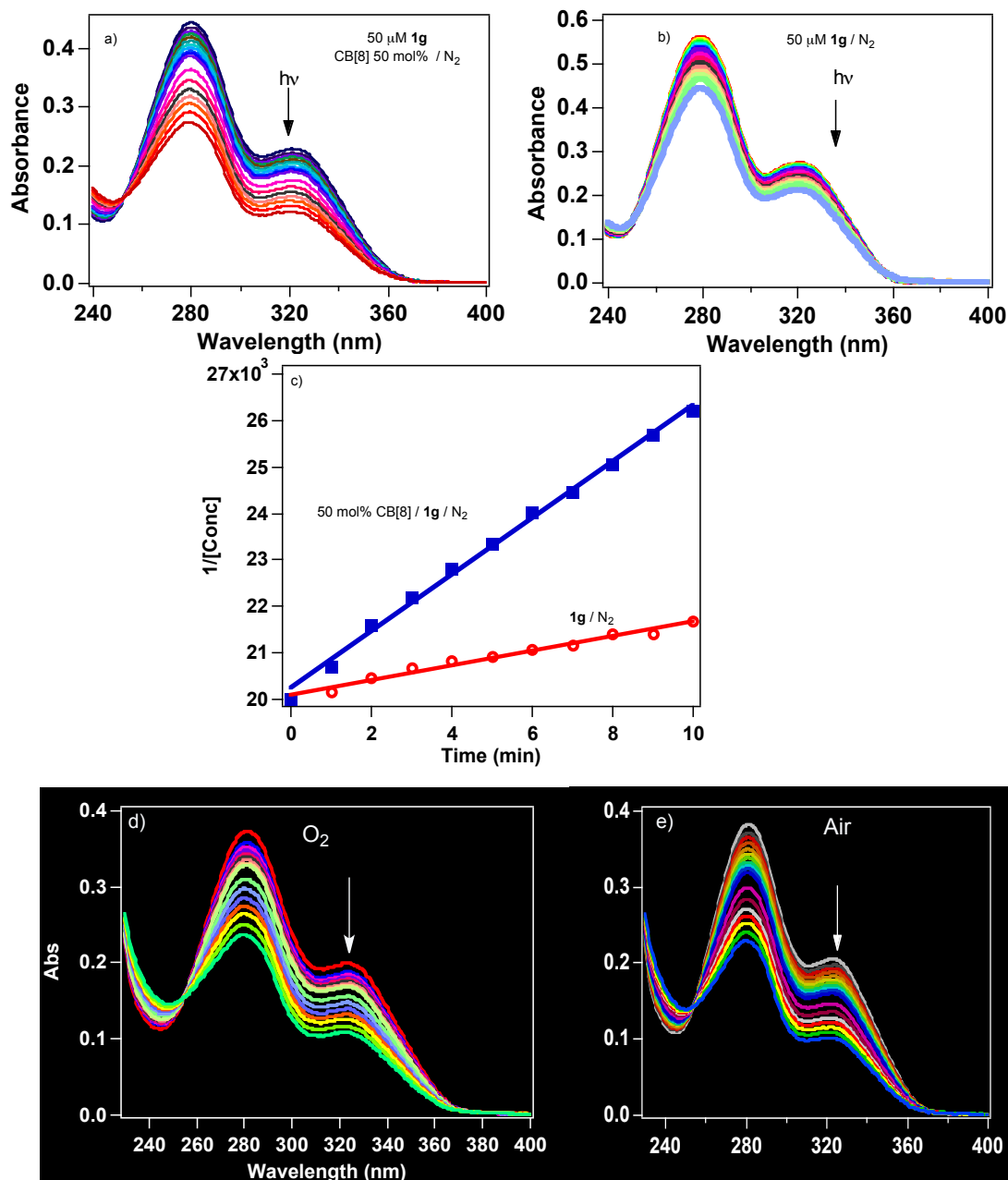


Figure 3.4 A) Monitoring the photodimerization process by measuring the decrease in absorbance of **1g** in the presence of 50mol% CB[8] under N₂ atmosphere by UV-vis spectroscopy. B) Monitoring the photodimerization process by measuring the decrease in absorbance of **1g** under N₂ atmosphere by UV-vis spectroscopy. C) Kinetics plot depicting the rates of reaction for **1g** with and without 50 mol% CB[8]. D and E) Photoreaction under O₂ and Air atmospheres monitored by UV-vis spectroscopy

The rates of dimerization mirror the observation of product conversion by ^1H NMR fairly well up to the stoichiometric 50 mol% studies. The rate at 5 mol% and 10 mol% are not much different than the uncatalyzed reaction which mirrors the relative conversion of **1g** at those concentrations of CB[8] when analyzed by ^1H NMR. The reaction appears to be clean as ascertained by the isosbestic point at 254 nm and no side photoproducts are observed from crude ^1H NMR data. The rates are sufficiently reasonable until we exceed the stoichiometric amount of CB[8] and go beyond 50 to 100 and 160 mol%.

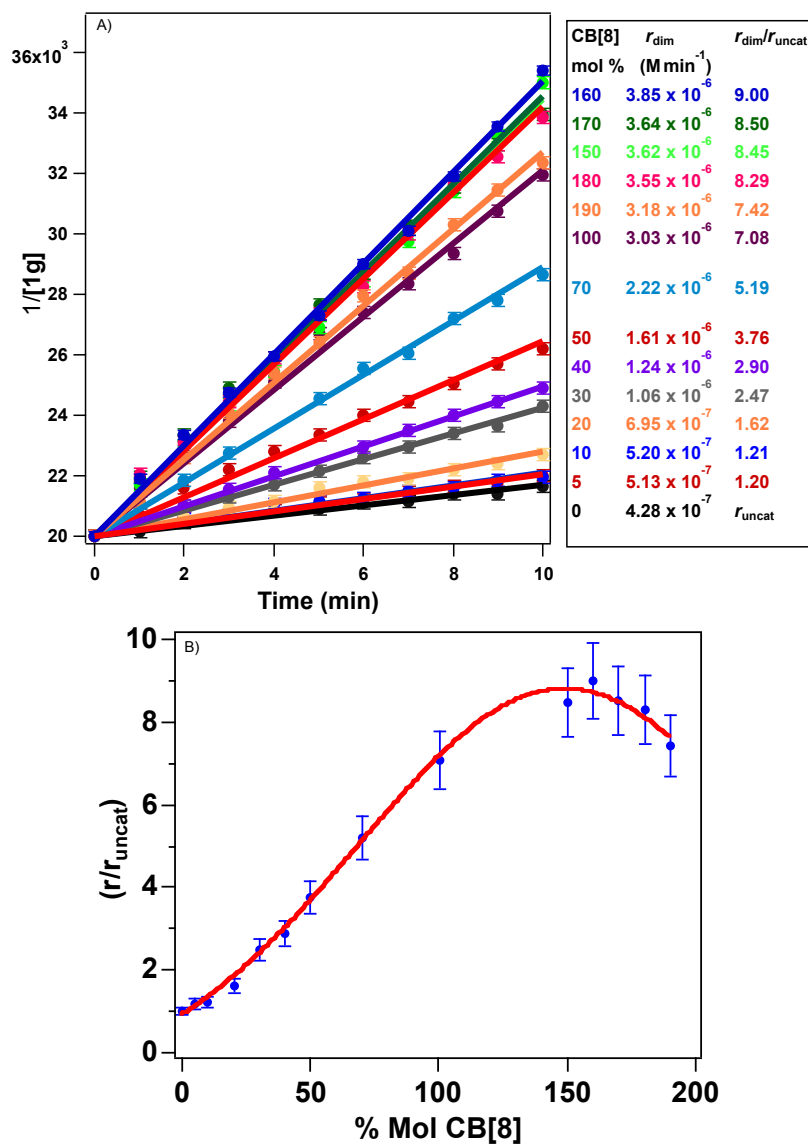


Figure 3.5 A) Kinetics photodimerization of **1g** at various mol% of CB[8]; B) Rate increase with various mol% of CB[8]

After the stoichiometric ratio of 1:2 host-to-guest we should expect a constant in the rate of reaction, instead we observed an increase in rate beyond a 1:1 host-guest ratio all the way up to a 160 mol% CB[8]. The acceleration factor is calculated as the rate of the catalyzed reaction divided by the rate of the uncatalyzed reaction ($\alpha = r_{\text{cat}} / r_{\text{uncat}}$) and the maximum acceleration factor was ~9 at 160 mol% CB[8]. This is a perplexing observation at first, but because the host-guest complex is dynamic it is feasible that the equilibrium observed in solution can be affected (ratio of free, 1:1 HG and 1:2 HG complexes) by increasing/decreasing the concentration of CB[8] (or) **1g**. Another aspect that might influence the rates of dimerization at high CB[8] concentration aggregation of CB[8] and **1g** (will be discussed in chapter 5). This will cause the rate of decrease at the onset of aggregation. The above hypothesis can be verified by performing the reaction under a lower or higher concentration of **1g**. When the irradiation was performed at the lower concentration of **1g** we observed a maximum rate shift to the right meaning that a higher concentration of CB[8] was required to reach the maximum rate of the reaction. Inspection of Table 3.2 (entry 11 and 12) demonstrates that the maximum reaction velocity if 0.05 mM **1g** was at 160 mol% of CB[8]. Whereas at 0.04 mM **1g** the max velocity was at 170 mol% of CB[8]. These observations indicate a dynamic host-guest system, where the individual concentrations of the of the reactive species (the 1:2 HG complex) is dictated by the initial concentrations of the CB[8] host and **1g** guest.

3.3.2. Substrate saturation kinetics

Saturation kinetics experiment was performed to determine the turnover number (TON) was for the catalytic cycle mediated by CB[8]. Under saturation conditions (guest concentrations at least 10 times of the host concentration) 1 μM of CB[8] along with increasing amounts of **1g** were irradiated and the monitored by UV-vis until the observed rate of reaction became constant (Table 3.3). The TON was calculated by dividing the maximum observed rate by the concentration of the catalyst.

Results from the saturation kinetics plot indicate an observed rate maximum of 3.4×10^{-6} Mol L⁻¹ min⁻¹. As the concentration of the CB[8] was 1 μM this corresponds to a TON of 3.4 min⁻¹ was observed for the supramolecular photocatalysis process. This implies that each CB[8] cavity performs the catalytic cycle 3.4 times per min under saturation conditions. Besides being able to calculate the TON, the shape of the plot yielded information about the mechanism of supramolecular photocatalysis.

Table 3.2 Comparison between the rates of dimerization using various mol% of CB[8] different concentrations of **1g**

Entry	CB[8] mol%	1g = [0.04 mM]		1g = [0.05 mM]	
		rate _{dim} (M min ⁻¹)	r _{dim} / r _{uncat}	rate _{dim} (M min ⁻¹)	r _{dim} / r _{uncat}
1	0 (r _{uncat})	3.76×10^{-7}	r _{uncat}	4.28×10^{-7}	r _{uncat}
2	5	7.07×10^{-7}	1.88	5.13×10^{-7}	1.20
3	10	8.21×10^{-7}	2.18	5.20×10^{-7}	1.21
4	20	-	-	6.95×10^{-7}	1.62
5	30	-	-	1.06×10^{-6}	2.47
6	40	-	-	1.24×10^{-6}	2.90
7	50	1.57×10^{-6}	4.18	1.61×10^{-6}	3.76
8	70	1.99×10^{-6}	5.29	2.22×10^{-6}	5.19
9	100	2.32×10^{-6}	6.17	3.03×10^{-6}	7.08
10	150	2.73×10^{-6}	7.26	3.62×10^{-6}	8.45
11	160	2.77×10^{-6}	7.36	3.85×10^{-6}	9.00
12	170	2.83×10^{-6}	7.52	3.64×10^{-6}	8.50
13	180	2.71×10^{-6}	7.20	3.55×10^{-6}	8.29
14	190	2.66×10^{-6}	7.07	3.18×10^{-6}	7.42

** The reported values carry an error of 10%. The mol % that corresponds to the maximum %

increase in rate is highlighted for a given concentration of **1g**.

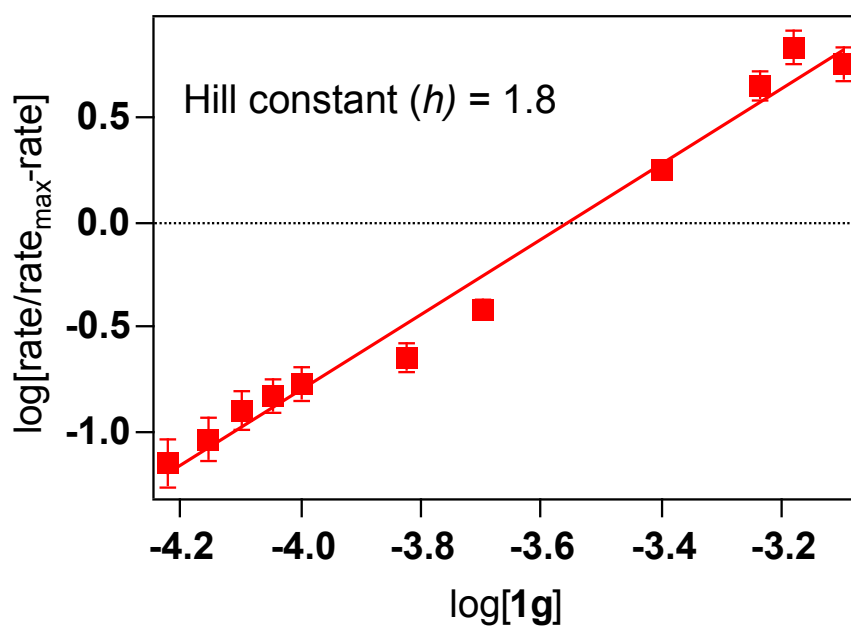
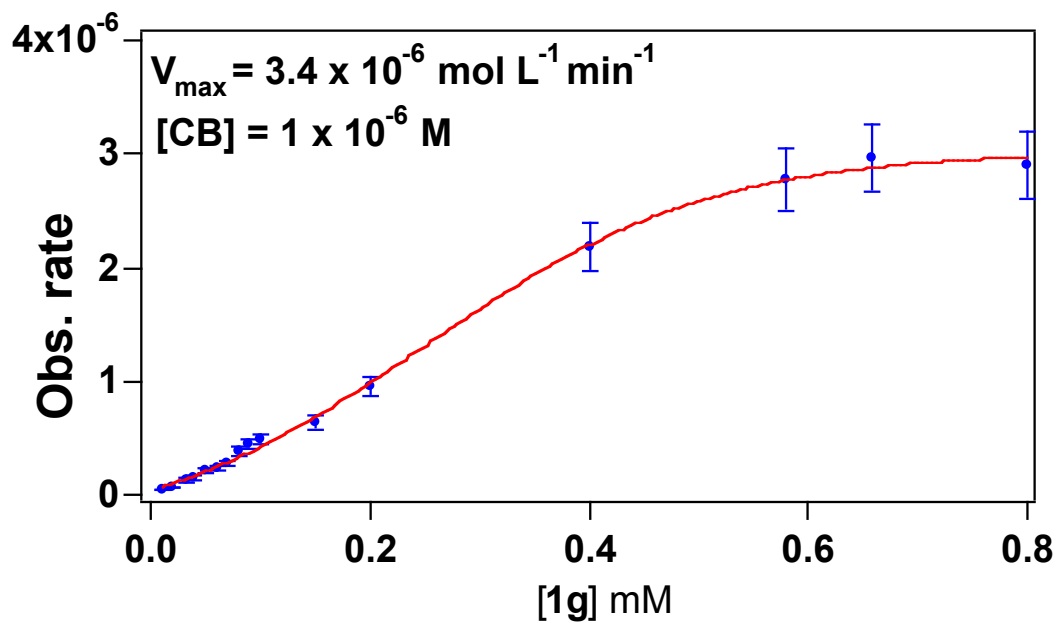


Figure 3.6 (Top) Saturation kinetics plot with an increasing concentration of 6-methylcoumarin **1g** showing sigmoidal behavior. (Bottom) Hill plot with a slope of 1.8 demonstrating positive cooperativity

Table 3.3 Concentrations of 6-methylcoumarin **1g** and CB[8] for saturation kinetics

Concentration		
CB[8] (μM)	6-methylcoumarin 1g (mM)	Obs rate _{dim} mol L ⁻¹ min ⁻¹
1.00	0.010	3.383×10^{-08}
1.00	0.020	7.1768×10^{-08}
1.00	0.033	1.2111×10^{-07}
1.00	0.040	1.4628×10^{-07}
1.00	0.050	2.157×10^{-07}
1.00	0.060	2.2542×10^{-07}
1.00	0.070	2.8483×10^{-07}
1.00	0.080	3.808×10^{-07}
1.00	0.090	4.3605×10^{-07}
1.00	0.100	4.927×10^{-07}
1.00	0.150	6.27×10^{-07}
1.00	0.200	9.472×10^{-07}
1.00	0.400	2.1848×10^{-06}
1.00	0.580	2.77762×10^{-06}
1.00	0.656	$2.96512\text{e-}06$
1.00	0.800	$2.8917\text{e-}06$

Solutions prepared from stock concentrations for CB[8] and **1g** of 1.0×10^{-4} M and 1×10^{-3} M respectively.

The sigmoidal behavior from the saturation kinetics plot is a common observation in enzyme kinetics and it implies there is some sort of cooperative effect occurring during the catalytic process. The degree of cooperativity can be positive, negative or neutral and can be calculated using the Hill equation. The Hill constant values (h) are relative to the value of 1, when $h=1$ the catalyst, enzyme, etc. obeys Michaelis-Menton kinetics. Positive cooperativity ($h > 1$) happens when the first guest interacts with the host to make room for the second guest. In a dimeric reaction, this positive cooperativity would enhance the rate of a reaction by preferentially bringing the second guest within a reaction ready distance. When observed in Michaelis-Menton kinetics a hyperbolic behavior is observed. Negative cooperativity ($h < 1$) occurs when the first guest inhibits the binding of the second guest thus in a dimeric photoreaction this would actually prevent the second guest from residing in the reaction ready distance. The Hill constant obtained from the saturation kinetics plots was 1.8 for CB[8] induced photocatalysis of **1g**. This is strikingly similar to the Job's plot value of 1.6 guests to 1.0 host. Beyond the observational evidence that

two guests are binding and reacting, the slope is telling us that after the first guest binds it makes room by altering the shape of the cavity for the second guest to bind. The sequential binding of the two guests is not necessarily novel here, it's that after the first guest binds it makes it more favorable for the second guest to bind. Reorganization of a synthetic cavity resembles a biological enzymatic function. It is quite extraordinary and deserves a thorough investigation.

3.4. X-ray Crystal Structure of 1g@CB[8] Complex

3.4.1. Single X-ray crystal structure

Host-guest studies are highly dependant on experimental conditions, the most important condition being the concentration of host and guest. Because optimal conditions are not always met one can observe numbers that are distorted from expectation. Such examples include a host-guest ratio of 1:1.6 in the case of the jobs plot, or a maximum reaction rate requiring 160 or 170 mol% of CB[8] when the concentration of guest is 50 or 40 μM respectively. However, single x-ray crystals provide direct observation about spatial representations for the location of atoms.

The crystal structure of two **1g** molecules bound to the interior cavity of CB[8] demonstrated without a doubt that two molecules of coumarin can fit inside the cavity (Figure 3.7). The templating of the molecules within the cavity however are not in the expected head-to-head orientation, they are more head-to-tail orientation. Since the crystal is technically in the lowest energy, it's likely that the head-to-tail orientation eliminates extraneous energy like dipole moments that would occur in water. It is important to remember that the photoreactions occur in a dynamic environment. The overall shape of the CB[8] cavity is no longer symmetrical, instead it takes on an oval-like shape that is caused by the distortion of the two molecules inside. This would explain why there is a sigmoidal behavior observed in the saturation kinetics plot. The crystalline complex also offers some insight into the "resting-state" of the catalytic cycle might look like as the two coumarin molecules distort the cavity to create the "reaction-ready" orientation.

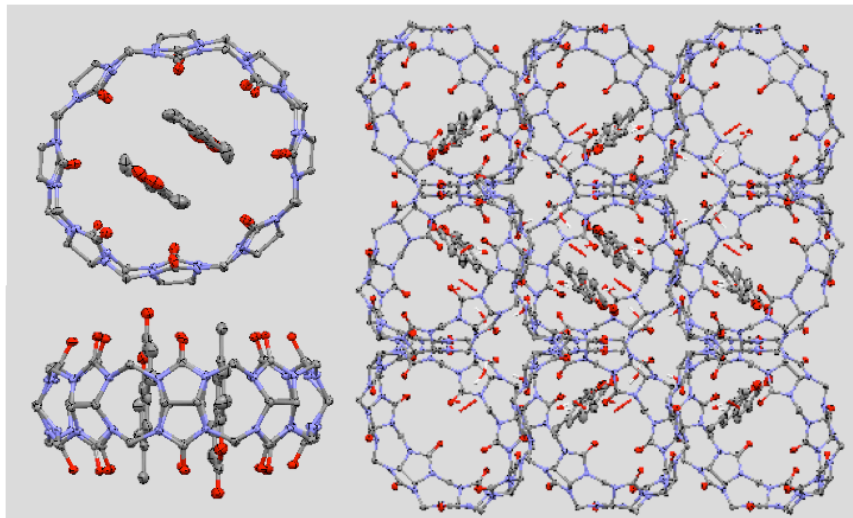


Figure 3.7 Single crystal X-ray of 1:2 H:G complex of CB[8] and 2 units of **1g**. (Left) Top and side views show the inclusion complex. (Right) Packing of CB[8] along an axis. Thermal ellipsoids are shown at 50%, water and hydrogens were removed for clarity

Beyond the structural features of the single host-guest complex, as displayed by single crystal XRD structure, its unit cell is quite large with dimensions 16.492 Å x 22.079 Å x 22.288 Å resulting in an orthorhombic unit cell that is 8115.4 Å³. This large unit cell contains four molecules of CB[8] and eight molecules of coumarin along with 54 water molecules. The crystals were grown by layering 10 mL of concentrated CB[8] ($\sim 1.0 \times 10^{-4}$ M) with 10 mL of **1g** (1.0×10^{-3} M) and allowing it to diffuse overnight. The single crystal was collected on a Bruker Apex Duo diffractometer with an Apex 2 CCD area detector at T = 100 K. The x-ray source used Cu radiation. The structure was processed with Apex 2 v2010.9-1 software package (SAINT v.7.68A, XSELL v.6.3.1). Direct method was used to solve the structures after multi-scan absorption corrections. Details of data collection and refinement are given Table 3.4. All non-hydrogen atoms of the main molecules, which are subject of interest of this paper, are refined anisotropically. All Hydrogen atoms are generated by HFIX. In addition to the host and the two guests, we observed 54 molecules of water per cell. Hydrogen atoms of all water molecules are not located or generated.

Table 3.4 Single crystal collection and refinement parameters for (**1g**)₂@CB[8] HG complex

Formula	C ₄₈ H ₄₈ O ₁₆ N ₃₂ 2x C ₁₀ H ₈ O ₂ · 13.5 H ₂ O
Formula weight	1892.78 g/mol
Crystal size [mm]	0.15 x 0.18 x 0.20
Crystal system	Orthorhombic
Space Group, Z	Pbca, 4
a [Å]	16.4918 (3)
b [Å]	22.0793 (4)
c [Å]	22.2875 (4)
α[Å]	90
β[Å]	90
γ[Å]	90
ρ _{calc} [g/cm ³]	1.527 (1.549) ^a
μ [cm ⁻¹]	1.078
F(000)	3856
# of measured reflections	44959
# of independent reflections	6974
# of reflections (I ≥ 2σ)	6587
R _{int} [%]	2.46
Resolution [Å]	0.84
R1/wR2 (I ≥ 2σ) ^b [%]	7.05/19.66
R1/wR2 (all data) [%]	7.70/20.84

^aThe density value of 1.549 was calculated by taking into account all the non-localized hydrogen atoms in the water molecules. For density value of 1.527, non-localized hydrogen atoms in the water molecules were not taken into account.

^bR1 = $\frac{\sum ||F_o| - |F_c||}{\sum |F_o|}$, wR2 = $\left\{ \frac{\sum [(F_o)^2 - (F_c)^2]^2}{\sum w(F_o)^2} \right\}^{1/2}$ for $F_o^2 > 2\sigma(F_o^2)$, $w = [\sigma^2(F_o^2) + (AP)^2 + BP]^{-1}$ where $P = [(F_o)^2 + 2(F_c)^2] / 3$; A (B) = 0.1168 (18.2196)

3.5. Conclusions

The initial studies to determine if supramolecular photocatalysis was feasible were successful. Our studies was the first to demonstrate that a substoichiometric amount of CB[8] (as low as 10 mol%) can be employed to control the [2+2] photodimerization. This produces a new avenue of using supramolecular motifs as photocatalysis. Sufficient evidence has shown that the [2+2] photodimerization of 6-methylcoumarin **1g** within CB[8] is an efficient and highly selective reaction. The reaction does have reversal in product selectivity that is different in 24 hours compared to the 1 hour irradiation. The 1 hour photoreaction is extremely clean both with and

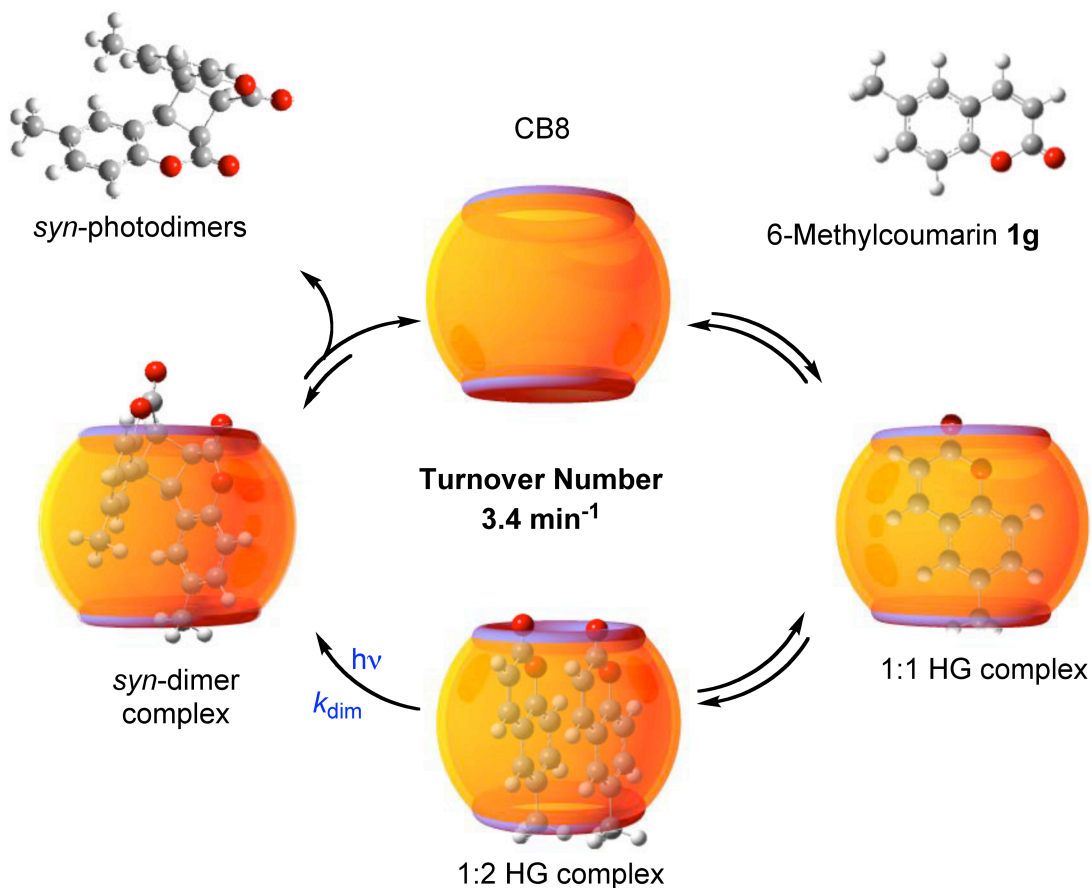
without CB[8] as observed by the isosbestic point at 254 nm suggesting that the starting material to product conversion results in little to no side product formation. In one hour we see *syn*-HH **2g** as the major product, whereas in 24 hours *syn*-HT **4g** is the major product. Similarly the photoreaction for **1g** in water under these times is highly inefficient and leads to very little conversion with a mixture of photoproducts.

We demonstrated that **1g**-CB[8] system meets the requirements for photocatalysis. The dynamic nature of the host-guest complex has shown that the reaction inside the cavity is far more efficient than the reaction outside the cavity. The reaction proceeds cleanly with substoichiometric amounts of CB[8] as a catalyst and exclusive *syn*-photoproducts are observed with as little as 10 mol% CB[8]. There is little to no evidence to suggest that the photoproduct binds to the cavity causing reaction inhibition as we see efficient 60% conversion rate using 30 mol% of CB[8] as a catalyst. The explanation for the superstoichiometric until after 160 mol% not hindering the reaction can be explained by the statistical amount of 1:2 host-guest complex is still in an excess over the 1:1. Once the 1:1 host-guest complex is in excess the reaction is impeded but not stopped completely.

The product conversion under various atmospheres was largely unchanged for the reactions. This poses the question regarding whether the photoreaction proceeds through the singlet or triplet mechanism. As previously mentioned there are examples that the CB[8] cavity can protect triplet states from being quenched by oxygen. While the various atmospheres offer little insight into the mechanisms, the saturation kinetics and single crystal x-ray diffraction do offer some clues to how the reaction proceeds.

Mechanistically the reaction proceeds through a stepwise cooperative binding as evidenced by the sigmoidal curve (Scheme 3.1). In-depth analysis of the curve revealed a hill-plot value ($h= 1.8$) that is near the ideal 1:2 host guest ratio needed for the reaction to occur. The resting state of the catalytic cycle appears to be a distorted CB[8] cavity with two **1g** molecules inside. From these observations we can conclude that the mechanism for the reaction proceeds through a 1:1 host-guest complex followed by reorganization and sequestering of a 2nd couminan molecule within the CB[8] cavity. The complex absorbs a photon of light becomes promoted to a

higher energy state and reacts to form the photoproducts. The photoproduct is extruded out of the cavity and the reaction or catalytic cycle continues with a maximum catalytic TON of 3.4 min^{-1} (Scheme 3.1).



Scheme 3.1 Proposed catalytic cycle for the [2+2] photodimerization of **1g** mediated by CB[8]

3.6. General Methods

3.6.1. General methods and materials

6-Methylcoumarin **1g** was purchased from Alfa Aesar and was used as received without further purification. Cucurbit[8]uril (CB[8]) was synthesized using previously reported procedures in chapter 2.⁶ Diethylether was used for the extraction process as received without further purification. Nanopure water ($\geq 17.8 \text{ M}\Omega\text{-cm}$, Barnstead Ultrapure) was used as the solvent for carrying out photoreactions and photophysical measurements. Stock solution ($1 \times 10^{-4} \text{ M}$) of

CB[8] was prepared in a 1000 mL volumetric flask. Stock solution (1×10^{-3} M) of **1g** was prepared in a separate 500 mL volumetric flask a solution. The photoreactions were irradiated with a 450 W medium pressure Hg-lamp at room temperature. The mercury-lamp cooling jacket was cleaned every 10 hours to maximize lamp intensity. Absorbance measurements were performed using Shimadzu UV-2501PC UV-vis spectrophotometer. Spectrophotometric solvents were used where ever necessary unless or otherwise mentioned. UV quality fluorimeter cells (with range until 190 nm) purchased from Luzchem®.

3.6.2. NMR Techniques

^1H NMR spectra were obtained on Varian 400 MHz or 500 MHz spectrometer. Coupling constants (3J) are reported in hertz (Hz). The product conversion was calculated from ^1H NMR using succinimide as an internal standard (IS). The characterization of photo-dimers was performed in chapter 2. The succinimide IS was prepared by making a solution with a concentration 1.0 mg/mL of CHCl_3 and sonicating for an hour. Even without an IS it is possible to compute the relative conversion which is the formation of the products divided by total of products and starting material.⁷

$$\text{Relative Conversion} = \frac{\text{Moles}_{\text{Analyte}}}{\text{Moles}_{\text{Analyte}} + \text{Moles}_{\text{Starting Material}}} \times 100\% \quad (3.1)$$

To determine the mass balance (the recovery of product) we need to quantify the amount of ^1H -proton signals by incorporating succinimide as an internal standard. The equation for mass balance can be derived from the conservation of mass equation from the moles of starting material and photoproduct in the reaction mixture.

$$\text{Massbalance} = 100\% \times \frac{\sum (\text{Starting Material}_{\text{final}} + \text{Product}_A + \text{Product}_B)}{\text{Starting Material}_{\text{initial}}} \quad (3.2)$$

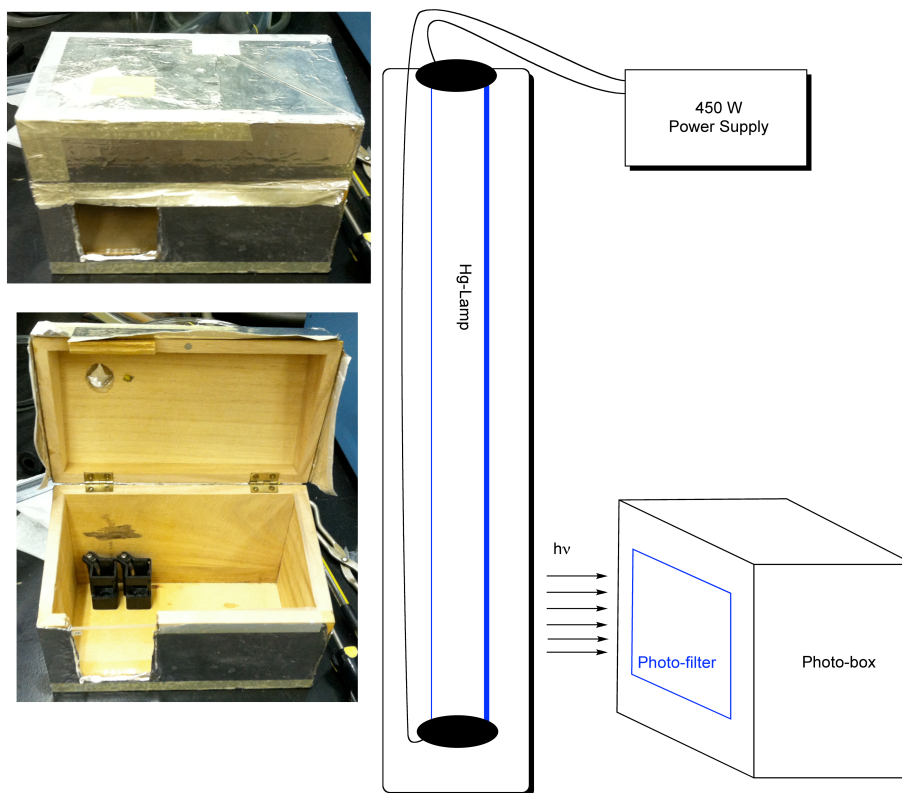
Relative conversion is not a quantifiable term and can only be used to determine the ratio between the product and remaining starting material. However if product and or starting material

are lost the relative conversions can vary greatly from actual values. A better approach to conversion studies uses the internal standard in a similar manner to the mass balance studies. The percent conversion is calculated by comparing the moles of unreacted starting material (analyte) after the reaction to moles of the internal standard reference. The remaining starting material can then be compared to the number of moles of the starting material prior to irradiation to determine relative conversion.

$$\text{Moles of analyte} = \text{Moles of reference} \times \frac{\text{Integral}_{\text{Analyte}}}{\text{Integral}_{\text{IS}}} \times \frac{\# \text{ protons}_{\text{IS}}}{\# \text{ protons}_{\text{Analyte}}} \quad (3.3)$$

3.6.3. UV-vis techniques for rate kinetics and saturation kinetics

The rate kinetics of various mol% CB[8] and saturation kinetics plots were performed using a photo-box (Scheme 3.2) with a pyrex cutoff filter (>295 nm) and irradiated two samples simultaneously for specific time intervals. The photo-box was set in the same location inside the photo-chamber such that the entrance of the photo-box was perpendicular to in the incident light (Scheme 3.2). Sample were prepared in volumes of 3 mL and samples under N₂ or O₂ atmospheres were purged for 15-20 min and then sealed up with paraffin-wax and promptly used to prevent diffusion of air into the samples. Samples under air atmosphere were prepared and promptly used. The samples were then monitored via UV-vis measurements. After the measurement the sample on the left side of the photo-box was moved to the right side and vice versa, this allowed for an average of the two sides eliminating error due to over irradiation. The observed rates of the reaction were calculated by determining the slope of 1/[Conc] versus time and fitting the function to linear fit using the linear equation $y = mx+b$ in ms-excel software.



Scheme 3.2 Photos of photo-box in both closed and open form. The glass window is for interchangeable photofilters and the two black sample holders will hold standard 10 mm x 10 mm cuvettes. The photobox was placed into the photochamber allowing the light from the lamp to irradiate the samples perpendicular to the window

3.7. References

**The material in this chapter was co-authored by Barry C Pemberton (BCP), Alexander C. Johnson (ACJ), Angel Ugrinov (AU), D.K. Srivastava (DKS) and J. Sivaguru (JS). BCP had primary responsibility for preparing samples and collecting data, whereas ACJ assisted in collection of data. Single crystal of the HG complex was grown independently by BCP and ACJ, the data collection and interpretation was performed by AU. Saturation kinetics experiments were performed under the guidance of DKS. BCP processed the data and with help of JS was the primary developer of the conclusions that are advanced here. BCP also drafted and revised all versions of this chapter. JS served as proofreader and checked the math in the statistical analysis conducted by BCP.

- (1) Wolff, T.; Gerner, H. Photodimerization of coumarin revisited: Effects of solvent polarity on the triplet reactivity and product pattern *Phys. Chem. Chem. Phys.* **2004**, *6*, 368-376.
- (2) Yu, X.; Scheller, D.; Rademacher, O.; Wolff, T. Selectivity in the Photodimerization of 6-Alkylcoumarins *J. Org. Chem.* **2003**, *68*, 7386-7399.
- (3) Görner, H.; Wolff, T. Lewis-acid-catalyzed Photodimerization of Coumarins and N-methyl-2-quinolone *Photochem. Photobiol.* **2008**, *84*, 1224-1230.
- (4) Gonzalez-Beajar, M.; Montes-Navajas, P.; Garcia, H.; Scaiano, J. C. Methylene Blue Encapsulation in Cucurbit[7]uril: Laser Flash Photolysis and Near-IR Luminescence Studies of the Interaction with Oxygen *Langmuir* **2009**, *25*, 10490-10494.
- (5) Mohanty, J.; Nau, W. M. Ultrastable rhodamine with cucurbituril *Angew. Chem., Int. Ed.* **2005**, *44*, 3750-3754.
- (6) Day, A.; Arnold, A. P.; Blanch, R. J.; Snushall, B. Controlling Factors in the Synthesis of Cucurbituril and Its Homologues *J. Org. Chem.* **2001**, *66*, 8094-8100.
- (7) Wallace, T. Quantitative analysis of a mixture by NMR spectroscopy *J. Chem. Ed.* **1984**, *61*, 1074.

CHAPTER 4. PHOTOPHYSICS OF 6-METHYLCOUMARIN IN THE PRESENCE OF CUCURBIT[8]URIL**

4.1. Introduction

6-Methylcoumarin (**1g**) is a fragrant molecule that has been used as an artificial scent resembling fresh-mowed grass. Because of its fragrance and ability to absorb ultra violet (UV) light, it has been used in cosmetics as a sunscreen additive or perfume.¹ However, **1g** has been banned since the late 1970's in cosmetics because it was reported to be a photo-allergen.² The mechanism of the photoallergy has been reported to occur through the generation of singlet oxygen. The highly reactive singlet oxygen species can cause irritation to the skin and produce a rash.³

Chapter 3 discussed the photoreaction of **1g** with various mol% of the CB[8] cavity. To understand how the CB[8] cavity influenced the photoreaction and product selectivity in the case of **1g** as well as with other coumarins, detailed photophysical investigations are required. In recent years there have been several photophysical studies on the photochemical properties of 6-methylcoumarins by Thomas Wolff and co-workers.^{4,5} Their detailed investigation revealed the mechanism for dimer products results from a singlet excited state that undergoes intersystem crossing (ISC) to the triplet state and then forms all four photoproducts (Figure 4.1, Scheme 4.1 and Scheme 2.1) from the excited triplet spin state. The rate of intersystem crossing (ISC) of **1g** from singlet to triplet is very efficient in polar solvents such as water and trifluoroethanol ($\Phi_{isc} = 0.3$), but in non-polar solvents like benzene ($\Phi_{isc} = 0.03$) the intersystem crossing rate decreases. These results along with other mechanistic and photophysical studies have been used as a spring board to propel our studies (Scheme 4.1) into deeper understanding of **1g** photodimerization inside CB[8].

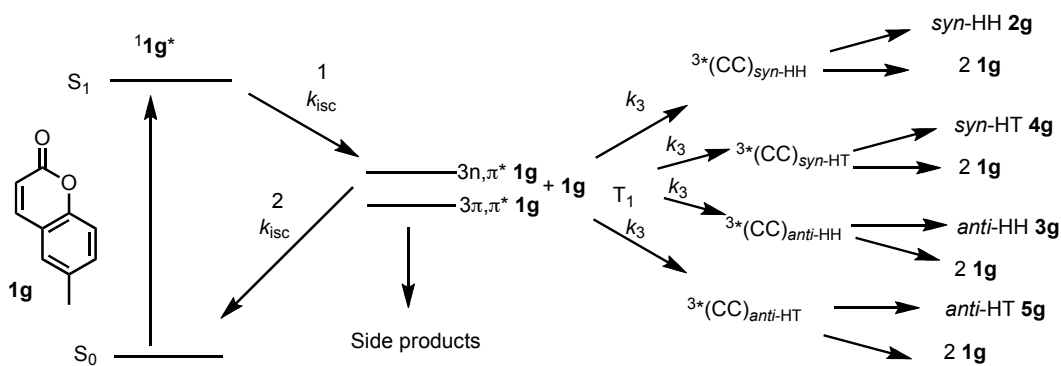
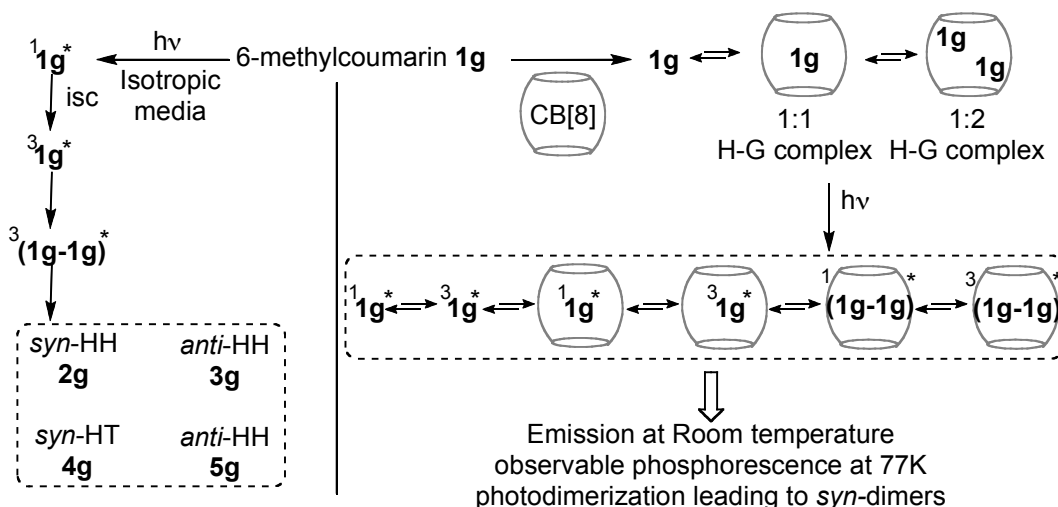


Figure 4.1 The postulated reactive pathway for the dimerization of **1g**



Scheme 4.1 The postulated photophysical/photochemical pathways of **1g** in solution and in the presence of CB[8]

Our investigation into the feasibility of supramolecular photocatalysis mediated by CB[8] resulted in exploring **1g** as a potential guest to undergo the photoreaction. The requirements established for a feasible photocatalytic system include:

- 1) A dynamic host-guest system, which is needed for formation of reactive species in the catalytic cycle. The Jobs' plots established in chapter 2 demonstrate that the ratio between CB[8] and **1g** was 1:1.6.
- 2) The reaction within the cavity needs to be more efficient than the reaction in solution. This is a relative comparison between the reaction quantum yields of the photoreaction in each environment (inside and outside the cavity). We can also control the reactivity if the reactant occurs from the triplet state, by employing oxygen-saturated solution would inhibit the background reaction. The photoreaction under different atmospheric conditions (performed in chapter 3) have shown that the photoreaction in the presence of the cavity is minimally affected under various atmospheres (N_2 , O_2 or air).
- 3) The photoproduct must not bind to the cavity with a greater affinity than the unreacted coumarins as it would inhibit the overall reaction process (product inhibition). This is probably the

most elusive feature of any catalytic system. Product inhibition/poisoning greatly reduces the turnover number (TON) of a catalytic system.

This chapter focuses on the photophysical aspects that give insights into the mechanism for supramolecular photocatalysis. The fluorescence spectroscopy and lifetime studies examine the host-guest complex and allow us to speculate on the reactive nature of the catalytic system. The binding constant studies provided enhanced understanding of the cooperative nature of how the host-guest system interacts with each other. The phosphorescence and triplet-triplet absorption studies demonstrate that the reactive species is possibly proceeding through a triplet excited state. The actinometry of the reaction was performed to quantify how efficient the catalytic reaction when compared to the reaction in solution.

4.2. Photophysical Studies of 6-methylcoumarin 1g in Presence and Absence of CB[8]

4.2.1. Absorbance studies of 6-methylcoumarin 1g

The absorbance profile of **1g** begins near 370 nm and like most coumarins is a good absorber of UV light (Figure 4.2). The chromophore has two distinct transitions, the band of higher energy (shorter wavelength) around 270 nm exists as $\pi - \pi^*$ transition whereas at the lower energy (longer wavelengths) around 321 nm is likely a mixture of $n - \pi^*$ and $\pi - \pi^*$ transition states (Figure 4.2).⁴ The molar extinction coefficient at 321 nm is $5500 \text{ M}^{-1} \text{ cm}^{-1}$. When **1g** is dissolved in the presence of CB[8] the overall absorbance profile changes and a hypochromic and bathochromic shift was observed.⁴ This change in absorbance is evidence of a guest that is having its' vibronic / translational / rotational motions suppressed when encapsulated within a host. The result of these drastic changes make it very obvious when monitoring the complexation of **1g** into CB[8] via both absorbance and fluorescence spectroscopy.

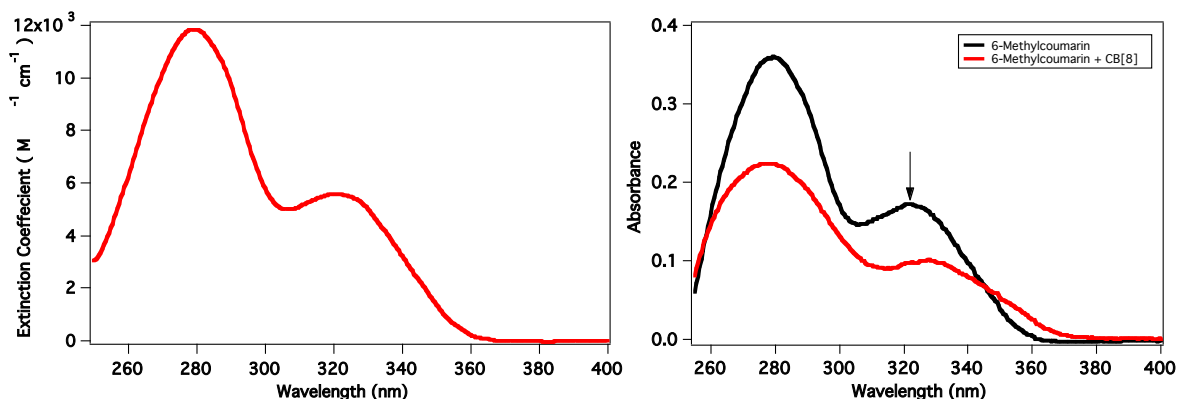


Figure 4.2 (Left) The molar extinction coefficient profile of 6-methylcoumarin in water. (Right) Absorbance changes of 6-Methylcoumarin **1g** when in water and in water/CB[8]

4.2.2. Fluorescence Studies of 6-Methylcoumarin with CB[8]

While there are several examples of highly fluorescent coumarins with quantum yields near 1.0, **1g** is not one of them. The fluorescence emission quantum yield of **1g** in ethanol is only $\Phi_{em} = 0.015$.⁵ In water we reported the fluorescence emission quantum yield to be $\Phi_{em} = 0.008$, which is much smaller than in ethanol. This could be the result of increased ISC from the triplet to singlet excited state. In addition, most of the energy from the excited molecule is lost as heat through vibrational deactivation from the singlet excited state. The complexation of **1g** inside CB[8] does significantly increase the fluorescence output (Figure 4.3). The fluorescence spectra of **1g** has an onset near 380 nm with an emission maximum at 411 nm. This corresponds to an energy of 69.6 kcal/mol (291 kJ/mol). When complexed with CB[8] we observed a redshift in fluorescence to an emission maximum of 443 nm corresponding to an energy of 64.8 kcal/mol (271 kJ/mol) resulting in an energy stabilization of 5.1 kcal/mol after complexation.

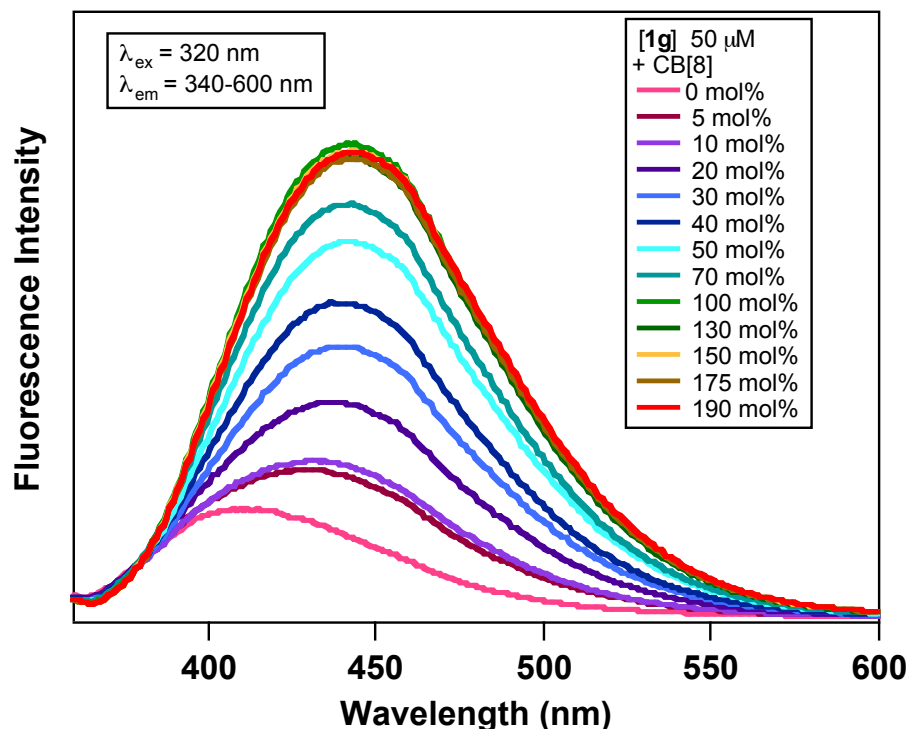


Figure 4.3 Emission of 6-methylcoumarin **1g** in the presence of varying concentrations of CB[8] in water

The quantum yield of 6-methylcoumarin **1g** when complexed within the CB[8] cavity was measured. The value of 0.008 obtained for the emission of **1g** in water is lower than the previously reported value of 0.015 for **1g** in ethanol. However the quantum yield increases as much as five times to ($\Phi_f = 0.04$) when complexed with a 1:1 ratio of host-guest. This is likely due to the restricted freedom of **1g** while inside the CB[8] cavity. This is likely as a result of a decrease in the non-radiative decay rate that increases the quantum yield of fluorescence. The process of thermal relaxation to the ground state is possibly restricted because of the encapsulation of the methyl group through the “loose-bolt” mechanism.⁶ The leveling off of the CB[8]:6-MC complex at a 1:1 ratio is likely due to a constant efficiency of emission of the singly bound coumarin to the CB[8] cavity. In other words, if we were to reverse this concept and go from a 1:1 host-guest complex to a 1:2 host-guest complex we would see a significant decrease in fluorescence output as the doubly bound coumarin complex will compete for deactivation from the excited state not only by fluorescence but also by photoreactions. This observation will have more important

implications in chapter 5 where the kinetics of complexation will be evaluated by stopped flow experiments.

The quantum yield was recorded by comparing the integration of the sample's fluorescence signal to a known quantum yield standard (Equation 4.1). Quantum yield standards are typically highly fluorescent materials with a well-defined emission range and falls within the emissive region of the sample whose emission quantum yield needs to be measured. Quinine sulfate in 0.5 M H₂SO₄ has a reported emission quantum yield of $\Phi_{em} = 0.55$. The quantum yield calculation compares the quantum yield of the reference (Φ_r) to the integration of the sample (I_s) and integration of reference (I_r). The formula takes into account the correction factors of refractive indices (η) of different solvents and inner-filter effects from changes in absorbance values. If there are differences in the solvent dielectric constant and absorbance values employed for the reference and sample, this can have a dramatic effect on the measured quantum yield, especially since the refractive indices are squared.

$$\Phi_s = \Phi_r \left(\frac{I_s}{I_r} \right) \left(\frac{Ab_{s_r}}{Ab_{s_s}} \right) \left(\frac{\eta_s^2}{\eta_r^2} \right) \quad (4.1)$$

Inspection of Figure 4.4 revealed that the quantum yield of fluorescence saturated at ~70 mol% of CB[8]. As we will demonstrate, 70 mol% appears to be the saturation limit for the photophysical and photochemical pathways of the **1g**-CB[8] system. In other words the efficiency in a light induced process for the host-guest system involving CB[8] and **1g** is unaffected beyond 70 mol% of CB[8]. The maximum quantum yield is likely due to dynamic exchange from complexation to solution. The quantum yield was performed at a concentration of 50 μ M for **1g** with an increasing amount of CB[8] (Table 4.1).

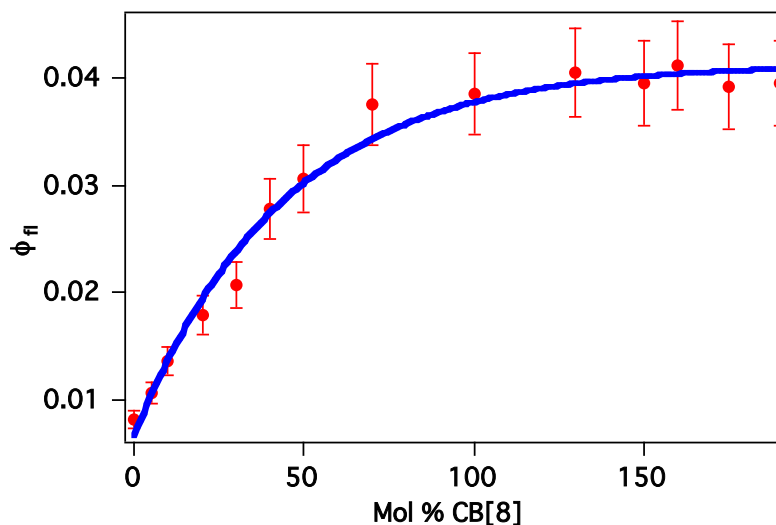


Figure 4.4 Quantum yield of fluorescence of 6-methylcoumarin **1g** ([50 μM]) with increasing concentration of CB[8] in water

Table 4.1 The quantum yield of fluorescence and emission maximum in various mol% CB[8] in water

Entry	CB[8] Mol%	$\lambda_{\text{max}}^{\text{a}}$	$\Phi_{\text{em}}^{\text{b}}$
1	0	411	0.008
2	5	430	0.010
3	10	432	0.013
4	20	436	0.018
5	30	441	0.020
6	40	442	0.027
7	50	443	0.030
8	70	443	0.037
9	100	443	0.038
10	130	443	0.040
11	150	443	0.040
12	160	443	0.041
13	170	443	0.039
14	190	443	0.039

^aSteady-state emission of **1g** was recorded with $\lambda_{\text{ex}} = 320$ or 340 nm. The concentration of **1g** was maintained at $50 \mu\text{M}$. ^bOptical density (absorbance) of **1g** is ~ 0.11 at $\lambda_{\text{ex}} = 345$ nm for determining the quantum yield. Quinine sulfate in $0.5 \text{ mol/L H}_2\text{SO}_4$ ($\Phi_{\text{fl}} = 0.55$) was used as the standard. Reported Φ_{em} are an average of a minimum of three runs with an error $< 5\%$.

Since there is a significant signal change when **1g** is complexed with CB[8], we can expect to observe a binding isotherm (Figure 4.5). Typical binding curves via fluorescence require one component

in large excess over the other. Due to solubility restrictions CB[8] was kept constant at a concentration of 1 μM and **1g** was screened from 3.33 – 50 μM (Table 4.2). The fluorescence (F) signal at 440 nm from the solution with CB[8] was subtracted from a control fluorescence (F_0) signal. The change in signal was plotted on the y-axis vs. the concentration of 6-methylcoumarin **1g** on the x-axis and non-linear regression analysis was used to fit the data to a two-site binding isotherm using Origin Pro 8.0. The equation is listed below (equation 4.2) was developed to address cooperative two-site binding models⁷ where $\Delta F_{\text{obs}} = F - F_0$, K_1 and K_2 are the binding constants for 1:1 and 1:2 host-guest complexes respectively. ΔF_{11} and ΔF_{22} are the relative changes in signal due to the binding of 1:1 and 1:2 host-guest complex respectively and the value C is the concentration of **1g**.

The binding values mirror the observations from the sigmoidal plots that were discussed in chapter 3. The equation used to fit the binding isotherm was a sequential binding equation that can differentiate the relative contributions from the 1:1 and 1:2 HG complexes (Equation 4.2).⁷ The 1:1 host-guest complex has a binding constant that is $1.33 \times 10^4 \text{ M}^{-1}$ (K_1) and the second binding constant is $2.00 \times 10^6 \text{ M}^{-1}$ (K_2). These binding constants are fairly large in comparison with typical organic host-guest complexes.⁸ The initial region of the binding isotherm shows sigmoidal behavior that demonstrates a cooperative behavior for the binding of two coumarin molecules. After the first coumarin enters the CB[8] cavity followed by some reorganization to accommodate a second coumarin molecule to enter the cavity. This phenomenon is essential for the photoreaction to be catalytic as the reaction can only occur if the second molecule enters the cavity. Since the second binding is higher than the first is we can also assume the 1:2 HG complex is more stable (thermodynamically) than the 1:1 HG complex.

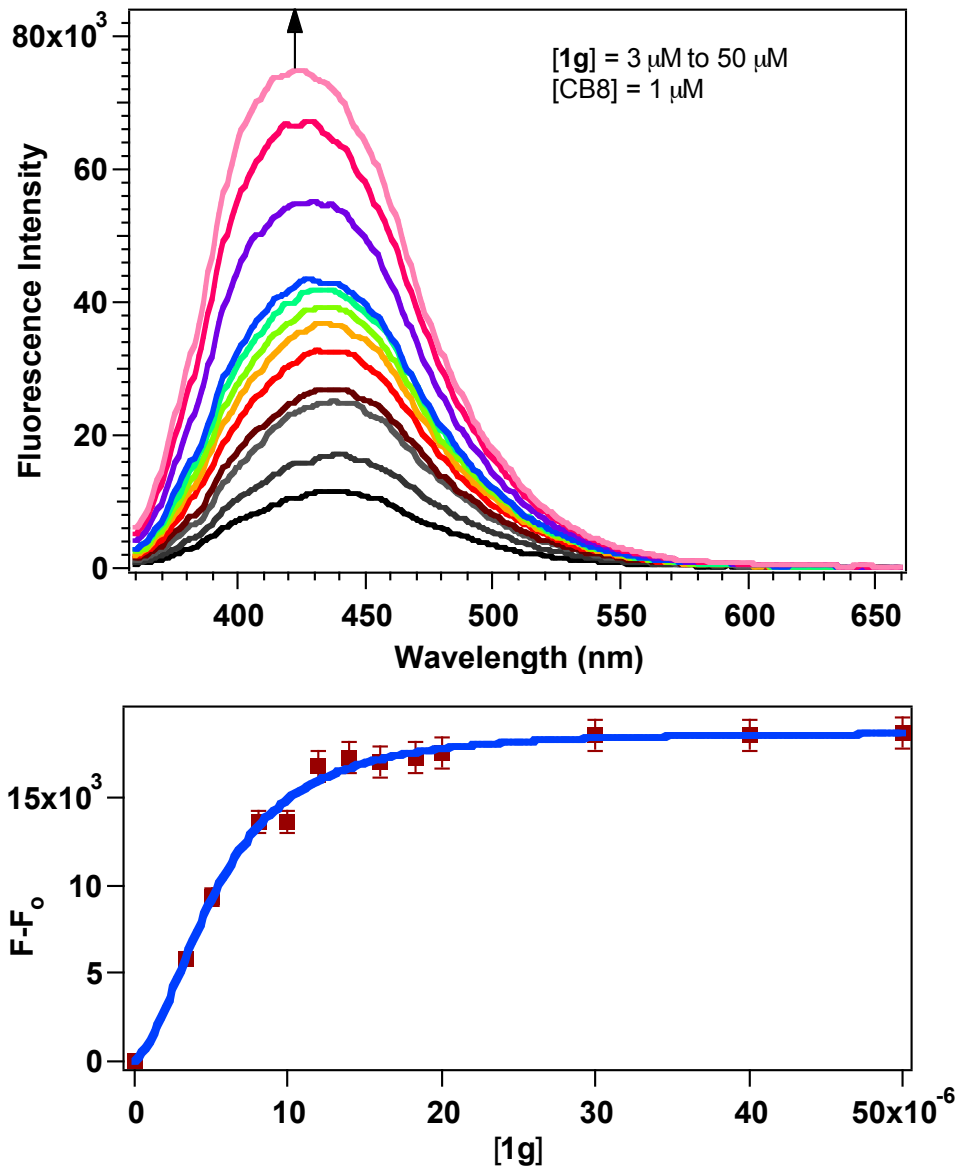


Figure 4.5 Top: the fluorescence curve of 1 μM CB[8] and increasing concentration of **1g**. Bottom: Integrated fluorescence signals for binding isotherm and fitted using a non-linear fit ($R^2 = 0.9900$) of $F-F_0$ of fluorescence data at 440 nm versus total concentration of **1g**

$$\Delta F_{obs} = \frac{(\Delta F_{11} \cdot K_1 \cdot C) + (\Delta F_{12} \cdot K_1 \times K_2 \cdot C^2)}{1 + (K_1 \cdot C) + (K_1 \cdot K_2 \cdot C^2)} \quad (4.2)$$

Table 4.2 The binding constant analysis and fluorescence signals of CB[8]-6-Methylcoumarin host-guest complexes

Entry	[6-Methylcoumarin]	[CB[8]]	F-F ₀
1	0	1.00 x 10 ⁻⁰⁶	0
2	3.33 x 10 ⁻⁶	1.00 x 10 ⁻⁰⁶	5.8200 x 10 ³
3	5.00 x 10 ⁻⁶	1.00 x 10 ⁻⁰⁶	9.4100 x 10 ³
4	8.00 x 10 ⁻⁶	1.00 x 10 ⁻⁰⁶	1.3640 x 10 ⁴
5	1.00 x 10 ⁻⁰⁵	1.00 x 10 ⁻⁰⁶	1.3680 x 10 ⁴
6	1.20 x 10 ⁻⁰⁵	1.00 x 10 ⁻⁰⁶	1.6760 x 10 ⁴
7	1.40 x 10 ⁻⁰⁵	1.00 x 10 ⁻⁰⁶	1.7360 x 10 ⁴
8	1.60 x 10 ⁻⁰⁵	1.00 x 10 ⁻⁰⁶	1.7070 x 10 ⁴
9	1.83 x 10 ⁻⁰⁵	1.00 x 10 ⁻⁰⁶	1.7350 x 10 ⁴
10	2.00 x 10 ⁻⁰⁵	1.00 x 10 ⁻⁰⁶	1.7620 x 10 ⁴
11	3.00 x 10 ⁻⁰⁵	1.00 x 10 ⁻⁰⁶	1.8610 x 10 ⁴
12	4.00 x 10 ⁻⁰⁵	1.00 x 10 ⁻⁰⁶	1.8520 x 10 ⁴
13	5.00 x 10 ⁻⁰⁵	1.00 x 10 ⁻⁰⁶	1.8660 x 10 ⁴
K ₁ = 1.33 x 10 ⁴ M ⁻¹ ^a			
K ₂ = 2.00 x 10 ⁶ M ⁻¹ ^a			
ΔF ₁₁ = 5.54 x 10 ⁴			
ΔF ₂₂ = 1.86 x 10 ⁴			
R ² = 0.99002			

^a Reported binding constants carry at 10% error

To determine the lifetime of the fluorescence, we performed time correlated single photon counting experiments (TCSPC) at room temperature. The lifetime kinetics were measured using a 340 nm nano-LED light source and with emission intensity monitored at 411 nm for **1g** in water and 443 nm for solutions with various CB[8] concentrations. The slit width was maintained at 5.0 nm for the detector. The lamp profile was obtained by monitoring the emission at 340 nm and using a solution of colloidal silica (Ludox® TM-40 from Sigma-Aldrich) solution causing light scatter. This light scatter was taken into account for the decay fit using proprietary DAS6® V6.4 software. Not only does the fluorescence quantum yield increase due to complexation, the fluorescence lifetime was also found to increase significantly.

The lifetime of **1g** in water was less than 0.1 ns (Figure 4.6). This is a very short lifetime that is most likely the result of the low fluorescence quantum yield and high internal conversion and ISC rates. As the concentration of CB[8] increases, an increase in the lifetimes was observed. The minor component slowly increases from 0.1 to 0.8 ns as the concentration of CB[8] is increased (Table 4.4). The minor component in water is the free **1g** coumarin lifetime, but when complexed with CB[8] it is likely that the

0.8 ns lifetime measured is actually the 1:2 host-guest complex. This lifetime for the 1:2 HG complex, while longer than what is observed in free solution of **1g**, is indicative of a fast quenching.

The major component lasts 3.7-3.8 ns and appears upon encapsulation with CB[8] (Figure 4.6). The relative ratios between the minor and the major component are deconvoluted as a function of fitting the curves to a tri or bi-exponential kinetic decay. Based on a sequential binding model (*cf* chapter 5) this long lived species is likely a 1:1 HG complex (Table 4.3).

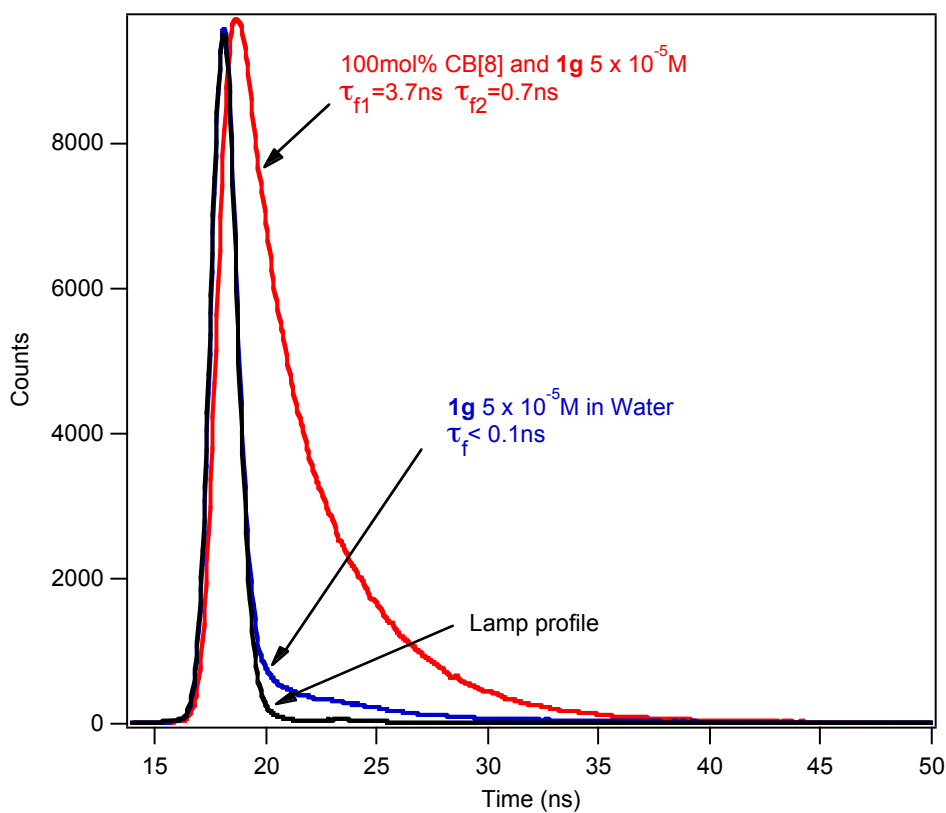


Figure 4.6 Fluorescence lifetime decays at 298 K for the lamp profile in black ($\lambda_{\text{ex}} = 340$ nm, $\lambda_{\text{em}} = 340$ nm) **1g** in blue ($\lambda_{\text{ex}} = 340$ nm, $\lambda_{\text{em}} = 411$ nm) and **1g**@CB[8] in red ($\lambda_{\text{ex}} = 340$ nm, $\lambda_{\text{em}} = 443$ nm)

Table 4.3 Fluorescence lifetimes of **1g@CB[8]** complexes

Entry	CB[8] mol%	τ (ns)
1 ^a	0	< 0.1
2	5	0.1 (41%); 3.7 (59%)
3	10	0.2 (41%); 3.7 (59%)
4	20	0.2 (41%); 3.7 (59%)
5	30	1.1 (41%); 3.7 (59%)
6	40	0.5 (41%); 3.7 (59%)
7	50	0.7 (15%); 3.7 (59%)
8	70	0.8 (14%); 3.7 (59%)
9	100	0.7 (14%); 3.7 (59%)
10	130	0.7 (14%); 3.7 (59%)
11	150	0.8 (15%); 3.7 (59%)
12	160	-
13	170	0.7 (15%); 3.7 (59%)
14	190	0.8 (15%); 3.7 (59%)

^aThe lifetime was monitored at the 411 nm emission wavelength, other lifetimes were monitored at 441 nm emission wavelength.

4.2.3. Phosphorescence studies of 6-Methylcoumarin in the presence of CB[8]

The reported mechanism for [2+2]-photocyclization of **1g** in solution involves the excited molecule to intersystem cross into a triplet excited state and then dimerize with another molecule.⁵ In order to see if the coumarin molecule was still reaching the triplet excited state, when complexed with CB[8], the phosphorescence emission was measured at 77 K (Figure 4.7). The problem with obtaining a spectra at 77 K is that CB[8] is only soluble in water and the formation of clear glass (transparent ice glass) is extremely difficult. The cracked glass increases the amount of light scatter from sample and results become unreliable to quantify the intensity of the emission signal. However the emission spectra are still acceptable under these conditions as relative spectra for line-shape and approximate amplitudes. While not quantifiable, the presence of a phosphorescence signal is indicative of an emissive triplet state.

The phosphorescence spectra were recorded for **1g** in water as well as in the presence of 30, 100 and 190 mol% CB[8]. The triplet energy of **1g** in water has an onset at 465 nm (62.7 kcal/mol) with a peak energy at 471 nm (60.7 kcal/mol). These results are mirrored in the presence of 30 mol% CB[8]. When stoichiometric and excess amounts of CB[8] are added there is a slight blue shift to 450 nm (63.5 kcal/mol) and 465 nm (62.7 kcal/mol) for the onset and the first peak, respectively. The observations of a triplet state at 77 K does not mean that the reaction still reacts from the triplet state as the photoreaction

was carried out at room temperature. To ascertain a reactive triplet species, Triplet-Triplet absorbance (TTA) studies were carried out in the presence of CB[8].

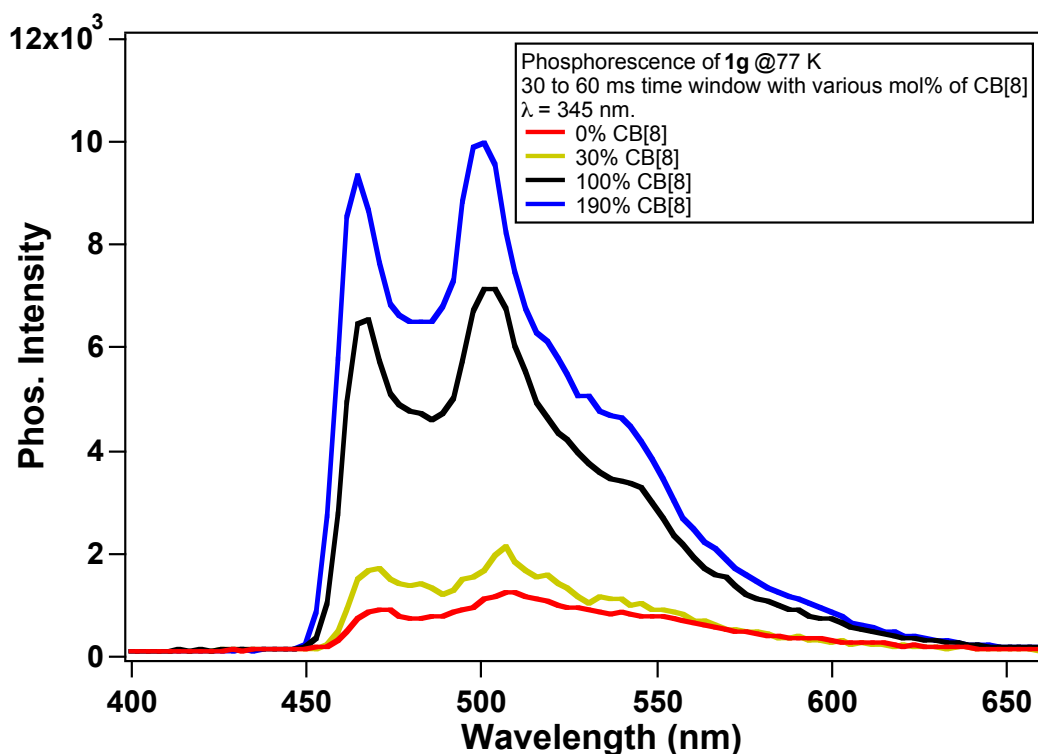


Figure 4.7 The phosphorescence emission profile at 77 K of **1g** in water and various CB[8] complexes.

$\lambda_{\text{ex}} = 345$ nm, $\lambda_{\text{em}} = 365$ - 670 nm, increments = 3 nm, 100 ms window, integration from 30 – 60 ms

4.2.4. Laser flash photolysis studies/ triplet-triplet absorbance studies

Since the phosphorescence emissions are not conclusive for determining whether the reaction occurs from the singlet or triplet state due to the low temperature and lack of triplet state quenching at 77 K. We carried out TTA measurements at room temperature. Wolff and co-workers have previously reported the TTA spectra for **1g** in water using laser flash photolysis, the experiment was repeated and it yielded the exact same spectra as shown in Figure 4.8.⁵

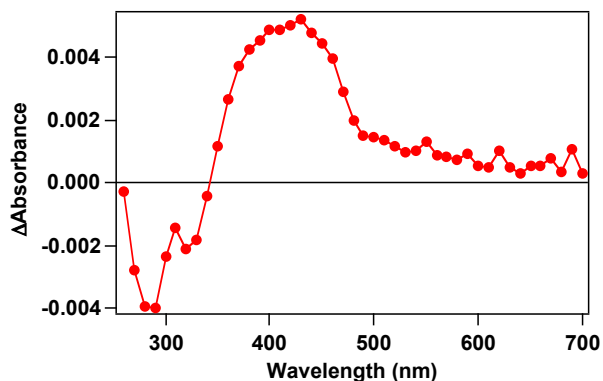


Figure 4.8 Triplet-triplet absorbance spectra of 6-methylcoumarin **1g** in deoxygenated water

The TTA kinetics were measured for **1g** in the presence of CB[8] at various concentrations. When the transient lifetime of **1g** at 50 μM concentration was performed in the absence of CB[8], a monoexponential decay of 4.6 μs was observed (Figure 4.9). When complexed with CB[8] two lifetimes were observed and were fitted to a bi-exponential decay the long lifetime component varied between from 4.6 μs to 12 μs . Beyond 100 mol% CB[8], the long component disappeared completely. However the short component with a lifetime of 0.75 μs was observed in every decay profile that contains CB[8] (Table 4.4) and increased in amplitude (increase in pre-exponential factor) as the concentration of CB[8] was increased.

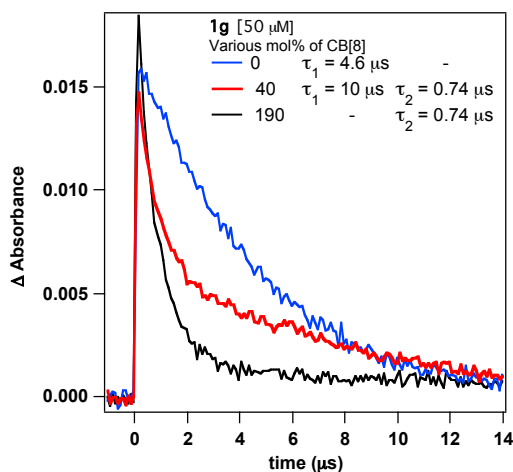


Figure 4.9 The transient lifetime decays for **1g** = 50 μM with various mol% CB[8]. The blue line represents decay kinetics of **1g** in water, red and black lines represent decay kinetics of **1g** with 40 mol% and 190 mol% CB[8] respectively

Table 4.4 Triplet lifetimes (τ) and pre-exponential factors (A) of transient absorption decays of $^3(\mathbf{1g})^*$ at 420 nm with various mol% CB[8]^a

Entry	mol% CB[8]	τ_1 (μs)	A_1	τ_2 (μs)	A_2
1	0	4.6	25	-	-
2	5	4.6	17	0.75	0.7
3	10	5.4	14	0.75	2.6
4	20	6.4	13	0.79	5.3
5	30	7.9	11	0.80	9.5
6	40	10	7.5	0.74	11
7	50	13	6.6	0.79	14
8	70	12	2.5	0.75	20
9	100	-	-	0.74	36
10	130	-	-	0.74	34
11	160	-	-	0.75	36
12	190	-	-	0.75	37

^a Laser pulse (308 nm, pulse width 15 ns). The decays were fitted to the equation:

$$\Delta\text{Absorbance}(t) = A_1\exp(-t/\tau_1) + A_2\exp(-t/\tau_2)$$

The long-lived component (τ_1) was assigned to uncomplexed $^3(\mathbf{1g})^*$ in aqueous solution (triplet excited $\mathbf{1g}$ outside the CB[8] cavity). The varying lifetime of $^3(\mathbf{1g})^*$ in solution is expected due to efficient self-quenching with a rate constant of $4.1 \times 10^9 \text{ M}^{-1} \text{ s}^{-1}$ (Figure 4.10). With increasing concentrations of CB[8], the fraction of uncomplexed $\mathbf{1g}$ in aqueous solution decreases. Consequently, the self-quenching decreases causing an increase in τ_1 . The decrease in the fraction of uncomplexed $\mathbf{1g}$ in aqueous solution with increasing CB[8] concentrations is also reflected in the decrease in Table 4.4. We believe that the 1:2 CB[8]- $^3(\mathbf{1g}-\mathbf{1g}^*)$ HG complex has a very short lifetime and is not detected under our experimental conditions due to fast photochemical or thermal/photophysical deactivation (proximity effect). Further, the shorter lifetime of 0.74 μs that corresponds to 1:1 CB[8]- $^3(\mathbf{1g})^*$ HG complex is quenched by molecular oxygen as evidenced by the rate constant $2.0 \times 10^8 \text{ M}^{-1} \text{ s}^{-1}$ (Figure 4.11). On the other hand, uncomplexed $^3(\mathbf{1g})^*$ in aqueous solution is quenched by molecular oxygen with a high bimolecular rate constant of $2 \times 10^9 \text{ M}^{-1} \text{ s}^{-1}$. Quenching data reveals that coumarin triplets, upon encapsulation by the CB[8] cavity, are protected from quenching by oxygen by an order in magnitude.

The photoreactions of $\mathbf{1g}$ in the presence of 50 mol% CB[8] under various atmospheres resulted in roughly the same photoproduct conversion and selectivity (chapter 3). However, there was a reasonable difference for the [2+2] dimerization of $\mathbf{1g}$ in water under various atmospheres. The reaction

in N₂ was approximately twice as fast as the reaction in Air or O₂. To better understand why the reaction under oxygen enriched atmospheres was not affected by the CB[8] we performed a laser flash photolysis oxygen quenching study.

The partial oxygen atmospheres were employed using N₂ (0%), air (20%) and O₂ (100%). The remaining partial oxygen concentrations were made by creating a 50:50 mixture using parallel flow-meters. The combinations of N₂, Air, and O₂ used to obtain the intermediate concentrations are as follows, N₂: Air (10%), N₂:O₂ (50%) and air:O₂ (60%). The oxygen quenching of **1g** (50 μM) in water under atmospheres with various oxygen concentrations (0, 10%, 20%, 50%, 60% 100%) resulted in the triplet state of **1g** quenching at a rate constant near the diffusion limit. When the study monitored a 1:1 ratio of CB[8] (190 mol%). Quenching by oxygen was lowered by an order of magnitude. This implies that the triplet exciting state of **1g**@CB[8] complex to be shielded by the host cavity (Figure 4.11).

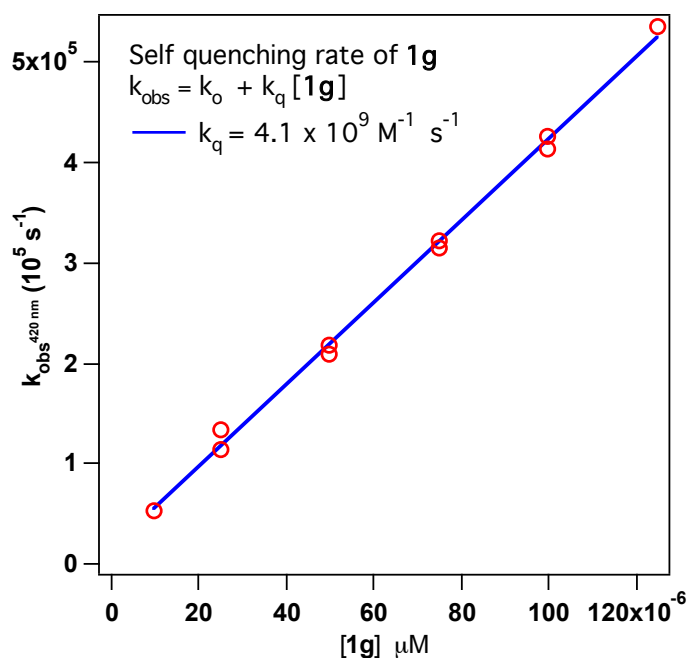


Figure 4.10 The first order decay rate constants of triplet-triplet absorption by laser flash photolysis excitation (308 nm) in deoxygenated aqueous solution of various **1g** monitored at 420 nm. The slope provides the bimolecular self-quenching rate constant of ³(**1g**)* by **1g**

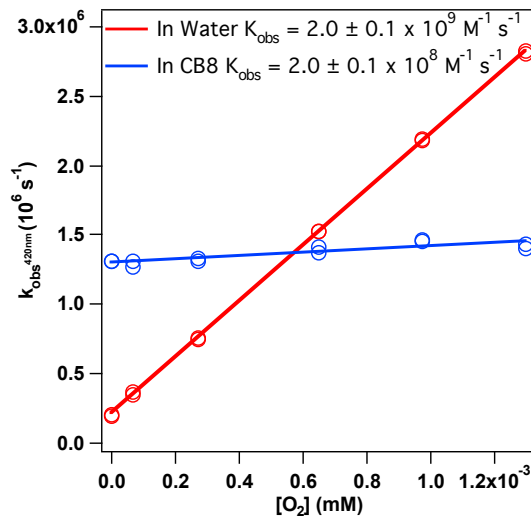


Figure 4.11 The first order decay rate constants of the triplet-triplet absorption generated by pulsed laser excitation (308 nm) and monitoring at 420 nm of aqueous solution of **1g** in the absence (red) and presence (blue) of CB[8] under various O₂ concentrations

4.2.5. Actinometry

The fluorescence quantum yield only revealed information about the lifetimes of the 1:1 HG complex and 1:2 HG complex, not about how the reaction occurs. Measuring the quantum yield of the photoreaction (actinometry) provided better insights into how the photoreaction proceeded compared to simple kinetic experiments that gave the rate constant of photodimerization. This is the most important indicator for how efficient the catalytic system is. Using a known actinometry solution (ferrioxalate solution) we can compare the moles of product formed to the moles of photons absorbed (Equation 4.3).

$$\Phi = \frac{\text{Moles of product formed}}{\text{Moles of photons absorbed}} \quad (4.3)$$

Ferrioxalate actinometry solution was prepared by following the Hammond variation of the Hatchard and Parker procedure outlined in *Handbook of Photochemistry*.^{9,10} The ferrioxalate actinometry solution measures the decomposition of ferric ions (Fe³⁺) to ferrous ion (Fe²⁺) through a reduction reaction that converts oxalate to CO₂ gas. The ferrous ions readily complex with three molecules of 1,10-phenanthroline that was observed by UV-vis absorbance at 510 nm (Figure 4.12). The iron-phenanthroline

complex absorbance at 510 nm has a molar extinction coefficient of $1.11 \times 10^4 \text{ mol}^{-1} \text{ cm}^{-1}$ and thus can be formed at μM concentrations and still provide reasonable absorbance signal.¹¹

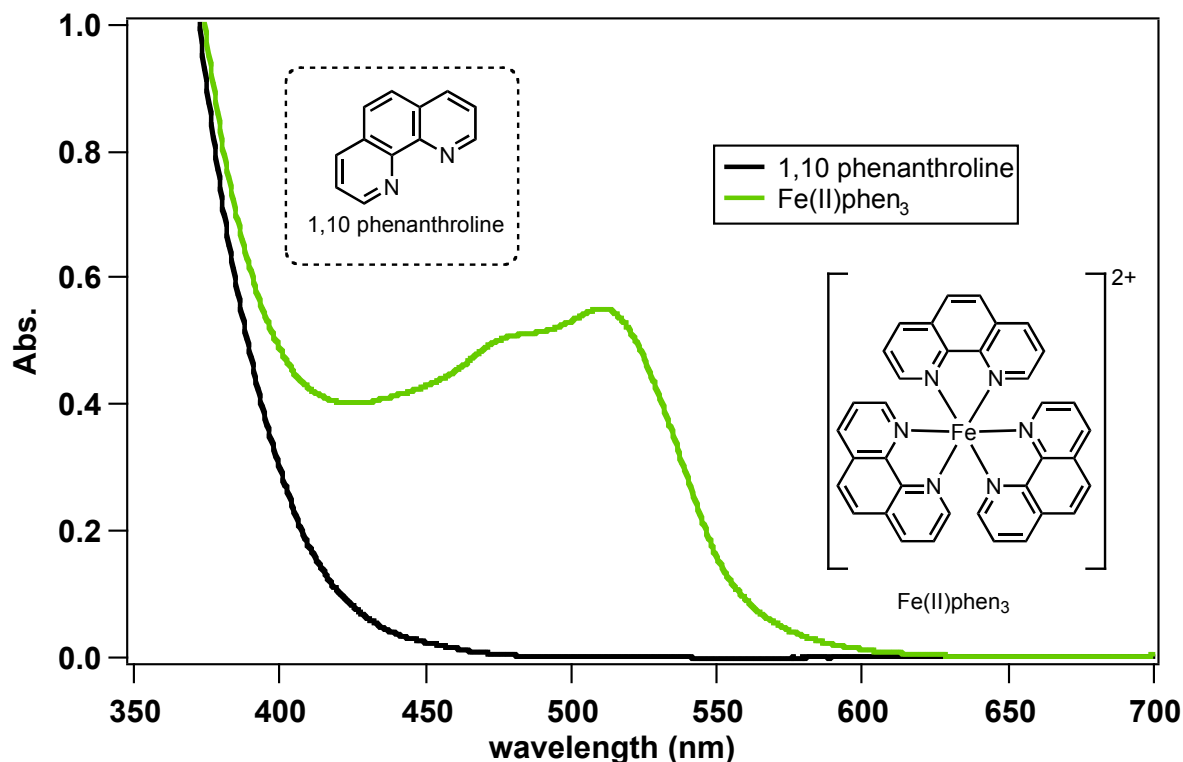


Figure 4.12 The UV-vis absorbance spectra of iron-phenanthroline complex (green) and phenanthroline (black)

By irradiating the sample and the actinometry solution next to each other (to minimize error due to differential light exposure) we can then proceed to monitor the reaction by comparing the moles of iron-phenanthroline complex to the photodimer product formed during the irradiation conditions. The quantum yield of the reaction for the ferrioxalate is known at various monochromatic wavelengths, hence a band pass filter was employed for irradiations. The bandpass filter used was an Ashi-Spectra ZBPA310 310 nm bandpass filter with a 60% transmittance at 313 nm with a ± 5 nm at full width half maximum (FWHM). The quantum yield for the ferrioxalate photoreaction is $\Phi_{\text{Fe}^{2+}} = 1.09$ at 313 nm.¹⁰

The precursor solutions needed for the preparation of the ferrioxalate actinometry solution include the following: a stock solution of 10 g ferric sulfate and 5.5 mL concentrated H_2SO_4 to a 100 mL

volumetric flask. The exact concentration was determined to be 0.2 M Fe^{3+} using two independent methods. The first method was the standardization of iron(III) using an EDTA titration of with eriochrome black T as the indicator.¹² The second method involved reduction of Fe^{3+} to Fe^{2+} using hydroxylamine hydrochloride and complexing the newly formed Fe^{2+} to 1,10 phenanthroline and making a standard curve.^{11,13} The results matched the original assay of 76% $\text{Fe}_2(\text{SO}_4)_3$ (399.88 g/mol) plus 24% water on the bottle. The potassium oxalate solution prepared was made in 6 times excess (1.2 M).

Other solutions that needed to be prepared included 100 mL of a 0.2% w/v 1,10 phenanthroline in water. This was used for both the actinometry as well as the standardization. A buffer solution of 8.2 g sodium acetate trihydrate and 1.0 mL of H_2SO_4 in a 100 mL volumetric flask filled in water was used. A 0.1 M EDTA solution was also prepared and used for the standardization. The preparation of the actinometry solution involves pipetting 5 mL of $\text{Fe}_2(\text{SO}_4)_3$ and 5 mL of $\text{K}_2\text{C}_2\text{O}_4$ solutions into 100 mL volumetric flask and filling to the mark with water. The stock solutions and actinometer solutions were stored in the dark.

The procedure for actinometry measurements were completed as follows. Approximately 3 mL of the actinometer solution was added to a quartz cuvette. The cuvette was placed in a sample holder with the 310 nm bandpass filter covering the light entrance. The sample and actinometry solutions were irradiated for specified time intervals (0, 5, 10, 15, 20, 25, 30 min).

After irradiation 1 mL of the actinometer solution was removed and transferred to a 10 mL volumetric flask. Then 0.5 mL of 1,10 phenanthroline solution and 2 mL of buffer solution were added and filled to the mark with water. The solutions were left to stand for one hour. The UV-Vis spectra of the reaction and actinometry solution samples were recorded for each time interval. The absorbance of the actinometry solution was monitored at 510 nm (Figure 4.13) The moles of Fe^{2+} formed for each sample were determined using Beer's Law: $c = A/\epsilon b$, where A = absorbance at 510 nm, b = path length (1 cm) and $\epsilon = 1.11 \times 10^4 \text{ mol}^{-1} \text{ cm}^{-1}$.

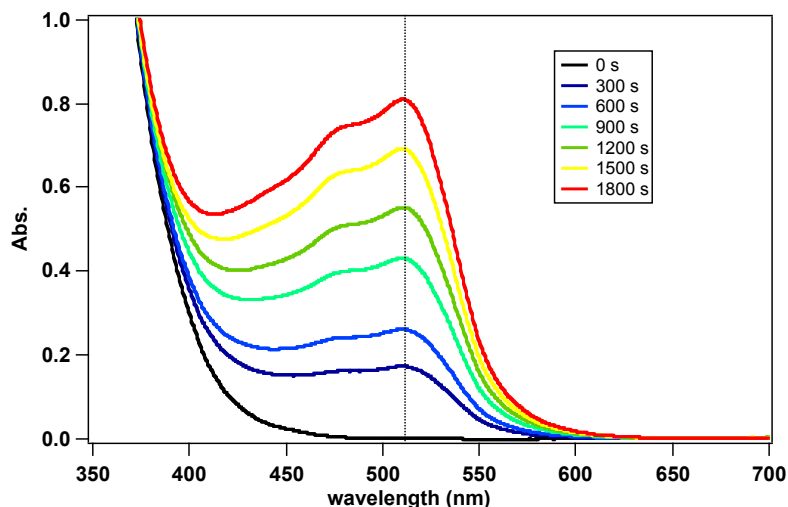


Figure 4.13 UV-Vis spectra recorded following the irradiation of the actinometer solution. Each run is an average of at least 3 runs

Converting the spectra into moles of Fe^{2+} formed (N) as a function of time (t) as shown in Figure 4.14 results in a slope that is the photon flux (F). The photon flux is defined as the number of photons sec^{-1} unit area $^{-1}$ or Einstein s^{-1} . Since the quantum yield of the actinometry solution is $\Phi_{\text{Fe}^{2+}} = 1.09$ at 313 nm. The flux ($F = N/\Phi_{\text{Fe}^{2+}} \cdot t$) was determined to be 3.66×10^{-10} Einstein s^{-1} .

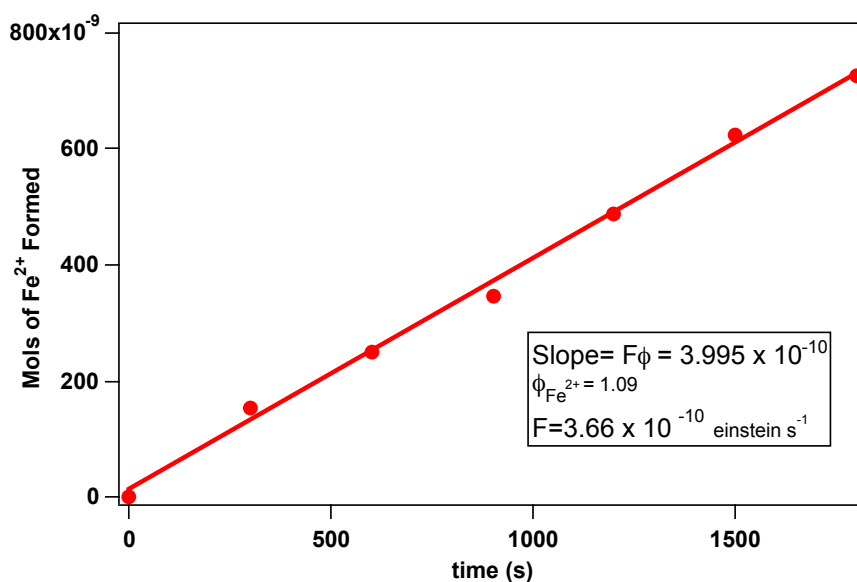


Figure 4.14 The plot of moles of Fe^{2+} formed over time determined from the absorbance plot in Figure 4.13

The moles of product formed for the [2+2] photocyclization of **1g** in the presence of CB[8] was done by irradiating the solution side-by-side with the actinometer solution as described above. The moles of product formed were determined by the disappearance of the reactant absorbance using UV-Vis spectroscopy. As the reaction (shown before chapter 2,) has a clear isobestic point, indicating a clean reaction of starting material to product, the moles of product formed could be computed by the decrease of the reacted starting material. The number of moles of product per unit time is related to the number of photons absorbed as shown in Figure 4.14. The slope gives the quantum yield of the photoreaction (Figure 4.15).

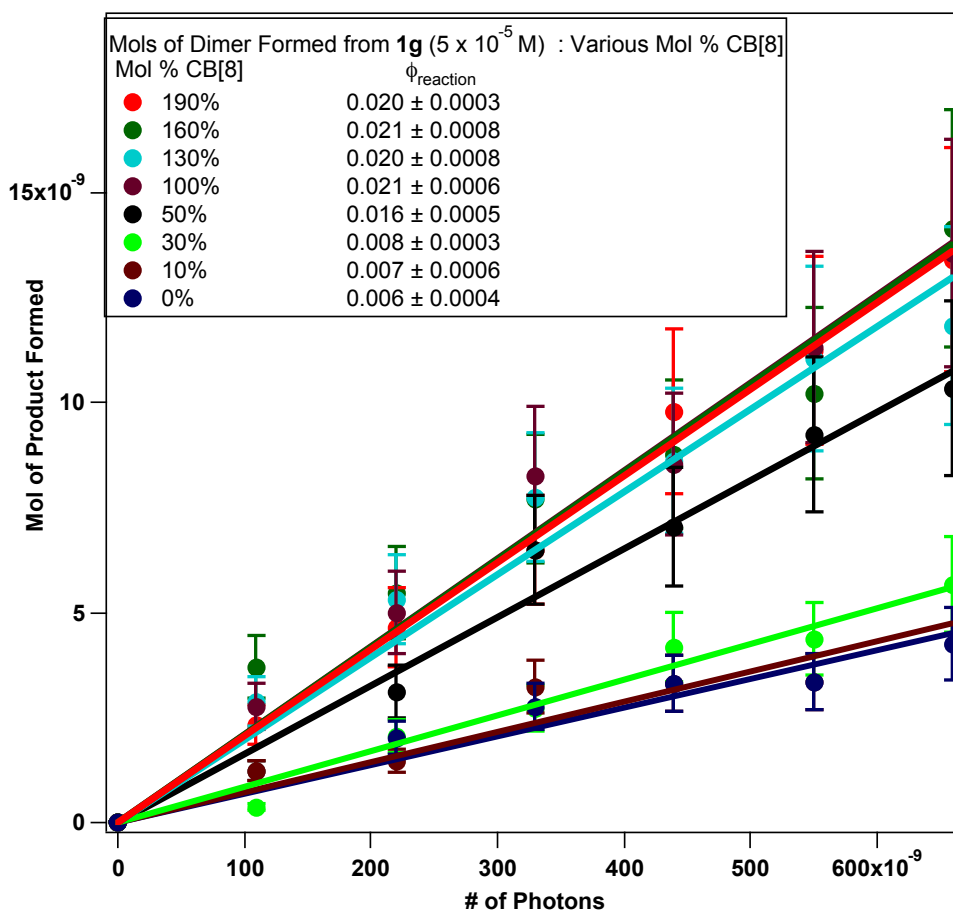


Figure 4.15 The number of moles of photoproduct formed compared to the number of photons absorbed. The number of photons absorbed is related to the flux in Figure 4.14

Previously the rate of dimerization was highest when 160 mol% CB[8] was added to the solution of **1g** (50 μM). After the results of the actinometry were compiled we observed that the quantum yield of

the reaction levels were near the stoichiometric 70 mol% of CB[8]:**1g** (Figure 4.16). The interpretation is that the reaction is as efficient to the same extent beyond 70 mol% of CB[8]. The quantum yield of the reaction increases from 0.006 for 50 μM **1g** in water to 0.021 with 100 mol% CB[8]. The photoreaction efficiency (Figure 4.16) is constant after 70 mol% CB[8] and the result mirrors the fluorescence lifetime which reaches the maximum at the same mol% of CB[8] (Table 4.3).

Table 4.5 The quantum yield of photodimerization of **1g** with various mol% of CB[8] in water

Entry	Mol% CB[8]	$\Phi_{\text{dim}}^{\text{a}}$
1	0	0.006 \pm 0.001
2	10	0.007 \pm 0.001
3	30	0.008 \pm 0.001
4	50	0.016 \pm 0.001
5	100	0.021 \pm 0.001
6	130	0.020 \pm 0.001
7	160	0.021 \pm 0.001
8	190	0.020 \pm 0.001

^aPhotodimerization quantum yields were measured using ferrioxalate actinometry. Irradiations were performed with a 450 W medium pressure Hg lamp using a 313 ± 5 nm band pass filter. Reported values are an average of a minimum of 10 runs with an error <10%. The number of moles of the photodimer formed was computed from the decrease in the absorbance of **1g**, as there was a clear isobestic point indicating a one-to-one conversion from **1g** to photodimer.

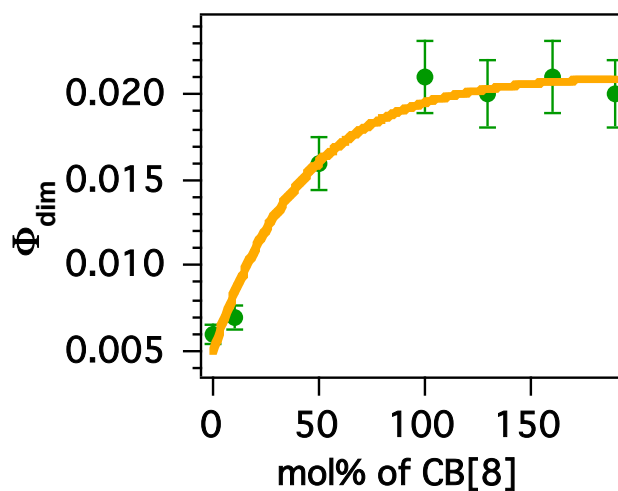
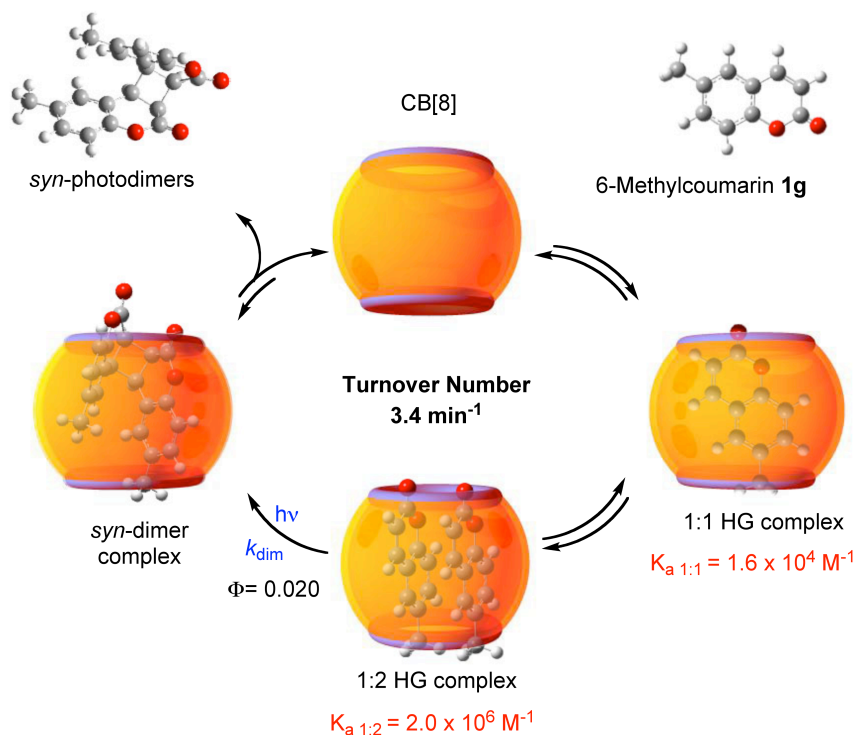


Figure 4.16 The quantum yield of dimerization plot vs. various mol% of CB[8] in water

4.3. Conclusions

The photophysical studies offered insights into the mechanism of the photodimerization reaction within CB[8] in water. When complexed with CB[8] the fluorescence Φ_{em} of **1g** increases from 0.008 to 0.041. We see an increase in the fluorescence lifetime from <0.1 ns to 3.7 ns for a 1:1 host-guest complex and a fluorescence lifetime of 0.7 ns for a 1:2 host-guest complex. There was also a significant increase in the Φ_{dim} from 0.006 to 0.02. The binding constant study corroborated the results from the saturation kinetic study in chapter 3. With the evidence of a two-site binding where the second guest binds more tightly than the first guest we started to develop a refined model for the catalytic cycle that was hypothesized at the end of chapter 3.

The catalytic cycle (Scheme 4.2) starts with an empty CB[8] cavity and a **1g** guest binds to the inside with an affinity of $1.33 \times 10^4 \text{ M}^{-1}$. The CB[8] cavity reorganizes to make room for the second **1g** guest with an even higher binding affinity of $2.00 \times 10^6 \text{ M}^{-1}$. The complex absorbs a photon of light where it reacts with an efficiency of quantum yield of dimerization $\Phi_{dim} = 0.020$. The photoproduct releases itself from the cavity and the catalytic cycle starts over again with a maximum turnover number of 3.4 min^{-1} .



Scheme 4.2 Catalytic cycle for the [2+2] photodimerization of **1g** in the presence of CB[8] in water

Phosphorescence, triplet-triplet absorbance (TTA) measurements, and quenching studies show that the reaction proceeded from the proposed triplet excited state as originally postulated by Wolff and co-authors.^{4,5} The transient lifetime for 1:1 host-guest complex lasted only 0.75 μ s. There was an order of magnitude difference in the quenching of the **1g** triplet complex with CB[8] by O₂. The phosphorescence emission increases, but it was not possible to quantify it. When the triplet-triplet absorbance and lifetimes are observed, a short component at 0.75 μ s that corresponds to a 1:1 host-guest complex was observed. The fluorescence signal, fluorescence lifetime, TTA kinetics as well as the Φ_{dim} seem to saturate at 70mol% of CB[8]. The rates of fluorescence quantum yield, TTA, and photodimerization quantum yield all increased within CB[8] in water compared to isotropic media (neat water). This is likely due to the decrease in the non-radiative pathways **1g** upon complexation with CB[8].

4.4. General Methods

UV quality fluorimeter cells (with range until 190 nm) were purchased from Luzchem®. Absorbance measurements were performed using a Shimadzu® UV-2501PC UV-Vis spectrophotometer. For actinometry studies, a 313 \pm 5 nm band pass filter purchased from Aashi Spectra®, Japan was used. Emission spectra were recorded on a Horiba Scientific® Fluorolog 3 spectrometer (FL3-22) equipped with double-grating monochromators, dual lamp housing containing a 450-watt CW xenon lamp and a UV xenon flash lamp (FL-1040), Fluorohub / MCA / MCS electronics and R928 PMT detector. Emission and excitation spectra were corrected in all the cases for source intensity (lamp and grating) and emission spectral response (detector and grating) by standard instrument correction provided in the instrument software. Fluorescence lifetime measurements were performed using a 340 nm nano-LED as light source with a pulse repetition rate of 1 MHz. The instrument response function was collected using a scatter solution (Sigma-Aldrich®, Ludox TM-40 colloidal silica, 40% suspension in water). The goodness-of-fit was assessed by minimizing the reduced chi squared function and further judged by the symmetrical distribution of the residuals. For fluorescence quantum yields (Φ_{em}) optically dilute solutions (absorbance value \sim 0.11) were used with quinine sulfate (recrystallized from water 3 times) in 0.5 M H₂SO₄ (Φ_{fl} = 0.55) as the standard. Steady state emission spectra were processed by FluorEssence® software. Lifetime measurements were computed using DAS6® V6.4 software.

4.5. References

**The material in this chapter was co-authored by Barry C Pemberton (BCP), Elango Kumarasamy (EK), DK Srivastava (DKS), Stephen Jockush (SJ) Nick Turro (NT) and J. Sivaguru (JS). BCP had primary responsibility for preparing samples and collecting data for photophysical data, except laser flash photolysis, which was performed in NT lab at Columbia University by SJ. Actinometry was primarily performed by BCP with assistance by EK. BCP processed the data and with help of JS was the primary developer of the conclusions that are advanced here. Binding constant experiments were performed under the guidance of Prof. DK. Srivastava. BCP also drafted and revised all versions of this chapter. JS served as proofreader and checked the math in the statistical analysis conducted by BCP.

- (1) Kaidbey K.H; A.M., K. Contact photoallergy to 6-methylcoumarin in proprietary sunscreens *Arch Dermatol* **1978**, *114*, 1709-1710.
- (2) DeLeo, V. A. Photodermatology *Dermatitis* **1993**, *4*, 106-107.
- (3) Allen, S. K.; Todd, A.; Allen, J. M. Photochemical Formation of Singlet Molecular Oxygen (1O_2) in Illuminated 6-Methylcoumarin Solutions *Biochem. Biophys. Res. Commun.* **1997**, *235*, 615-618.
- (4) Yu, X.; Scheller, D.; Rademacher, O.; Wolff, T. Selectivity in the Photodimerization of 6-Alkylcoumarins *J. Org. Chem.* **2003**, *68*, 7386-7399.
- (5) Wolff, T.; Gerner, H. Photodimerization of coumarin revisited: Effects of solvent polarity on the triplet reactivity and product pattern *Phys. Chem. Chem. Phys.* **2004**, *6*, 368-376.
- (6) Turro, N. J.; Ramamurthy, V.; Scaiano, J. C. *Modern Molecular Photochemistry of Organic Molecules*; University Science Books: Sausalito, Ca, 2010.
- (7) Wang, Z. X.; Srivastava, D. K. A Graphical Method for Determining the Number of Essential Sites in Enzymes with Multiple Binding Sites for a Ligand *Anal. Biochem* **1994**, *216*, 15-26.
- (8) Connors, K. A. *Binding Constants*; John Wiley: New York, 1987.
- (9) Murov, S. L.; Carmichael, I.; Hug, G. L. *Handbook of Photochemistry*; Marcel Dekker: New York, 1973.

- (10) Hatchard, C. G.; Parker, C. A. A New Sensitive Chemical Actinometer. II. Potassium Ferrioxalate as a Standard Chemical Actinometer *Proc. of the Royal Soc of London. Series A* **1956**, 235, 518-536.
- (11) Fortune, W. B.; Mellon, M. G. Determination of Iron with o-Phenanthroline: A Spectrophotometric Study *Ind. Eng. Chem. Res.* **1938**, 10, 60-64.
- (12) Lucchesi, C. A.; Hirn, C. F. EDTA Titration of Total Iron in Iron(II) and Iron(III) Mixtures *Anal. Chem.* **1960**, 32.
- (13) Mehlig, J. P.; Hulett, H. R. Spectrophotometric Determination of Iron with o-Phenanthroline and with Nitro-o-Phenanthroline *Ind. Eng. Chem. Res.* **1942**, 14, 869-871.

CHAPTER 5. KINETICS AND MECHANISTIC INVESTIGATIONS OF HOST-GUEST COMPLEXES INVOLVING 6-METHYLCOUMARIN AND CUCURBIT[8]URIL**

5.1. Introduction to Analytical Techniques for Examining HG Complexes

The photophysical studies of the complex between CB[8] and **1g** yielded some promising thermodynamic information about the affinities related to step-wise binding between the host and guest. The overall binding was $1.33 \times 10^4 \text{ M}^{-1}$ for the 1:1 HG complex and $2.00 \times 10^6 \text{ M}^{-1}$ for the 1:2 HG complexes respectively (Figure 4.5). The catalytic reaction was determined to take place on a minute timescale with a turnover number (TON) of 3.4 min^{-1} (Figure 3.6). The quantum yield for the photoreaction was determined to be $\Phi=0.020$ (Figure 4.15). Regardless of the thermodynamic and kinetic aspect of the overall reaction, it is important to determine the kinetics for each step in the reaction to ascertain the fundamental features of the supramolecular photocatalytic cycle mediated by CB[8].

Before we detail the results from different analytical techniques a brief overview of the analytical techniques employed to obtain the data are detailed. Insight into the HG complexation and how they are formed enhances our understanding of the requirements for HG chemistry and to control and comprehend potential photoreactions within a supramolecular system. We have performed stopped flow kinetics measurements with fluorescence to ascertain real-time changes in solution. This works by simultaneously mixing two solutions of host (Cell A) and guest (Cell B) together in a cell resulting in a sudden perturbation of the system (Figure 5.1). The cell is then monitored via using either absorbance or fluorescence emission. The result is highly sensitive spectroscopic technique that can be employed on time scales from three milliseconds to twenty minutes. The shortcomings of stopped flow kinetics result from an inability to determine how the complex is formed beyond what can be determined from absorbance or fluorescence. We can observe how the interactions affect various spectroscopic techniques, it cannot tell us the orientation of the interactions.

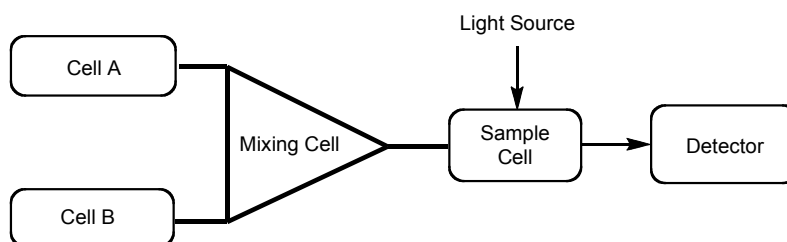


Figure 5.1 Cartoon representing fluorescence stopped flow technique to ascertain kinetic pathways

According to the Arrhenius equation, reaction rates typically double as the temperature increases by ten degrees Celsius.¹ Catalysts often demonstrate this phenomenon especially when the rate-determining step is the product release step (unimolecular reaction) and the individual microscopic steps are not coupled. Enzymes can show this behavior, when the rate (or velocity) of the reaction increases upon increasing the temperature. At sufficiently high enough temperatures these enzymes lose their hydrogen bonds and three-dimensional structures, thus destroying their enzymatic activity (Scheme 5.2). This results in an inverted bell curve (Figure 5.2).

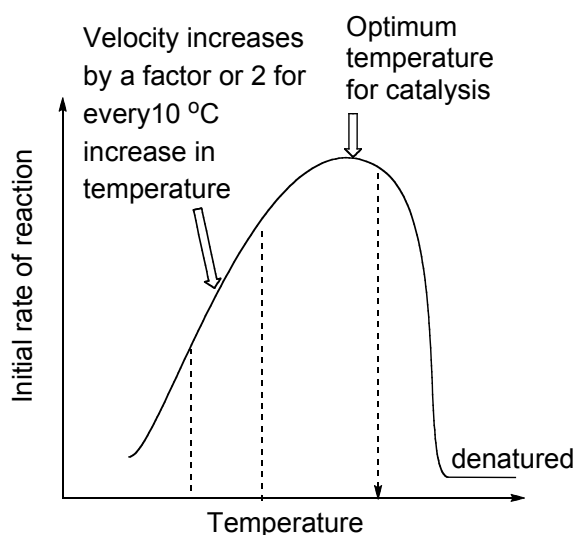


Figure 5.2 Arrhenius temperature relationship for unimolecular reactions

5.2. Eyring Plot Curves

Eyring plots can decipher if a reaction proceeds through an enthalpic or entropic transition state.² For typical enzyme catalyzed reactions with a change in the temperature, most reactions, catalyzed or not, will show a linear dependence from a graph of the natural log rate divided by temperature versus the inverse temperature (Figure 5.3) when using an Eyring plot.

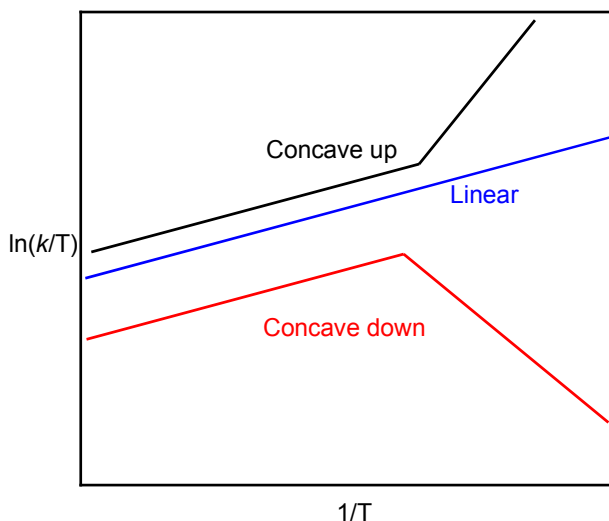


Figure 5.3 Representation of Eyring plots

If an Eyring plot is non-linear this describes a change in the activation energy barrier. There are two types of non-linear Eyring plots. If the line curves up it is called concave up, and if the Eyring plot line curves down and is called concave down (convex). A concave up Eyring plot can be interpreted as two different mechanisms that are responsible for the reaction progress at different temperature ranges. This means the mechanism for reaction fundamentally changes upon changing of temperature. A convex (concave down) Eyring plot can be interpreted as a change in the rate limiting step even though the mechanism is the same for a given reaction. Where the inflection points intersect, the contribution from each rate determining step is the same. When this happens, the most likely scenario occurs when the progression of the reaction switches from a dependency on enthalpic energies to entropic energies.³ Such observations are not uncommon in biology or chemistry.¹⁻⁴

The slope of an Eyring plot is $\Delta H^\ddagger/R$ where ΔH^\ddagger is the activation enthalpy and R is the gas constant. The values for ΔH^\ddagger are typically influenced by the bond-breaking and bond-making processes resulting in endothermic (or positive) values. Solvation effects can lower the enthalpic values. Values near zero are often the result of radical reactions. Where the line intercepts the y-axis is the term $\Delta S^\ddagger/R$ where ΔS^\ddagger is the entropy of activation. The contribution from ΔS^\ddagger is the result of energy lost or gained from translational, vibrational and rotational degrees of freedom as well as solvent effects (bound or unbound solvent molecules).

True HG complexes are typically observed using only a few techniques, including NMR spectroscopy. Studies performed via NMR spectroscopy provide information about how tightly complexes are formed and how fast they exchange relative to the NMR time scale based on their chemical shifts and line shapes.^{5 6} Chemical shifts provide an understanding of where complexes are located due to shielding parameters, since these rely shifts rely on unique chemical environments. Complexation via NMR can be categorized into slow, moderate and fast exchange, which are determined by the line shapes.

Homogenous signals result in peaks that are sharp and narrow, which are said to have a Lorentzian line shape.⁷ A Lorentzian line shape usually denotes a nuclear spin signal (proton, carbon, nitrogen, etc.) that will precess homogeneously. If the precession rate from the NMR signals are not homogenous, that is, they decay under different time regimes, the line shape will be less sharp and more Gaussian like (Figure 5.4).^{5,6} A Lorentzian line shape is caused by the precession of a proton within a stable chemical environment, whereas a Gaussian line shape typically denotes variance within a chemical environment. The broadening of a peak is often likely due to some change in a signal's environment, for example, exchange of a substrate (guest) from solution to inside a host or by inhomogeneity in the sample. HG systems have been thoroughly investigated via NMR, however they require high concentrations, which can make it difficult to study complexes with limited solubility.

Ion-trap mass spectrometry is a sensitive technique to detect HG complexes in the gas phase. The ions are generated via electrospray ionization prior to being selectively trapped inside a three-dimensional chamber with an oscillating electric field. These trapped ions are gathered and then probed by bombarding them with neutral helium atoms. The mass-counter can detect multiple ions at virtually the same time allowing for nearly real-time update of HG complexes.

The analytical techniques introduced in the first part of this chapter provide insights into how quickly HG complexes are formed, how fast the HH complex dissociates, where the guest resides within the host and as an approximation of how tightly they bind. They are useful tools to study any HG system. The results from the analytical techniques in this chapter provided will be the final pieces of the puzzle to determine how the catalytic cycle proceeds for the [2+2] photocdimerization of **1g** inside CB[8] cavity.

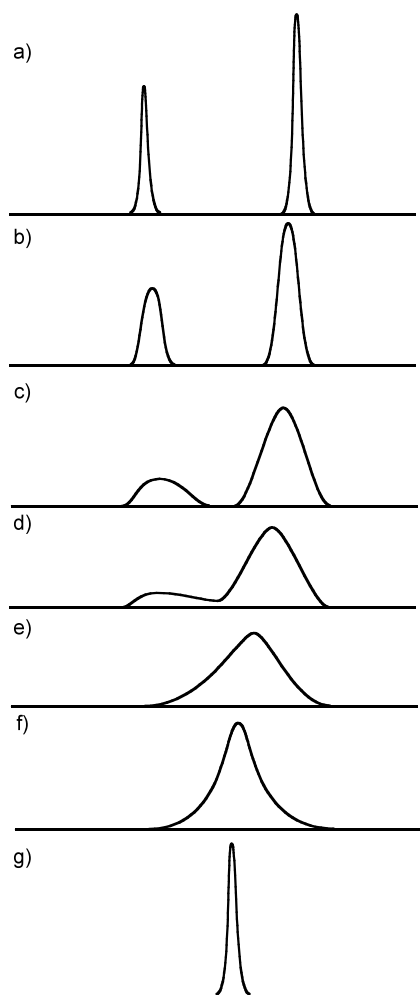


Figure 5.4 Line shape and relative chemical shift for a two-site exchange. The line shapes for “a” and “g” demonstrate a Lorentzian peak where the exchange rate is slower (a) than the measurement and the exchange rate is faster (g) than the measurement respectively. The line shapes for “b” through “f” demonstrate an exchange rate that is within the time scale of the measurement taken resulting peak broadening from inhomogeneity

5.3. Stopped Flow Reaction Kinetics Measurements

Experimental setup for stopped flow analysis was performed using a SX20 system from Applied Photophysics. The excitation source was an Hg-Xe lamp (L2382-Hamamatsu Photonics) and the slit bandwidth for the excitation monochromator was either 1 mm or 0.1 mm (1 mm = 4.65 nm for the 368 nm excitation wavelength). The emission was monitored using a <400 nm cutoff filter. The samples were

thermostated at 20.0 ± 0.1 °C for 15 min and then mixed at a 1:1 volumetric ratio from the two syringes. The injection pressure maintained for the duration of the acquisition for the short time component (0.5 sec). The long-time component (30 sec) had the pressure released during the acquisition to prevent leaking of the cell. The photomultiplier values were kept at or less than 462 mV for the samples. The deionized water used was from a Barnstead NANOpure system with a resistivity of ≥ 17.8 M Ω cm⁻¹. The formation of the 1:1 complex studies were performed with the monochromator slit width at both 1 mm and 0.1 mm. The slit widths for the dilution studies on the monochromator were 0.465 nm as established by the 1:1 experiments.

Stopped flow kinetics measure the change in a HG system when two solutions are mixed together. The observations from stopped flow kinetics provide insight into the k_{on} and/or k_{off} rates. These rates are determined by either driving the reaction towards the complex (k_{on}) by mixing the host solution and guest solution together. The opposite experiment (k_{off}) drives the reaction towards the unbound complex by mixing the HG complex with the solvent media (dilution studies). Typically these two reactions are performed under identical conditions such that they can yield the rates of the forward and backward complexation so that the rate complexes can be measured independently and cross-verified. Kinetically k_{on} is a bimolecular rate constant and k_{off} is a unimolecular rate constant for the process detailed in Equation 5.1.



The fluorescence signal in stopped flow is incredibly sensitive, and it is capable of picking up artifacts within the measurement. The artifacts most often picked up in stopped flow measurements are air-bubbles that are produced when the solutions are forced into the cell at high pressures. Under high pressure these air bubbles are fairly small, but after the pressure has been released they increase in volume and take up a large volume inside the cell. Not only do air bubbles change the refractive indices of the solvent in the cell, they also make the sample inhomogeneous which can create other artifacts in the resulting signal. One of the most common errors perpetuated in stopped flow kinetics is observation and misinterpretation of aggregation.

The conditions we used to perform the stopped flow kinetics for the 1:1 and 1:2 HG complexes were extremely concentrated (1 μM CB[8] and 500 μM **1g**). Initial stopped flow investigations used the conditions employed for saturation kinetics that were used to evaluate catalytic turnover (Chapter 3). Since there were two complexes that we were trying to observe, the mixing times were monitored for either five seconds or sixteen minutes. The results showed an increase in fluorescence signal for the short component and a decrease in the fluorescence signal for the long component (Figure 5.5). The change in fluorescence signal was expected to increase for the 1:1 and decrease for 1:2 HG complexes because the fluorescence signal (from chapter 3) at 50 mol% CB[8] is lower than the fluorescence signal at 100 mol% CB[8].

These results seemed to be in line with our previous observations, not just exclusive to the fluorescence signal changes but with respect to the overall reaction rate of the system. Our previous kinetic results demonstrated that the catalytic cycle occurs on a minute time scale. The results from the long-term component was close to the expected results. As we observed aggregation of both CB[8] and **1g**, it posed a perplexing question about what was causing the fluorescent signal was decreasing at a longer time scales.

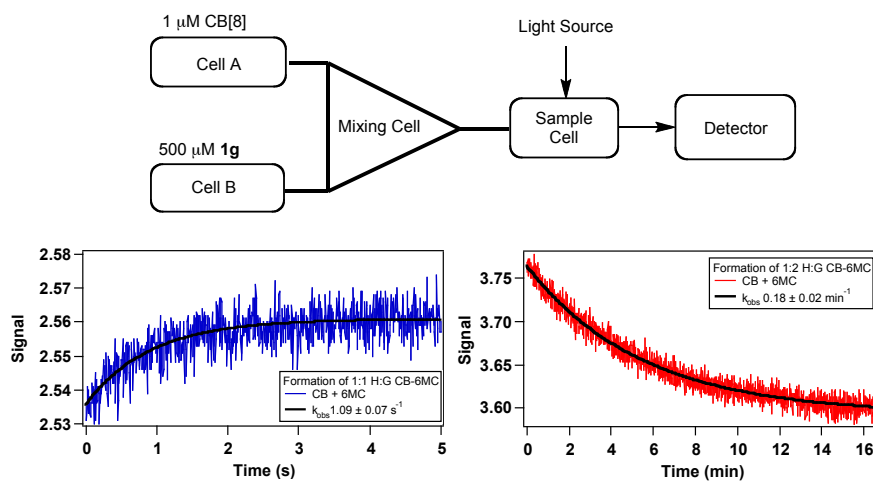
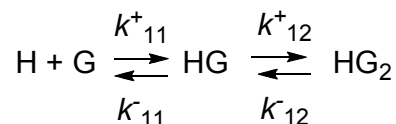


Figure 5.5 Initial stopped flow studies of CB[8]-**1g** HG complex. The short component (Left) has a $k_{obs} = 1.09 \pm 0.07 \text{ s}^{-1}$ and the long component (Right) has a $k_{obs} = 0.18 \pm 0.02 \text{ min}^{-1}$. The excitation wavelength $\lambda_{ex} = 325 \text{ nm}$, the signal was monitored with a $< 395 \text{ nm}$ cutoff filter

5.3.1. Determination of HG complexation rate constant for 1:1 1g@CB[8] HG complex

To decrease the aggregation and other complex phenomenon occurring at high concentration, we re-studied the system under very dilute conditions. The HG complexation kinetics are far more complicated than initially thought. Since the 1:2 HG complex is favored due to its higher binding constant, in order to study the 1:1 complex the initial concentrations of the host and guest molecules must be very small. More specifically the guest concentrations must be lower than the host concentrations to more favorably form the 1:1 complex. Our observations using stopped flow kinetics have shown that CB[8] at concentrations higher than 15 μM in water demonstrate aggregation. The fluorescence signal from 1g in water is very weak, therefore the concentration would need to be large enough to result in a viable signal. With these conditions in mind, the experimental setup for stopped flow to study the 1:1 HG complex was established (Table 5.1).

Table 5.1 The experimental concentrations and pertinent equation for stopped flow kinetics to determine the k_{11}^+ and k_{11}^- for on and off rate constants for 1:1 HG complex



$$K_{\text{obs}} = k^+ [\text{H}] + k^- \text{ (Excess host)}$$

[CB[8]] ^a	[1g] ^a	$k_{\text{obs}} \text{M}^{-1} \text{s}^{-1}$ Run #1	$k_{\text{obs}} \text{M}^{-1} \text{s}^{-1}$ Run #2
12.6 μM	1.0 μM	26.36	26.26
10.5 μM	1.0 μM	24.74	25.00
8.4 μM	1.0 μM	23.14	21.80
6.3 μM	1.0 μM	20.48	20.50
6.3 μM	1.0 μM	20.11	-
4.2 μM	1.0 μM	19.27	17.8

^aThe concentrations listed are the final concentrations after mixing in stopped flow cell using two injection syringe.

Two independent runs to determine k_{obs} for the 1:1 complex were performed. The concentrations were kept constant but the monochromator on the light source was changed between the two runs (Figure 5.6). This was to determine if the light intensity would impart any artifacts to the results, such as

photobleaching. The observation of photobleaching in stopped flow measurements can cause errors to propagate throughout the measurements. It is important to keep the light intensity as small as possible to minimize photobleaching. The results for the runs are within 5% of each other and have good agreement. Each slope is an average of at least 25 runs.

The stopped flow data was fitted for mono/bi/triexponential decays using Equations 5.2 and 5.3. The goodness of fit was gauged by the symmetrical distribution of the residuals that gave k_{obs} for a given concentration of CB[8]. The results of the stopped flow experiment can be observed by plotting the k_{obs} (y-axis) versus the concentration of CB[8] (x-axis) and fitting to a linear slope. The slopes for each experiment were calculated independently. The y-intercept value represents the k_{-11}^{-1} term, which is the off rate constant for the 1:1 complex (k_{off}) the on rate constant (k_{on}), whereas the slope represents the k_{+11}^{+1} term. The average values for k_{+11}^{+1} was $0.96 \times 10^6 \text{ M}^{-1} \text{ s}^{-1}$ and k_{-11}^{-1} was 14.368 s^{-1} (Figure 5.7).

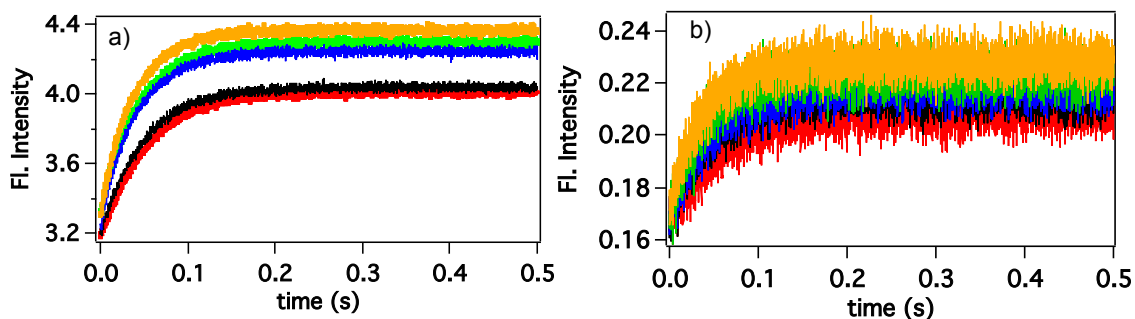


Figure 5.6 Stopped flow spectra for k_{obs} for the 1:1 complex. Signals increase with increasing concentration of CB[8] (see Table 5.1). a) emission slit widths = 1 mm and b) emission slit widths = 0.1 mm

$$I = I_0 + I_\infty (1 - e^{-k_{obs} t}) \quad (5.2)$$

$$I = I_0 + \sum [I_i (1 - e^{-k_{obs} t})] \quad (5.3)$$

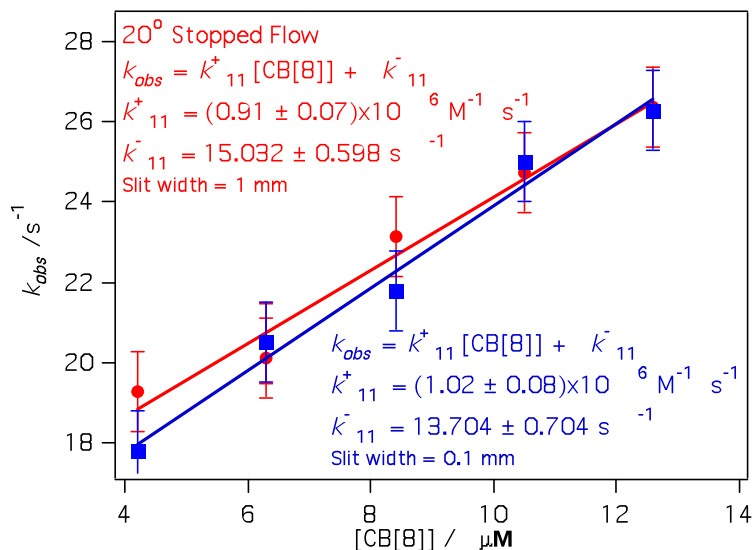


Figure 5.7 The plotted k_{obs} data versus concentration of CB[8] to determine k^+_{11} and k^-_{11} terms at 1 mm (red) and 0.1 mm (blue) monochromatic light

The binding constant for the formation of the 1:1 HG complex can also be calculated with the k^+_{11} and k^-_{11} values by using the equation $K_1 = k^+_{11} / k^-_{11}$. When this is performed from the stopped flow measurement, the rate constant gave a binding constant value of $6.68 \times 10^4 \text{ M}^{-1}$ for the 1:1 HG complex. This value is very similar to the K_1 binding constant value previously obtained through fluorescence titration measurements in chapter 4 ($K_{a1} = 1.33 \times 10^4 \text{ M}^{-1}$). The error may be a result of different experimental conditions between the stopped flow and fluorescence-binding isotherm but is within acceptable experimental error limits.

A comparison test between the stopped flow data and fluorescence data for binding of 1:1 complex provided evidence that the measurements are reliable. Our results were further verified when the normalized stopped flow signal was compared to the integrated signal from the normalized fluorescence spectra. The fluorescence spectra are obtained under the same excitation conditions and the signal is integrated and normalized. Since the stopped flow data were obtained using a 400 nm cutoff filter, the integration value from the fluorescence spectra will begin at 400 nm. As both data points (*viz.*) from fluorescence signal and stopped flow experiments correlate to each other. (Figure 5.8) the signal from the 1:1 complex is indeed reliable and not an experimental artifact.

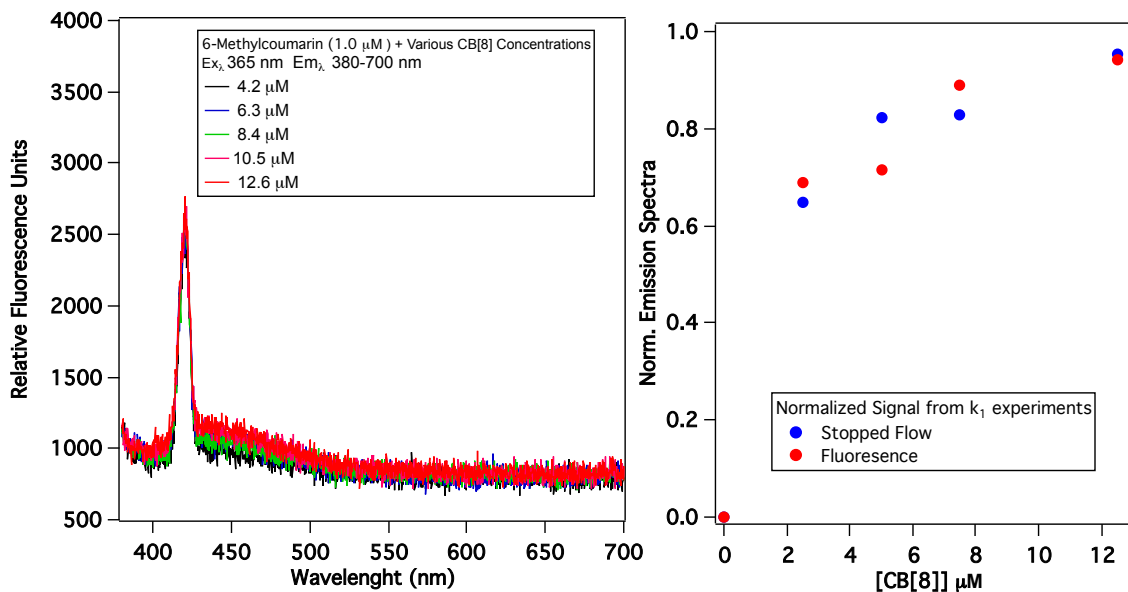


Figure 5.8 (Left) Fluorescence spectra of **1g** (1 μM) and various concentrations of CB[8]. (Right) Normalized signal intensity from fluorescence and stopped flow data for k_1 experiment

5.3.2. Determination of complex formation constant for the 1:2 host-guest complex

Conditions for the 1:2 HG complex are not easily obtained and can be obtained only through trial and error. Typically the approach to determine the conditions to form predominately a 1:2 HG complex involve preparing solutions of HG complexes at various concentrations and then diluting them with water to drive the formation from 1:2 to 1:1. These dilution studies are performed to find quality signals at mixing conditions that are free from artifacts such as aggregation or photobleaching.

Concentrations of **1g** higher than 7.5 μM showed some artifacts that might be attributed to aggregation. It was determined experimentally that the following concentrations employed in Table 5.2 with an acceptable signal to noise ratio would yield two rates from the biexponential fit (Table 5.2, Equation 5.2). The overall concentrations are barely forced the formation of 1:2 HG complex, however these solutions were prepared at twice the concentration and had reached equilibrium favoring the 1:2 complex prior to dilution. The samples were also investigated for an increased amount of time to observe the slower formation of the 1:2 HG interaction. While the k_{obs} values are a good approximation for the actual values, these are not the final values. Dilution studies are used to find the correct conditions for the forward reaction.

Table 5.2 Concentrations and k_{obs} values employed for dilution studies

[CB[8]]+[6-MeC] ^a	System	k_{2obs} (s ⁻¹)	k_{1obs} (s ⁻¹)
1.05 μM+ 0.625 μM	H-G + W	0.20 ± 0.05	8.5 ± 0.3
1.05 μM+ 1.00 μM	H-G + W	0.27 ± 0.03	9.2 ± 0.2
1.05 μM+ 1.25 μM	H-G + W	0.29 ± 0.02	10.1 ± 0.1
1.05 μM+ 1.50 μM	H-G + W	0.30 ± 0.02	10.3 ± 0.1
1.05 μM+ 2.50 μM	H-G + W	0.35 ± 0.02	10.4 ± 0.1

^aConcentrations list are final concentrations after mixing with equal volume of water.



$$k_{obs} = k^+[\text{G}] + k^-(\text{excess guest}) \quad (5.5)$$

Once the dilution conditions are established studying the forward reaction is relatively straightforward to perform. The experiments for the 1:2 HG complex under the same conditions were performed by mixing stock solutions of CB[8] (2.1 μM) with various concentrations of **1g** (Table 5.3) and the fluorescence signal was monitored for thirty seconds. The fluorescence decays are then calculated using a biexponential decay curve fit from the stopped flow software (Equation 5.2 and 5.3). Run #1 and #2 were performed as an independent experiment on different days and each value acquired is an average of at least 25 individual injections. The results obtained provide k_{obs} , but in order to determine the actual k_2^+ and k_2^- values more data analysis will be required due to the complex nature of the system under investigation.

Table 5.3 Concentrations employed and observed k_{obs} rates for 1:2 HG complex

[CB[8]]+[1g] ^a	System	k_{1obs} (s ⁻¹) Run #1	k_{1obs} (s ⁻¹) Run #2	k_{2obs} (s ⁻¹) Run #1	k_{2obs} (s ⁻¹) Run #2
1.05 μM+ 0.625 μM	H + G	11.0 ± 0.6	8.9 ± 0.3	0.31 ± 0.06	0.38 ± 0.05
1.05 μM+ 1.00 μM	H + G	11.3 ± 0.4	10.1 ± 0.2	0.33 ± 0.05	0.27 ± 0.03
1.05 μM+ 1.25 μM	H + G	11.8 ± 0.4	12.7 ± 0.2	0.40 ± 0.04	0.26 ± 0.02
1.05 μM+ 1.50 μM	H + G	12.8 ± 0.3	13.8 ± 0.2	0.29 ± 0.02	0.29 ± 0.02
1.05 μM+ 2.50 μM	H + G	17.4 ± 0.2	15.8 ± 0.2	0.47 ± 0.02	0.37 ± 0.02

^aThe concentrations listed are final concentrations after mixing with equal volume of water in the mixing cell from the two stopped flow syringes.

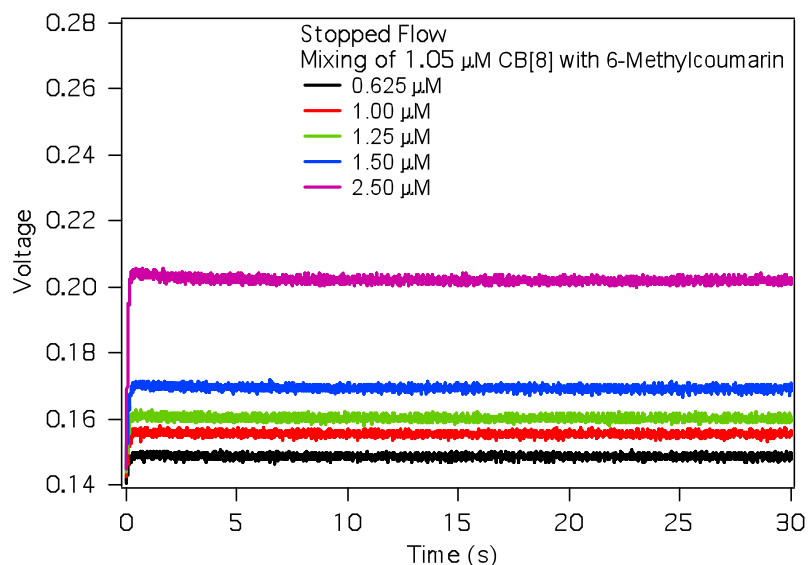


Figure 5.9 The stopped flow decay traces of mixing 1.05 μM CB[8] with various concentrations of **1g** generating the 1:2 HG complexation. Each trace corresponds to an average of 25 injections

The traces for the stopped flow experiment for 1:2 HG complexation show a quick rise which was attributed to the formation of the 1:1 complex followed by a decay which was assigned for the formation of the 1:2 complex (Figure 5.9). This shows that the formation of the 1:1 HG complex is very fast and the formation of the 1:2 HG complex is very slow under our experimental conditions. The explanation for the decay is because the quantum yield of fluorescence for the 50 mol% CB[8] (1:2 HG stoichiometric ratio) is less than the 100 mol% CB[8] (1:1 HG stoichiometric ratio) that was probably the result of enhanced quenching of the coumarin molecules within the CB[8] cavity presumably due to enhanced photodimerization (proximal effect). The normalization and comparison of the stopped flow spectra and fluorescence spectra was performed to ascertain the quality of signal (Figure 5.10). It's important to compare the resting state of a kinetic experiment with a static solution. The accuracy for the first five points are sufficient, however the fluorescence signal from the last point is low. This error in signal could be contributed to error in sample preparation and hence we will use the data from the first five points.

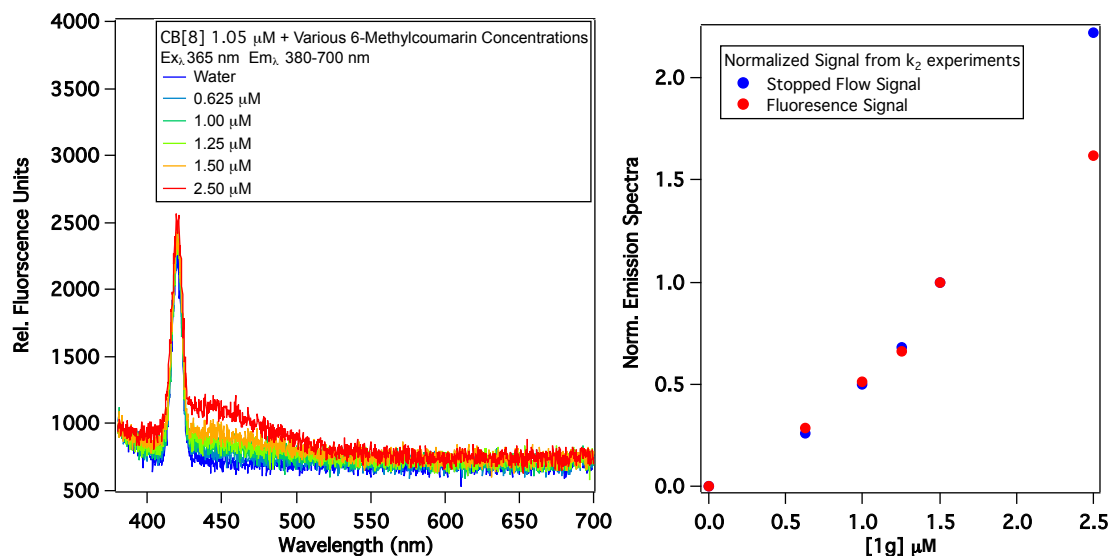


Figure 5.10 (Left) Fluorescence spectra of CB[8] (1.05 μM) and various concentrations of **1g**. (Right) Normalized signal intensity from fluorescence and stopped flow data for k_1 experiment

The k_{obs} for the 1:1 and 1:2 complexes were determined but the k_2^+ and k_2^- require global fitting analysis (Equation 5.5). The calculation uses a sequential binding model system to calculate k_2^+ and k_2^- values. This model assumes that the uncomplexed host and guest molecules do not fluoresce (which is an approximation in our case). The global fitting analysis requires an importing of actual kinetic spectral traces into the software so that traces can be calculated to the best-fit, resulting in random residuals. This is performed using non-linear fitting analysis from the individual kinetic traces. The values that determined for the k_{11}^+ , k_{11}^- and K_1 from stopped flow experiment (Fig 5.6 and 5.9) were used as approximations for the fitting formula for the 1:1 complexation kinetics. The model for sequential binding is Equation 5.6. The symbols are H, G, C and D, which represent the host, guest, 1:1 complex, and 1:2 complex respectively.



The results from the global fitting analysis allowed us to compare the binding constants K_1 (for the 1:1 HG complex) and K_2 (for the 1:2 HG complex) values from both stopped flow kinetics and the fluorescence-binding isotherm. The β value is the overall binding of a host guest system, in this case it is

$K_1 \times K_2$. The β value from the previously determined fluorescence-binding isotherm in chapter 3 was $2.6 \times 10^{10} \text{ M}^{-2}$, whereas the β value from the stopped flow was $7.54 \times 10^{10} \text{ M}^{-2}$. The major difference between the binding constants is that the observed K_1 for stopped flow is slightly six times higher than calculated from the fluorescence-binding isotherm. The differences between the K_2 values are rather small. When the K values obtained from the stopped flow experiments are used to determine the fluorescence-binding curve, the results provide nearly the same fitting curve.

Table 5.4 Results of global fitting analysis

Global fitting analysis variables	Computed Values
k_1^+	$(0.97) \times 10^6 \text{ M}^{-1} \text{ s}^{-1 \text{ a}}$
k_1^-	$14.4 \text{ s}^{-1 \text{ a}}$
$K_1 = k_1^+ / k_1^-$	$6.74 \times 10^4 \text{ M}^{-1}$
k_2^+	$1.4 \times 10^5 \text{ M}^{-1} \text{ s}^{-1 \text{ a}}$
k_2^-	$0.13 \text{ s}^{-1 \text{ a}}$
$K_2 = k_2^+ / k_2^-$	$1.12 \times 10^6 \text{ M}^{-1}$

^aValues for k_{obs} are averages of two independent runs with at least 25 signal traces per run.

From the global analysis, we were able to calculate the relative concentrations of each species (free **1g**, 1:1, and 1:2 HG complex) at various times (Figure 5.11). This allows for a visual representation over time, showing that the initial increase leading to the formation of the 1:1 HG complex was very quick. Followed by a slow decay as the in 1:1 concentration decreases (fluorescence decrease) whereas the 1:2 concentration slowly develops and seemingly remains constant after about 15 seconds. It is important to note that the concentrations of free CB[8] and **1g** are much higher than the concentrations of 1:1 and 1:2 complexes. It is important to emphasize the TON in chapter 3 (Figure 3.6) and the stopped flow experiments are done at different concentrations due to experimental limitations.

The initial mixing of the coumarins at high concentrations leads to large formations of **1g** aggregates. This reduces the effective concentration of **1g** floating around in solution freely, thus reducing the signal response from the fluorimeter or stopped flow. Subsequent processes (complexation, photoreaction, etc) disrupt the aggregates, likely resulting in a signal variation.

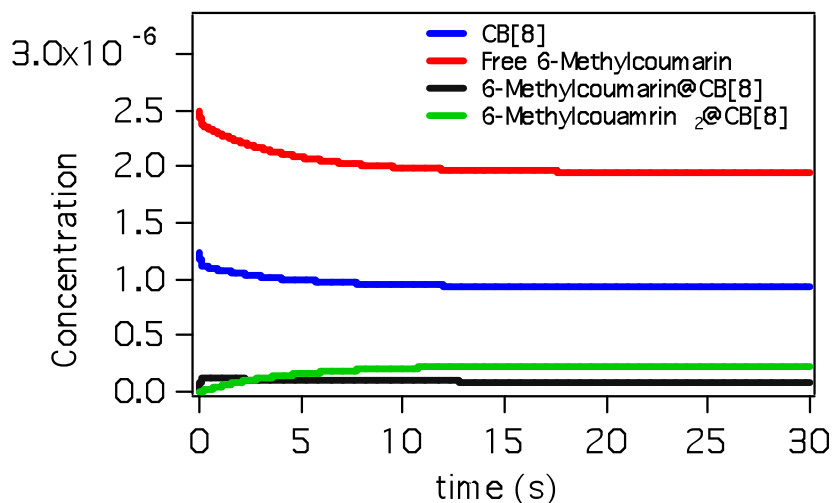


Figure 5.11 The calculated relative concentrations of each species in the HG system over time with starting concentrations for CB[8] and **1g** at 1.05 and 2.5 μM respectively

The stopped flow analysis demonstrated that the first inclusion complex (1:1) is a fast process whereas the second inclusion complex is relatively slow. This seems like a contradiction to the thermodynamics data that showed the formation of the 1:2 HG complex is more favored. The relative concentrations of the 1:1 and 1:2 complex in solution remain relatively small compared to the free **1g** and CB[8] under the stopped flow conditions.

5.4. Inhibition Studies of Photoproducts

Control experiments were carried out with the *syn*-HH photoproduct to see if product inhibition was a concern during the catalytic cycle. The synthesis of *syn*-HH photoproduct and crystalline structure has been known for some time and the process of synthesis and isolation will be presented in chapter 6.⁸ These experiments failed due to the lack of solubility of the crystalline *syn*-HH product in water. It appears that the photoproduct, while insoluble from pure crystalline material, becomes somehow soluble when synthesized in situ (likely due to the crystalline lattice energy in water). Hence the *syn*-photoproducts were synthesized in situ by irradiating a 10 μM solution of CB[8] with various concentrations of **1g** (Table 5.5) for a period of 12 hours and monitoring the disappearance of the reactants absorption peak at 360

nm using UV-vis measurements as the initial concentration of reactant is known, the concentration of dimers at complete conversion upon irradiation can be computed (Table 5.4).

Table 5.5 Relative starting concentrations of CB[8] and **1g** for inhibition studies

Entry	CB[8]	1g	CB[8] : Photoproduct after irradiation
1	10 μM	10 μM	1 : 0.5
2	10 μM	20 μM	1 : 1
3	10 μM	40 μM	1 : 2

The *syn*-HH photoproduct with CB[8] was then diluted so that the concentration of CB[8] would be 1 μM with a predetermined ratio of CB[8] : photoproduct as shown in Table 5.5. To this CB[8]-photoproduct mixture **1g** was added at a given concentration as shown in Table 5.6. A solution of known concentrations of CB[8], **1g** and *syn*-photoproducts (Table 5.6) were irradiated for specific time intervals to compute the rates of dimerization. This studied was performed to see if the photoproduct can inhibit the photocatalytic reaction by binding to the reactive site. These reactions were performed in an identical manner to the saturation kinetic reactions from chapter 3.

Table 5.6 Pseudo 1st order rates of reaction with various concentrations of **1g** and Photoproduct inhibitor

Entry	CB[8]	1g	Photoproduct	k_{obs} (s^{-1}) ^b
1	1 μM	50 μM	0.5 μM	2.15×10^{-7}
2	1 μM	50 μM	1.0 μM	2.08×10^{-7}
3	1 μM	50 μM	2.0 μM	2.38×10^{-7}
4	1 μM	100 μM	0.5 μM	4.37×10^{-7}
5	1 μM	100 μM	1.0 μM	3.79×10^{-7}
6	1 μM	100 μM	2.0 μM	4.68×10^{-7}
7	1 μM	150 μM	0.5 μM	5.67×10^{-7}
8	1 μM	150 μM	1.0 μM	5.12×10^{-7}
9	1 μM	150 μM	2.0 μM	5.84×10^{-7}

^aRuns are reported of an average of three runs. ^bPseudo 1st order rate constants.

Inspection of Table 5.6 revealed that there is no observed inhibition from the photoproducts (Figure 5.12). This is probably because after the photoreaction occurs the photoproduct expelled from the cavity allowing the catalytic cycle to continue. We have already observed CB[8]-photoproduct HG

complex by means of spectrometric studies, showing the possibility of photoproducts formed within the cavity (Figure 5.24) and being subsequently expelled is quite reasonable.

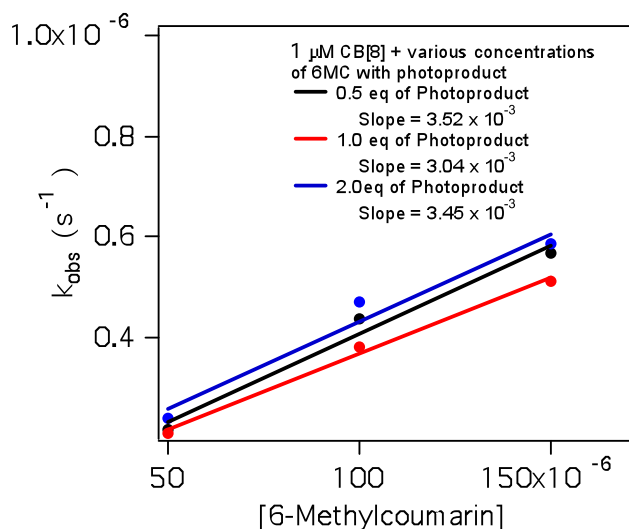


Figure 5.12 Inhibition studies of 1 mM CB[8] with various concentrations of photoproduct inhibitor and **1g**

To validate the stopped flow data and product inhibition studies, control studies were carried out using premixed solutions to ascertain the contributions to photobleaching. Two pre-mixed solutions of **1g** (500 μ M) and CB[8] (1 μ M) were injected into a stopped flow, mixed and monitored to see if photobleaching during the acquisition time was occurring. Two slopes were observed during the experiment (Figure 5.13). The first decay signal, which appeared to be the photoreaction both in solution and in the cavity (high concentration of **1g**.) The second decay was likely an increase in signal that may be due to the release of a photoproduct from the CB[8] and then subsequent complexation of new **1g** molecules. The signal response was reproducible under the concentrations but interpretation was quite complex. This experiment clearly demonstrated that there is a slow step during the complexation that ultimately dictates the photoreactions.

Based on the data observed with product inhibition studies, we carried out stopped flow experiments under saturated conditions of the substrate (1 μ M CB[8]; 100 μ M **1g**). In this control experiment the stopped flow syringes were premixed and allowed to equilibrate. When stopped flow kinetics were performed with the premixed solution (Figure 5.9 A) we saw a fast decay which is presumably the photoreaction followed by an increase (which is due to the formation) of the HG complex

after expulsion of the photoproduct. When a stopped flow reaction under identical final concentrations (under substrate saturated conditions of photocatalysis) is performed, only the decrease in signal is observed (Figure 5.9 B) This clearly shows that there is a slow process that is responsible for the slow decay prior to what (likely the formation of the 1:2 HG complex and or the aggregation of **1g** or CB[8]) to the photoreaction in the supramolecular photocatalytic cycle.)

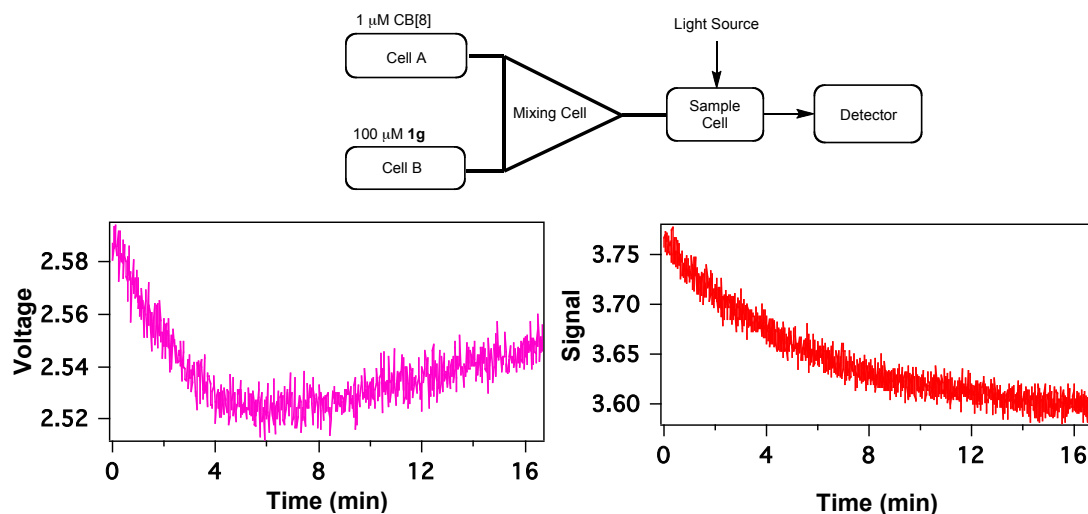


Figure 5.13 The long-term irradiation of pre-mixed (A) and mixed (B) of **1g** (100 μM) and CB[8] (1 μM) with an average of four runs

5.5. Temperature Dependence on Photoreactions

As the photocatalysis mediated by CB[8] occurred effectively in water with likely no observed product inhibition, it was critical to ascertain the optimal temperature for maximum turnover during the catalytic process. During a typical reaction, increasing the temperature by 10 °C will cause the rate of that reaction to double according to the Arrhenius equation. In order to see how the photocatalysts would be affected by temperature, rates of dimerization of **1g** in the presence of 10 mol% CB[8] were investigated along with the control study of **1g** in water in the absence of CB[8] at various temperatures. The reaction velocity was monitored by UV-vis spectroscopy. The temperature dependent reactions were performed by preparing fresh solutions of 50 μM **1g** along with or without 5 μM CB[8] in 5 mL quantities in 13 x 100 mm test tubes. Barnstead NANOpure water system with a resistivity of $\geq 17.8 \text{ M}\Omega \text{ cm}^{-1}$ was used to make the standard solution. These test tubes were fastened together and equilibrated at a given temperature for 5

minutes in a water bath prior to irradiation. The solutions were then irradiated for 2 minute intervals in a Pyrex (<295 nm cutoff) water bath at a set temperature. The reaction progression was monitored via UV-vis spectroscopy as previously described in chapter 3. The temperatures below 25 °C were cooled using constant additions of ice. Temperatures above 25 °C were heated using a water circulator and heater attachment. A thermometer was used to monitor temperature inside the photo-chamber.

As a control, the dimerization of **1g** at a concentration of 50 μM in water in the absence of CB[8] was performed at various temperatures ranging from 10 °C – 50 °C. Inspection of Figure 5.10 showed that as temperature for the reaction increases, the velocity of the reaction decreases. The decrease in velocity is likely caused by the dispersion of coumarin aggregates in solution that is *i.e.*, the aggregation of coumarin likely determines the velocity of the reaction in water in the absence of CB[8].

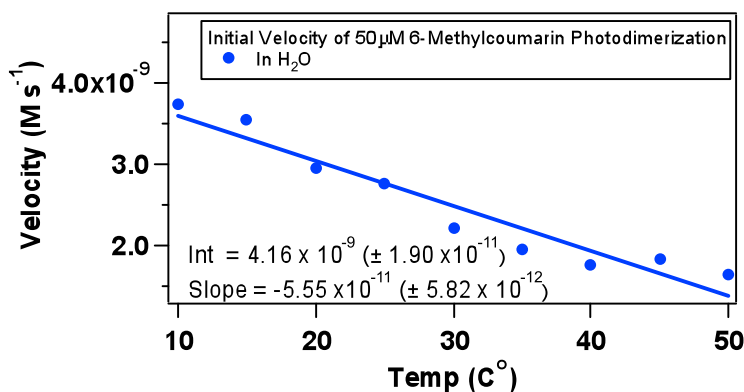


Figure 5.14 Reaction velocity at various temperatures for [2+2] photodimerization of **1g** (50 μM) in water

With 10 mol% of CB[8] was added, the reaction velocity increased upon changing the temperature from 10 °C to 30 °C. Beyond 30 °C the reaction velocity decreased (Figure 5.15). The increase in reaction rate is likely due to the lowering of the activation barrier leading to the formation of 1:2 HG complex. As the energy in the system increases the time it takes the cavity to rearrange decreases and this allows the formation of the 1:2 HG complex to occur sooner. As the temperature increases beyond the optimum 30 °C, the entropy prohibits the formation of the 1:2 HG complex and most likely stops at the formation of the 1:1 complex. In other words the formation of the relative 1:2 HG complex is inhibited due to the increase in temperature resulting in a decrease in reaction velocity. This

process is similar to the denaturing of enzymes at high temperatures that causes a decrease in reaction velocity.

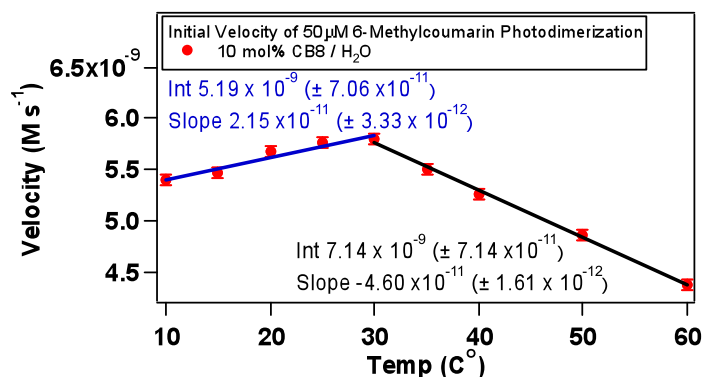


Figure 5.15 Reaction velocity at various temperatures for [2+2] photodimerization of **1g** at 50 μM with 10 mol% CB[8] in water

To better understand the effect of temperatures on the reaction velocity during photocatalysis mediated by CB[8], we computed the Eyring plot using the Eyring equation (Equation 5.7). The slope of the **1g** dimerization in water reveals a small positive value (as the temperature decreases) for the enthalpic term that could be the result of solvation, hydrophobic aggregation, or radical reaction effects.² The intercept value (ΔH^\ddagger) for **1g** was negative and small which was likely the reflection of aggregation of coumarin. Aggregation in solution controls the dimerization and a temperature increase will lower the aggregation, thereby decreasing the reaction velocity.

$$k_{obs} = \frac{k_B T}{h} e^{\frac{\Delta S^\ddagger}{R}} e^{\frac{-\Delta H^\ddagger}{RT}} \quad (5.7)$$

The dimerization in the presence of CB[8] showed that the enthalpic value (slope) was low and there was a significant contribution from the entropic value (intercept). This is because in the presence of CB[8], entropic contributions (release of water molecules) will likely play a role in HG complexation thereby promoting the reaction. Additionally the hydrophobic effect (enthalpy) will play a role in bringing the two coumarin units together. The inversion of the slope around 30 °C is likely a reflection of the reaction occurring outside the cavity and competing with the reaction inside the cavity. In other words the

inflection shows a change in the rate determining step. The reaction predominantly occurs inside the cavity below 30 °C and predominantly occurs outside the cavity above 30 °C (Figure 5.16 right).

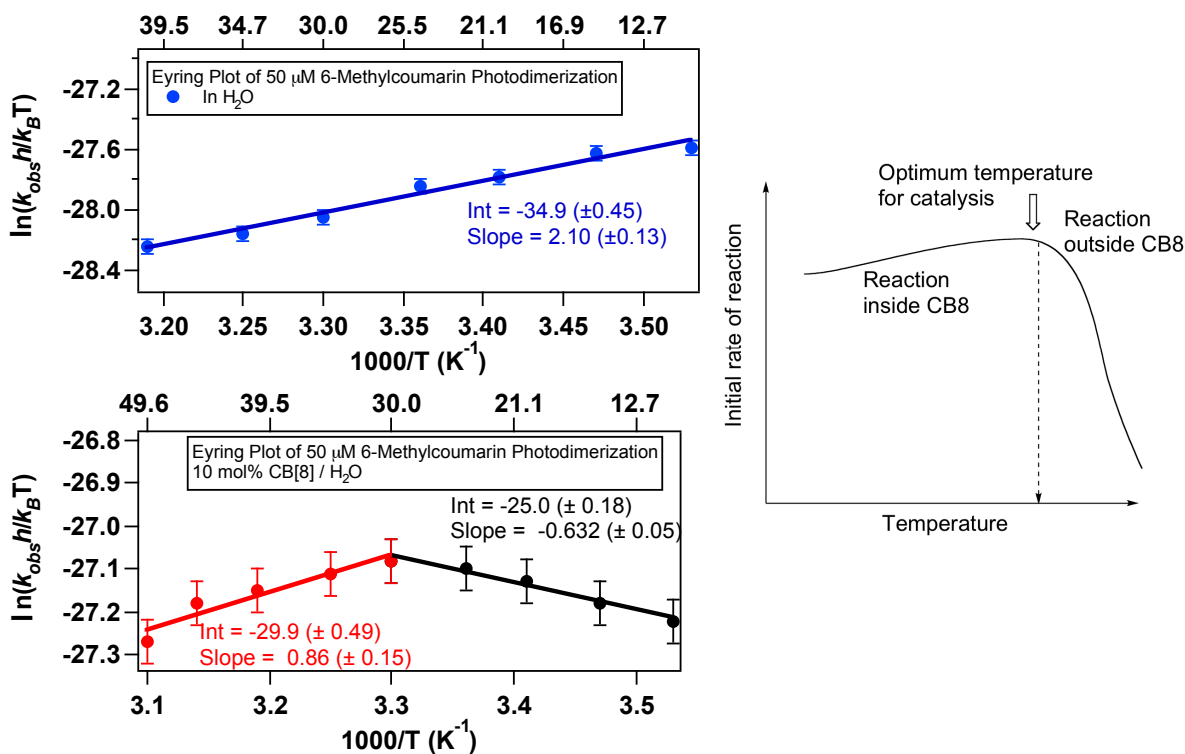


Figure 5.16 The Eyring plots for the dimerization of **1g** in water (Top) and in water-CB[8] (Bottom). (Right) Cartoon depicting the rate of reaction versus temperature

5.6. NMR Studies of CB[8]: **1g** Complex

While stopped flow can show a spectroscopic change in fluorescence that was interpreted as HG complex formation, it was critical to substantiate the complexation process by other spectroscopic techniques. To show definitive spectroscopic proof of a dynamic HG complex ^1H NMR spectroscopic studies were performed.

Creating the conditions for studying HG complexation by ^1H NMR took several attempts because the solubility of CB[8] was poor in neat D_2O and **1g** was completely insoluble in 35% $\text{DCI}/\text{D}_2\text{O}$. In neutral solution the solubility of CB[8] is limited to only about 0.1 mM and when mixed with **1g** this solubility decreases. This was evidenced by the single crystal growth that occurs when **1g** is dissolved in a saturated solution of CB[8]. We used the 6-methyl peak as an NMR handle as we employed **1g** at a 1.5

mM concentration. The **1g** guest solution was prepared by dissolving 3.0 mg in 3 mL of D₂O. The solution was sealed and sonicated under heat, resulting in a concentration of 6.2 mM. The solution was then diluted to a concentration 1.5 mM by serial dilution. The CB[8] host solution was prepared by dissolving 4.0 mg in 2 mL 35% DCI/D₂O resulting in a concentration of 1.5 mM. The NMR samples were prepared by mixing various ratios of the two solutions and adding additional DCI to make to the volume (450 μL) as needed (Table 5.7).

Table 5.7 Mixing of various volumes of CB[8] and **1g** for NMR studies

Solution	Vol CB[8] μL [1.5 mM]	Vol 1g μL [1.5 mM]	Vol DCI/D ₂ O μL	H :G ratio
1	300	150	-	2:1
2	150	150	150	1:1
3	100	150	200	1:3
4	0	150	300	-

NMR samples were prepared individually and shimmed via gradient shimming. This, along with increasing the number of scans to 512 from 16 increased the signal-to-noise ratio nine times. Since the HG complex has a relatively large molecular weight (1649 g/mol), the relaxation time was also increased. To counter this, the window acquisition time (d₂) was increased from the typical 0.3 seconds to 3 seconds. As our stopped flow experiments revealed the formation of HG complexes on the seconds time scale, the exchange in NMR should also reveal a similar phenomenon. A slight difference between stopped flow data and NMR data is expected. The concentration of the NMR studies are relatively high, and they are under different solvents as well. Additionally, several studies have established that cations can slow down the kinetic rates of guests entering and leaving the CB[8] cavities.^{9,10} In the NMR experiments, these protons came from the solvent mixture of DCI/D₂O. The results from the NMR (Figures 5.17 and 5.18) show a considerable decrease in signal intensities from the free **1g** methyl proton resonances, when compared to the methyl resonances from the 1:1 and 1:2 complexes. The broadening of the free coumarin shows that exchange between free and 1:1 complex is relatively slow.

Inspection of the methyl signals in Figures 5.17 and 5.18 show an upfield shift. The upfield shifts are indicative of enhanced shielding of methyl resonances from the CB[8] cavity. This enhanced shielding is likely due to an interaction between the carbonyls of the CB[8] and the methyl group of the **1g** as well

as a change in the chemical environment by switching from hydrophilic solution to the hydrophobic cavity. The various forms of complexation are likely from the slow dynamic exchange, resulting in distinct NMR peaks of free **1g**, 1:1 and 1:2 HG complexes. This is also in line with our UV-vis Jobs' plot observations. . If the complexation is allowed to sit for an extended period of time (>24 hours), crystals form. These crystals were not analyzed and were redissolved by sonication and heating.

Analysis of the line shapes of the free **1g** methyl resonances show that the peaks are predominantly Gaussian in shape with the exception of neat **1g** in DCI/D₂O, which were Lorentzian (Figure 5.19). The formation of the 1:1 complex is likely a mixture between both the Gaussian and Lorentzian lineshapes because it is the intermediate species in the HG complexation process (Figure 5.19). The 1:2 complex line shape is exclusively Gaussian in nature which is the result of exchange of species to the 1:1 and free complex as well as an increase in anisotropy due to the large molecular mass of the complex (Figure 5.14 Bottom).

5.7. Ion-trap and Liquid Chromatography Mass Spectrometry Studies

Ion trap mass spectrometry studies were performed to obtain a higher resolution of the HG complexes in gas phase. Unlike in NMR where the solubility needs to be relatively high, the ion-trap solutions can be micromolar or lower concentrations. This technique allowed us to view the various complexes in real-time conditions that demonstrates definitively that the complexes are formed despite the complexation conditions (low or high concentrations). The trapped complexes can be probed by bombarding them with helium atoms which allows for a sequential decomplexation of the guest(s) from the CB[8] cavity.

5.7.1. Liquid chromatography mass-spectrometry studies

Liquid chromatography mass spectrometry studies were performed on irradiated and non-irradiated solutions of the HG complexes to observe the mass of the photodimer and **1g** when in free solution and complexed to CB[8]. The solutions were prepared with a concentration of 100 μ M **1g**, 100 μ M CB[8] and 0.01% HBr. The solution was irradiated for 4 hours and in a quartz cell with a xenon lamp using a Pyrex cutoff filter (>295 nm) and water filter to prevent light less than 295 nm as well as near-

infrared light. The conversion to photoproduct for the irradiated sample was greater than 90%. The result from the UV-Vis spectra shows the absorbance of the photoproduct as well as the absorbance profile of the **1g** starting material (Figure 5.20 left).

When the solution was monitored by Liquid chromatography-mass spectrometry (LC-MS) three masses were found (Figure 5.15 right). The first eluent was CB[8] which appears at approximately 1 minute. The mass corresponded to $m/z = 665$ which was the mass of CB[8] and the two protons associated with it. Since the $z = 2$ the mass of 1331 is halved to 665 (m/z value). The 2nd peak was that of **1g** and a proton that corresponded to a m/z of 161 and elutes around 9 minutes. The last peak that eluted around 11 minutes was the *syn*-photoproduct. It corresponds to the predicted $m/z = 321$ which was the result of the photoproduct associated with a proton.

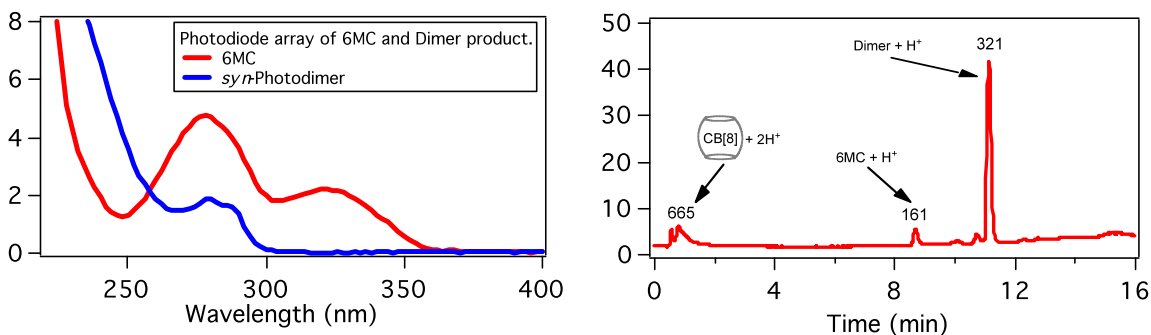


Figure 5.17 (Left) The UV absorbance spectra of **1g** and *syn*-photodimer from LC. (Right) LC-MS trace of the irradiated aqueous solution of **1g** :CB[8] complex with 0.01% of HBr (>90% conversion). The mass assignments: m/z 321 = [*syn*-photodimer + H]⁺; 161 = [**1g** + H]⁺; 665 = [CB[8] + 2H]²⁺

The separation was performed by a 1200 Series LC by Agilent using a Puropher STAR (Merck) LiChroCART 125.2 column (12.5 cm x 2 mm, RP-18, 5 μ M) with a thermostated temperature of 30 °C. The mobile phase was a gradient of water and acetonitrile both with 0.1% formic acid volume by volume. The composition of mobile phase for the first two minutes of the LC run was 20:80 acetonitrile : water. The solution changed to 80:20 acetonitrile : water over the course of the next 10 minutes and was held constant for at 80:20 for the next 4 min. The column was when flushed with 100% acetonitrile to ensure the column was clean prior to and after injections.

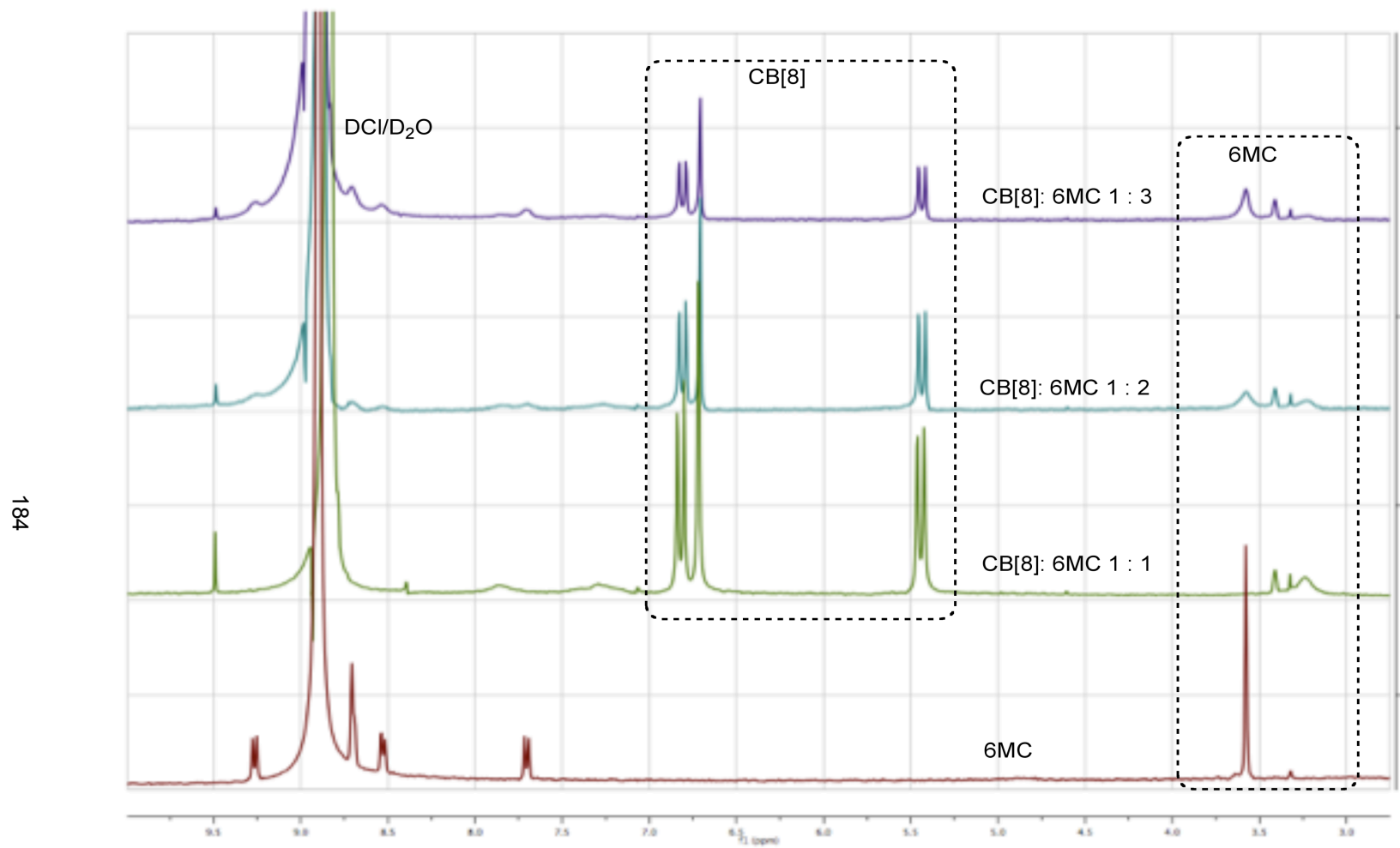


Figure 5.18 ^1H NMR spectra of methyl resonances of **1g** in the presence of various amounts of CB[8] in $\text{D}_2\text{O}/\text{DCI}$

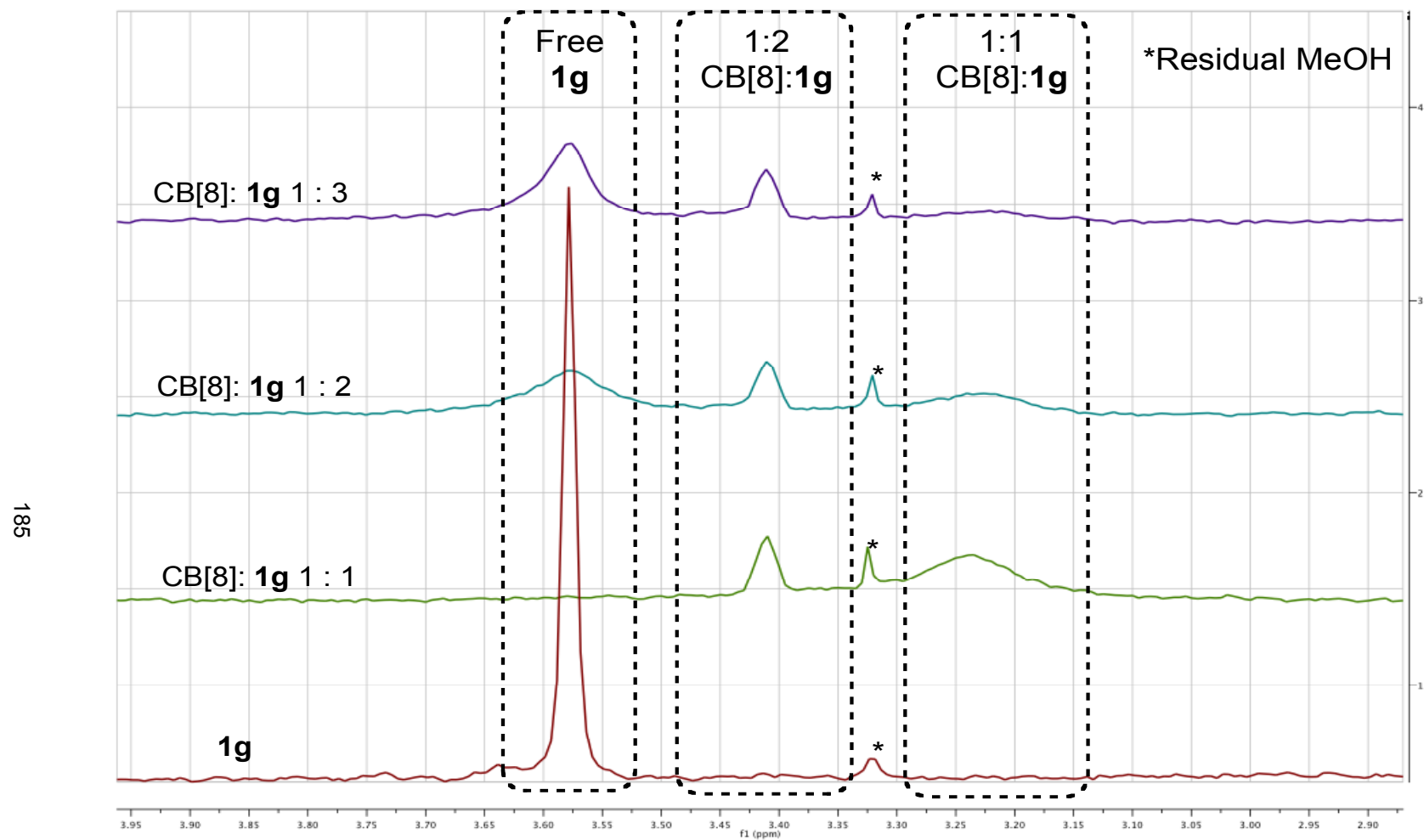


Figure 5.19 Expanded ^1H NMR spectra showing methyl resonances of **1g** in the presence of various amounts of CB[8] in $\text{D}_2\text{O}/\text{DCI}$

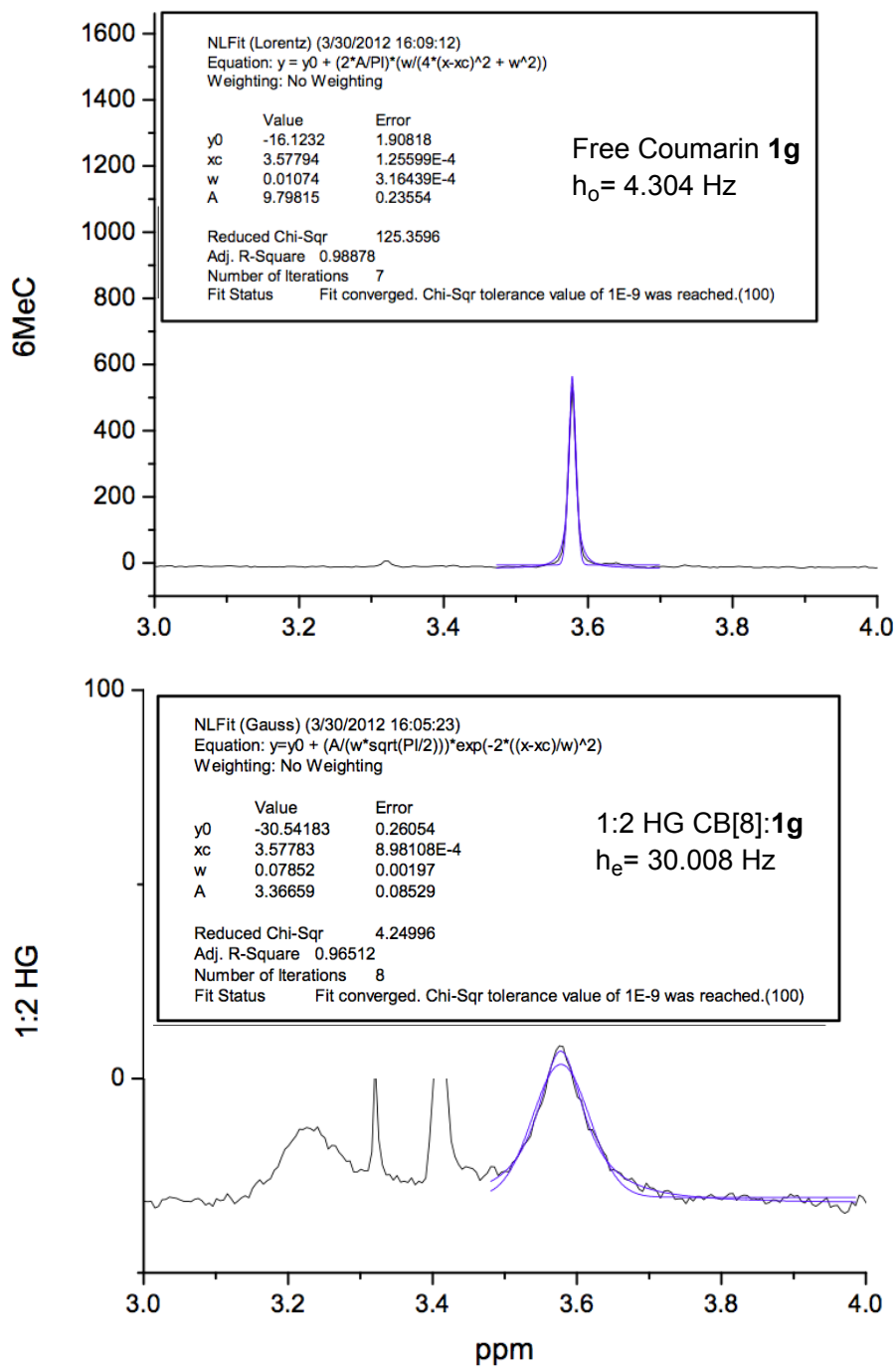


Figure 5.20 ^1H NMR ($\text{D}_2\text{O}/\text{DCI}$) line-shape analysis of (Top) free **1g** showing a Lorentzian line shape and (Bottom) Free **1g** methyl resonance fitted to Gaussian line shape in the presence of **1g**-CB[8]

The LC-MS studies identified that the photoproduct absorbance begins lower than 310 nm. This result could explain why the product selectivity of *syn*-HH and *syn*-HT are different at different time intervals. In chapter 3, the observation that the major photoproduct for the 1 hour irradiation was *syn*-HH and the major photoproduct for the 24 hour irradiation was *syn*-HT. This is a possible result of the long irradiation times and the reversal in the photoproduct selectivity was likely due to the absorbance near 300 nm leading to photolysis. This reverted the photoproducts to the starting materials, or caused a rearrangement to form the *syn*-HT photoproduct (major product at longer irradiation times).

5.7.2. Ion-trap mass spectrometric studies

Ion-trap mass spectrometric studies were performed to study the HG complexes. Solutions of CB[8] and **1g** were prepared in the same manner as the solutions prepared for the LC-MS studies (section 5.5.2). When the non-irradiated solution mixture of CB[8] and **1g** was injected into the mass spectrometer and analyzed, it revealed that the solution was dynamic and that at any given time there are free host and guest, 1:1 HG complex, and 1:2 HG complex (Figure 5.16). The relative abundance of each species in solution was not necessarily representative of what would be observed under other conditions because the ionization potential for each species is likely different under our analysis conditions in a mass spectrometer.

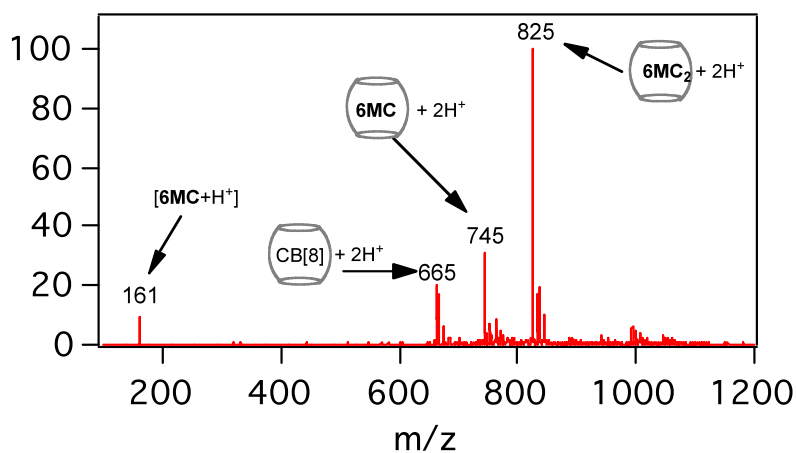


Figure 5.21 ESI-MS spectrum (full scan) Fragmentation of m/z 825 (1:2 complex). Assignments: m/z 825: $[\text{CB}8 + 2 \cdot \mathbf{1g} + 2 \cdot \text{H}]^{2+}$; 745: $[\text{CB}8 + \mathbf{1g} + 2 \cdot \text{H}]^{2+}$ (1:1 complex); 665: $[\text{CB}8 + 2 \cdot \text{H}]^{2+}$ (empty host); 161: $[\mathbf{1g} + \text{H}]^{1+}$

Ion-trap mass-spectrometry was particularly powerful due to the ability to trap and fragment specific signals. The peak observed at 825 corresponded to a 1:2 HG complex of CB[8] and **1g**. By trapping that signal and bombarding it with a helium atom a single molecule of **1g** was ejected from the CB[8] cavity that resulted in a mass of 745 (Figure 5.22). This showed that the two coumarins were bound within the CB[8] cavity and are not associated at the rim under these concentrations, rim bound coumarins have lower ionization potentials, *vide infra*. The 1:2 complex does not entirely disappear because the bombardment only happens for a short period of time and does not allow the complete decomplexation of the species through fragmentation. However, the relative abundance of the 1:1 HG complex becomes much higher relative to the 1:2 HG complex at very low concentrations of **1g**.

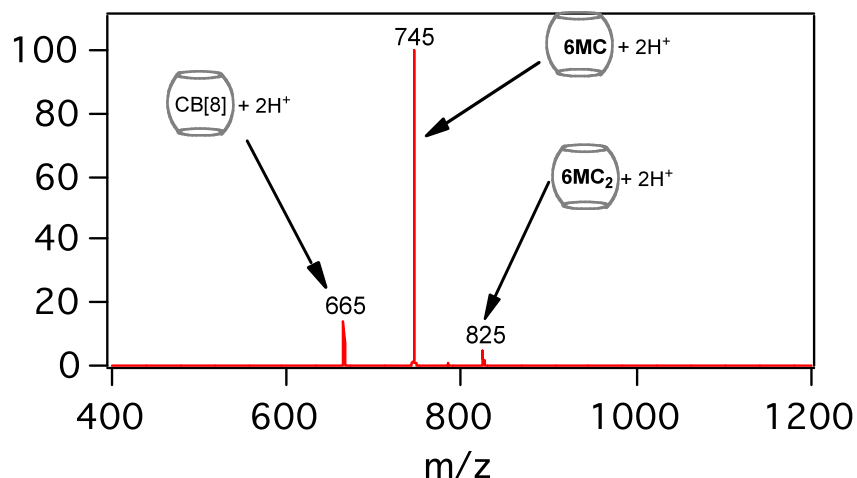


Figure 5.22 Fragmentation of m/z 825 (1:2 complex) by He bombardment using ion-trap mass spectrometry. Assignments: m/z 825: $[\text{CB8} + 2 \cdot \mathbf{1g} + 2 \cdot \text{H}]^{2+}$; 745: $[\text{CB8} + \mathbf{1g} + 2 \cdot \text{H}]^{2+}$ (1:1 complex); 665: $[\text{CB8} + 2 \cdot \text{H}]^{2+}$ (empty host). The fragmentation of the 1:2 HG complex (m/z 825) leads mainly to the loss of one guest and subsequent formation of the 1:1 HG complex (m/z 745)

Repeating the bombardment of the major peak at m/z of 745 freed the second encapsulated coumarin **1g** and produced an empty cavity of CB[8] (Figure 5.23). This resulted in an m/z peak of 665 that was observed from the LC-MS studies. A minor peak at 745 remained due to partial fragmentation of the 1:1 HG complex.

Fragmentation studies were also performed in irradiated solutions of CB[8] and **1g**. To investigate the possibility of observing the photoproduct bound to the CB[8] cavity. The irradiated solution was prepared under the same conditions as the LC-MS studies and injected into the mass spectrometry. The results from Figure 5.19 show that three compounds in the solution include unreacted **1g**, free CB[8] and a complex of CB[8] and photoproduct. The photodimer mass was observed with an extra water molecule which was not observed with the previous 1:2 HG complex. Explanation for why a water molecule is observed is not clear when the fragmentation of the HG complex was performed.

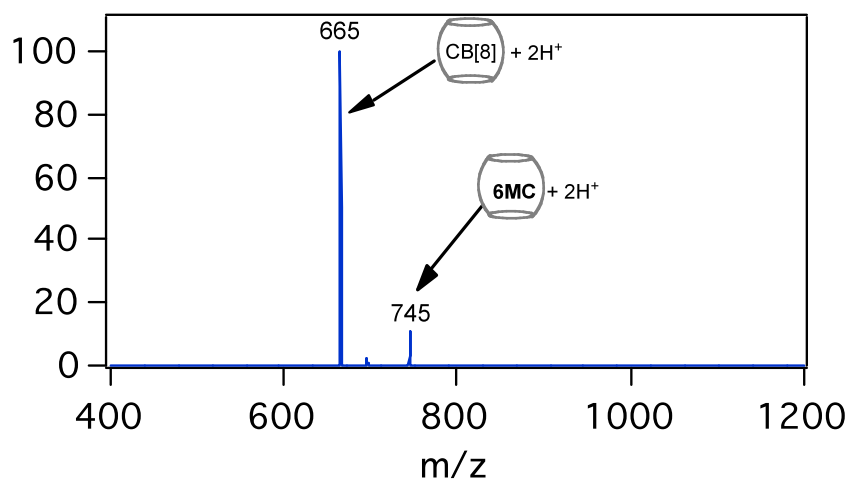


Figure 5.23 Fragmentation of m/z 745 (1:1 complex) by He bombardment using ion-trap mass spectrometry. Assignments: m/z 745: [CB8 + **1g** + 2•H]²⁺; 665: [CB8 + 2•H]²⁺. The fragmentation of the 1:1 complex (m/z 745) leads to the loss of the guest and consequent formation of the empty host (m/z 665)

Bombarding the photoproduct@CB[8] complex with a helium atom resulted in the fragmentation of the photoproduct and empty CB[8] with and without a water molecule and a ratio between the two which is about 2:1 respectively (Figure 5.24). The reason why the water molecule remains with photoproduct@CB[8] is unknown as there is hardly an observation of the water molecule from ionization of just the CB[8] cavity alone. Also, when the photoproduct leaves the cavity, if there was a water molecule templated to the exit, preventing its escape, then presumably the water molecule would leave as well. However this was not observed. If the water molecule is active in the complexation of the

photoproduct, it is perhaps positioned on the non-exiting side of the cavity. A more likely explanation is that the H^+ source (HBr) used for ionization is bound at the carbonyl portal and is also associated with the H_2O from the solvent solution.

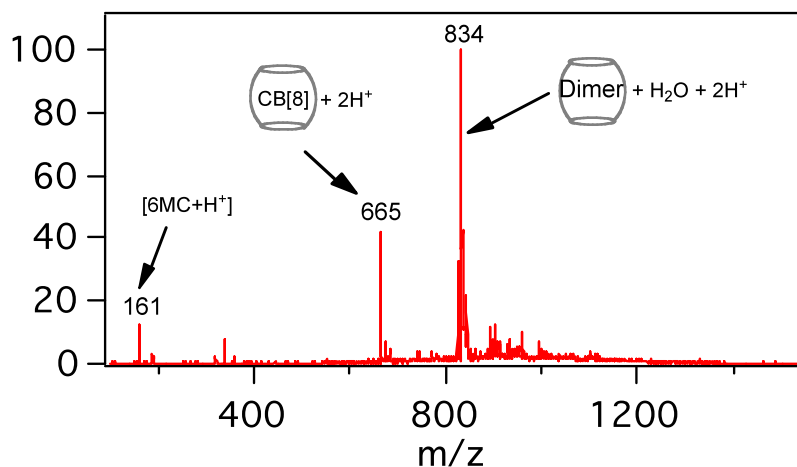


Figure 5.24 ESI-MS spectrum (full scan) of an irradiated aqueous solution of **1g@CB[8]** with HBr 0.01% (> 90% conversion). Assignments: m/z 161 [**1g** + H]⁺; 665 [CB8 + 2•H]²⁺; 834 [CB[8]-(H₂O) + *syn*-photodimer + 2•H]²⁺

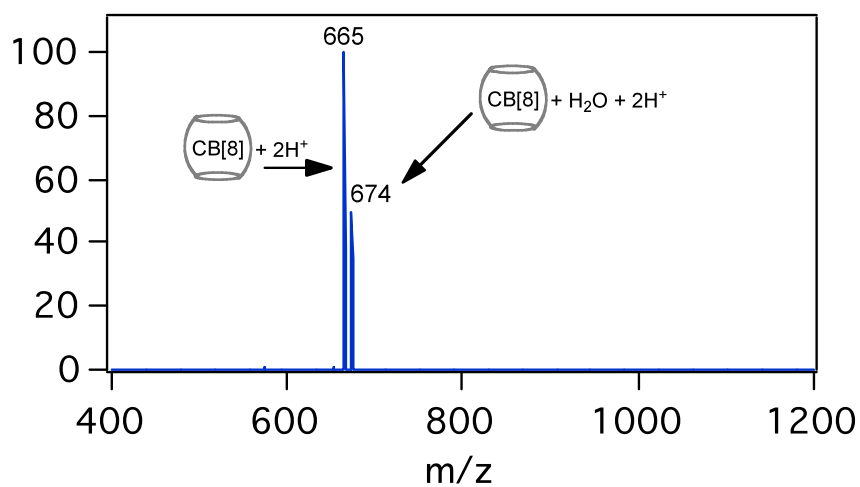


Figure 5.25 Fragmentation of photoproduct@CB[8] Assignments: m/z 665 [CB[8] + 2•H]²⁺; 674 [CB[8] (H₂O) + 2•H]²⁺. The loss of the *syn*-photodimer and the loss of a water molecule results in an m/z 674 confirms the assignment

Aggregation studies were performed using mass spectrometry to learn more about the complexation phenomena that could not be deconvoluted via stopped flow experiments. The stopped flow excels at measuring change over time but is limited to deconvoluting a few mechanisms, whereas the mass spectrometer is really only limited to measurements against time. In the following studies we have attempted to understand the various processes of aggregation and HG complex formation through time-dependent mass spectrometry. The results of iontrap mass spectrometry paint a fairly complicated picture for both the aggregation of CB[8] and **1g**.

Aggregation of CB[8] in the stopped flow is observed above concentrations of 15 μM resulting from signals that cannot be fit with mono or biexponential curve fits. Repetition of experiment was performed using a mass spectrometer and monitoring m/z values (Figure 5.26 – 5.28) over time (Figure 5.30). Hard evidence for CB[8] aggregation was nearly impossible from a stopped flow system since CB[8] is essentially unresponsive to light. An injection of CB[8] at near saturation conditions into a mass spectrometer resulted in clearly defined clusters of CB[8] (Figure 5.26).

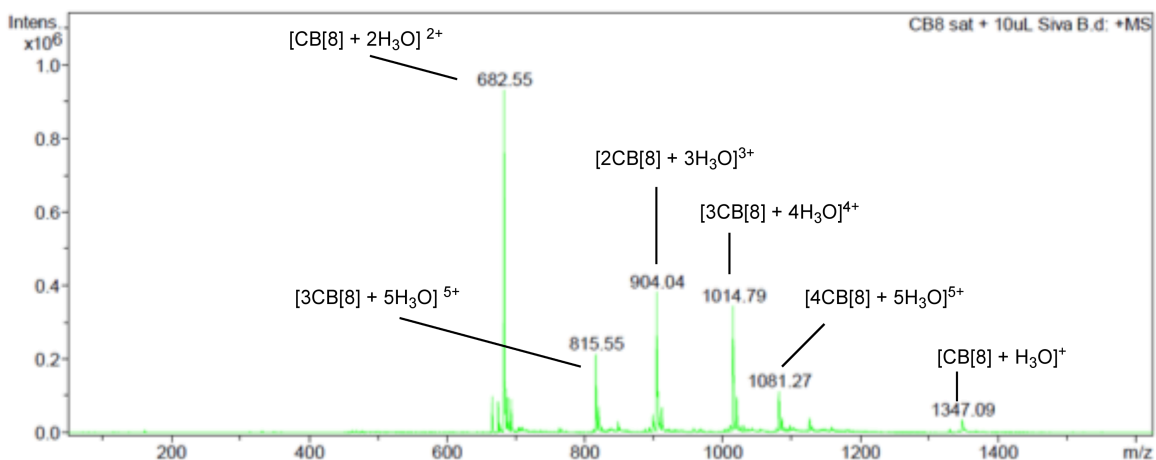


Figure 5.26 The CB[8] aggregation clusters formed at near saturation conditions as analyzed by Ion-trap mass spectrometry. All assignments were determined based on fragmentation patterns

The mass spectrometric studies by mixing **1g** (35 μM) with CB[8] at near saturation conditions provides a unique look into the process of HG complexation. In dilute conditions it revealed that the process of complexation for the 1:1 HG complex was bimolecular. However, at higher concentrations we

not only observe 1:1 HG complexes but we observe 2:1 HG complexes (Figure 5.27), where two CB[8] molecules are associated with one **1g** molecule. These new peaks show up along with the previous CB[8] aggregates observed in the neat CB[8] solution (Figure 5.26). The mixing and subsequent injection timescale is rather short (within 1 second) using a auto syringe-pump and a mixer, hence there is the lack of 1:2 HG complex (which is formed slowly according to our stopped flow experiments).

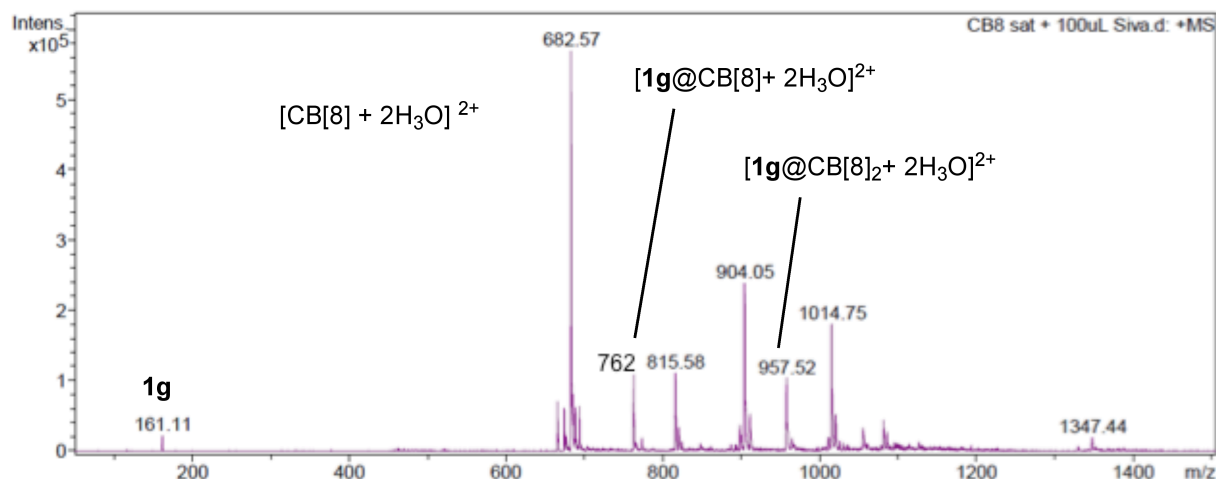


Figure 5.27 The **1g@CB[8]** complexes in the presence of CB[8] aggregates at concentrations of 35 μM for **1g** and near saturation conditions for CB[8]

If we double the concentration of **1g** (78 μM) in the presence of a near saturated solution of CB[8] we see an increase in the 1:1 as well as the 2:1 HG complex (Figure 5.23). This indicated that at near stoichiometric concentrations of host and guest the formation of the 1:1 is much faster than the 1:2 HG complex as previously observed in the stopped flow studies, albeit at lower concentrations. It was also evident (upon comparison of Figures 5.26-5.28) that addition of **1g** to CB[8] led to the de-aggregation of CB[8] species as some masses of CB[8] aggregates are no longer visible in the presence of **1g** ($M/Z = 815.55, 1014.79, 1081.27$ see Figure 5.26).

Previous reports have established that HCl increases the solubility of CB[8] in solution.¹² We were interested in investigating if the addition of HCl to the **1g@CB[8]** mixture would break up the

remaining CB[8] aggregates (Figure 5.29). The addition of 0.3% HCl solution reduced the amount of CB[8] aggregation and it unexpectedly increased the formation of the 1:2 HG complex as revealed by m/z intensity. Thus the small addition of HCl completely changed the complexation of **1g** and CB[8] in solution. It appears that the addition of the HCl promotes the disruption of the CB[8] aggregates and aids the formation of the HG complex (Figure 5.29).

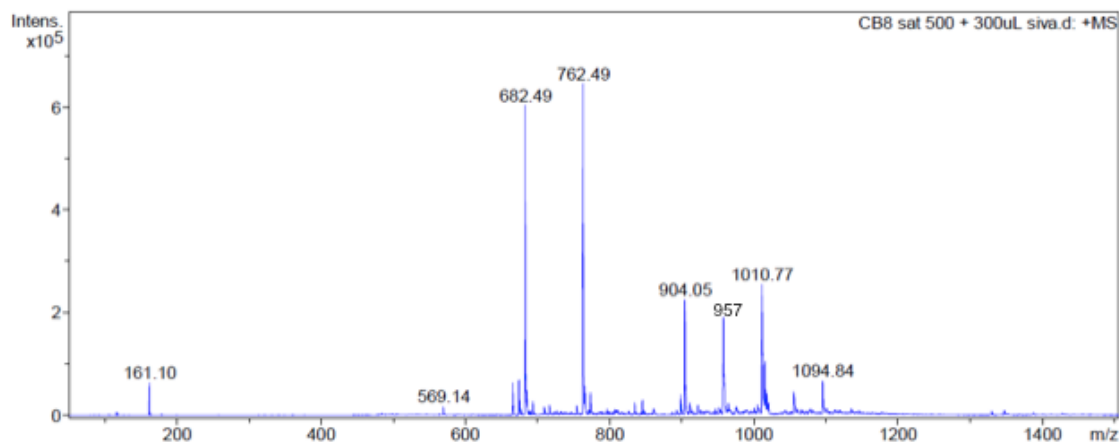


Figure 5.28 The **1g@CB[8]** complexes in the presence of CB[8] aggregates at concentrations of 78 μM for **1g** and near saturation conditions for CB[8]

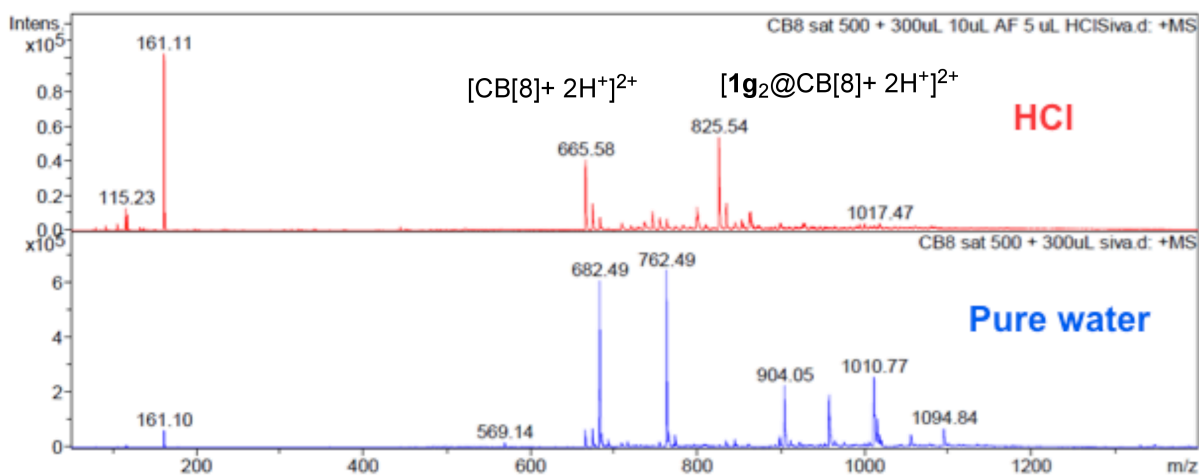


Figure 5.29 A comparison of HG complex (Top) with 0.3% HCl and (Bottom) in pure water of **1g@CB[8]** at concentrations of 78 μM for **1g** and near saturation conditions for CB[8]

An attempt to monitor the formation of the various HG complexes over time was performed by mixing and injecting a solution of CB[8] (50 μM) and **1g** (100 μM) into the mass spectrometer (Figure 5.25). The injections were done using independent syringes of the guest **1g** and host CB[8]. The solutions were mixed together from independent chambers using a T-shaped syringe flow-cell leading to the Ion-Trap mass-spectrometer. The traces show a decrease in the amount of free **1g** (m/z 161) in solution as well as a slight decrease in **1g**@CB[8] (m/z 745). The higher order HG complexes like **1g**₂@CB[8] (m/z 825) and **1g**₃@CB[8] (m/z 904) show a slight increase in formation over time. This result mirrors the relative concentrations that were simulated from the global fitting of the 1:2 HG complex in the stopped flow experiments (Figure 5.12). An additional point to emphasize is that while not quantitative, the time dependent data observed in mass spectrometry is qualitative and clearly shows the decrease in the free **1g** signal and an increase in the HG complex signals. The time dependent measurements show the rise or decay of individual m/z peaks that correspond to free **1g** (m/z 161), 1:1 HG complex (m/z 745) and 1:2 HG complex (825) over a period of 10 minutes.

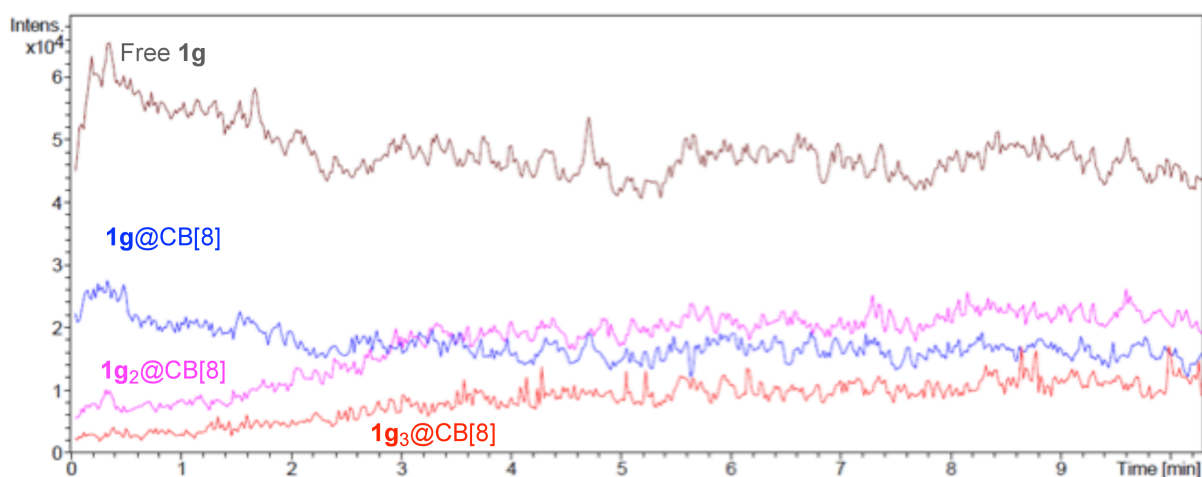


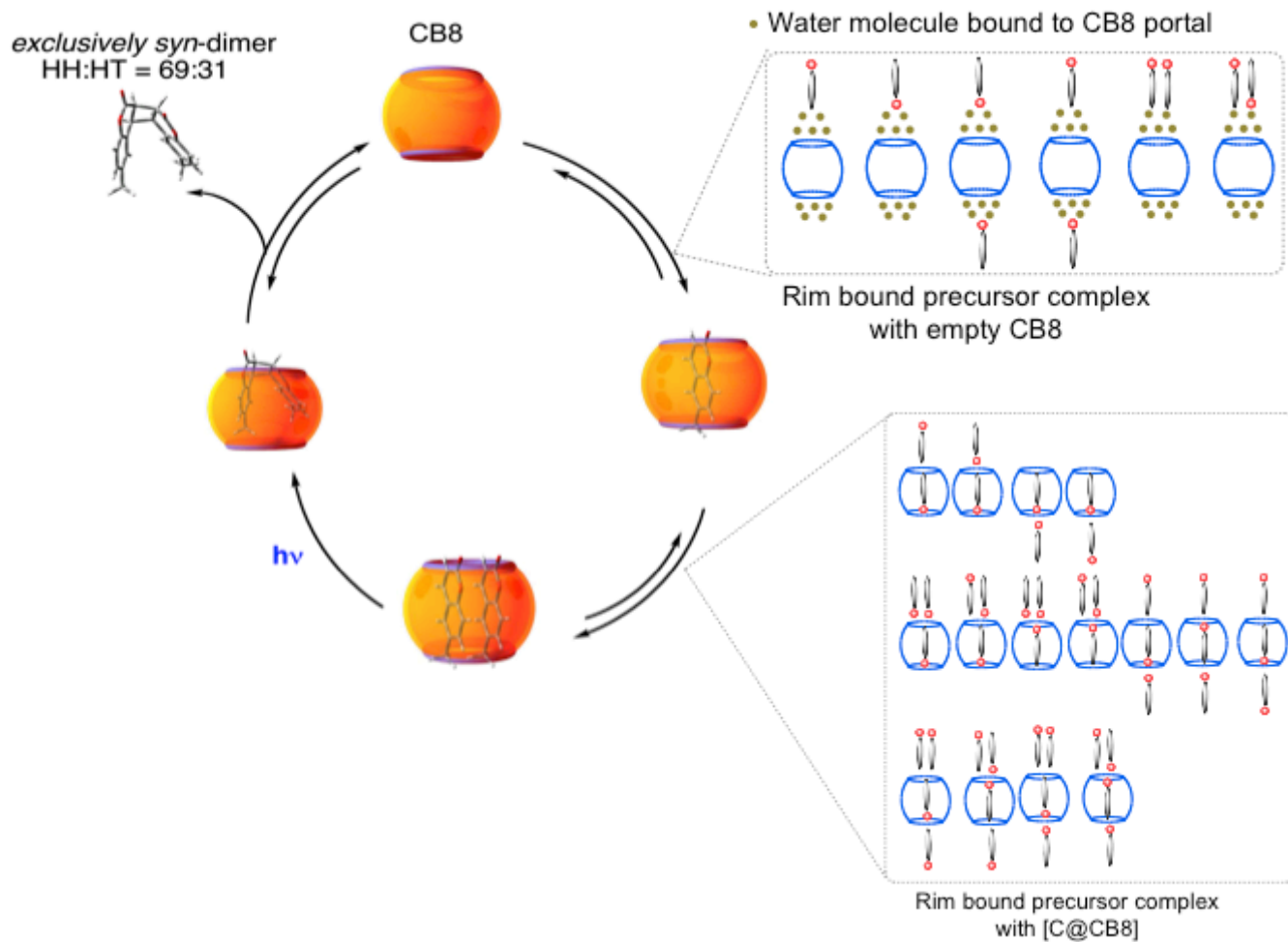
Figure 5.30 Time dependent traces of various HG complexes observed in mass spectroscopic studies. The delay time from mixing to injection is approximately 30 seconds

We believe, due to the results of the aggregation, that there are distinct types of HG complexes involving **1g** and CB[8]. The first type is the HG complex formed within the CB[8] cavity and is observed through the change in photophysical measurements such as absorbance and or fluorescence

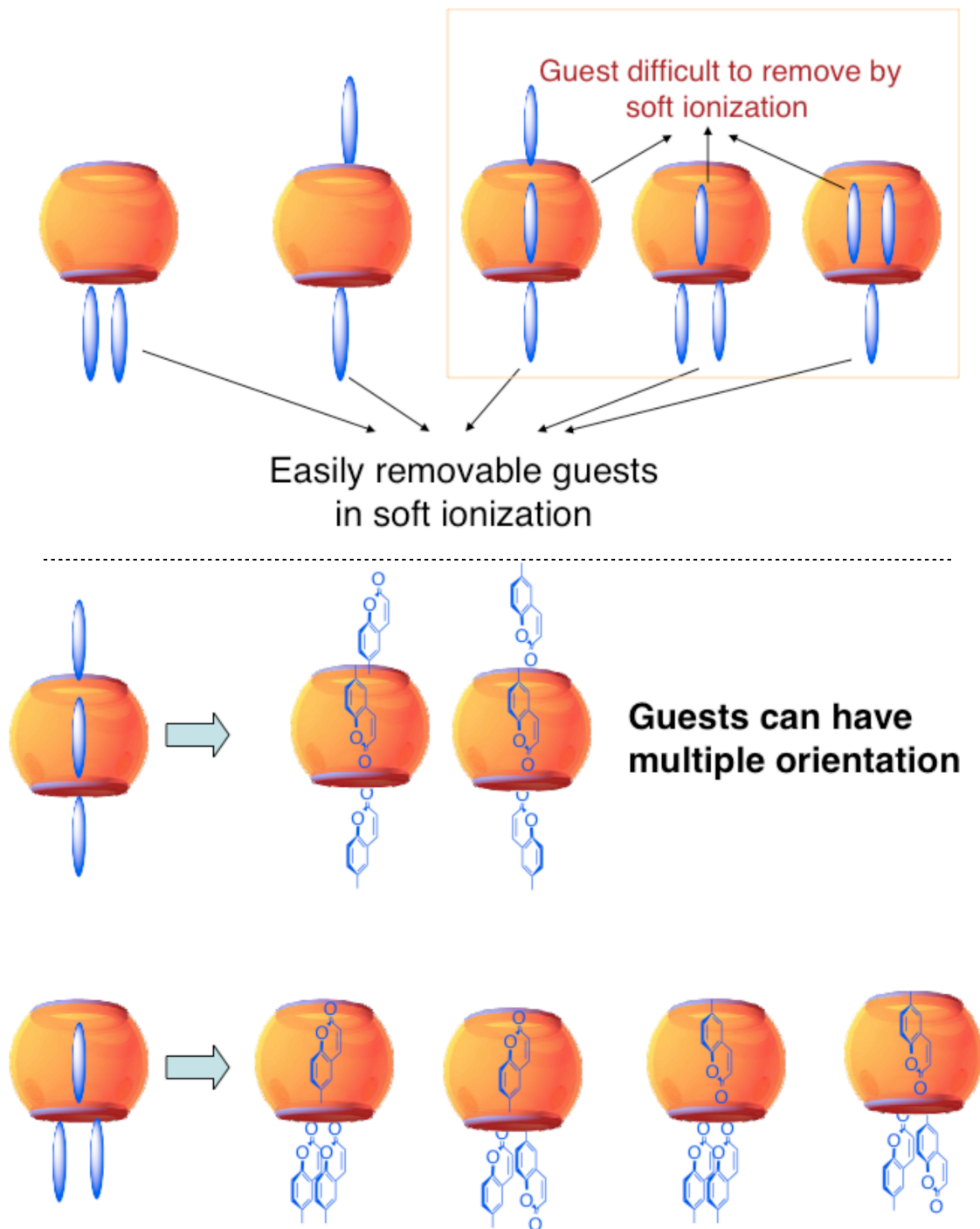
spectroscopy and it can also be observed with single crystal growth of the complex *i.e.*, encapsulated complex or inclusion complex. The second is from the interaction (briefly mentioned in chapter 1) of **1g** with the carbonyl rim of CB[8]. We believe the rim bound **1g** CB[8] complex precedes the inclusion complex, as the guest must interact with the hosts rim before it enters the cavity (Scheme 5.1 and 5.2). Using soft-ionization techniques on the ion-trap mass spectrometry we have observed these complexes in 1:3 HG ratios (Scheme 5.1 and 5.2). Since the volume of the cavity will only allow two guests to be encapsulated, these ratios are the result of rim-bound guests and they can be easily removed using soft-ionization unlike their inclusive counterparts that require higher ionization potentials.

The HG complex observed by mass spectrometry is likely a mixture of HT (observed in single crystal XRD) and HH (the major product in photoreaction). So its likely that the HT orientation is more stable and HH is less stable in solution. Reactivity wise, HH might be more reactive than HT due to the distance and orientation of the double bonds. One can speculate that the minimal increase of reaction velocity (similar velocity) at 10 °C and 30 °C might be due to the offsetting phenomenon with HG complex formation and increased reactivity. In other words, increasing the temperature, favors the HG formation of the HT orientation so the reactivity does not change appreciably.

Time dependent mass spectrometry studies were performed by injecting the samples into a Bruker Daltonics HCT *ultra* mass spectrometer, equipped with an ESI source (Agilent) that utilized a nickel coated glass capillary with an inner diameter of 0.6 mm. Ions were continuously generated by infusing the aqueous solution samples into the source with a syringe pump (Kd Scientific, model 781100, USA) at flow rates of 4 mL/min. The parameters were adjusted and are typically as follows: polarity: positive; capillary voltage: - 4.0 kV; capillary exit voltage: CE = 70 V; skimmer voltage: 25 V; temperature of drying gas: 300 °C. The experiments were carried out with a nebulizer gas pressure of 20 psi and a drying gas flow of 6 L/min. A dual chamber T-shaped syringe with CB[8] and **1g** solutions was used to inject samples into the mass spectrometer for time dependent studies.



Scheme 5.1 Mechanism for rim bound precursory guests forming the 1:1 and 1:2 HG complexes



Scheme 5.2 Guest molecules interacting with CB[8] at the rim

molecule within the cavity, while kinetically slower ($k_{on} = 1.4 \times 10^5 \text{ M}^{-1} \text{ s}^{-1}$ and $k_{off} = 0.13 \text{ s}^{-1} = 7.5 \text{ min}^{-1}$), is thermodynamically more favorable ($K_2 \approx 10^6 \text{ M}^{-1}$). It is clear that there is little to no observed product inhibition preventing the continuation of the catalytic cycle. However, at this moment it is unclear whether or not the rate determining step in the catalytic process is the formation of the 1:2 complex, but current experiments lead us to believe that the rate determining step is related to the formation of the 1:2 complex or steps proceeding it, possibly due to aggregation.

The dynamic nature of the 1:2 HG complex, as observed through stopped flow studies, does not necessarily describe how the produced photoproducts are either *syn*-HH or *syn*-HT. Our current hypothesis for the observed catalytic process is a bifurcated catalytic cycle that can explain why one product is favored over another, along with the observed spectroscopic observations.

The major piece of evidence was the redshift observed in both UV-vis and fluorescence spectroscopy. This is likely the result of a head-to-tail orientation of the coumarin within the CB[8] cavity. This evidence was also backed up by the formation of **4g**, the *syn*-HT photoproduct. A red shift from HT aggregation is not observed for UV-vis absorbance or fluorescence studies of **1e** which would explain why there is no *syn*-HT photoproduct of **4e** formed during the photoreaction (*cf.* chapter 2).

Bifurcated catalysts (Scheme 5.3) begin with both CB[8] and guest (**1g**) aggregates in solution. These aggregates break down in the presence of each other leading to the formation of the 1:1 HG complex which is kinetically fast ($k_{on} = 0.97 \times 10^6 \text{ M}^{-1} \text{ s}^{-1}$ $k_{off} = 14.4 \text{ s}^{-1}$) and driven thermodynamically with a binding association of 10^4 M^{-1} . The subsequent 1:2 HG complex likely forms in two orientations *viz.* head-to-head and head-to-tail as demonstrated by product selectivity (chapter 2 and 3). The head-to-tail orientation is likely red shifted and can be easily observed using UV-vis absorbance and fluorescence, whereas the head-to-head orientation is likely blue shift and is difficult to observe under experimental conditions. The formations of the 1:2 HG complex appears to be rate determining and both of these orientations are likely coupled and impossible to deconvolute both kinetically and thermodynamically. The process for the 1:2 HG complex appears to be driven thermodynamically with a binding association of 10^6 M^{-1} and kinetically slow ($k_{on} = 1.4 \times 10^5 \text{ M}^{-1} \text{ s}^{-1}$ $k_{off} = 0.13 \text{ s}^{-1}$). Upon complexation, the complex absorbs a photon of light and a [2+2] photoreaction occurs efficiently. After the photoreaction has occurred, the photoproduct irreversibly leaves the cavity and the process continues with a turnover number of 3.4 min^{-1} .

5.9. References

**The material in this chapter was co-authored by Barry C Pemberton (BCP), José DaSilva (JDS), Hao Tang (HT), Cornelia Bohne (CB), DK Srivastava, Raushan Singh (RS) and J. Sivaguru (JS). BCP had primary responsibility for preparing samples and collecting data. Ion-trap mass spec and LC/MS studies were performed by JDS. Initial stopped-flow data was collected by RS under the guidance of DK and the data was compiled by BCP. In-depth stopped-flow studies were performed by BCP under the guidance of HT and CB at University of Victoria. BCP processed the data and with help of JS was the primary developer of the conclusions that are advanced here. BCP also drafted and revised all versions of this chapter. JS served as proofreader and checked the math in the statistical analysis conducted by BCP.

- (1) Laidler, K. J.; Meiser, J. H.; Sanctuary, B. C. *Physical Chemistry*; 4th ed.; Houghton Mifflin Company: New York, 2003.
- (2) Buschmann, H.; Scharf, H.-D.; Hoffmann, N.; Esser, P. The Isoinversion Principle—a General Model of Chemical Selectivity *Angew. Chem., Int. Ed.* 1991, 30, 477-515.
- (3) Anslyn, E. V.; Dougherty, D. A. *Modern Physical Organic Chemistry*; University Science Books: Sausalito, Ca, 2006.
- (4) Chan, H. S.; Dill, K. A. Protein folding in the landscape perspective: Chevron plots and non-arrhenius kinetics *Protiens* 1998, 30, 2-33.
- (5) Sandstrom, J. *Dyanmic NMR Spectroscopy*; Academic Press: New York, 1982.
- (6) Connors, K. A. *Binding Constants*; John Wiley: New York, 1987.
- (7) Hollas, M. J. *Modern Spectroscopy*; 4th ed.; John Wiley & Sons: Hoboken, 2004.
- (8) Yu, X.; Scheller, D.; Rademacher, O.; Wolff, T. Selectivity in the Photodimerization of 6-Alkylcoumarins *J. Org. Chem.* 2003, 68, 7386-7399.
- (9) Tang, H.; Fuentealba, D.; Ko, Y. H.; Selvapalam, N.; Kim, K.; Bohne, C. Guest Binding Dynamics with Cucurbit[7]uril in the Presence of Cations *J. Am. Chem. Soc.*, 133, 20623-20633.
- (10) Tang, H.; de Oliveira, C. S.; Sonntag, G.; Gibb, C. L. D.; Gibb, B. C.; Bohne, C. Dynamics of a Supramolecular Capsule Assembly with Pyrene *J. Am. Chem. Soc.*, 134, 5544-5547.

- (11) Pinjari, R. V.; Gejji, S. P. Inverted Cucurbit[n]urils: Density Functional Investigations on the Electronic Structure, Electrostatic Potential, and NMR Chemical Shifts *J. Phys. Chem. A* 2009, *113*, 1368-1376.
- (12) Behrend, R.; Meyer, E.; Rusche, F. I. Ueber Condensationsproducte aus Glycoluril und Formaldehyd *Liebigs. Ann. Chem.* 1905, *339*, 1-37.

CHAPTER 6. MISCELLANEOUS INVESTIGATION: TIPS AND TRICKS LEARNED DURING INVESTIGATIONS**

6.1. Introduction

With five years of research come many side projects. Often these endeavors show an initial promising result, but follow-up experiments do not bear such fruit. Successful and stalled investigations yield subtle techniques that are learned but not always communicated beyond the research group. This chapter will highlight the several small investigations that provide some insight into CB[8] chemistry. The tips and tricks mentioned in this chapter will most likely become outdated in the future as CB research groups spend more time addressing the needs for synthesis, purification and quantification.

6.2. Solid State Dimerization

Solid-state supramolecular complexes have been known for sometime in the form of co-crystalline coordination and as host-guest inclusion complexes.¹⁻¹⁰ Typically these host-guest complexes are formed through mechanical grinding techniques. These solid state complexes have shown increased reactivity as well as the ability to use the coordinating molecule in a catalytic amount.¹¹ Following the report of catalytic photoreaction of solid state host-guest complexes formed through mechanical grinding, we quickly pursued the idea of using CB[8] in catalytic amount to synthesize *syn*-HH **2g** photoproducts by mechanical grinding followed by irradiation.

6.2.1. Solid state host-guest complexes with **1g** and CB[8]

Testing the feasibility of a catalytic solid state complex first requires a test to see if the complex is formed. Previously fluorescence studies were used to show if the **1g** would complex within CB[8]. Therefore the first experiment required would be to grind **1g** and CB[8] together and obtain a solid state fluorescence spectra. The solid state complex was prepared by grinding two equivalents of **1g** with one equivalent of CB[8] in agate mortar and pestle. The mixture was ground for at least 15 minutes until homogenous. The solid mixture was then evenly distributed between two microscope slides and the fluorescence was examined using front-face detection (Figure 6.1). A control sample of neat **1g** was

prepared by grinding for the same period of time. The excitation wavelength was maintained at 340 nm and the emission wavelength was monitored from 360 - 660 nm.

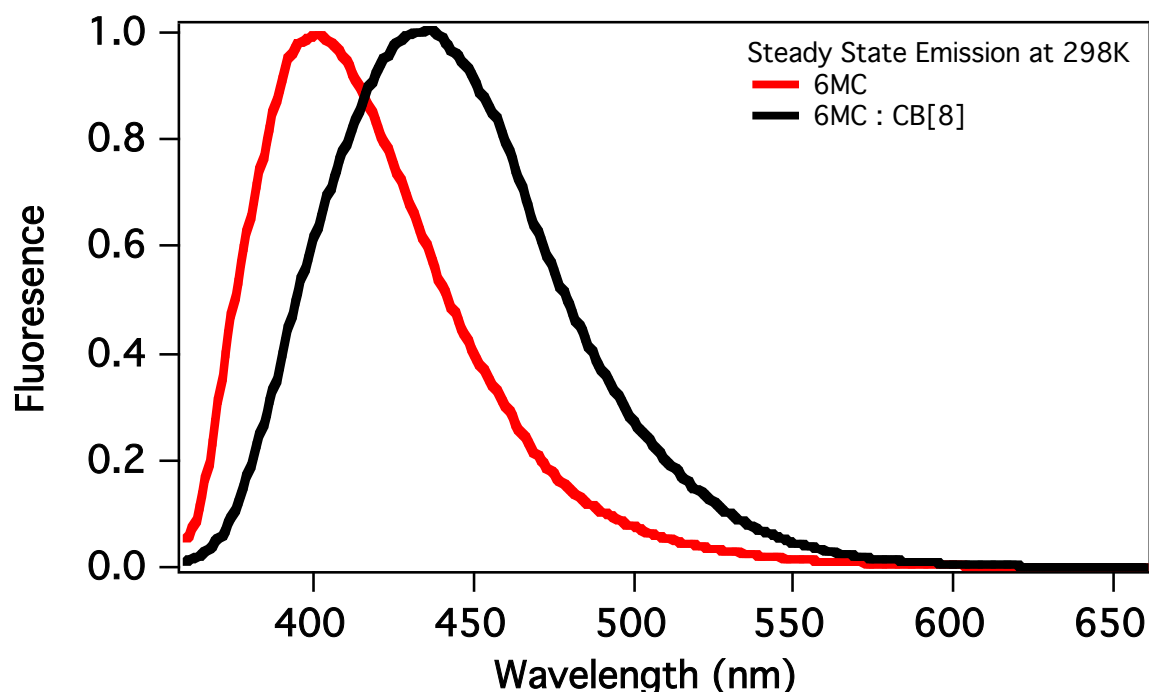


Figure 6.1 The solid state emission spectra of **1g** (red) and a 1:2 mixture of CB[8] : **1g** at 298 K. (black).

$\lambda_{\text{ex}} = 340 \text{ nm}$, $\lambda_{\text{em}} = 360 - 660 \text{ nm}$. Slit width = 4 nm. Front face detection

The emission profile demonstrated a clean redshift for the emission of **1g** when ground with CB[8]. This result mirrored the emission of **1g** in water and demonstrates that a complex can be forced together using mechanical mixing. The host-guest ratio is likely 1:1 because of the fluorescence. Since the mixture had shown a shift in fluorescence the next experiment was to pack the solid into a capillary tube and seal the end. Once the capillary tube is sealed it can be placed in a solution of liquid nitrogen to study the possible phosphorescence signal.

Using the exact same excitation and emission properties as the fluorescence spectra, a steady state emission was taken at 77 K (Figure 6.2). The results from this emission profile were slightly different than the phosphorescence spectra taken in cracked glass. The fine structures for neat **1g** have peaks at 470, 505, and 548 nm. These differences correspond to differences of 1475 and 1553 cm^{-1} . These values do not correspond to carbonyl frequencies and are likely from the aromatic region. The fine structure for

the host-guest complex has lost the third peak in the fine spectra. The differences between the two remaining peaks correspond to a wavenumber of 1404 cm^{-1} , which might be caused by aromaticity as well.

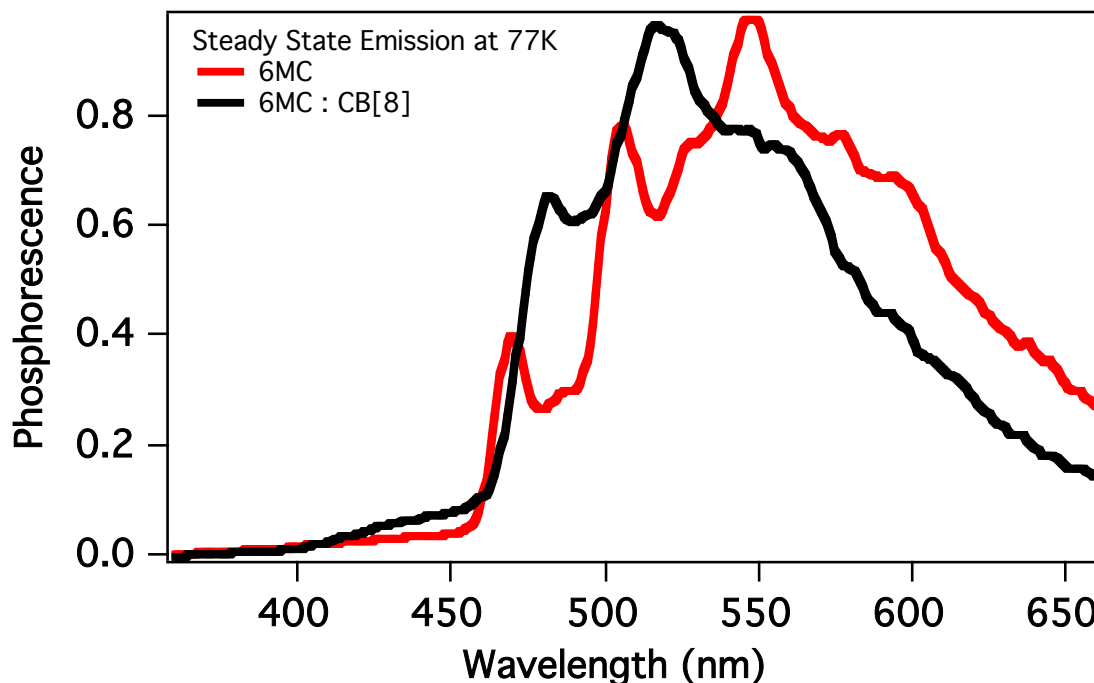


Figure 6.2 The solid state emission spectra of **1g** (red) and a 1:2 mixture of CB[8] : **1g** at 77 K. (black).

$\lambda_{\text{ex}} = 340\text{ nm}$, $\lambda_{\text{em}} = 360 - 660\text{ nm}$. Slit width = 4 nm. Front face detection

6.2.2. Solid state photoreactions of **1g** with various additives after mechanical grinding

These initial results from the complexation study were promising, the next step was to evaluate if the host-guest complex would dimerize under irradiation. Ramamurthy and co-workers have shown that **1g** does not dimerize in solid state.⁹ To see how the orientation of individual **1g** molecules were arranged in the solid state a single crystal of **1g** was grown from a saturated solution of **1g** in water. The crystals grew in the shape of small flat sheets. The analysis of the crystal structure revealed that there was a head-to-head (HH) orientation of the coumarin molecules (Figure 6.3) in one direction and a head-to-tail (HT) orientation in another direction. The distance between the reactive alkene bonds in the HH orientation was on average 4.695 \AA and the distance in the HT orientation is on average 4.40 \AA . These

values are larger than the ideal Schmidt distance (4.20 Å) that is often required for solid state dimerization to occur efficiently.

When the **1g** in the crystalline form was irradiated the product distribution is a ratio of 75 : 8 :12 : 5 for the *syn*-HH **2g** : *syn*-HT **4g** : *anti*-HH **3g** : *anti*-HT **5g** orientations respectively.¹² It is very likely the reaction in the solid state was occurring from defective sites in the crystalline matrix.⁹ Since all the photoproducts are formed from solid state irradiation, we can see if complexation of **1g** with CB[8] or some other compound would effect the dimerization rate and/or selectivity. We can do this by grinding in a catalytic amount of CB[8] along with **1g** into a powder and irradiating it along with a control of ground **1g**.

Mixtures of **1g** with various mol% of CB[8] were ground for 15 minutes and irradiated for 1 hour intervals. These steps were repeated several times for the same sample such that sufficient photoreactions could occur. The photoreactions appeared to give almost exclusively *syn*-HH **2g** photoproducts during these irradiations (Figure 6.4). The product conversion for the ground mixture of **1g**-CB[8] appeared to be higher than the **1g** control. The acceleration of *syn*-HH **2g** photoproduct formation was observed by comparing the methyl peaks of the starting material to product. The presumption was that the CB[8] cavity or at least the carbonyls at the portals were templating the **1g** into an orientation that had a more favorable Schmidt distance for dimerization leading to the *syn*-HH **2g** photoproduct selectivity.

An attempt to monitor the solid state dimerization in the presence of CB[8] was performed by using x-ray powder diffraction. The samples were prepared by grinding 1 equivalent of CB[8] and 2 equivalents of **1g** for 15 minutes and placing the powder on a glass slide. The samples were measured and irradiated over various time intervals. The powder x-ray diffractometer is a Phillips X'pert-MPD (Cu K α X-radiation 40 mA and 45 kV) utilizing Bragg-Brentano para-focusing optics with a scanning rate of 0.01 °/s. The results show a decrease in peaks over time. During the irradiation process the crystallinity was likely changing, but it is unlikely that it is the photoproduct and more likely a melting of the crystal structure (Figure 6.5).

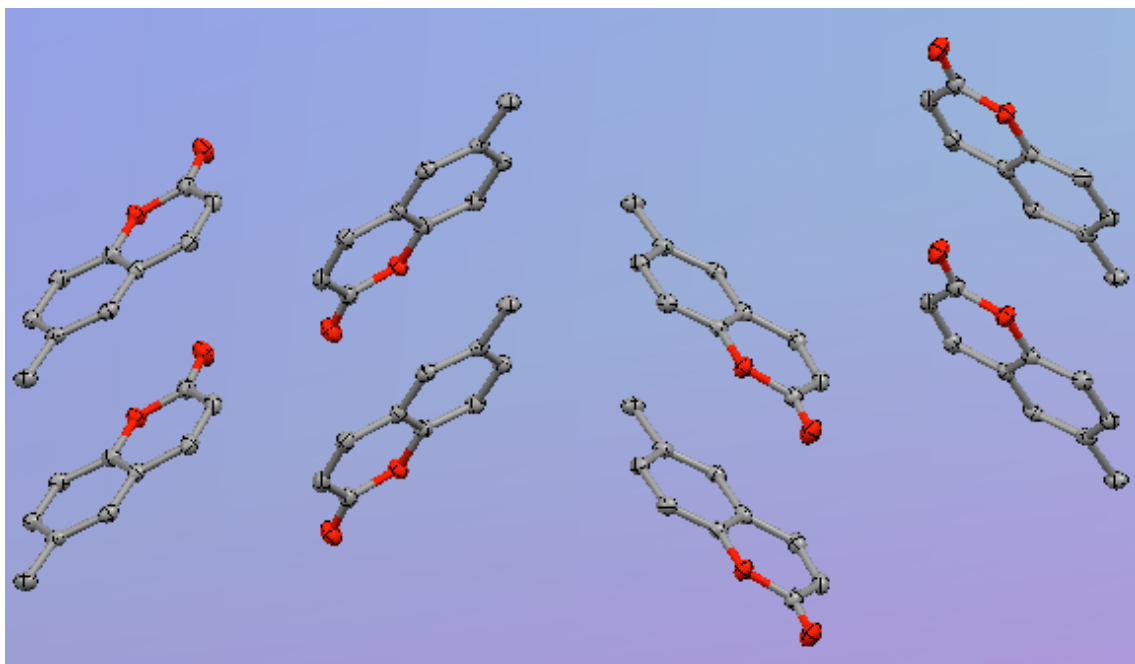


Figure 6.3 Thermal ellipsoid plot showing the packing of **1g** in the *syn*-HH **2g** orientation in the vertical direction and *syn*-HT **4g** in the horizontal direction. Thermal ellipsoids shown at 50%.

To see if the carbonyls from the CB[8] rim were templating the and affecting the dimerization we tested the reaction by templating with thiourea by grinding it with **1g**. The thiourea functional group has been used extensively as a catalytic reagent and a templating additive.^{11,13-15} The thiourea moiety functions as a bifurcated hydrogen bond donor. These hydrogen bonds are especially efficient at donating to carbonyl groups like the ones found on coumarin. The NMR results show more of the same photoproducts that the addition of a hydrogen bonding co-crystal allows for enhanced rates of dimerization (Figure 6.6) of **1g** with selective formation of *syn*-HH **2g** photoproduct.

The effect of thiourea on conversion appeared to slow down the rate of dimerization compared to the results from CB[8] mechanical grinding and pure **1g** followed by irradiation. This was interpreted as the CB[8] was templating and promoting the dimerization process in the solid state upon irradiation. Mechanical grinding of thiourea and **1g** followed by irradiation led to **2g** formation and this was thought to bind thiourea and **1g** through hydrogen bonding that promotes an increased rate of dimerization. The increased rate of dimerization is not exactly quantifiable since powdered samples aren't completely uniform due to scattering of light.

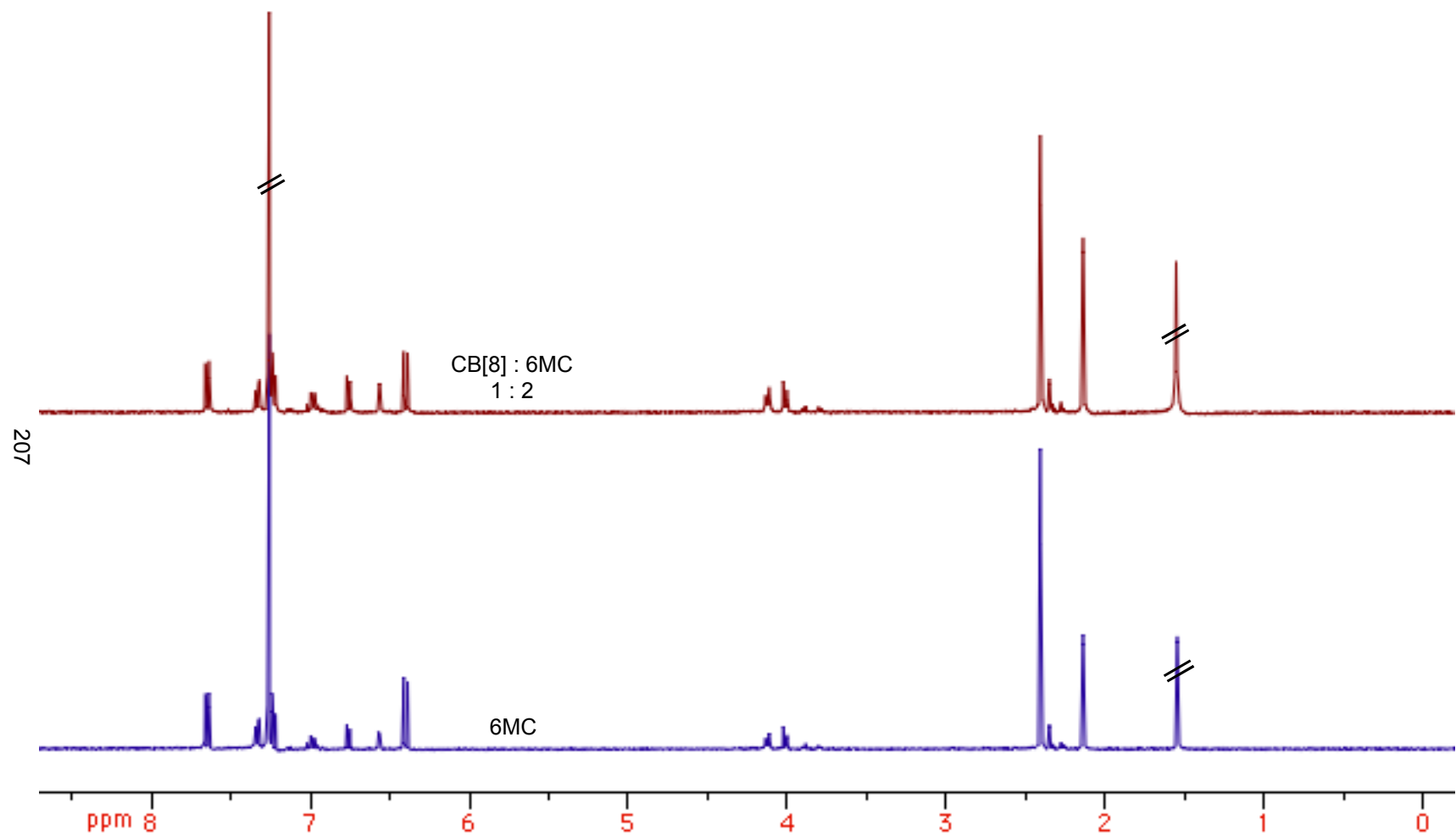


Figure 6.4 ¹H-NMR spectra of solid state dimerization (1 h irradiation) of **1g** with and without CB[8] after mechanical grinding

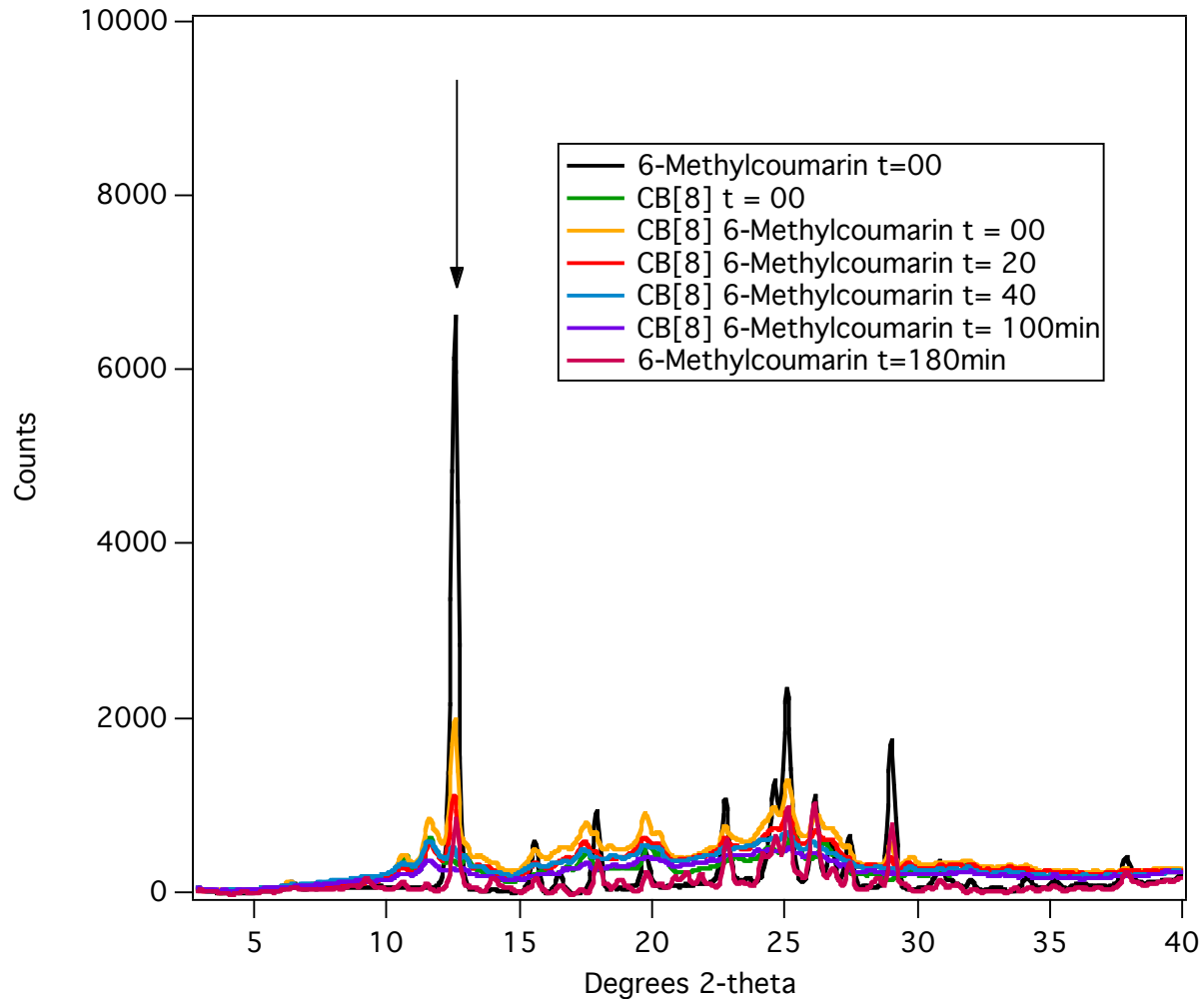


Figure 6.5 Powder x-ray diffraction of **1g** with and without CB[8] at various time intervals. The poor baseline is likely due to x-ray reflections from the amorphous glass slide

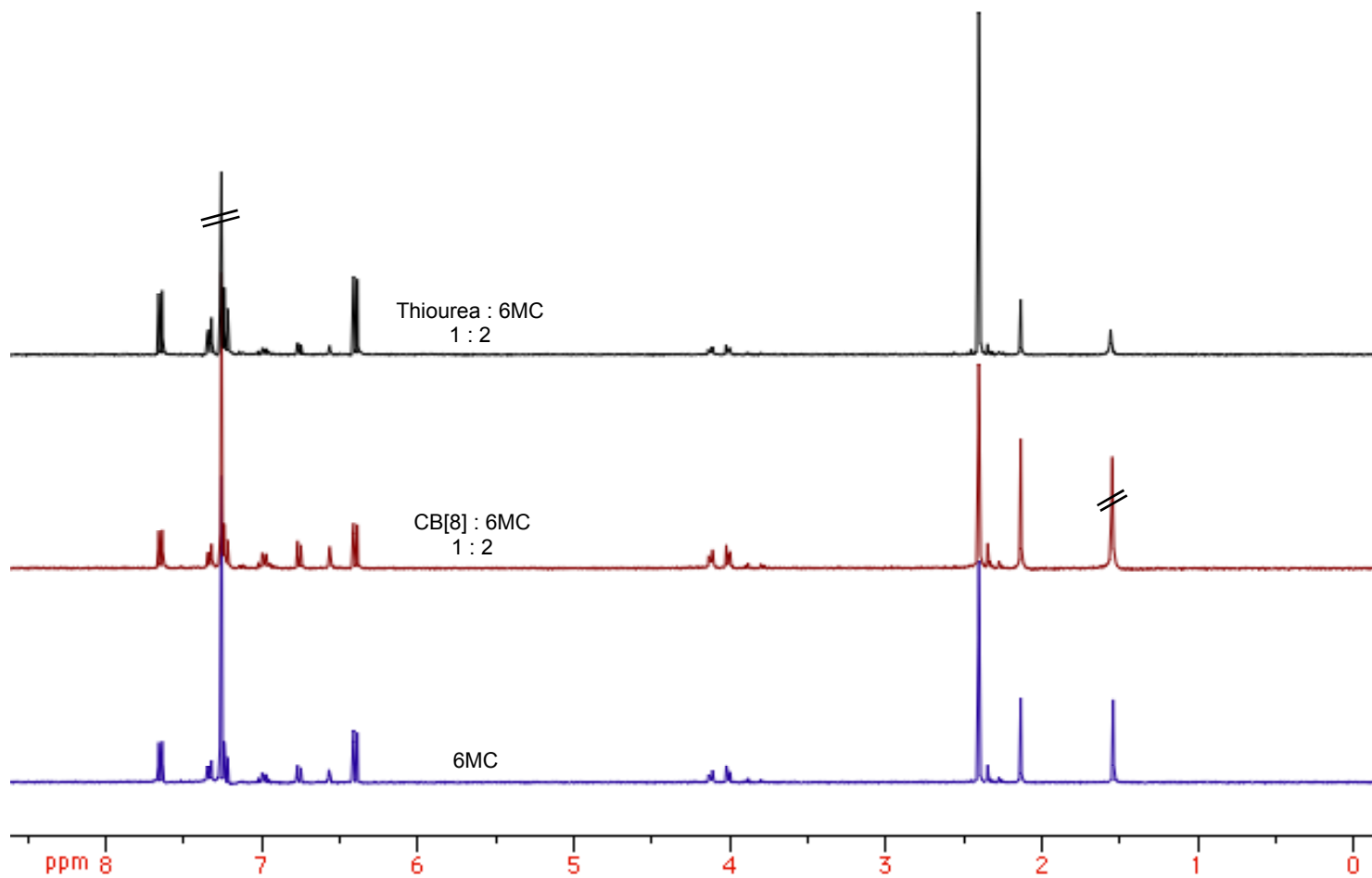


Figure 6.6 $^1\text{H-NMR}$ spectra of solid-state dimerization (1 h irradiation) of **1g** with and without mechanical grinding: (Blue) **1g**, (Red) with CB[8] and (Black) with thiourea

A large-scale reaction was performed by using 100 mg of **1g** along with one-equivalent of thiourea. A mixture of thiourea and **1g** were ground together and sandwiched between two 20 x 20 cm glass plates and irradiated for 13 hours in the photo-cabinet. After the irradiation time the sample was placed into a filter lined Buchner funnel under vacuum and rinsed with chloroform. Since thiourea was completely insoluble in chloroform the **1g** and the photoproduct formed was efficiently extracted from the photo-irradiated mixture. Instead of inhibiting the reaction, the increased amount of thiourea actually increased the rate of dimerization.

Due to the large conversion of **1g** to *syn*-HH **2g** with the addition of thiourea followed by mechanical grinding and photo irradiation, the photoreaction appeared to be accelerated. The purification of the *syn*-HH **2g** was accomplished by running a chromatography on a silica column using 100% hexane as the solvent. Other photoproducts of **1g** have been shown to break down on the silica column.¹² The first compound eluted was the **1g** starting material, and the second compound eluted was the *syn*-HH **2g** dimer. The photoproduct was allowed to recrystallize from the hexane.

The *syn*-HH **2g** photoproduct appeared to be completely insoluble in water. The product was soluble in polar organic solvents such as dimethylsulfoxide (DMSO) and ethylacetate. Crystals of the *syn*-HH **2g** photoproduct were dissolved in DMSO and slowly added to water in an attempt to create solutions for inhibition studies (Chapter 5) by overcoming the crystal lattice energy of the structure. The moment water was added to the solution became cloudy and precipitated. Similarly when the **2g** crystals were mixed with a solution of CB[8], and sonicated with heating for several days there was no noticeable solubilization.

A single crystal x-ray of the **1g** *syn*-HH **2g** photoproduct was collected and was found to be identical to the reported structural features in literature.¹² The synthesis and purification of the compound was facile, other characterization such as ¹³C and ¹H-¹H COSY-NMR was performed (Figure 6.7 and Figure 6.8 respectively). The ¹³C NMR clearly shows ten carbon peaks, which was expected since the photoproduct is symmetrical. The ¹H-¹H COSY-NMR shows the correlation between the cyclobutyl protons as well as the correlation between the aromatic protons. The synthesis and purification of *syn*-HH **2g** through solid state grinding with thiourea was quite surprising as mechanical grinding that led to templating of **1g** was selective leading to the formation of **2g**.

As mechanical grinding of **1g** with thiourea (or CB[8]) followed by photoirradiation led to efficient and selective dimerization, it led us to question if the mechanical grinding of **1g** with additives is creating defects in the **1g** crystals. To test this we added 1 equivalent of adamantane, which lacks the ability to hydrogen bond, to two equivalents of **1g** and repeated the grinding and irradiation procedures. The photoirradiation of the mechanically ground mixture of adamantane-**1g** led to the **2g** photoproduct exclusively but with a slower rate of conversions.

6.2.3. Results and discussion

The mechanically ground complexes of **1g** with the various additives (CB[8], thiourea, (or) adamantane) show an increased rate of dimerization compared to neat **1g**. Our current understanding of the mechanism of dimerization for the **1g**, leading to selectivity of the **2g** product, likely proceeds through crystalline defects produced by mechanical grinding with additives. The addition of any additive (CB[8], thiourea, adamantane (or) any solid) to **1g** followed by mechanically grinding increases the number of imperfections and allows the dimerization to proceed more efficiently. This hypothesis was substantiated by the increased conversion during photoreactions by increasing the number of grinding intervals and time used for each grinding. While the resulting initial investigations looked promising and the ability to synthesize and purify *syn*-HH **2g** in large-scale quantities were successful, the investigation yielded little interest.

6.2.4. General methods

The solid-state chemicals **1g**, thiourea, and adamantane were all purchased from Alfa Aesar. Thiourea and **1g** were used without further purification. Adamantane was recrystallized from petroleum ether to remove the brown color from the solid. Organic solvents such as chloroform and hexane were used without further purification. CB[8] was synthesized as previously noted in Chapter 2. Each sample was ground for 15 minutes using a mortar and pestle and then sandwiched between two sheets of glass (<295 nm cutoff) and irradiated at a perpendicular angle to the light source. The organic compounds were then extracted with chloroform and the NMR spectra were recorded in CDCl₃.

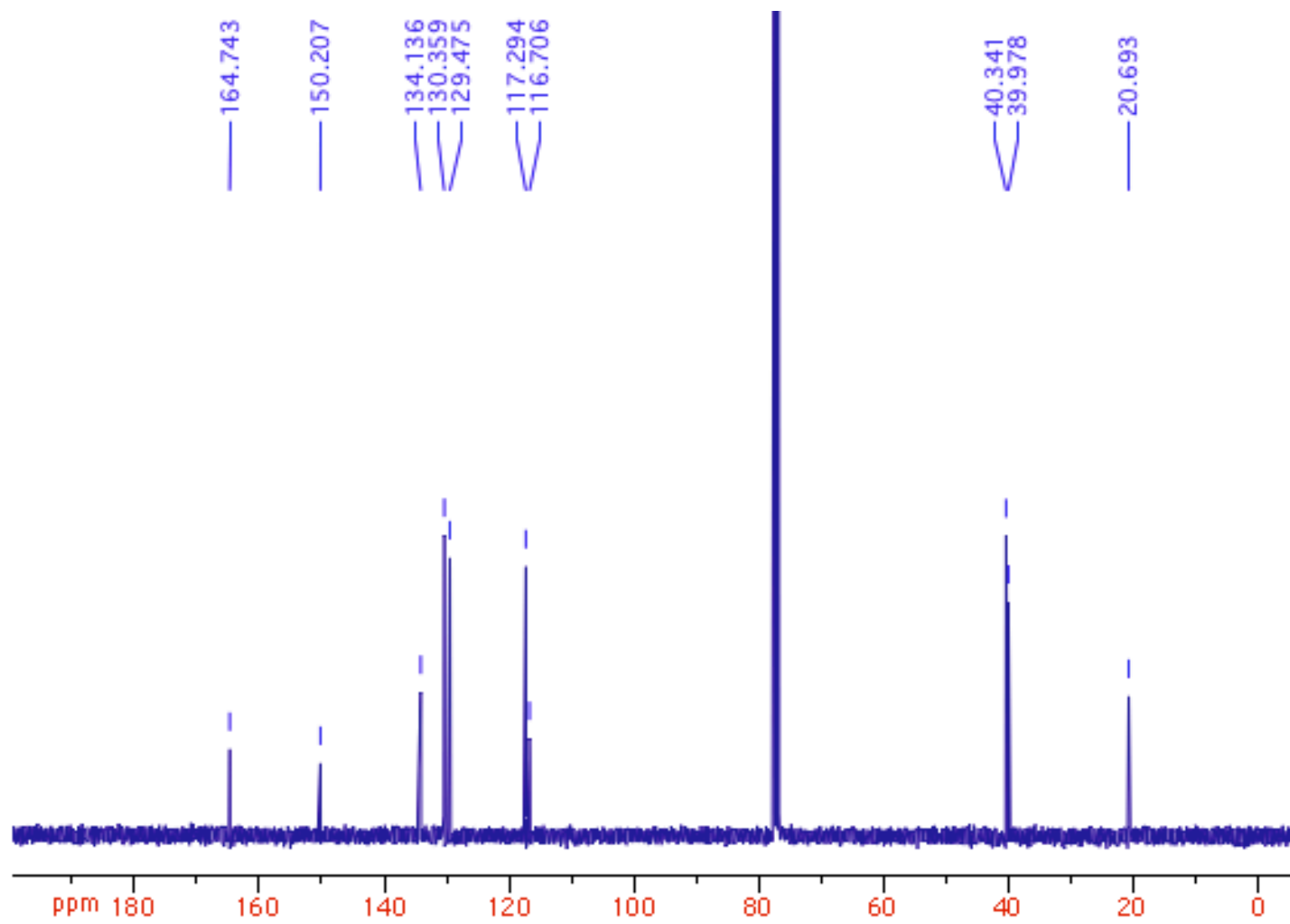


Figure 6.7 ^{13}C NMR of *syn*-HH **2g** photoproduct in CDCl_3

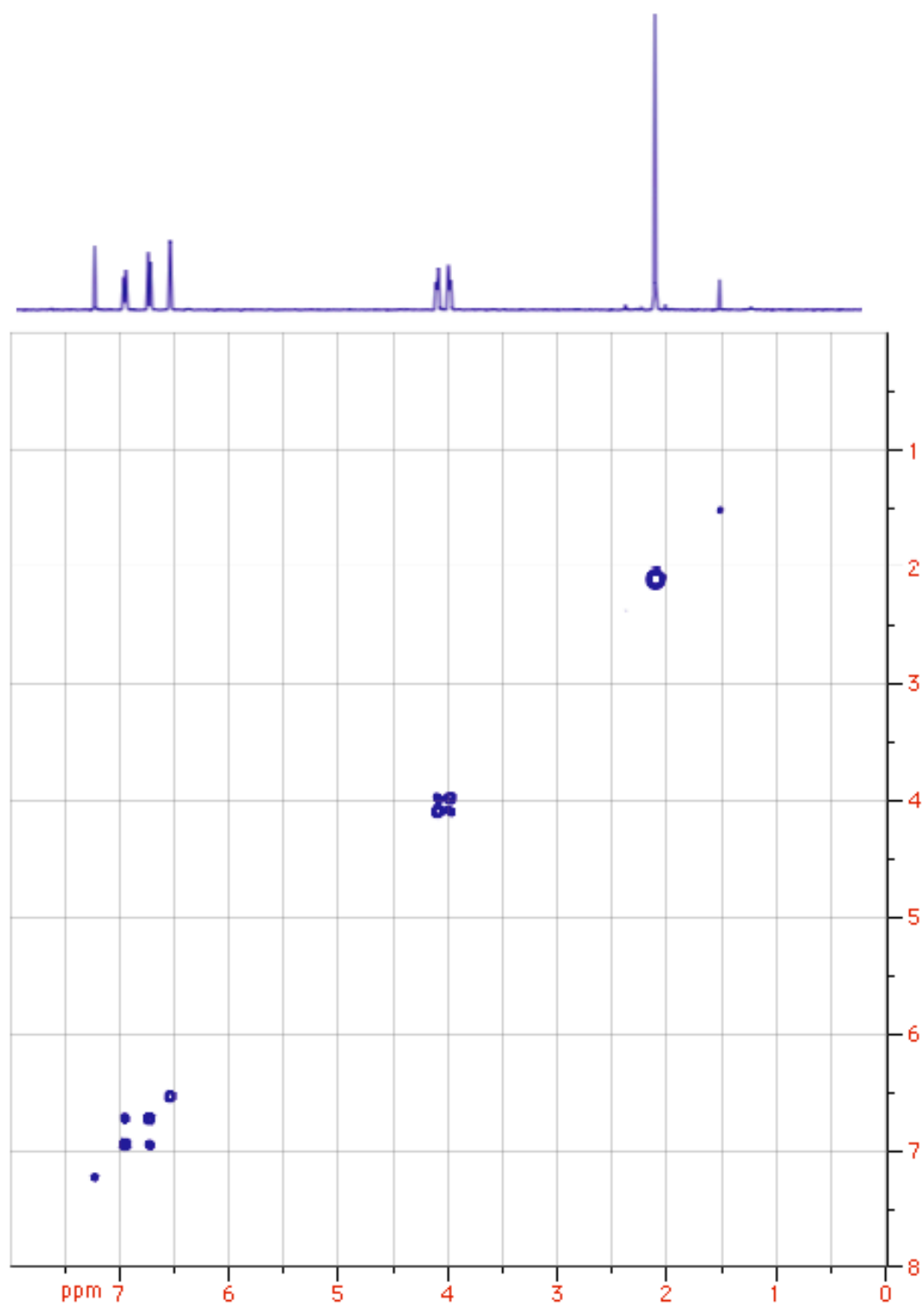


Figure 6.8 ^1H - ^1H COSY-NMR spectra of *syn*-HH **2g** photoproduct in CDCl_3

6.2.5. Characterization of **2g** *syn*-HH **2g** photoproduct via ^1H and ^{13}C NMR

NMR resonances for the purified *syn*-HH **2g** photoproduct. ^1H NMR (400 MHz, CDCl_3 , δ ppm) 6.957 (d, 1 H $J = 8.4\text{Hz}$), 6.731 (d, 1 H, $J = 8.4\text{Hz}$), 6.543 (s, 1H), 4.12-3.974 (m, 1H), 2.11 (s, 3H). ^{13}C NMR (100 MHz, CDCl_3 , δ ppm) 164.7, 150.2, 134.1, 130.4, 129.5, 117.3, 116.7, 40.3, 39.9, 20.7.

6.2.6. Characterization of **1g** and **2g** by single crystal X-ray diffraction

Parameters for the single crystal x-ray analysis for **1g** and the *syn*-HH **2g** photoproduct were collected on a Bruker Apex Duo diffractometer with a Apex 2 CCD area detector at $T = 100\text{K}$. Cu. All structures were processed with the Apex 2 v2010.9-1 software package (SAINT v. 7.68A, XSELL v. 6.3.1). Direct method was used to solve the structures after multi-scan absorption corrections. Details of data collection and refinement are given in the Table 6.1 below.

6.3. Synthesis of *syn*-HT **4g** Photoproduct

A report by Wolff and co-workers¹² shown the irradiation of **1g** (0.2 M) with $\text{BF}_3\text{-Et}_2\text{O}$ (0.2 M) in dry dichloromethane for 7.5 hours produced *syn*-HT **4g** photoproduct in 63.3%. Adding $\text{BF}_3\text{-Et}_2\text{O}$ to **1g** in dry dichloromethane resulted in crystals that were analyzed by XRD. The crystals were collected and taken for x-ray analysis. The results show that the BF_3 molecule bound to a **1g** molecule and this $\text{BF}_3\text{-1g}$ complex is insoluble in solution (Figure 6.10). The photoirradiation of this solution with crystalline **1g**- BF_3 yielded *syn*-HH, *syn*-HT **4g** and *anti*-HT **5g**. *syn*-HT **4g** was the major product with a total conversion of 14%. The reported photoproduct selectivity was trace : 56 : 28 : 12 for *syn*-HH, *syn*-HT **4g**, *anti*-HH **3g** and *anti*-HT **5g** respectively with a total conversion of 30.7%. The conversion of *syn*-HT **4g** photoproduct is roughly 56% a value that was close to the report literature value (63.3%).¹²

While the conversion of *syn*-HT **4g** was close in value, there was no mention of a crystalline complex between **1g** and BF_3 in the Wolff paper.¹² The crystalline structure does not allow for the orientation of *syn*-HT **4g** photoproduct to be formed, so the orientation of the photoproduct must occur in solution. Any trace of water would change the BF_3 to boronic acid, therefore this crystal structure is a testament to the absolute dry conditions that is needed for the formation of the **1g**- BF_3 complex. The

addition of the BF₃ a lewis acid likely promotes the n-π* excited singlet state in **1g** increases the quantum yield of the reaction.^{12,16} Such BF₃ mediate control of excited states is well established in literature.^{16,17}

Table 6.1 Single crystal X-ray parameters of **1g** and **2g**

	1g	<i>syn</i> -HH 2g
Formula	C ₁₀ H ₈ O ₂	C ₂₀ H ₁₆ O ₄
FW	160.16	320.33
cryst. size_max [mm]	.21	.171
cryst. size_mid [mm]	.09	.098
cryst. size_min [mm]	.05	.057
cryst. system	Orthorhombic	Monoclinic
Space Group, Z	P2(1)2(1)2(1), 4	C2/c, 8
a [Å]	4.6946(1)	21.8547(13)
b [Å]	5.8090(1)	7.0665(4)
c [Å]	28.1141(5)	19.7561
α [Å]	90	90
β [Å]	90	97.699
γ [Å]	90	90
V [Å³]	766.70(3)	3023.6(3)
ρ_{calc} [g/cm³]	1.388	1.407
μ [cm⁻¹]	0.789	.800
Radiation Type	Cu	Cu
F(000)	336	1344
no of measured refl.	4454	11676
no of indep. refl.	1326	2589
no of refl. (I ≥ 2σ)	1300	2471
Resolution [Å]	.84	.84
R1/wR2 (I ≥ 2σ)^a [%]	3.05 / 8.82	3.58 / 9.81
R1/wR2 (all data) [%]	3.43 / 10.39	3.46 / 9.69

[a]] $R1 = \sum ||F_o| - |F_c|| / \sum |F_o|$, $wR2 = [\sum w[(F_o)^2 - (F_c)^2]^2 / \sum w(F_o)^2]^{1/2}$ for $F_o^2 > 2\sigma(F_o^2)$, $w = [\sigma^2(F_o)^2$

+ (AP)² + BP]⁻¹ where $P = [(F_o)^2 + 2(F_c)^2] / 3$ and A, B coefficients for your compounds as follow.

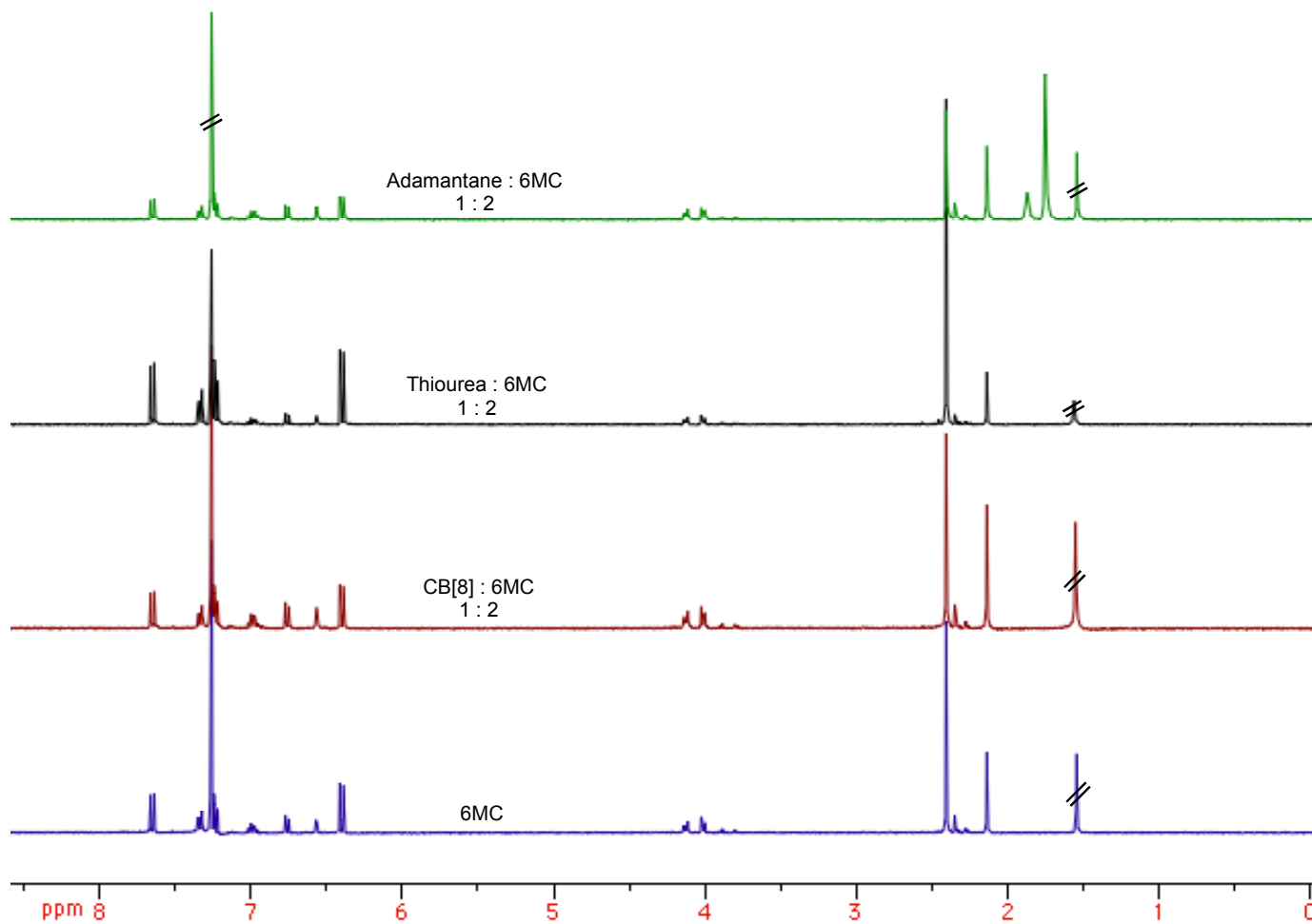


Figure 6.9 ^1H NMR spectra of solid-state photodimerization (1 hour irradiation) of **1g** upon mechanical grinding: (Blue) **1g**, (Red) in the presence of CB[8], (black) in the presence of thiourea, (green) in the presence of adamantane

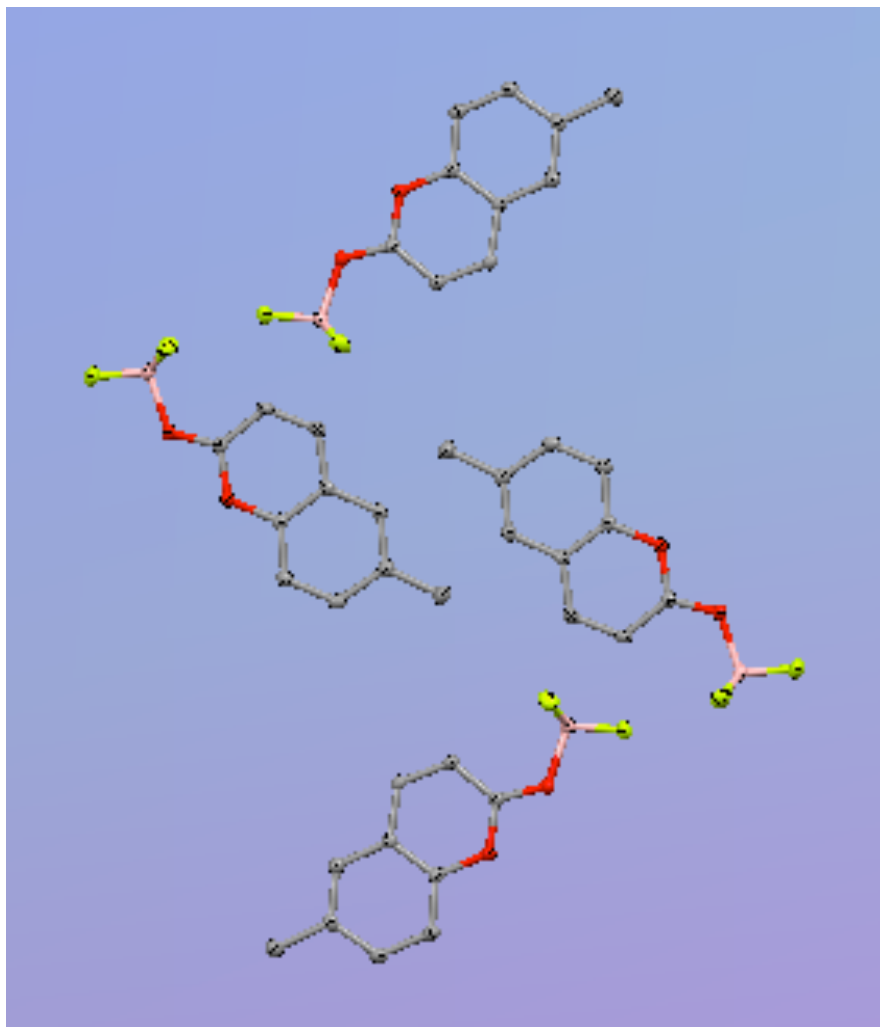


Figure 6.10 Top view of the thermal ellipsoid plot of **1g** templated by BF_3 with the thermal ellipsoids shown at 50%

6.4. Miscellaneous Tips and Tricks

6.4.1. CB[8] synthesis and cleanup

Beyond the synthesis and characterization of CB[8] written in chapter 2 there are several tricks that need to be noted. Through the advancement of future synthetic strategies these techniques will not be required, but they currently provide a troubleshooting platform. When washing samples, all CB[n] compounds are slightly soluble, with CB[8] being the least soluble. This does not mean washing and purification can be performed with little care. The CB[n] synthesis process is nearly quantitative.¹⁸

Recycling of impure mixtures is perfectly acceptable. Therefore one should never dispose of CB[n] solutions until reclamation of all desired CB[n] oligomers is achieved. As subsequent washing steps lead to purer products it is also important to use as little of the 60% formic acid and water solution as possible to remove CB[6] and CB[7] from CB[8].

Table 6.2 Single crystal X-ray parameters of BF₃-**1g** complex

Parameters	1g -BF ₃
Formula	C ₁₀ H ₈ BF ₃ O ₂
FW	227.97
cryst. size_max [mm]	0.22
cryst. size_mid [mm]	0.11
cryst. size_min [mm]	0.10
cryst. system	Orthorhombic
Space Group, Z	Pnma, 4
a [Å]	17.196(2)
b [Å]	6.6177(8)
c [Å]	8.3291(11)
α [Å]	90
β [Å]	90
γ [Å]	90
V [Å ³]	947.8(2)
ρ _{calc} [g/cm ³]	1.598
μ [cm ⁻¹]	.146
Radiation Type	Mo
F(000)	464
no of measured refl.	8428
no of indep. refl.	1174
no of refl. (I ≥ 2σ)	1072
Resolution [Å]	.77
R1/wR2 (I ≥ 2σ) ^a [%]	2.84 / 7.81
R1/wR2 (all data) [%]	3.12 / 8.05

[a]] $R1 = \sum ||F_o| - |F_c|| / \sum |F_o|$, $wR2 = [\sum w[(F_o)^2 - (F_c)^2]^2 / \sum w(F_o)^2]^1/2$ for $F_o^2 > 2\sigma(F_o^2)$, $w = [\sigma^2(F_o)^2 + (AP)^2 + BP]^{-1}$ where $P = [(F_o)^2 + 2(F_c)^2] / 3$ and $A (B) = 0.0436 (0.3746)$;

Washing glassware containing CB[n]s can be difficult, this is compounded by the solubility and “stickiness” of the samples from the acid conditions. The best way to wash glassware is to use saturated sodium chloride solutions. The sodium ions bind to the cavity increasing the solubility and dissolving the

remaining CB[n]. If the sodium chloride solution fails to clean the glassware, the glassware can be baked at approximately 550 °C for 24 hours. Any remaining carbon residuals can be rinsed with methanol.

6.4.2. Photophysical measurements

When performing binding constants the measurement of a signal change at a specific wavelength can introduce noise into the experiment. This can be avoided by taking an average of three runs. A better option is to integrate the signal thus removing any noise. If the integration of the signal over the entire emission wavelength yields a similar value for each sample, then integration from one specific wavelength to another should remedy this problem. Ideally one should not need to integrate the Raman scattering of fluorescence light near the beginning of the spectra.

When performing fluorescence lifetime measurements the NANOLed light source will be slightly different over time. The NANOLed will heat up and this will change the response and the lamp profile. When using the light source over extended periods of time one must take care to periodically take prompts with a light scattering solution of Ludox or starch in water. The transmission of the light without scattering is important to consider as well. During the collection of lifetimes there is a green or red icon at the bottom right hand corner of the DataStation program screen that tells if the light intensity is too high (Figure 6.11) . The correct concentration of scattering solution should yield both a signal and a green icon at the bottom of the screen, if the scattering solution is too high a red icon will show up. If the scattering solution is too high, dilute by removing the majority of the sample and replacing with clean water. This will reduce the amount of offset required when fitting to the signal – lamp response.

When fitting the fluorescence signal, one may encounter various errors. The most common error will be the “shift limit exceeded.” This occurs when too much light is allowed to reach the detector and can be controlled by either collecting data for a shorter period of time or closing the monochromator to the detector. If the quantum yield of fluorescence is sufficiently low then this cannot be avoided. The second fix should be to collect the lamp profile with scatter solution under such conditions that the collection time for sample and lamp profile are nearly identical. This will give both traces a similar offset, and the fitting program will be accurate. If both controls have been performed and the error still exists, then it is proper to change the offset value in the fitting program.

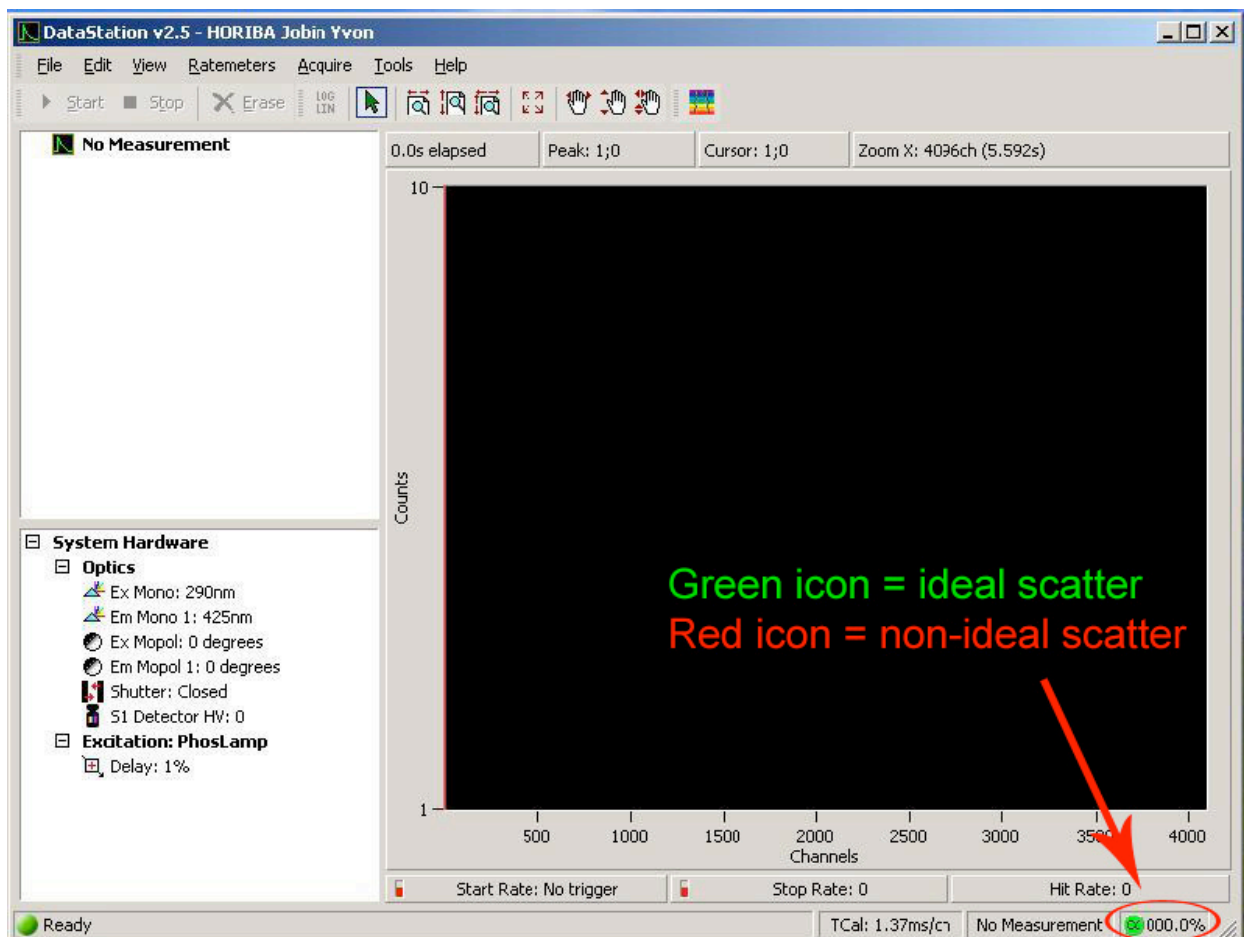


Figure 6.11 Screen shots from DataStation v2.5 computer program showing the light scatter icon

Job's plot parameters can be ascertained, especially if one of the interacting compounds is "uncolored" at the region of interest. In the typical method of continuous variation, the total concentration of the two compounds is constant. You do not need to perform a method of continuous variation (total concentration) if one compound is uncolored as the change in epsilon ($\Delta\epsilon$) of the colored compound and complex will be a result of the total amount of compound added and correcting for total concentration.¹⁹

6.5. References

**The material in this chapter was co-authored by Barry C Pemberton (BCP), Sabine Volla (SV), Angel Ugrinov (AU) and J. Sivaguru (JS). BCP had primary responsibility for preparing samples and collecting data, whereas SV assisted in collection of reaction data. Both single crystal and powder X-ray

diffraction samples were created by BCP and SV whereas the data was collected and processed by AU. BCP with help of JS was the primary developer of the conclusions that are advanced here. BCP also drafted and revised all versions of this chapter. JS served as proofreader and checked the math in the statistical analysis conducted by BCP.

- (1) MacGillivray, L. R.; Siebke, M. M.; Reid, J. L. Coplanar Recognition by a Rebek Cleft Is Provided by Cooperative Structural Effects Involving a Combination of Forces *Org. Lett.* **2001**, *3*, 1257-1260.
- (2) Papaefstathiou, G. S.; MacGillivray, L. R. Discrete versus Infinite Molecular Self-Assembly: Control in Crystalline Hydrogen-Bonded Assemblies Based on Resorcinol *Org. Lett.* **2001**, *3*, 3835-3838.
- (3) Elacqua, E.; Bucar, D.-K.; Skvortsova, Y.; Baltrusaitis, J.; Geng, M. L.; MacGillivray, L. R. Dramatic Red-Shifted Fluorescence of [2.2]Paracyclophanes with Peripheral Substituents Attached to the Saturated Bridges *Org. Lett.* **2009**, *11*, 5106-5109.
- (4) Hamilton, T. D.; MacGillivray, L. R. Enclosed Chiral Environments from Self-Assembled Metal-Organic Polyhedra *Cryst. Growth Des.* **2004**, *4*, 419-430.
- (5) Sokolov, A. N.; Frišćić, T.; Blais, S.; Ripmeester, J. A.; MacGillivray, L. R. Persistent One-Dimensional Face-to-Face π -Stacks within Organic Cocrystals *Cryst. Growth Des.* **2006**, *6*, 2427-2428.
- (6) Dutta, S.; Bucar, D.-K.; MacGillivray, L. R. Resorcinol-Templated Synthesis of a Cofacial Terpyridine in Crystalline π -Stacked Columns *Org. Lett.*, *13*, 2260-2262.
- (7) MacGillivray, L. R.; Papaefstathiou, G. S.; Reid, J. L.; Ripmeester, J. A. A Rod-Shaped Guest Leads to Architectural Isomerism in a Multicomponent Crystalline Framework Based on a Resorcin[4]arene *Cryst. Growth Des.* **2001**, *1*, 373-375.
- (8) Sokolov, A. N.; MacGillivray, L. R. Supramolecular Ladders: Self-Assembly Fintium to Adfintium *Cryst. Growth Des.* **2006**, *6*, 2615-2624.
- (9) Gnanaguru, K.; Ramasubbu, N.; Venkatesan, K.; Ramamurthy, V. A study on the photochemical dimerization of coumarins in the solid state *J. Org. Chem.* **1985**, *50*, 2337-2346.

- (10) Pattabiraman, M.; Natarajan, A.; Kaanumalle, L. S.; Ramamurthy, V. Templating Photodimerization of trans-Cinnamic Acids with Cucurbit[8]uril and γ -Cyclodextrin *Org. Lett.* **2005**, *7*, 529-532.
- (11) Sokolov, A. N.; Bucar, D.-K.; Baltrusaitis, J.; Gu, S. X.; MacGillivray, L. R. Supramolecular Catalysis in the Organic Solid State via Dry Grinding. *Angew. Chem., Int. Ed.* **2010**, *49*, 4273-4277.
- (12) Yu, X.; Scheller, D.; Rademacher, O.; Wolff, T. Selectivity in the Photodimerization of 6-Alkylcoumarins *J. Org. Chem.* **2003**, *68*, 7386-7399.
- (13) Lam, C.-K.; Mak, T. C. W. Carbonate and oxalate dianions as prolific hydrogen-bond acceptors in supramolecular assembly *Chem. Commun.* **2003**, 2660-2661.
- (14) Yamaoka, Y.; Miyabe, H.; Takemoto, Y. Catalytic Enantioselective Petasis-Type Reaction of Quinolines Catalyzed by a Newly Designed Thiourea Catalyst *J. Am. Chem. Soc.* **2007**, *129*, 6686-6687.
- (15) Bhogala, B. R.; Captain, B.; Parthasarathy, A.; Ramamurthy, V. Thiourea as a Template for Photodimerization of Azastilbenes *J. Am. Chem. Soc.*, *132*, 13434-13442.
- (16) Lewis, F. D.; Howard, D. K.; Oxman, J. D. Lewis acid catalysis of coumarin photodimerization *J. Am. Chem. Soc.* **1983**, *105*, 3344-3345.
- (17) Görner, H.; Wolff, T. Lewis-acid-catalyzed Photodimerization of Coumarins and N-methyl-2-quinolone *Photochem. Photobiol.* **2008**, *84*, 1224-1230.
- (18) Day, A.; Arnold, A. P.; Blanch, R. J.; Snushall, B. Controlling Factors in the Synthesis of Cucurbituril and Its Homologues *J. Org. Chem.* **2001**, *66*, 8094-8100.
- (19) Harris, D. C. *Quantitative Chemical Analysis*; 6th ed.; W.H. Freeman and Company: New York, 2003.

APPENDIX. COMPUTATIONAL OUTPUTS OF COUMARIN DERIVATIVES TO DETERMINE VOLUME AND GEOMETRIES OF PHOTOPRODUCTS

A1.1. Optimized Geometric Outputs for Photodimers of 1c

Table A1 Optimized geometric parameters for *anti*-HT dimer of 1c

Standard orientation for <i>anti</i> -HT of 1c						
Center Number	Atomic Number	Atomic Type	Coordinates (Angstroms)			
			X	Y	Z	
1	6	0	4.373047	1.695051	0.227556	
2	6	0	3.001341	1.690135	0.421775	
3	6	0	2.258625	0.497882	0.414828	
4	6	0	2.95608	-0.687848	0.19712	
5	6	0	4.339226	-0.718914	0.002248	
6	6	0	5.051773	0.481749	0.019235	
7	1	0	4.943236	2.617183	0.233028	
8	1	0	2.47313	2.627705	0.573338	
9	6	0	0.776237	0.485023	0.629077	
10	1	0	4.812103	-1.678594	-0.158836	
11	6	0	0.127081	-0.92388	0.58599	
12	6	0	-0.775894	-0.484389	-0.628291	
13	6	0	-2.258366	-0.497641	-0.414701	
14	6	0	-0.127049	0.924637	-0.584908	
15	6	0	-2.95614	0.687895	-0.196942	
16	6	0	-3.000849	-1.690035	-0.422311	
17	6	0	-4.339378	0.718649	-0.002695	
18	6	0	-4.372641	-1.69526	-0.228715	
19	1	0	-2.472393	-2.627466	-0.573863	
20	6	0	-5.051688	-0.482143	-0.020369	
21	1	0	-4.812511	1.678191	0.158474	
22	1	0	-4.942656	-2.617497	-0.234695	
23	6	0	0.996991	-2.119937	0.285952	
24	6	0	-0.997257	2.120354	-0.284346	
25	8	0	2.344572	-1.939493	0.14556	
26	8	0	0.547067	-3.230622	0.144036	
27	8	0	-0.547504	3.230974	-0.141387	
28	8	0	-2.344875	1.939634	-0.144682	
29	1	0	0.52458	1.039718	1.538123	
30	1	0	-0.461872	-1.178165	1.470155	
31	1	0	-0.523678	-1.038931	-1.537275	
32	1	0	0.461604	1.179415	-1.469141	
33	8	0	-6.397713	-0.578649	0.156234	
34	8	0	6.397739	0.577963	-0.15802	
35	6	0	-7.136595	0.614684	0.377416	
36	1	0	-8.176487	0.306566	0.49142	
37	1	0	-6.809109	1.128163	1.289961	

(continued)

Table A1 Optimized geometric parameters for *anti*-HT dimer of 1c (continued)

Standard orientation for <i>anti</i> -HT of 1c					
Center Number	Atomic Number	Atomic Type	Coordinates (Angstroms)		
			X	Y	Z
38	1	0	-7.054441	1.303671	-0.472425
39	6	0	7.136326	-0.615553	-0.379217
40	1	0	6.80831	-1.129242	-1.291453
41	1	0	8.176212	-0.307637	-0.493818
42	1	0	7.054477	-1.304282	0.470862

Table A2 Optimized geometric parameters for *anti*-HH dimer of 1c

Standard orientation for <i>anti</i> -HH dimer of 1c					
Center Number	Atomic Number	Atomic Type	Coordinates (Angstroms)		
			X	Y	Z
1	6	0	3.154148	-2.083735	-0.767626
2	6	0	1.962577	-1.373918	-0.92198
3	6	0	1.801178	-0.077301	-0.430369
4	6	0	2.899442	0.501081	0.222359
5	6	0	4.100686	-0.172327	0.387384
6	6	0	4.231149	-1.476286	-0.107668
7	1	0	3.233551	-3.087704	-1.164971
8	6	0	0.545861	0.716221	-0.574363
9	1	0	4.931458	0.304049	0.893854
10	6	0	1.803464	2.64118	0.602869
11	6	0	0.692073	2.244549	-0.353285
12	6	0	-0.545798	0.716105	0.574213
13	6	0	-1.801122	-0.077387	0.430233
14	6	0	-0.692043	2.244481	0.353395
15	6	0	-2.899387	0.501044	-0.222448
16	6	0	-1.962582	-1.373978	0.921892
17	6	0	-1.803398	2.641181	-0.602802
18	6	0	-4.100683	-0.172282	-0.3874
19	6	0	-3.154205	-2.083724	0.767604
20	1	0	-1.132056	-1.842956	1.442984
21	6	0	-4.231202	-1.476227	0.107684
22	1	0	-4.931448	0.30414	-0.893838
23	1	0	-3.233644	-3.087681	1.164973
24	8	0	1.815375	3.680716	1.209886
25	8	0	2.856773	1.779121	0.769152
26	8	0	-2.856631	1.77906	-0.769292
27	8	0	-1.815343	3.68078	-1.209704
28	1	0	1.13204	-1.842855	-1.443093
29	8	0	-5.443164	-2.061287	-0.100543
30	8	0	5.44307	-2.061412	0.100612

(continued)

Table A2 Optimized geometric parameters for *anti*-HH dimer of 1c (continued)

Standard orientation for <i>anti</i> -HH dimer of 1c					
Center Number	Atomic Number	Atomic Type	Coordinates (Angstroms)		
			X	Y	Z
32	1	0	5.536622	-3.437158	-1.470456
33	1	0	6.667212	-3.647311	-0.107216
34	1	0	4.951126	-4.092895	0.086787
35	6	0	-5.645182	-3.382508	0.380168
36	1	0	-5.536717	-3.436985	1.470566
37	1	0	-6.667409	-3.647091	0.107402
38	1	0	-4.95137	-4.092808	-0.086698
39	1	0	-0.057719	0.508436	1.531798
40	1	0	-0.771872	2.886505	1.23579
41	1	0	0.057816	0.508699	-1.532008
42	1	0	0.771789	2.886723	-1.235594

Table A3 Optimized geometric parameters for *syn*-HH dimer of 1c

Standard orientation for <i>syn</i> -HH dimer of 1c					
Center Number	Atomic Number	Atomic Type	Coordinates (Angstroms)		
			X	Y	Z
1	6	0	0.726694	-2.550946	0.028614
2	6	0	0.603994	-1.840621	1.365707
3	6	0	-1.5611	-0.962329	0.698895
4	6	0	-2.721002	-0.381872	1.191096
5	6	0	-3.787049	-0.128132	0.319266
6	6	0	-3.678304	-0.471593	-1.035602
7	6	0	-2.499394	-1.060837	-1.494183
8	6	0	-1.414493	-1.309819	-0.651342
9	6	0	-0.145052	-1.954514	-1.101975
10	6	0	1.993445	-2.164352	-0.804824
11	6	0	3.252154	-1.698998	-0.111392
12	6	0	2.368367	0.553077	-0.169516
13	6	0	2.56188	1.827668	0.347571
14	6	0	1.678025	2.856064	0.00701
15	6	0	0.60504	2.593389	-0.856365
16	6	0	0.434105	1.302981	-1.353626
17	6	0	1.294987	0.250646	-1.024256
18	6	0	1.12518	-1.136244	-1.584777
19	8	0	-0.558124	-1.166767	1.636462
20	8	0	1.45256	-1.88659	2.218369
21	8	0	3.339151	-0.368623	0.195125
22	8	0	4.179166	-2.420135	0.150117
23	1	0	0.616541	-3.620133	0.235872
24	1	0	-2.802681	-0.127062	2.240848
25	1	0	-2.422813	-1.338621	-2.542599
26	1	0	2.279648	-3.016435	-1.423378
27	1	0	3.398723	2.022767	1.007059

(continued)

Table A3 Optimized geometric parameters for *syn*-HH dimer of 1c (continued)

Standard orientation for <i>syn</i> -HH dimer of 1c					
Center Number	Atomic Number	Atomic Type	Coordinates (Angstroms)		
			X	Y	Z
				1.105891	-2.018873
30	1	0	-0.091548	3.371783	-1.141055
31	8	0	1.949465	4.071133	0.558715
32	8	0	-4.882787	0.446809	0.887858
33	6	0	1.083602	5.155666	0.258257
34	1	0	1.478454	6.013814	0.803415
35	1	0	1.076707	5.38245	-0.815369
36	1	0	0.057095	4.95743	0.590982
37	6	0	-6.00617	0.71985	0.062802
38	1	0	-6.41679	-0.19728	-0.377641
39	1	0	-6.754391	1.170635	0.715739
40	1	0	-5.756306	1.424512	-0.740296
41	1	0	-0.353506	-2.718782	-1.857652
42	1	0	1.259841	-1.136216	-2.671765

Table A4 Optimized geometric parameters for *syn*-HT dimer of 1c

Standard orientation for <i>syn</i> -HT dimer of 1c					
Center Number	Atomic Number	Atomic Type	Coordinates (Angstroms)		
			X	Y	Z
1	6	0	-0.032497	-2.536685	-1.087814
2	6	0	-0.118183	-1.638494	-2.294134
4	6	0	2.079248	1.102446	-1.406087
5	6	0	2.989394	1.549712	-0.442216
6	6	0	3.291879	0.736419	0.658433
7	6	0	2.674346	-0.507575	0.775858
8	6	0	1.751598	-0.975359	-0.166012
9	6	0	1.105364	-2.330042	-0.053379
10	6	0	-1.105357	-2.330042	0.053391
11	6	0	0.118192	-1.638476	2.29414
12	6	0	-1.480237	-0.141139	1.259565
13	6	0	-2.07925	1.10245	1.406081
14	6	0	-2.9894	1.549707	0.442209
15	6	0	-3.291885	0.736407	-0.658434
16	6	0	-2.674348	-0.507585	-0.775853
17	6	0	-1.751594	-0.97536	0.166016
18	6	0	0.032504	-2.536677	1.087827
19	8	0	0.61699	-0.489905	-2.293565
20	8	0	-0.825398	-1.872555	-3.24414
21	8	0	-0.616985	-0.48989	2.293565
22	8	0	0.82541	-1.87253	3.244145
23	1	0	-0.081386	-3.562711	-1.457151
24	1	0	1.845191	1.721177	-2.26388
25	1	0	2.904793	-1.129626	1.635364
26	1	0	-1.845193	1.721187	2.26387
27	1	0	-2.904796	-1.129642	-1.635355

(continued)

Table A4 Optimized geometric parameters for *syn*-HT dimer of 1c (continued)

Standard orientation for <i>syn</i> -HT dimer of 1c					
Center Number	Atomic Number	Atomic Type	Coordinates (Angstroms)		
			X	Y	Z
28	1	0	0.081395	-3.5627	1.457172
29	1	0	3.993702	1.055758	1.418278
30	1	0	-3.993712	1.055739	-1.418279
31	8	0	-3.525091	2.780739	0.668613
32	8	0	3.525079	2.780745	-0.668625
33	6	0	4.450761	3.296572	0.277804
34	1	0	5.343279	2.66342	0.356483
35	1	0	4.740293	4.280506	-0.093019
36	1	0	3.996139	3.40346	1.270376
37	6	0	-4.450774	3.296559	-0.277819
38	1	0	-5.343291	2.663405	-0.356494
39	1	0	-4.740307	4.280495	0.092999
40	1	0	-3.996152	3.403442	-1.270391
41	1	0	1.869245	-3.113444	-0.050973
42	1	0	-1.869237	-3.113446	0.050992

A1.2. Optimized Geometric Outputs for Photodimers of 1d**Table A5** Optimized geometric parameters for *anti*-HT dimer of 1d

Standard orientation for <i>anti</i> -HT dimer of 1d					
Center Number	Atomic Number	Atomic Type	Coordinates (Angstroms)		
			X	Y	Z
1	6	0	-0.758186	-0.353401	-0.66344
2	6	0	-3.039617	-1.409939	-0.280297
3	1	0	-2.561364	-2.384198	-0.330787
4	6	0	-4.414646	-1.341542	-0.062813
5	1	0	-4.985302	-2.25653	0.033975
6	6	0	-5.030984	-0.085465	0.029252
7	6	0	-4.257754	1.075014	-0.078692
8	1	0	-4.722313	2.049821	0.008458
9	6	0	-2.888535	0.971083	-0.290174
10	6	0	-2.244598	-0.266663	-0.412478
11	8	0	-6.362995	0.113266	0.232473
12	6	0	-0.440859	-1.120735	-1.953291
13	1	0	-0.792727	-2.153896	-1.901289
14	1	0	0.638106	-1.143924	-2.142181
15	1	0	-0.92429	-0.633151	-2.805561
16	6	0	-0.86125	2.289502	-0.432809
17	8	0	-0.358171	3.385864	-0.376578
18	8	0	-2.2212	2.191575	-0.351143
19	6	0	-0.04929	1.030286	-0.588861
20	1	0	0.610619	1.212393	-1.440177
21	6	0	4.429858	1.522621	0.01751
22	1	0	5.042032	2.409	-0.105377
23	6	0	3.067288	1.611243	0.251557
24	1	0	2.595837	2.589006	0.296804

(continued)

Table A5 Optimized geometric parameters for *anti*-HT dimer of 1d (continued)

Standard orientation for <i>anti</i> -HT dimer of 1d					
Center Number	Atomic Number	Atomic Type	Coordinates (Angstroms)		
			X	Y	Z
25	6	0	2.263204	0.468752	0.410717
26	6	0	2.894911	-0.767823	0.296939
27	6	0	4.267952	-0.893346	0.066499
28	1	0	4.683877	-1.889457	-0.007314
29	6	0	5.041663	0.260238	-0.06752
30	6	0	0.781532	0.569997	0.682239
29	6	0	5.041663	0.260238	-0.06752
30	6	0	0.781532	0.569997	0.682239
31	8	0	6.384222	0.26323	-0.291996
32	6	0	0.490424	1.341558	1.975486
33	1	0	-0.585452	1.375836	2.179875
34	1	0	0.851178	2.371163	1.917117
35	1	0	0.981428	0.849913	2.821127
36	6	0	0.864428	-2.075624	0.47671
37	8	0	0.355671	-3.170424	0.440455
38	8	0	2.224574	-1.986396	0.383669
39	6	0	0.062471	-0.808407	0.616153
40	1	0	-0.604834	-0.97564	1.46464
41	6	0	7.053019	-0.986494	-0.389984
42	1	0	6.958188	-1.567762	0.535574
43	1	0	6.673321	-1.582405	-1.229349
44	1	0	8.104045	-0.751712	-0.561895
45	6	0	-7.201932	-1.025807	0.360786
46	1	0	-8.210499	-0.638941	0.511124
47	1	0	-7.184057	-1.645304	-0.544568
48	1	0	-6.919191	-1.641429	1.223831

Table A6 Optimized geometric parameters for *anti*-HH dimer of 1d

Standard orientation for <i>anti</i> -HH dimer of 1d					
Center Number	Atomic Number	Atomic Type	Coordinates (Angstroms)		
			X	Y	Z
1	6	0	1.299822	2.32487	-1.161276
2	6	0	0.193841	1.389474	-0.757315
3	6	0	0.455882	-0.143314	-0.669303
4	6	0	1.92576	-0.399558	-0.391342
5	6	0	2.412808	-1.673006	-0.072721
6	1	0	1.712133	-2.500154	-0.008628
7	6	0	3.759882	-1.928228	0.17673
8	6	0	4.679252	-0.872727	0.101642
9	6	0	4.231359	0.407577	-0.235222
10	1	0	4.935153	1.226849	-0.319633
11	6	0	2.881107	0.62574	-0.483491
12	8	0	2.577838	1.925795	-0.866035
13	8	0	1.131457	3.398299	-1.678876
14	6	0	-1.299832	2.324841	1.161346

(continued)

Table A6 Optimized geometric parameters for *anti*-HH dimer of 1d (continued)

Standard orientation for <i>anti</i> -HH dimer of 1d					
Center Number	Atomic Number	Atomic Type	Coordinates (Angstroms)		
			X	Y	Z
15	6	0	-0.193845	1.389463	0.757359
16	1	0	0.672007	1.618083	1.381433
17	6	0	-0.455883	-0.143325	0.669324
18	6	0	-1.925761	-0.399568	0.391359
19	6	0	-2.412811	-1.673019	0.072751
20	1	0	-1.712141	-2.500171	0.008681
21	6	0	-3.759883	-1.928236	-0.176717
22	6	0	-4.679248	-0.872729	-0.101662
23	6	0	-4.231353	0.407578	0.235189
24	1	0	-4.935144	1.226855	0.319578
25	6	0	-2.881104	0.625736	0.48348
26	8	0	-2.577838	1.925791	0.866027
27	8	0	-1.131469	3.398318	1.678846
28	1	0	-4.075967	-2.933705	-0.424127
29	1	0	4.075964	-2.933695	0.424151
30	8	0	-6.016667	-0.989262	-0.327083
31	8	0	6.016674	-0.989263	0.327045
32	6	0	0.006676	-0.941574	1.89186
33	1	0	-0.101113	-2.020005	1.739101
34	1	0	1.051373	-0.736839	2.135608
35	1	0	-0.609037	-0.672305	2.756735
36	1	0	-0.672011	1.618097	-1.381389
37	6	0	-0.006672	-0.941547	-1.891852
38	1	0	0.101117	-2.01998	-1.739108
39	1	0	-1.051367	-0.736808	-2.135604
40	1	0	0.609046	-0.672265	-2.756719
41	6	0	-6.535787	-2.269321	-0.658169
42	1	0	-6.361249	-2.996368	0.144772
43	1	0	-7.609481	-2.131621	-0.790453
44	1	0	-6.103489	-2.652117	-1.591172
45	6	0	6.535793	-2.269322	0.658134
46	1	0	6.361234	-2.996377	-0.144795
47	1	0	7.60949	-2.131626	0.790395
48	1	0	6.103512	-2.652105	1.59115

Table A7 Optimized geometric parameters for *syn*-HH dimer of 1d

Standard orientation for <i>syn</i> -HH dimer of 1d					
Center Number	Atomic Number	Atomic Type	Coordinates (Angstroms)		
			X	Y	Z
1	6	0	-1.059963	-2.198835	-0.620205
2	6	0	-0.787878	-1.329826	-1.83158
3	6	0	1.435033	-0.854136	-0.989663
4	6	0	2.661083	-0.320662	-1.362545
5	6	0	3.718562	-0.30905	-0.447153
6	6	0	3.52892	-0.841531	0.83459

(continued)

Table A7 Optimized geometric parameters for *syn*-HH dimer of 1d (continued)

Standard orientation for <i>syn</i> -HH dimer of 1d					
Center Number	Atomic Number	Atomic Type	Coordinates (Angstroms)		
			X	Y	Z
7	6	0	2.285717	-1.378367	1.171261
8	6	0	1.205196	-1.398275	0.28322
9	6	0	-0.14141	-1.9891	0.618527
10	6	0	-2.282986	-1.754716	0.243941
11	6	0	-3.416228	-0.976886	-0.378282
12	6	0	-2.138378	1.03152	0.015104
13	6	0	-2.069688	2.377401	-0.323869
14	6	0	-1.030182	3.167272	0.17354
15	6	0	-0.06774	2.593885	1.01596
16	6	0	-0.160571	1.239875	1.330529
17	6	0	-1.178952	0.415024	0.837333
18	6	0	-1.302703	-1.047289	1.228363
19	8	0	0.460103	-0.790975	-1.974343
20	8	0	-1.599683	-1.140575	-2.701007
21	8	0	-3.249962	0.374995	-0.491472
22	8	0	-4.45226	-1.470929	-0.740588
23	1	0	-1.125433	-3.225889	-0.99575
24	1	0	2.795895	0.086012	-2.357567
25	1	0	2.160235	-1.7934	2.16649
26	1	0	-2.741889	-2.637361	0.69162
27	1	0	-2.826617	2.810876	-0.96607
28	1	0	0.594769	0.809	1.979015
29	1	0	4.328754	-0.850158	1.564421
30	1	0	0.746155	3.180975	1.422389
31	8	0	-1.046333	4.473473	-0.210929
32	8	0	4.881903	0.236358	-0.89891
33	6	0	0.010103	-3.308849	1.393237
34	1	0	0.669624	-3.98629	0.842431
35	1	0	0.440965	-3.1557	2.386327
36	1	0	-0.950236	-3.813898	1.529437
37	6	0	-1.622042	-1.178759	2.720829
38	1	0	-1.790469	-2.217542	3.017504
39	1	0	-0.811403	-0.774239	3.335816
40	1	0	-2.526805	-0.610312	2.960076
41	6	0	-0.010256	5.325147	0.255154
42	1	0	-0.213208	6.306634	-0.175026
43	1	0	-0.012342	5.403894	1.349703
44	1	0	0.976605	4.981262	-0.079
45	6	0	5.99714	0.265765	-0.020236
46	1	0	6.302426	-0.744514	0.279736
47	1	0	6.807413	0.734102	-0.580189
48	1	0	5.788755	0.860142	0.878316

Table A8 Optimized geometric parameters for *syn*-HT dimer of 1d

Standard orientation for <i>syn</i> -HT dimer of 1d					
Center Number	Atomic Number	Atomic Type	Coordinates (Angstroms)		
			X	Y	Z
1	6	0	-0.035854	-2.312812	-1.083804
2	6	0	-0.115968	-1.460815	-2.32063
3	6	0	1.408877	0.105383	-1.28659
4	6	0	1.946398	1.376666	-1.435779
5	6	0	2.785326	1.895044	-0.443944
6	6	0	3.075232	1.125052	0.690014
7	6	0	2.521846	-0.148922	0.808173
8	6	0	1.673562	-0.692242	-0.163534
9	6	0	1.113251	-2.096264	-0.058021
10	6	0	-1.113267	-2.096254	0.058001
11	6	0	0.115954	-1.460836	2.320617
12	6	0	-1.408882	0.105382	1.286593
13	6	0	-1.946393	1.376667	1.435795
14	6	0	-2.785305	1.895066	0.443959
15	6	0	-3.075206	1.125094	-0.690013
16	6	0	-2.521831	-0.148884	-0.808184
17	6	0	-1.673562	-0.692226	0.163524
18	6	0	0.035836	-2.312821	1.083783
19	8	0	0.608019	-0.305189	-2.346801
20	8	0	-0.799269	-1.737445	-3.277527
21	8	0	-0.608038	-0.305214	2.346806
22	8	0	0.799203	-1.737512	3.277538
23	1	0	-0.080828	-3.350972	-1.422087
24	1	0	1.716495	1.963122	-2.317067
25	1	0	2.746286	-0.731666	1.695928
26	1	0	-1.716493	1.963108	2.317094
27	1	0	-2.746267	-0.731613	-1.695951
28	1	0	0.080802	-3.350983	1.422058
29	1	0	3.717984	1.500036	1.476252
30	1	0	-3.717947	1.500095	-1.476253
31	8	0	-3.264236	3.148465	0.675752
32	8	0	3.264264	3.148441	-0.675723
33	6	0	2.229	-3.145624	-0.081907
34	1	0	1.814061	-4.159158	-0.059303
35	1	0	2.835763	-3.042032	-0.987433
36	1	0	2.890883	-3.032554	0.781925
37	6	0	-2.229027	-3.145603	0.081881
38	1	0	-1.814098	-4.159141	0.059267
39	1	0	-2.835787	-3.042012	0.987409
40	1	0	-2.89091	-3.032518	-0.781949
41	6	0	4.112898	3.735607	0.300813
42	1	0	5.033574	3.15489	0.438238
43	1	0	4.366755	4.725547	-0.08011
44	1	0	3.604961	3.839472	1.267551
45	6	0	-4.112837	3.735661	-0.300796
46	1	0	-5.033523	3.154967	-0.438245
47	1	0	-4.366678	4.725603	0.080133
48	1	0	-3.604878	3.839525	-1.267522

A1.3. Optimized Geometric Outputs for Photodimers of 1e

Table A9 Optimized geometric parameters for *anti*-HT dimer of 1e

Standard orientation for <i>anti</i> -HT dimer of 1e					
Center Number	Atomic Number	Atomic Type	Coordinates (Angstroms)		
			X	Y	Z
1	6	0	4.465708	1.43841	-0.153782
2	6	0	3.096493	1.515462	-0.380246
3	6	0	2.292637	0.367114	-0.373605
4	6	0	2.916022	-0.855116	-0.123687
5	6	0	4.290157	-0.945786	0.100226
6	6	0	5.085245	0.201131	0.088257
7	1	0	5.063898	2.34532	-0.167201
8	1	0	2.623337	2.477539	-0.559402
9	6	0	0.816705	0.432446	-0.625902
10	1	0	4.719308	-1.925494	0.284316
11	6	0	0.086876	-0.936092	-0.572059
12	6	0	-0.810797	-0.423705	0.615999
13	6	0	-2.288666	-0.364482	0.374568
14	6	0	-0.085869	0.947085	0.557128
15	6	0	-2.917295	0.854607	0.122589
16	6	0	-3.089135	-1.515126	0.392691
17	6	0	-4.293319	0.940315	-0.091644
18	6	0	-4.460101	-1.443078	0.175667
19	1	0	-2.61187	-2.475049	0.572367
20	6	0	-5.084997	-0.208716	-0.067804
21	1	0	-4.726557	1.91779	-0.277972
22	1	0	-5.055502	-2.351668	0.197483
23	6	0	0.880739	-2.175467	-0.235683
24	6	0	-0.88476	2.180839	0.211441
25	8	0	2.231883	-2.069291	-0.07056
26	8	0	0.362792	-3.255451	-0.087322
27	8	0	-0.370036	3.260327	0.049004
28	8	0	-2.236722	2.070224	0.056804
29	6	0	-6.572656	-0.131214	-0.314769
30	1	0	-6.833754	-0.560307	-1.289445
31	1	0	-7.130422	-0.691353	0.442943
32	1	0	-6.928092	0.902229	-0.301326
33	6	0	6.570492	0.118003	0.347654
34	1	0	7.135169	0.699434	-0.388441
35	1	0	6.821325	0.519833	1.336623
36	1	0	6.927098	-0.914443	0.309399
37	1	0	-0.499247	-1.171442	-1.463313
38	1	0	0.622046	0.983093	-1.551081
39	1	0	0.495918	1.190737	1.449073
40	1	0	-0.606867	-0.972465	1.540326

Table A10 Optimized geometric parameters for *anti*-HH dimer of 1e

Standard orientation for <i>anti</i> -HH dimer of 1e					
Center Number	Atomic Number	Atomic Type	Coordinates (Angstroms)		
			X	Y	Z
1	6	0	1.38285	2.041694	-1.110222
2	6	0	0.231507	1.137672	-0.752113
3	6	0	0.47113	-0.391757	-0.629912
4	6	0	1.910686	-0.703077	-0.316589
5	6	0	2.321799	-1.983987	0.078341
6	1	0	1.578416	-2.774806	0.145463
7	6	0	3.649378	-2.263809	0.380012
8	6	0	4.62806	-1.259619	0.302099
9	6	0	4.231809	0.016974	-0.09667
10	1	0	4.949429	0.826404	-0.184581
11	6	0	2.895898	0.28371	-0.401868
12	8	0	2.643347	1.585191	-0.822051
13	8	0	1.259205	3.134377	-1.598981
14	6	0	-1.382742	2.041704	1.110202
15	6	0	-0.231441	1.137643	0.752048
16	1	0	0.598678	1.383205	1.415658
17	6	0	-0.471131	-0.391769	0.629768
18	6	0	-1.910708	-0.703004	0.316469
19	6	0	-2.321881	-1.983886	-0.078609
20	1	0	-1.578501	-2.774692	-0.145911
21	6	0	-3.649443	-2.26363	-0.380273
22	6	0	-4.628124	-1.259402	-0.302156
23	6	0	-4.231817	0.017118	0.096658
24	1	0	-4.949395	0.826576	0.184596
25	6	0	-2.895856	0.283789	0.401855
26	8	0	-2.643265	1.585252	0.822067
27	8	0	-1.259039	3.134373	1.59898
28	1	0	-3.932967	-3.269006	-0.679063
29	1	0	3.932876	-3.269241	0.678618
30	1	0	-0.598601	1.383302	-1.415712
31	6	0	-6.066698	-1.550936	-0.655647
32	1	0	-6.734476	-0.761953	-0.300499
33	1	0	-6.197106	-1.630939	-1.741594
34	1	0	-6.39883	-2.498835	-0.220322
35	6	0	6.066514	-1.550873	0.656295
36	1	0	6.735547	-0.767008	0.292232
37	1	0	6.198403	-1.61996	1.742836
38	1	0	6.395819	-2.503891	0.230202
39	1	0	-0.109306	-0.995057	1.468516
40	1	0	0.109292	-0.994983	-1.468697

Table A11 Optimized geometric parameters for *syn*-HT dimer of 1e

Standard orientation for <i>syn</i> -HT dimer of 1e					
Center Number	Atomic Number	Atomic Type	Coordinates (Angstroms)		
			X	Y	Z
1	6	0	-3.254429	1.005021	-0.901749
2	6	0	-2.630354	-0.234297	-0.978261
3	6	0	-1.768033	-0.682918	0.034228
4	6	0	-1.577525	0.15999	1.131046
5	6	0	-2.199576	1.405695	1.218411
6	6	0	-3.046449	1.847594	0.201876
7	1	0	-3.910105	1.324661	-1.706835
8	1	0	-2.795145	-0.868169	-1.84428
9	6	0	-1.103241	-2.03195	-0.023064
10	1	0	-2.00842	2.014864	2.095957
11	6	0	-0.044886	-2.228019	1.094397
12	6	0	1.108792	-2.029199	0.033774
13	6	0	1.770094	-0.678725	-0.030308
14	6	0	0.050978	-2.233776	-1.08261
15	6	0	1.578568	0.157587	-1.132531
16	6	0	2.633596	-0.224344	0.977971
17	6	0	2.2009	1.402	-1.228562
18	6	0	3.258448	1.014489	0.892737
19	1	0	2.802587	-0.854604	1.845812
20	6	0	3.047435	1.851114	-0.214237
21	1	0	2.012058	2.004146	-2.111504
22	1	0	3.918793	1.336985	1.692792
23	6	0	-0.05077	-1.317489	2.29568
24	6	0	0.055347	-1.330124	-2.289063
25	8	0	-0.78349	-0.16962	2.226626
26	8	0	0.5818	-1.54272	3.298728
27	8	0	-0.57671	-1.562265	-3.290883
28	8	0	0.786167	-0.18071	-2.226668
29	6	0	3.70544	3.207358	-0.296957
30	1	0	3.204228	3.92811	0.360356
31	1	0	4.753366	3.160653	0.015833
32	1	0	3.67182	3.608563	-1.313255
33	6	0	-3.731168	3.190431	0.288733
34	1	0	-3.537871	3.791726	-0.606192
35	1	0	-4.818271	3.075405	0.370064
36	1	0	-3.390118	3.759148	1.157436
37	1	0	-1.860991	-2.819145	-0.080046
38	1	0	-0.022294	-3.250161	1.476544
39	1	0	1.868471	-2.814203	0.094842
40	1	0	0.03075	-3.258098	-1.459033

Table A12 Optimized geometric parameters for *syn*-HH dimer of 1e

Standard orientation for <i>syn</i> -HH dimer of 1e					
Center Number	Atomic Number	Atomic Type	Coordinates (Angstroms)		
			X	Y	Z
1	6	0	-3.897411	-0.159595	-1.05638
2	6	0	-2.727327	-0.748039	-1.528621
3	6	0	-1.650807	-1.016606	-0.675308
4	6	0	-1.805158	-0.690205	0.674502
5	6	0	-2.972272	-0.107375	1.162499
6	6	0	-4.034995	0.173531	0.299467
7	1	0	-4.716555	0.035419	-1.742831
8	6	0	-0.383794	-1.6687	-1.123926
9	1	0	-3.03353	0.118908	2.22224
10	6	0	0.34623	-1.595192	1.35152
11	6	0	0.475349	-2.286749	0.004815
12	6	0	0.895361	-0.854984	-1.588477
13	6	0	1.069166	0.525876	-1.013505
14	6	0	1.751108	-1.89799	-0.813933
15	6	0	2.130929	0.808866	-0.145427
16	6	0	0.218294	1.589203	-1.348499
17	6	0	3.005872	-1.447396	-0.103219
18	6	0	2.324832	2.084246	0.385177
19	6	0	0.406879	2.865359	-0.829771
20	1	0	-0.60658	1.404977	-2.03003
21	6	0	1.463134	3.130718	0.055011
22	1	0	3.166502	2.236941	1.053026
23	1	0	-0.271256	3.665439	-1.113186
24	8	0	1.187307	-1.660953	2.210648
25	8	0	-0.812107	-0.916288	1.620189
26	8	0	3.094217	-0.121816	0.220721
27	8	0	3.92692	-2.17633	0.158028
28	1	0	-2.643467	-1.01451	-2.579515
29	1	0	1.036739	-0.841228	-2.674337
30	1	0	-0.595162	-2.420658	-1.890834
31	1	0	2.037893	-2.744005	-1.440438
32	1	0	0.356441	-3.358059	0.195419
33	6	0	1.651834	4.504203	0.652508
34	1	0	1.060476	4.617641	1.569378
35	1	0	2.697583	4.687341	0.914399
36	1	0	1.331168	5.287826	-0.040365
37	6	0	-5.289992	0.83667	0.814326
38	1	0	-5.468176	0.595679	1.86603
39	1	0	-5.217756	1.928586	0.737479
40	1	0	-6.168396	0.527761	0.240322

A1.4. Optimized Geometric Outputs for Photodimers of 1f**Table A13** Optimized geometric parameters for *anti*-HT dimer of 1f

Standard orientation for <i>anti</i> -HT dimer of 1f					
Center Number	Atomic Number	Atomic Type	Coordinates (Angstroms)		
			X	Y	Z
1	6	0	-3.283437	-0.903322	-0.184015
2	1	0	-2.989424	-1.94535	-0.283419
3	6	0	-4.613276	-0.592928	0.105965
4	6	0	-4.955109	0.760094	0.260698
5	6	0	-3.995857	1.757861	0.142659
6	1	0	-4.244133	2.805185	0.276932
7	6	0	-2.674445	1.413208	-0.145028
8	6	0	-2.295955	0.082928	-0.328485
9	6	0	-0.440394	2.325625	-0.346049
10	8	0	0.269289	3.301261	-0.285423
11	8	0	-1.787923	2.487521	-0.209725
12	6	0	0.103306	0.93753	-0.567283
13	1	0	0.758573	1.015661	-1.437888
14	6	0	4.613279	0.592889	-0.10604
15	6	0	3.283452	0.903308	0.183961
16	1	0	2.989458	1.94534	0.283383
17	6	0	2.295958	-0.082926	0.328464
18	6	0	2.67442	-1.413215	0.145034
19	6	0	3.995827	-1.757892	-0.14266
20	1	0	4.24409	-2.805226	-0.276889
21	6	0	4.955091	-0.760145	-0.260736
22	6	0	0.865713	0.277954	0.655976
23	6	0	0.440359	-2.325591	0.346156
24	8	0	-0.269335	-3.301219	0.285575
25	8	0	1.787886	-2.487512	0.209783
26	6	0	-0.103302	-0.93748	0.567351
27	1	0	-0.758593	-1.015558	1.437942
28	6	0	-5.658647	-1.675398	0.235588
29	1	0	-6.295099	-1.513305	1.1117
30	1	0	-6.317277	-1.699143	-0.641127
31	1	0	-5.20044	-2.663387	0.329898
32	6	0	5.658646	1.675344	-0.235827
33	1	0	6.318271	1.698188	0.640158
34	1	0	6.294085	1.513983	-1.112815
35	1	0	5.200461	2.663476	-0.328728
36	1	0	-5.982077	1.033736	0.487538
37	1	0	5.982056	-1.03381	-0.487559
38	6	0	-0.865691	-0.277918	-0.655941
39	6	0	0.761372	1.034423	1.98631
40	1	0	1.174775	0.424624	2.795709
41	1	0	1.306135	1.980683	1.953916
42	1	0	-0.283047	1.258392	2.229373
43	6	0	-0.76126	-1.034395	-1.98626
44	1	0	-1.305981	-1.980679	-1.953879
45	1	0	-1.174659	-0.424627	-2.795684
46	1	0	0.28318	-1.258318	-2.229277

Table A14 Optimized geometric parameters for *anti*-HH dimer of 1f

Standard orientation for <i>anti</i> -HH dimer of 1f					
Center Number	Atomic Number	Atomic Type	Coordinates (Angstroms)		
			X	Y	Z
1	6	0	1.821972	-0.453465	0.437092
2	6	0	1.966325	-1.823192	0.700964
4	6	0	4.328393	-1.774953	0.13582
5	6	0	4.199079	-0.410742	-0.13307
6	6	0	2.967374	0.226163	0.008441
7	1	0	1.103538	-2.390218	1.036964
8	1	0	3.257763	-3.537116	0.769139
9	1	0	5.047981	0.180838	-0.461203
10	6	0	0.521269	0.287541	0.617289
11	6	0	0.64001	1.831615	0.439869
12	1	0	0.549945	2.419763	1.359161
13	6	0	1.857384	2.366483	-0.283934
14	8	0	2.971977	1.57328	-0.339344
15	8	0	1.906779	3.46208	-0.780799
16	6	0	-0.13948	-0.055055	1.960629
17	1	0	-0.447173	-1.102535	2.005892
18	1	0	0.562097	0.132871	2.779174
19	1	0	-1.032738	0.55036	2.139433
20	6	0	5.652507	-2.476634	-0.047924
21	1	0	5.755021	-2.863173	-1.069433
22	1	0	6.492774	-1.799534	0.129478
23	1	0	5.750525	-3.327057	0.63297
24	8	0	-1.906915	3.462635	0.779179
25	6	0	-1.857359	2.366545	0.283402
26	6	0	-0.640024	1.831421	-0.440177
27	8	0	-2.971601	1.572996	0.340284
28	6	0	-0.521062	0.287207	-0.616766
29	1	0	-0.54973	2.419246	-1.359676
30	6	0	-2.967269	0.226037	-0.008033
31	6	0	-1.821875	-0.453734	-0.436612
32	6	0	0.140127	-0.0561	-1.959691
33	6	0	-4.199118	-0.410638	0.133235
34	6	0	-1.966551	-1.82337	-0.700868
35	1	0	0.448833	-1.103276	-2.003709
36	1	0	-0.561485	0.130347	-2.778544
37	1	0	1.032934	0.549823	-2.139089
38	6	0	-4.328705	-1.774737	-0.136047
39	1	0	-5.047872	0.181045	0.46156
40	6	0	-3.187711	-2.474819	-0.55217
41	1	0	-1.1039	-2.390561	-1.036897
42	6	0	-5.652964	-2.476234	0.047394
43	1	0	-3.258412	-3.536965	-0.769642
44	1	0	-5.755837	-2.862644	1.068916
45	1	0	-6.493104	-1.799059	-0.130334
46	1	0	-5.750872	-3.326716	-0.63344

Table A15 Optimized geometric parameters for *syn*-HT dimer of 1f

Standard orientation for <i>anti</i> -HH dimer of 1f					
Center Number	Atomic Number	Atomic Type	Coordinates (Angstroms)		
			X	Y	Z
1	6	0	1.684439	-0.382422	-0.018777
2	6	0	2.449972	0.156309	1.027334
3	6	0	3.003379	1.429231	0.944735
4	6	0	2.822415	2.218926	-0.200536
5	6	0	2.066931	1.692437	-1.248532
6	6	0	1.514363	0.415404	-1.153833
7	1	0	2.595651	-0.428999	1.929787
8	1	0	3.580568	1.815971	1.779896
9	1	0	1.891899	2.26032	-2.156687
10	6	0	1.113377	-1.785313	0.036889
11	6	0	0.056146	-1.999909	-1.083545
12	1	0	0.038553	-3.037608	-1.425614
13	6	0	0.083855	-1.146266	-2.322143
14	8	0	0.802858	0.011668	-2.279892
15	8	0	-0.508606	-1.42473	-3.337128
16	6	0	2.22736	-2.834432	0.109552
17	1	0	1.810834	-3.847378	0.097026
18	1	0	2.910443	-2.732493	-0.740074
19	1	0	2.811805	-2.720831	1.027387
20	6	0	3.4442	3.590761	-0.304481
21	1	0	4.51339	3.522324	-0.539299
22	1	0	2.972131	4.186385	-1.090248
23	1	0	3.355385	4.139362	0.638415
24	8	0	0.50796	-1.425824	3.336898
25	6	0	-0.056872	-2.000163	1.083113
26	8	0	-0.802865	0.011378	2.279959
27	6	0	-1.114045	-1.784901	-0.03726
28	1	0	-0.039667	-3.037957	1.424915
29	6	0	-1.51416	0.415606	1.153952
30	6	0	-1.684521	-0.381791	0.018768
31	6	0	-2.228418	-2.833577	-0.110187
32	6	0	-2.066514	1.692817	1.249077
33	6	0	-2.450121	0.157442	-1.027178
34	1	0	-2.911446	-2.731612	0.739482
35	1	0	-2.812844	-2.719515	-1.027977
36	1	0	-1.812278	-3.846685	-0.097936
37	6	0	-2.821868	2.219769	0.201373
38	1	0	-1.891453	2.260322	2.157449
39	6	0	-3.003268	1.430338	-0.944154
40	1	0	-2.596163	-0.427704	-1.929677
41	6	0	-3.442034	3.592394	0.304586
42	1	0	-3.580701	1.817325	-1.779049
43	1	0	-3.324387	4.152269	-0.628623
44	1	0	-4.517757	3.524956	0.507342
45	1	0	-2.990524	4.176714	1.110584
46	6	0	-0.084318	-1.146845	2.32195

Table A16 Optimized geometric parameters for *syn*-HH dimer of 1f

Standard orientation for <i>syn</i> -HH dimer of 1f					
Center Number	Atomic Number	Atomic Type	Coordinates (Angstroms)		
			X	Y	Z
1	6	0	3.792918	-0.371087	0.879471
2	6	0	2.595647	-1.012717	1.185212
3	6	0	1.533897	-1.073195	0.2716
4	6	0	1.742127	-0.463815	-0.970178
5	6	0	2.937944	0.17391	-1.293678
6	6	0	3.985374	0.230079	-0.371882
7	1	0	4.588386	-0.340674	1.618824
8	6	0	0.227979	-1.772969	0.557426
9	1	0	3.028567	0.625149	-2.276735
10	6	0	-0.431978	-1.047922	-1.871063
11	6	0	-0.660731	-1.98576	-0.70247
12	6	0	-1.002004	-0.944495	1.196431
13	6	0	-0.97214	0.541711	0.884107
14	6	0	-1.92062	-1.665512	0.163413
15	6	0	-1.952248	1.130324	0.074098
16	6	0	-0.01787	1.405986	1.443553
17	6	0	-3.093971	-0.932591	-0.439539
18	6	0	-1.963109	2.499666	-0.195373
19	6	0	-0.02407	2.772372	1.188448
20	1	0	0.749293	0.993238	2.090054
21	6	0	-0.996339	3.341674	0.352574
22	1	0	-2.750143	2.885926	-0.834992
23	1	0	0.734425	3.405108	1.640888
24	8	0	-1.244066	-0.874201	-2.743799
25	8	0	0.77945	-0.424677	-1.970432
26	8	0	-3.011934	0.430529	-0.48607
27	8	0	-4.09103	-1.473839	-0.841774
28	1	0	2.481885	-1.47351	2.161672
29	6	0	5.293448	0.893509	-0.729584
30	1	0	5.965529	0.191239	-1.237947
31	1	0	5.141065	1.741829	-1.403103
32	1	0	5.813711	1.255217	0.161835
33	6	0	-0.985713	4.817754	0.036896
34	1	0	-0.334434	5.030838	-0.819662
35	1	0	-1.985635	5.181283	-0.215422
36	1	0	-0.612566	5.403353	0.882452
37	6	0	-1.32797	-1.173709	2.675538
38	1	0	-0.556446	-0.743993	3.322591
39	1	0	-2.275004	-0.686198	2.929282
40	1	0	-1.422131	-2.236154	2.914994
41	1	0	0.871592	-2.981343	2.275717
42	6	0	0.465705	-3.115025	1.269573
43	1	0	-0.45669	-3.69495	1.363818
44	1	0	1.180282	-3.714177	0.697073
45	1	0	-0.652723	-2.997054	-1.123664
46	1	0	-2.325995	-2.596746	0.561485

A1.5. Optimized Geometric Outputs for Photodimers of 1g**Table A17** Optimized geometric parameters for *anti*-HT dimer of 1g

Standard orientation for <i>anti</i> -HT dimer of 1g					
Center Number	Atomic Number	Atomic Type	Coordinates (Angstroms)		
			X	Y	Z
1	6	0	0.03813	0.006547	0.014054
2	1	0	0.055981	0.005757	1.004673
3	6	0	1.232596	0.008892	-0.704237
4	6	0	1.201626	-0.029461	-2.098
5	6	0	-0.012453	0.007027	-2.780297
6	1	0	-0.033639	0.027354	-3.769545
7	6	0	-1.207853	0.015627	-2.048296
8	6	0	-1.184835	0.004965	-0.65963
9	6	0	-3.649732	-0.190203	-2.076063
10	8	0	-4.664976	-0.05063	-2.711403
11	8	0	-2.453633	-0.010979	-2.712187
12	6	0	-3.652085	-0.330044	-0.594669
13	1	0	-4.384827	0.305943	-0.276029
14	6	0	-7.52941	-1.615508	1.22067
15	6	0	-6.353389	-1.665606	0.488794
16	1	0	-6.401859	-1.687727	-0.500544
17	6	0	-5.103157	-1.681535	1.106415
18	6	0	-5.071188	-1.485048	2.481425
19	6	0	-6.245914	-1.546432	3.240059
20	1	0	-6.190871	-1.623306	4.225805
21	6	0	-7.484227	-1.50099	2.608734
22	6	0	-3.855043	-1.666041	0.258308
23	6	0	-2.648282	-1.22871	2.514802
24	8	0	-1.673981	-1.109412	3.221549
25	8	0	-3.846925	-1.371028	3.143966
26	6	0	-2.575429	-1.226951	1.032081
27	1	0	-1.820557	-1.867574	0.771115
28	6	0	2.576702	0.050159	0.035437
29	1	0	3.180418	-0.79429	-0.257154
30	1	0	3.09996	0.960756	-0.210475
31	1	0	2.409148	0.014182	1.09962
32	6	0	-8.883058	-1.684233	0.49969
33	1	0	-9.440495	-2.536594	0.854465
34	1	0	-9.44804	-0.786308	0.695037
35	1	0	-8.727204	-1.780041	-0.562561
36	1	0	2.099771	0.058588	-2.683789
37	1	0	-8.399775	-1.432071	3.168937
38	1	0	-3.796088	-2.587181	-0.298888
39	6	0	-2.454576	0.010215	0.170989
40	1	0	-2.454359	0.986774	0.630965

Table A18 Optimized geometric parameters for *anti*-HH dimer of 1g

Standard orientation for <i>anti</i> -HH dimer of 1g					
Center Number	Atomic Number	Atomic Type	Coordinates (Angstroms)		
			X	Y	Z
1	6	0	-0.026134	-0.040871	-0.019009
2	6	0	-0.048424	-0.005254	1.485834
3	6	0	1.292735	0.010914	2.271293
4	6	0	2.39944	0.615531	1.443757
5	6	0	3.638679	0.949372	2.008312
6	1	0	3.792114	0.767294	3.070411
7	6	0	4.676977	1.51113	1.264449
8	6	0	4.462401	1.742702	-0.099342
9	6	0	3.244728	1.411198	-0.693842
10	1	0	3.071153	1.57267	-1.751785
11	6	0	2.228293	0.847283	0.074774
12	8	0	1.071388	0.513864	-0.626374
13	8	0	-0.914834	-0.478597	-0.702381
14	6	0	-1.848856	1.583888	2.522863
15	6	0	-0.405827	1.364297	2.154414
16	1	0	-0.090588	2.198236	1.52523
17	6	0	0.628246	1.040535	3.268785
18	6	0	-0.035966	0.378654	4.450272
19	6	0	0.713963	-0.212895	5.476647
20	1	0	1.799914	-0.191363	5.40581
21	6	0	0.123069	-0.832719	6.57833
22	6	0	-1.2746	-0.855581	6.652499
23	6	0	-2.049392	-0.265863	5.65345
24	1	0	-3.13228	-0.264756	5.706344
25	6	0	-1.429743	0.349562	4.567588
26	8	0	-2.294564	0.944751	3.651598
27	8	0	-2.624586	2.237234	1.874966
28	1	0	-0.721055	-0.792897	1.829178
29	1	0	5.241684	2.181215	-0.714492
30	1	0	1.602579	-0.942692	2.702573
31	1	0	1.258096	1.872437	3.589088
32	1	0	-1.775607	-1.330296	7.490116
33	6	0	6.001228	1.870389	1.925943
34	1	0	5.888125	2.755032	2.558862
35	1	0	6.354984	1.047327	2.551199
36	1	0	6.759873	2.083103	1.171277
37	6	0	0.980588	-1.473502	7.662027
38	1	0	1.454518	-2.385717	7.289063
39	1	0	1.767947	-0.788415	7.985174
40	1	0	0.370329	-1.733102	8.528305

Table A19 Optimized geometric parameters for *syn*-HT dimer of 1g

Standard orientation for <i>syn</i> -HT dimer of 1g					
Center Number	Atomic Number	Atomic Type	Coordinates (Angstroms)		
			X	Y	Z
1	6	0	0.022307	-0.01233	0.017742
2	6	0	0.026563	0.001361	1.523366
3	6	0	2.449471	0.023986	1.467751
4	6	0	3.580934	-0.09646	2.270282
5	6	0	4.848646	-0.06273	1.689331
6	6	0	4.995681	0.092755	0.306388
7	6	0	3.843618	0.214353	-0.472205
8	6	0	2.554876	0.171894	0.082176
9	6	0	1.316189	0.347833	-0.761943
10	6	0	-0.0355	-1.404623	-0.726453
11	6	0	2.076116	-1.677738	-2.298805
12	6	0	1.68527	-3.231991	-0.480668
13	6	0	2.207235	-4.357799	0.15091
14	6	0	1.575955	-4.871238	1.283866
15	6	0	0.42077	-4.266848	1.79239
16	6	0	-0.081198	-3.141736	1.136352
17	6	0	0.538794	-2.595208	0.001924
18	6	0	0.960036	-0.819582	-1.764912
19	8	0	1.235221	0.011957	2.153928
20	8	0	-0.980031	-0.006016	2.190315
21	8	0	2.373739	-2.823656	-1.622885
22	8	0	2.718563	-1.395809	-3.281599
23	1	0	-0.828901	0.596316	-0.296301
24	1	0	3.454334	-0.209518	3.341061
25	1	0	3.945599	0.331713	-1.547411
26	1	0	3.098664	-4.821216	-0.256489
27	1	0	-0.975326	-2.662023	1.524485
28	1	0	0.447404	-0.40023	-2.633806
29	1	0	-1.026986	-1.643458	-1.115023
30	1	0	1.317785	1.332797	-1.231962
31	1	0	5.719782	-0.155972	2.330625
32	1	0	1.995658	-5.750951	1.762182
33	6	0	-0.26266	-4.81162	3.038956
34	1	0	-0.1817	-5.90014	3.07607
35	1	0	0.203468	-4.402668	3.940097
36	1	0	-1.319686	-4.539463	3.048791
37	6	0	6.375864	0.112319	-0.335872
38	1	0	7.100024	0.592556	0.325763
39	1	0	6.718628	-0.906916	-0.536481
40	1	0	6.352771	0.656265	-1.281951

Table A20 Optimized geometric parameters for *syn*-HH dimer of 1g

Standard orientation for <i>syn</i> -HH dimer of 1g					
Center Number	Atomic Number	Atomic Type	Coordinates (Angstroms)		
			X	Y	Z
1	6	0	-0.010187	0.006693	0.010829
2	6	0	-0.007866	0.005033	1.522545
3	6	0	2.418464	0.023462	1.547417
4	6	0	3.5169	0.16266	2.387706
5	6	0	4.792657	0.175207	1.834612
6	6	0	4.980488	0.063549	0.451005
7	6	0	3.846663	-0.044823	-0.361552
8	6	0	2.553778	-0.073095	0.164931
9	6	0	1.339819	-0.236367	-0.697338
10	6	0	6.365587	0.081301	-0.149211
11	6	0	-0.59094	-1.298743	-0.659167
12	6	0	-1.38667	-2.222686	0.212334
13	6	0	0.649556	-3.423343	0.745253
14	6	0	1.173054	-4.433212	1.547136
15	6	0	2.487554	-4.844059	1.361881
16	6	0	3.285223	-4.270483	0.369042
17	6	0	2.726756	-3.264139	-0.420456
18	6	0	1.411702	-2.812828	-0.248246
19	6	0	0.849304	-1.699261	-1.080292
20	6	0	4.714103	-4.72482	0.136762
21	8	0	1.176372	0.007959	2.188633
22	8	0	-1.026304	0.013384	2.169897
23	8	0	-0.697213	-3.127861	0.97255
24	8	0	-2.587186	-2.195408	0.304578
25	1	0	-0.555501	0.875718	-0.243486
26	1	0	3.369324	0.259992	3.423593
27	1	0	5.640456	0.342465	2.444622
28	1	0	3.976074	-0.06244	-1.410527
29	1	0	1.444322	0.333172	-1.57956
30	1	0	7.101441	0.425052	0.521539
31	1	0	6.360963	0.597583	-1.071342
32	1	0	6.669872	-0.89519	-0.420229
33	1	0	-1.181399	-1.0238	-1.506475
34	1	0	0.539404	-4.871046	2.272788
35	1	0	2.891686	-5.590526	1.985477
36	1	0	3.299348	-2.84341	-1.206681
37	1	0	0.966459	-1.874126	-2.119166
38	1	0	5.363295	-3.903382	0.086576
39	1	0	5.022076	-5.197584	1.041505
40	1	0	4.80886	-5.453627	-0.595801

A1.6. Optimized Geometric Outputs for Photodimers of 1h**Table A21** Optimized geometric parameters for *anti*-HT dimer of 1h

Standard orientation for <i>anti</i> -HT dimer of 1h					
Center Number	Atomic Number	Atomic Type	Coordinates (Angstroms)		
			X	Y	Z
1	6	0	4.954845	-0.760407	-0.261651
2	6	0	3.99547	-1.758025	-0.143442
3	6	0	2.674214	-1.413187	0.144772
4	6	0	2.295998	-0.08288	0.328557
5	6	0	3.283617	0.903227	0.183931
6	6	0	4.613293	0.592652	-0.106552
7	1	0	5.98169	-1.034171	-0.488901
8	1	0	4.243523	-2.805373	-0.277936
9	6	0	0.865858	0.278161	0.656331
10	1	0	2.989832	1.945288	0.283629
11	6	0	-0.103303	-0.937182	0.567938
12	6	0	0.440161	-2.325392	0.346985
13	1	0	-0.758666	-1.014958	1.438498
14	6	0	-0.440494	2.325773	-0.345427
15	6	0	0.103359	0.937773	-0.566797
16	6	0	-0.865521	-0.277768	-0.655587
17	1	0	0.758555	1.016088	-1.43745
18	6	0	-2.67456	1.413209	-0.145343
19	6	0	-2.295899	0.08293	-0.328579
20	6	0	-3.996067	1.757747	0.142011
21	6	0	-3.283313	-0.903397	-0.184243
22	6	0	-4.955253	0.759889	0.259918
23	1	0	-4.244494	2.805051	0.276157
24	6	0	-4.613262	-0.593104	0.10538
25	1	0	-2.989171	-1.945407	-0.283453
26	1	0	-5.982293	1.033454	0.48652
27	8	0	-1.788129	2.48759	-0.209961
28	8	0	1.787578	-2.48739	0.209722
29	8	0	0.26913	3.301406	-0.284159
30	8	0	-0.269609	-3.301013	0.287096
31	6	0	-5.65854	-1.675688	0.234766
32	1	0	-5.200253	-2.663631	0.329175
33	1	0	-6.295226	-1.51367	1.110716
34	1	0	-6.316942	-1.699497	-0.642122
35	6	0	5.65883	1.674929	-0.236476
36	1	0	6.293031	1.514402	-1.114517
37	1	0	5.200854	2.663316	-0.327579
38	1	0	6.319657	1.69647	0.638634
39	6	0	-0.760469	-1.034445	-1.985752
40	1	0	0.284095	-1.258291	-2.228304
41	1	0	-1.305098	-1.980791	-1.953401
42	1	0	-1.173623	-0.424896	-2.795467
43	6	0	0.761684	1.034719	1.986638
44	1	0	1.306475	1.980958	1.954139
45	1	0	-0.28271	1.258748	2.229748
46	1	0	1.175106	0.424951	2.796049

Table A22 Optimized geometric parameters for *anti*-HH dimer of 1h

Standard orientation for <i>anti</i> -HH dimer of 1h					
Center Number	Atomic Number	Atomic Type	Coordinates (Angstroms)		
			X	Y	Z
1	6	0	-3.696286	1.660316	-0.625009
2	6	0	-2.37044	1.274734	-0.767908
3	6	0	-1.873421	0.064397	-0.208533
4	6	0	-2.809323	-0.779339	0.460678
5	6	0	-4.134097	-0.402267	0.615288
6	6	0	-4.571793	0.813564	0.087074
7	1	0	-1.676971	1.921253	-1.297695
8	6	0	-0.549255	-0.390252	-0.238828
9	1	0	-4.815535	-1.075625	1.124032
10	1	0	-5.611313	1.102545	0.213019
11	6	0	-1.235102	-2.632618	0.716223
12	1	0	4.857548	0.073714	0.901255
13	6	0	3.980324	0.596195	0.535241
14	6	0	2.952823	-0.149488	-0.047353
15	6	0	3.860678	1.975692	0.63356
16	6	0	1.800187	0.468198	-0.535625
17	6	0	2.71674	2.637482	0.15778
18	1	0	4.663864	2.548653	1.089006
19	6	0	0.669541	-0.347816	-1.152386
20	6	0	2.236311	-2.413931	-0.528287
21	6	0	0.851982	-1.87334	-0.788999
22	1	0	0.383342	-2.52366	-1.529053
23	1	0	0.804686	2.353993	-0.77118
24	6	0	1.706112	1.862597	-0.413003
25	8	0	3.186754	-1.517713	-0.114847
26	8	0	-2.474791	-2.053147	0.901661
27	8	0	-1.122303	-3.821408	0.840821
28	8	0	2.545708	-3.57002	-0.651417
29	6	0	-4.201198	2.960447	-1.204989
30	1	0	-3.416703	3.483607	-1.758021
31	1	0	-5.038691	2.791078	-1.890934
32	1	0	-4.561269	3.633637	-0.418559
33	6	0	2.595176	4.139868	0.254814
34	1	0	2.827411	4.495484	1.264194
35	1	0	3.289528	4.640563	-0.430508
36	1	0	1.585188	4.476384	0.005815
37	6	0	0.461375	-0.034151	-2.636897
38	1	0	0.23898	1.025392	-2.793663
39	1	0	1.367076	-0.269723	-3.205226
40	1	0	-0.368116	-0.619993	-3.044375
41	6	0	-0.118873	-1.65686	0.428021
42	1	0	-1.131597	1.210491	3.038245
43	6	0	-0.167596	1.450145	3.491648
44	1	0	0.184029	0.597084	4.07606
45	1	0	0.556391	1.679972	2.707166
46	1	0	-0.280639	2.314822	4.149085
47	1	0	0.436648	-1.502804	1.366516

Table A23 Optimized geometric parameters for *syn*-HT dimer of 1h

Standard orientation for <i>syn</i> -HT dimer of 1h					
Center Number	Atomic Number	Atomic Type	Coordinates (Angstroms)		
			X	Y	Z
1	6	0	3.163764	-1.579256	0.258407
2	6	0	2.657854	-0.3047	-0.010826
3	6	0	1.550206	0.224862	0.667717
4	6	0	0.954127	-0.56882	1.65215
5	6	0	1.435162	-1.843833	1.944861
6	6	0	2.53154	-2.341794	1.250508
7	1	0	3.127138	0.293249	-0.786657
8	6	0	1.041551	1.627517	0.39565
9	1	0	0.935591	-2.424906	2.712382
10	1	0	2.899251	-3.338191	1.480253
11	6	0	-0.366575	1.841343	1.020613
12	6	0	-1.041512	1.627129	-0.396696
13	6	0	-1.550284	0.224442	-0.667937
14	6	0	0.366548	1.840709	-1.021748
15	6	0	-0.954077	-0.569948	-1.651769
16	6	0	-2.658034	-0.30459	0.010783
17	6	0	-1.435065	-1.845138	-1.943635
18	6	0	-3.163947	-1.579347	-0.257641
19	1	0	-3.12742	0.293914	0.786128
20	6	0	-2.53157	-2.342592	-1.249068
21	1	0	-0.935423	-2.426796	-2.710666
22	1	0	-2.899258	-3.339149	-1.478157
23	8	0	0.136091	-0.166408	-2.418234
24	8	0	-0.135928	-0.164787	2.418489
25	6	0	4.36953	-2.106704	-0.482603
26	1	0	4.44972	-1.664011	-1.479307
27	1	0	5.298641	-1.877216	0.054007
28	1	0	4.322347	-3.193712	-0.597901
29	6	0	-4.36982	-2.106239	0.483581
30	1	0	-4.44995	-1.663072	1.480083
31	1	0	-5.298888	-1.876836	-0.05314
32	1	0	-4.322813	-3.193198	0.59939
33	6	0	2.095484	2.677746	0.761004
34	1	0	2.397029	2.573554	1.808418
35	1	0	2.989495	2.567625	0.140269
36	1	0	1.704275	3.690279	0.614716
37	6	0	-2.095404	2.677334	-0.762502
38	1	0	-2.397254	2.572572	-1.809782
39	1	0	-2.989256	2.567765	-0.141448
40	1	0	-1.703856	3.689814	-0.616914
41	1	0	-0.514345	2.879363	1.328565
42	1	0	0.514206	2.878514	-1.330437
43	6	0	0.818603	0.98806	-2.176431
44	6	0	-0.818475	0.989514	2.175975
45	8	0	-1.758255	1.268832	2.881842
46	8	0	1.758485	1.266897	-2.882368

Table A24 Optimized geometric parameters for *syn*-HH dimer of 1h

Standard orientation for <i>syn</i> -HH dimer of 1h					
Center Number	Atomic Number	Atomic Type	Coordinates (Angstroms)		
			X	Y	Z
1	6	0	3.7665	-0.547408	0.0516
2	6	0	2.592003	-0.96874	0.679695
3	6	0	1.367837	-1.084078	0.00251
4	6	0	1.35862	-0.76595	-1.357775
5	6	0	2.514149	-0.34989	-2.018964
6	6	0	3.707163	-0.240376	-1.316059
7	1	0	2.630595	-1.214745	1.737014
8	6	0	0.098218	-1.558568	0.66854
9	1	0	2.45263	-0.116329	-3.076358
10	1	0	4.604268	0.085386	-1.83583
11	6	0	-0.988087	-1.263769	-1.697248
12	6	0	-1.039565	-1.918052	-0.331085
13	1	0	-1.187481	-2.987648	-0.516263
14	1	0	-2.755652	3.043072	-1.132689
15	6	0	-1.891011	2.692845	-0.579778
16	6	0	-1.928583	1.410559	-0.029511
17	6	0	-0.768704	3.489196	-0.398306
18	6	0	-0.844759	0.895997	0.692923
19	6	0	0.332831	3.023894	0.335246
20	1	0	-0.749046	4.488007	-0.826004
21	6	0	-0.914851	-0.485599	1.323497
22	6	0	-3.290871	-0.572513	0.137573
23	6	0	-2.072265	-1.293372	0.659792
24	1	0	-2.451285	-2.075131	1.319389
25	1	0	1.113412	1.362773	1.436466
26	6	0	0.266605	1.735844	0.868748
27	8	0	-3.127114	0.735829	-0.217582
28	8	0	0.219018	-0.815043	-2.150399
29	8	0	-1.94702	-1.176985	-2.421461
30	8	0	-4.382992	-1.071864	0.053203
31	6	0	0.374439	-2.749748	1.60159
32	1	0	0.912329	-3.529639	1.054107
33	1	0	0.982364	-2.466103	2.464558
34	1	0	-0.551299	-3.188179	1.984324
35	6	0	5.066596	-0.438486	0.813209
36	1	0	4.920866	-0.618506	1.88178
37	1	0	5.803129	-1.165878	0.452272
38	1	0	5.515079	0.554668	0.699595
39	6	0	1.5628	3.881482	0.516864
40	1	0	2.210714	3.839358	-0.367303
41	1	0	1.298228	4.931911	0.674225
42	1	0	2.158039	3.551926	1.373211
43	6	0	-0.95218	-0.372302	2.850593
44	1	0	-0.037895	0.089389	3.236986
45	1	0	-1.79157	0.260698	3.156647
46	1	0	-1.073866	-1.346326	3.331858

1.7. Optimized Geometric Outputs for Photodimers of 1k

Table A25 Optimized geometric parameters for *anti*-HT dimer of 1k

Standard orientation for <i>anti</i> -HT dimer of 1k					
Center Number	Atomic Number	Atomic Type	Coordinates (Angstroms)		
			X	Y	Z
1	6	0	-0.780657	-0.449491	-0.645891
2	6	0	-3.048465	-1.515535	-0.209365
3	1	0	-2.56924	-2.488428	-0.272067
4	6	0	-4.414747	-1.443638	0.040702
5	1	0	-4.998735	-2.353578	0.154215
6	6	0	-5.0314	-0.190098	0.148809
7	6	0	-4.270748	0.972466	0.024572
8	1	0	-4.732469	1.947404	0.123515
9	6	0	-2.904112	0.868219	-0.219996
10	6	0	-2.260814	-0.36661	-0.359378
11	8	0	-6.365682	-0.040466	0.386118
12	6	0	-0.4921	-1.214948	-1.943581
13	1	0	-0.840691	-2.248859	-1.885216
14	1	0	0.582231	-1.235883	-2.157503
15	1	0	-0.995869	-0.727099	-2.783817
16	6	0	-0.884148	2.192194	-0.409199
17	8	0	-0.383432	3.289801	-0.363091
18	8	0	-2.241905	2.08993	-0.294265
19	6	0	-0.073115	0.935489	-0.587827
20	1	0	0.563594	1.12023	-1.456104
21	6	0	4.423077	1.434158	-0.094784
22	1	0	5.028506	2.322739	-0.233196
23	6	0	3.063605	1.517889	0.171854
24	1	0	2.591212	2.494689	0.227352
25	6	0	2.265856	0.376066	0.351902
26	6	0	2.894849	-0.863314	0.225599
27	6	0	4.260457	-0.980446	-0.036857
28	1	0	4.693619	-1.972558	-0.122746
29	6	0	5.028226	0.173439	-0.190646
30	6	0	0.791109	0.475873	0.660747
31	8	0	6.366708	0.136243	-0.4468
32	6	0	0.532526	1.246103	1.961735
33	1	0	-0.537866	1.279838	2.193167
34	1	0	0.891432	2.275832	1.895483
35	1	0	1.044779	0.75378	2.794265
36	6	0	0.869899	-2.170453	0.454994
37	8	0	0.3614	-3.26538	0.430962
38	8	0	2.228265	-2.080971	0.329482
39	6	0	0.071762	-0.903309	0.613062
40	1	0	-0.574034	-1.069668	1.478225
41	1	0	6.659989	-0.783462	-0.490378
42	1	0	-6.775641	-0.912573	0.456845

Table A26 Optimized geometric parameters for *anti*-HH dimer of 1k

Standard orientation for <i>anti</i> -HH dimer of 1k					
Center Number	Atomic Number	Atomic Type	Coordinates (Angstroms)		
			X	Y	Z
1	6	0	-1.351086	2.115834	1.102244
2	6	0	-0.227604	1.181355	0.747809
4	6	0	-1.941325	-0.607462	0.302869
5	6	0	-2.410465	-1.883529	-0.040983
6	1	0	-1.707471	-2.710346	-0.073851
7	6	0	-3.743044	-2.131186	-0.352085
8	6	0	-4.664563	-1.076629	-0.318305
9	6	0	-4.239943	0.201608	0.040003
10	1	0	-4.944661	1.0226	0.092975
11	6	0	-2.899328	0.416523	0.351761
12	8	0	-2.614805	1.715398	0.749389
13	8	0	-1.207812	3.188911	1.627409
14	6	0	1.351036	2.115758	-1.102349
15	6	0	0.227576	1.181324	-0.747775
16	1	0	-0.609468	1.409472	-1.410088
17	6	0	0.485763	-0.351323	-0.647983
18	6	0	1.941331	-0.607468	-0.302798
19	6	0	2.410522	-1.883529	0.041008
20	1	0	1.707557	-2.710369	0.073888
21	6	0	3.74312	-2.131157	0.352057
22	6	0	4.664611	-1.07658	0.318257
23	6	0	4.239951	0.201651	-0.040032
24	1	0	4.944648	1.022657	-0.093044
25	6	0	2.899321	0.416534	-0.351745
26	8	0	2.614766	1.715374	-0.749436
27	8	0	1.207756	3.18885	-1.627484
28	1	0	4.065944	-3.134252	0.619252
29	1	0	-4.065834	-3.134286	-0.619305
30	8	0	5.985066	-1.237343	0.614605
31	1	0	6.151746	-2.162435	0.838162
32	8	0	-5.985003	-1.237414	-0.614708
33	1	0	-6.151656	-2.162507	-0.838283
34	6	0	0.078966	-1.149776	-1.890034
35	1	0	0.180574	-2.22823	-1.733159
36	1	0	-0.953826	-0.945139	-2.180047
37	1	0	0.732324	-0.88001	-2.726643
38	1	0	0.609436	1.409486	1.41008
39	6	0	-0.079023	-1.149656	1.890219
40	1	0	-0.180489	-2.228122	1.733348
41	1	0	0.953708	-0.94489	2.180349
42	1	0	-0.732507	-0.879953	2.72675

Table A27 Optimized geometric parameters for *syn*-HT dimer of 1k

Standard orientation for <i>syn</i> -HT dimer of 1k					
Center Number	Atomic Number	Atomic Type	Coordinates (Angstroms)		
			X	Y	Z
1	6	0	0.041012	-1.976591	-1.083883
2	6	0	0.046092	-1.120406	-2.319992
3	6	0	1.496814	0.44209	-1.178652
4	6	0	2.045226	1.715642	-1.291194
5	6	0	2.813998	2.223018	-0.243764
6	6	0	3.025573	1.449439	0.903833
7	6	0	2.467051	0.178202	0.987071
8	6	0	1.683712	-0.359219	-0.044148
9	6	0	1.114659	-1.762222	0.020557
10	6	0	-1.114613	-1.762237	-0.020571
11	6	0	-0.046043	-1.120402	2.319975
12	6	0	-1.496826	0.442053	1.178657
13	6	0	-2.045274	1.715588	1.29121
14	6	0	-2.814046	2.222958	0.243777
15	6	0	-3.025587	1.44939	-0.903834
16	6	0	-2.467031	0.178168	-0.987081
17	6	0	-1.683689	-0.359245	0.044139
18	6	0	-0.040963	-1.976593	1.08387
19	8	0	0.766561	0.038077	-2.290385
20	8	0	-0.568121	-1.393615	-3.323309
21	8	0	-0.76657	0.038046	2.29039
22	8	0	0.568102	-1.393651	3.323323
23	1	0	0.019575	-3.013618	-1.427737
24	1	0	1.873911	2.302732	-2.185184
25	1	0	2.629839	-0.406845	1.886462
26	1	0	-1.873986	2.302671	2.18521
27	1	0	-2.629796	-0.406873	-1.88648
28	1	0	-0.019519	-3.01362	1.427723
29	1	0	3.620266	1.838324	1.726473
30	1	0	-3.620281	1.83827	-1.726475
31	8	0	-3.330681	3.474862	0.397974
32	1	0	-3.826927	3.713213	-0.396164
33	8	0	3.330598	3.474937	-0.39795
34	1	0	3.826848	3.71329	0.396186
35	6	0	2.2268	-2.8142	0.077373
36	1	0	1.808707	-3.826625	0.069516
37	1	0	2.898924	-2.712292	-0.780927
38	1	0	2.823521	-2.703022	0.987701
39	6	0	-2.226738	-2.814232	-0.077392
40	1	0	-1.808631	-3.826651	-0.069502
41	1	0	-2.898887	-2.712314	0.780886
42	1	0	-2.823436	-2.703083	-0.987739

Table A28 Optimized geometric parameters for *syn*-HH dimer of 1k

Standard orientation for <i>syn</i> -HH dimer of 1k					
Center Number	Atomic Number	Atomic Type	Coordinates (Angstroms)		
			X	Y	Z
1	6	0	-0.630057	-1.979973	-0.686313
2	6	0	-0.425658	-1.044949	-1.861032
3	6	0	1.750243	-0.426231	-0.989258
4	6	0	2.930672	0.222177	-1.337336
5	6	0	3.975306	0.280534	-0.414699
6	6	0	3.826257	-0.315514	0.843142
7	6	0	2.635066	-0.964795	1.156841
8	6	0	1.561978	-1.03597	0.259101
9	6	0	0.266817	-1.746664	0.563945
10	6	0	-1.886278	-1.670046	0.18881
11	6	0	-3.076425	-0.960277	-0.408062
12	6	0	-1.962395	1.125823	0.069888
13	6	0	-2.000829	2.487261	-0.220482
14	6	0	-1.028172	3.329548	0.314349
15	6	0	-0.027904	2.801604	1.140731
16	6	0	-0.009855	1.437191	1.406497
17	6	0	-0.961594	0.555616	0.873703
18	6	0	-0.968161	-0.926152	1.205473
19	8	0	0.777687	-0.405097	-1.976718
20	8	0	-1.247544	-0.884966	-2.72644
21	8	0	-3.016212	0.404628	-0.468734
22	8	0	-4.069872	-1.518979	-0.793994
23	1	0	-0.612012	-2.993351	-1.102168
24	1	0	3.032006	0.675685	-2.315868
25	1	0	2.54158	-1.428141	2.133916
26	1	0	-2.273881	-2.603466	0.59913
27	1	0	-2.78766	2.881361	-0.851868
28	1	0	0.774092	1.041881	2.043249
29	1	0	4.636392	-0.279034	1.567312
30	1	0	0.730864	3.452202	1.568402
31	8	0	-1.107625	4.65448	0.004405
32	1	0	-0.373166	5.123061	0.422133
33	8	0	5.112326	0.927857	-0.798076
34	1	0	5.759453	0.885995	-0.0818
35	6	0	0.523459	-3.080154	1.285717
36	1	0	1.238577	-3.677877	0.712425
37	1	0	0.936365	-2.933571	2.287378
38	1	0	-0.392338	-3.667994	1.394147
39	6	0	-1.277655	-1.144297	2.689809
40	1	0	-1.355201	-2.205066	2.942664
41	1	0	-0.505686	-0.697226	3.324868
42	1	0	-2.228357	-0.666222	2.947604